Unione Europea
Fondo Sociale Europeo

Ministero dell'Istruzione,
dell' Università e della Ricerca

Università degli studi di
Palermo

# *Optical properties of point defects in silica: Role of the local dynamics of the host matrix*

*Andrea Cannizzo*

Supervisor Prof. Maurizio Leone

Coordinatore Prof. Natale Robba ____________________

DOTTORATO DI RICERCA IN FISICA

*Dipartimento di Scienze Fisiche ed Astronomiche*

Tesi cofinanziata dal Fondo Sociale Europeo

**PROGRAMMA OPERATIVO NAZIONALE 2000/2006**

***"Ricerca Scientifica, Sviluppo Tecnologico, Alta Formazione"***
***Misura III.4. "Formazione Superiore e Universitaria"***

# CONTENTS

# Abstract

Silica, the amorphous silicon dioxide (a-$SiO_2$), is characterized by several physical properties, some ones already well known in the past, as a wide optical transmission range from infrared up to vacuum ultraviolet, high endurance to chemical and mechanical treatments and low thermal dilatation, some ones else discovered more recently, as its photosensitivity. These properties, together with a low production cost and an easy workableness, make it a material largely used in many scientific and technological fields (**Nalwa, 2001, Devine *et al.*, 2000, Pacchioni *et al.*, 2000, Neustruev, 1994, Griscom, 1991** and references therein), such as in optical waveguides and in photonic devices. A particular attention has been devoted to the investigation of point defects embedded in silica, since their presence can influence many properties of the host matrix, as magnetic response, electronic behavior, vibrational and mechanical properties, optical features, etc. [**Elliot, 1984**].

In spite of more than fifty years of research on these issues, it has been only recently evidenced that a significant part of these remarkable properties of vitreous silica are related to its amorphous nature and to the presence of significant conformational heterogeneities [**Skuja, 1998, Leone *et al.*, 2001**]. These aspects are particularly evidenced by the studies on physical properties of point defects, whose coupling with surroundings is usually strong and non perturbative. In particular, the role played by the local dynamics in modulating the spectroscopic properties of optically active centers is not completely clarified.

In this thesis we focused our attention on three optically active point defects involving a silicon, a germanium and a tin atom (chapter 1). They constitute an iso-electronic and iso-structural series, and can be generated both inside (*bulk variant*) and on the surface (*surface variant*) of silica specimens (chapter 1). We performed a comparative investigation of their optical activities, both with steady state and with time resolved spectroscopic techniques, in order to shed new light on the effective role of the conformational disorder and of the local low frequencies dynamics of the matrix, separating them from the effects due to the particular atomic structure of the defects, such as heavy atom effects and spin-orbit interaction or short-range organization effects.

This thesis is organized in 9 chapters. In chapter 1, we introduce the physical features of the amorphous silica and of the investigated point defects; we also review the related literature and the open questions. Chapter 2 supplies the basic theoretical background to describe the optical properties of a single point defect embedded in a solid matrix. In chapter 3, we report the main details on the employed samples and on the adopted experimental techniques. In chapter 4, we report and discuss the experimental results on the optical activity of the Ge related defect; in conclusion of this chapter, a theoretical model able to rationalize the previous results is proposed. Chapter 5 shows an experimental study of Sn and Ge related defects to investigate the effects of the iso-electronic and iso-structural substitution on defect-matrix coupling. In chapter 6, we compare the experimental results of surface and bulk Ge related activities to investigate the role of the matrix on their optical and dynamical features. The role of the environment on the iso-electronic substitution is also investigated by comparing the surface Si and Ge activities. In chapter 7, we investigate the effects of matrix dynamics on the optical activities involving forbidden transitions localized on Sn and Ge related defects. Chapter 8 reports an experimental study of the sub-picoseconds relaxation dynamics in non thermalized regime in excited states. Finally, the main results are summarized in chapter 9.

The research activity reported in this thesis was carried out thanks to some collaborations between the research group of Prof. R. Boscaino of this Department and other institutions. In particular, the investigation of Ge and Sn related bulk activities was performed in collaboration with the Department of Physical Chemistry (University of Pavia, Italy) and with

the Department of Material Science (University of Milano-Bicocca, Italy), respectively , which also took care for the samples synthesis. These collaborations were supported by a national project (PRIN2002) by Italian Ministry of University Research and Technology. Concerning the investigation of surface activity, it was performed with Prof. V.A. Radzig of the N.N. Semenov Institute of Chemical Physics (Russian Academy of Sciences of Moscow, Russian Federation), who also took care for the samples synthesis.

The lifetimes of the excited states of all the activities were investigated by time resolved emission measurements in the nsec and μsec time domain, carried out at the SUPERLUMI station on the I-beamline of HASYLAB at DESY, Hamburg (Germany); whereas the study reported in chapter 8 was performed only on the Sn and Ge related bulk activities, in the laboratories of the Laboratoire de Spectroscopie Ultrarapide, Ecole Polytechnique Fédérale de Lausanne, Lausanne (Switzerland).

The results reported in this thesis have been subjects of the papers listed in appendix B.

# Chapter 1

# The Physical System

## 1.1 Amorphous silica and conformational disorder

The amorphous silica is the non crystalline form of the silicon dioxide (a-$SiO_2$) and is produced by rapid quenching of the melt (see figure 1.1). At the glass transition temperature, $T_g$(1), the liquid structure of the melt is frozen, giving rise to a material in a stable state at room temperature and, in agreement with a liquid structure, isotropic on a macroscopic scale (for a more detailed discussion on glass transition see for example **Elliot, 1984,** and **Angell, 2002**). It is worth to note that, at variance with the crystalline state, the structure associated with the amorphous state is not unique (or however discrete) and, as suggested in figure 1.1, the particular thermal history of the silica specimen affects the density but also many other properties as, for example, the refractive index, the optical scattering loss, the defects concentration, the atomic and molecular species diffusion, the mechanical strength, etc. (see **Tomozawa, 2001,** and references therein). Furthermore, the vitreous silica is related to remarkable vibrational and relaxation dynamics in spite of the strength of the Si-O bond, the

---

(1) It is worth to note that, since the transition to the glassy state is continuous, $T_g$ is not univocally defined and its value somewhat depends on the operative definition. A detailed discussion is reported by **Angell, 2002.**

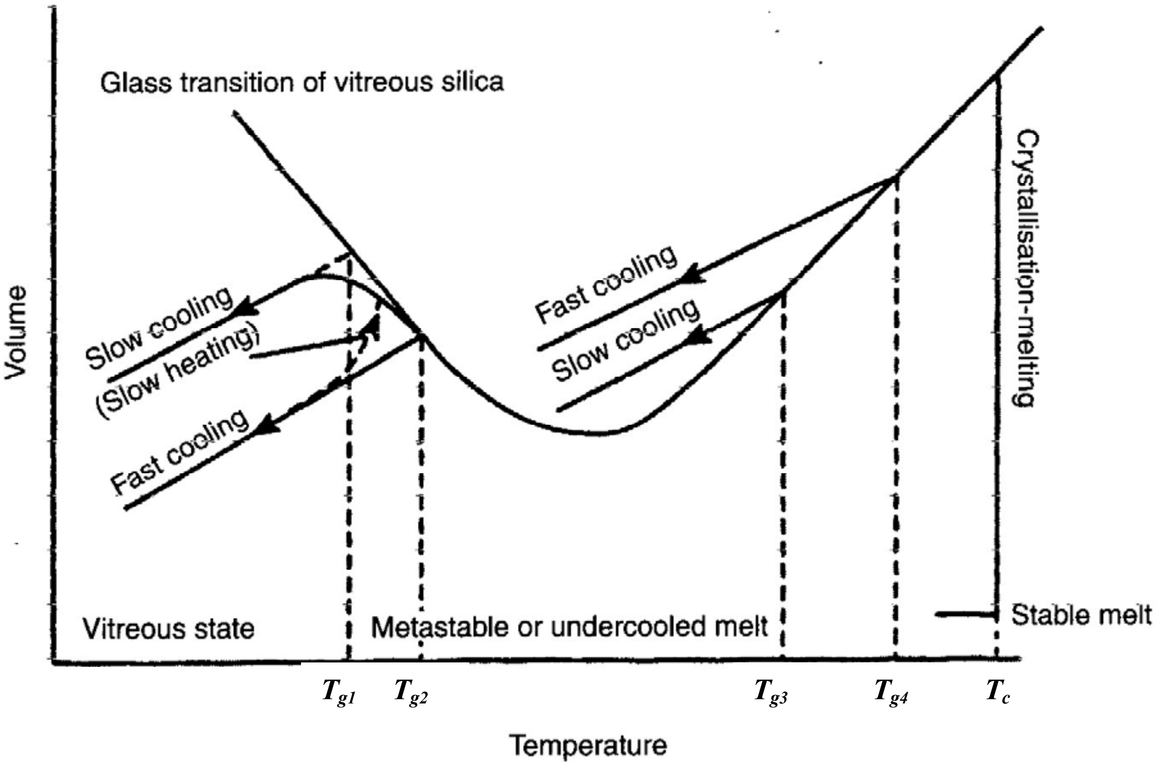

Figure 1.1. Schematic illustration of the volume change with temperature as the silica melt is cooled through the glass transition temperature, $T_g$. The arrows indicate different glass transition pathways, corresponding to different cooling rates. Each transition is characterized by a particular $T_g$. The first order melt-crystal transition at $T_c$ is also shown (from **Brückner, 1970**).

only bond of silica matrix, and characterized by a binding energy of 9 eV. The a-$SiO_2$ is indeed characterized by a vibrational density of states which, from ~1300 $cm^{-1}$, extends down to very low frequency values of ~30 $cm^{-1}$ (see figure 1.2), as proved experimentally by neutron, Raman and infrared vibrational spectra [see **Galeener, 1983,** and references therein] and, more recently, by computational methods [**Uchino and Yoko, 1997, Pasquarello and Car, 1998, Zotov *et al.*, 1999, Benoit and Kob, 2002, Umari *et al.*, 2003**]. The silica matrix, as other glassy systems (see **Elliot, 1984**), is also characterized by internal structural relaxations also at temperatures far below $T_g$. In particular, **Wakabayashi and Tomozawa, 1989,** and **Davis and Tomozawa, 1995,** observed a time dependence of the water diffusion coefficient in silica samples at 350 °C, rationalizing this behavior as an effect of structural relaxations during the diffusion process [**Tomozawa and Davis, 1999**]. More recently, **Agnello *et al.*, 2002,** reported experimental evidences of structural relaxations already at 100 °C in silica samples containing point defects.

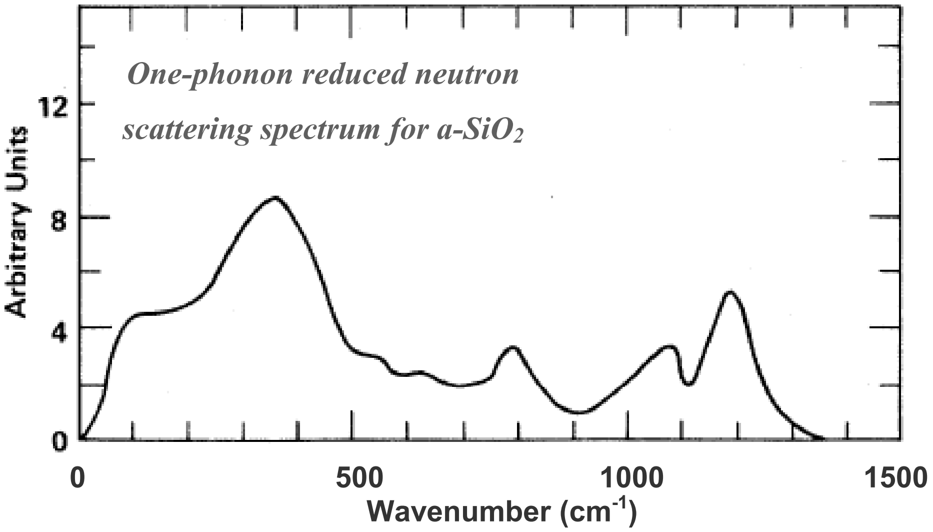

Figure 1.2. Vibrational density of states for amorphous silica (from **Galeener *et al.*, 1983**).

Regarding the microscopic scale, studies with X-ray and neutron scattering techniques revealed that the short range order of the vitreous silica is dominated by tetrahedral units (see figure 1.3(a)), very close to the ones of the crystalline silica, where a central $sp^3$ hybridized Si atom coordinates four O atoms with a Si-O distance of 1.62 Å and an O-Si-O angle of 109.5°. The silica matrix is constituted by a network of these tetrahedrons linked by Si-O-Si bridges, as reported in figure 1.3(a). Due to the absence of regularity, the X-ray and neutron diffraction studies can supply only a radial correlation function and, to extract information about the medium and the long range order, a modeling is required. The more accepted structural model for a-$SiO_2$ is the so-called *continuous random network* (CRN) model (2). It was proposed by **Zachariasen** in **1932,** and assumes that the tetrahedral units are randomly connected (in other

---

(2) Even if the CNR model is the most accepted one, it is still debated. For a detailed discussion on this issue see **Wright and Sinclair, 2000**.

words, the $\theta$ and $\phi$ angles of figure 1.3(a) are distributed) to form a matrix which lacks of any translational and orientational symmetry at a medium range order. In the light of this model, **Mozzi and Warren, 1969,** were able to extract from X-ray diffraction data the distribution of the distance between the nearest Si atoms and of the O-Si-O angle $\theta$ (see figure 1.3), with a uniform distribution for the dihedral angle $\phi$.

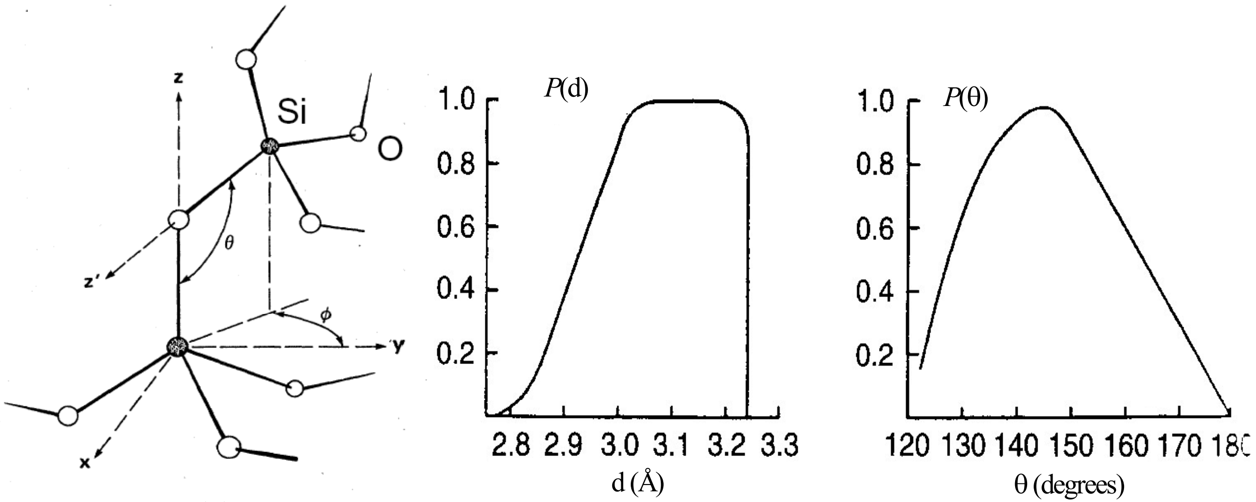

(a) (b) (c)

Figure 1.3. (a) Fragment of amorphous silica. The Si-Ô-Si angle, $\theta$, and the dihedral angle, $\phi$, are shown (from **Barrio *et al.*, 1985**). Normalized distribution function for (b) the distance between the nearest Si atoms, *d*, and (c) the Si-O-Si angle $\theta$ [**Mozzi and Warren, 1969**].

All these features prove that the vitreous silica matrix is characterized by relevant flexibility mainly due to the occurrence of low energy dihedral and bending angles, in spite of a very stiff fundamental unit. The dependence on the thermal history speaks for a system characterized by a highly degenerate amount of possible configurational minima where the system can be trapped during glass transition; whereas the presence of relaxation processes indicates that the configurational barriers separating different minima are highly dispersed [**Goldstein, 1969, Middleton and Wales, 2001**]. This complex configurational landscape reflects on the presence, inside the matrix, of different local configurational rearrangements (conformational heterogeneity), whose statistic is described by distributions in figure 1.3(b) and (c).

## 1.2 Point defects and vitreous matrix

A point defect is a localized imperfection of the host matrix. Regarding the *intrinsic* defects, i.e. involving only Si or O atoms, they include a bond rupture, a O-O or a Si-Si bond, an incorrect coordination of an Si or O atom. The presence of an impurity is, by itself, a defect, termed *extrinsic* defect. Further classifications are usually adopted with respect to particular features. With respect to the regular lattice, a defect will be named *vacancy* if due to the lack of an atom from a regular lattice position, or it will be *interstitial* if due to an atom in a non reticular position. With respect to the magnetic properties, a defect can be *dia*- or *para-magnetic*, if characterized by a zero or non zero magnetic moment, or, equivalently, by a zero or non zero total spin, respectively. In particular, two classification are noteworthy: the *substitutional* defects , i.e. extrinsic defects referable to an intrinsic defect by substitution of a matrix atom (i.e. a Si or an O atom) with the impurity, and the *bulk* and *surface* defects, i.e. defects that are surrounded by the matrix or that are located on the surface of the sample, respectively. We note that, in the case of porous silica, it is common to refer to the defects located on the internal surface of the pores as surface defects too.

The importance of defects, and the main reason of a so wide investigation devoted to this issue, lies in the fact that their presence can control many properties of the silica, both amorphous and crystalline, as magnetic response, electronic behavior, vibrational and mechanical properties, optical features, etc. [**Elliot, 1984**]. The demand of a good control of the defects growth has induced more than five decades of experimental research which showed that their presence and concentration is strongly affected by the thermal history of the sample, as already discussed, but also by the specific manufacturing process and successive treatments, as heating, mechanical stresses, exposure to reactive atmospheres or to particle and ionizing radiation, etc. [**Deeryhée *et al.*, 2000**, **Paillet *et al.*, 2000**].

Regarding the optical properties of silica and the presence of point defects, since the fifties it has been seen that the typical transmittance range (8000÷0.11 nm or 0.16÷9 eV) is completely dominated by the presence of point defects [**Garino-Canina, 1954** and **1956**]. They are, indeed, characterized by localized energy levels which allow electronic transitions with energies lower than the conduction band. These localized transitions are responsible of the optical absorption (OA) bands and of the related photoluminescence (PL) bands that are detected in the visible (Vis) and ultraviolet (UV) range, 1.8÷9 eV (see chapter 2). The optical bands usually observed in vitreous silica are quite broadened, with typical values of full width at half maximum (FWHM) of ~0.5 eV, without a resolved vibrational structure and with an almost gaussian shape. Apart from the term due to the finite lifetime of the excited states, two main contributions are present: i) the *homogeneous broadening*, common to amorphous and crystalline systems, is due to the electron-phonon coupling (see chapter 2) of the defect with the local vibrational modes and affects all the defects in the same way; ii) the *inhomogeneous broadening* is due to the effects of the site-to-site non-equivalence (local disorder), which induces a random orientation and a spread of the geometries of the defect and of the local surrounding. This spread will reflect on a dispersion of all the properties (3) of point defects, which will be described by a proper probability distribution, and in particular of the transition energies which will induce an additional inhomogeneous broadening in the optical line profiles. It is worth to note that the effects of local disorder can concern not only static features, as the energy level spacing or the defect geometry, but also dynamical processes, both thermally (structural relaxations, inter-system crossing processes, diffusions, chemical reactions, etc.) and not thermally activated (internal conversions, photolysis mechanisms, etc.).

To take account of these effects on the optical activity in silica, it is usually assumed the simplest model which considers that the main consequence of the amorphous nature of the host matrix is to induce a random orientation of the defect, whereas the inhomogeneous broadening rising from the geometry dispersion is assumed negligible. As discussed by **Skuja, 1998,** the main idea is that, since regular matrix has a short range order, no dramatic distortions are expected on the geometry of point defects, mainly on those defects with very localized structures. Furthermore, the optical bands in silica are usually characterized by a homogenous broadening which is comparable or greater then the inhomogeneous one [**Skuja, 1998**]. The most part of experimental and computational works of previous century were silently based on this simplified model, however detailed studies in the last decade has shown that this assumption is rather rough.

Firstly, in the light of the previous scheme, several analogies between defects in glassy and in crystalline silica should be expected, since both systems show the same short range order, and this is not the case. Moreover it is by now universally accepted that there exist many defects which are specific to the glassy state and can not find a stable configuration within the crystalline structure constraints. This result is not surprising, considering the relevant flexibility of the silica matrix previously evidenced and the occurrence of many possible host configurations, but it strongly suggests that this flexibility is reflected also on the structures of embedded point defects. Accordingly, the surface defects, for which further

---

(3) Particularly relevant is the inhomogeneous broadening effects on the electron paramagnetic resonance (EPR) spectra of paramagnetic defects in vitreous silica [see review papers of **Griscom, 1991,** and **Skuja**, **1998**].

freedom degrees are added, show significant differences with respect to those in the bulk environment [**Radzig, 1995a** and **2000**].

A further and tricky effect of the conformational heterogeneity in disagreement with the previous simplified model is the rising of anomalous correlations between different properties associated with a particular point defect (see chapter 4). Even if this aspect was pointed out already ten years ago [**Skuja, 1992, Amossov and Rybaltovsky, 1994, Radzig, 1995a**], only in few recent works it has been expressly studied [**Skuja *et al.*, 1995, Bagratashvili *et al.*, 1995** and **2000, Nishikawa *et al.*, 1997, Leone *et al.*, 1997** and **1999a, Martini *et al.*, 1998, Anedda, 2002, Rybaltovsky *et al.*, 2002, Sakoh *et al.*, 2003**]. Some authors [**Bagratashvili *et al.*, 1995** and **2000, Radzig, 1995a, Leone *et al.*, 1999a**] suggested that these cross-correlations are due to the effects of the same geometry distortion on the different measurable properties of a point defects, which do not result any more independent. This microscopic link is reflected on mutual dependences between different properties experimentally detectable. It is worth to note that this picture assumes silently the CRN model, giving the impression to be model depending. In this respect, we want to observe that also those models that suppose the presence of middle order range, as the *crystallite model* [**Frankenheim, 1835,** and **Lebedev, 1921**], localize the defects in less ordered regions where a great dispersion of the conformational coordinates is predicted [**Wright and Sinclair, 2000**].

### *1.2.1 The oxygen deficient point defects and B-type activity*

Among the different point defects in silica, a particular attention has been devoted to the study of centers related to an oxygen deficiency, or Oxygen Deficiency Centers (ODCs), since they play a key role in photosensitivity and in Bragg grating writing processes in optical fiber (see **Askins, 2000,** and references therein).

There are three main intrinsic ODCs in silica which are experimentally distinguishable by their optical and magnetic properties (see the review paper of **Skuja, 1998,** for a detailed discussion): i) the *E' center* [**Weeks, 1956**], which is a paramagnetic defect and consists of an unpaired electron on a dangling bond of a three-coordinated Si atom; it is associated with an OA band (the E' band) at 5.8 eV, which does not induce any luminescence; ii) the *neutral oxygen vacancy*, whose structure is a direct bond between two Si atoms [**O'Reilly and Robertson, 1983**]; it is a diamagnetic defect and it is almost universally considered accountable for an OA band at 7.6 eV, named E band [**Imai *et al.*, 1988**]; iii) the *two-fold coordinated silicon*, which consists of a lone pair localized on a Si atom, which coordinates two O atoms [**Skuja *et al.*, 1984**]; it is diamagnetic and is associated with an optical activity, called A activity, made up by an OA band at 5.03 eV with two related emission at 4.4 eV and 2.7 eV [**Tohmon *et al.*, 1989, Skuja, 1992** and **1994a**].

In this thesis we will focus our attention on the last defect and on the related substitutional defects: the *two-fold coordinated germanium* and the *two-fold coordinated tin*. In this section we will outline the state of the art on these three defects, while their history will be reported in the next section. The occurrence of this iso-electronic and iso-strucutural series in bulk a-$SiO_2$ was evidenced by **Skuja, 1992,** on the basis of the comparison of respective optical properties and later supported by computational works of **Zang and Raghavachari, 1997,** and **Pacchioni and Ferrario**, **1998**. All these three defects are, indeed, characterized by similar optical activities. They show to have a $C_{2v}$ symmetry and are characterized by an OA band at ~5 eV and by two related PL bands: a fast decaying, allowed, transition at ~4 eV and a slowly decaying, forbidden, transition at ~3 eV. Both the emissions can be excited within the 5 eV OA band, while the slow one can be also weakly excited around 3.5 eV for all the three activities. The 5 eV OA band is assigned to an electronic promotion from the singlet ground state $\boldsymbol{S_0}$ to the first excited singlet state $\boldsymbol{S_1}$ of these centers, while the fast emission is associated with the inverse $\boldsymbol{S_1 \rightarrow S_0}$ transition. The presence, in all the three activities, of a thermally activated intersystem crossing process (ISC) between $\boldsymbol{S_1}$ and the triplet excited state $\boldsymbol{T_1}$ gives rise to the slow emission, corresponding to the $\boldsymbol{T_1 \rightarrow S_0}$ transition. The $\boldsymbol{T_1}$ state can be populated also by a direct $\boldsymbol{S_0 \rightarrow T_1}$ excitation, which corresponds to the weak absorption at ~3.5 eV. The energy level scheme, which accounts for all the three activities, and the respective observed optical transitions are reported in figure 1.4**.** For the sake of clarity, we have adopted here and in the following an unified notation for these activities: the 5 eV OA band will be named *$B_{2T}$ band*, the fast emission *$\alpha_T$ band* and the slow emission *$\beta_T$ band*, where T stands for Si, Ge or Sn. To indicate the three optical activities, we will speak of Si, Ge or Sn related *B-type* activity, since the most studied and the most discussed in literature among the three it is the Ge related one, which is also called B activity(4). Furthermore, to indicate the belonging to the same iso-valence series, it is been adopted the symbol $=T^{\bullet\bullet}$ or $T_2^0$ to designate the structural model(5), with the same previous meaning of T. In agreement with the allowed and forbidden character for the $\alpha_T$ and $\beta_T$ emissions, respectively, we observe in the table of figure 1.4 that the $\boldsymbol{S_1}$ radiative decay time is typically 10 ns, whereas the $\boldsymbol{T_1}$ related one is longer than 10 μs for all the activities. It is worth to note that, in agreement with **Skuja, 1994a, Leone *et al.*, 1997** and **2001**, and **Rybaltovskii, 2002**, the only non radiative relaxation process which affects the B-type activity is the inter-system crossing process linking $\boldsymbol{S_1}$ and $\boldsymbol{T_1}$. In agreement with the picture of a very localized center, the pure

---

(4) Since the different activities were studied separately, a common notation has not been developed. Regarding the notation here used, the main variations are: $B_{2Si}$, $B_{2Ge}$, $\alpha_{Si}$, $\alpha_{Ge}$ and $\beta_{Si}$ instead of $B_{2\alpha}$, $B_{2\beta}$, $\alpha_I$, $\alpha_E$ and $\gamma$, respectively, while Si, Ge and Sn related B-type activities correspond, in the same order, to A, B and C activities.

(5) Concerning the notation $=T^{\bullet\bullet}$, the symbol (=) represents the bond with two oxygen atoms and the symbol (••) represents the two paired electrons. About the notation $T_2^0$, the subscript indicates the coordination number and the superscript the total electric charge.

triplet nature of $T_1$ is more and more weakened increasing the atomic number of the constituent atom, as proved by the shortening of the $T_1$ radiative decay time and the increasing of the ISC efficiency [**Skuja, 1992**]. All the previous results concern the bulk variant of the $=T^{\bullet\bullet}$ and were obtained in the previous simplified model. As already discussed, this frame is usually inappropriate to a detailed reading of the experimental results and to a deep understanding of the role of the matrix, and its disorder, on the properties of point defects. This aspect has been expressly faced in few works [**Bagratashvili *et al.*, 1995** and **2000, Nishikawa *et al.*, 1997, Leone *et al.*, 1997** and **1999a, Martini *et al.*, 1998, Anedda, 2002, Rybaltovsky *et al.*, 2002, Sakoh *et al.*, 2003**] and, in particular, Ge-doped silica samples containing $=Ge^{\bullet\bullet}$ proved to be a good system to study the structural and dynamic properties of silica matrix and to point out the role of the conformational disorder [**Leone *et al.*, 1997** and **1999a**]. Indeed, the detailed analysis of the $\alpha_{Ge}$ and $\beta_{Ge}$ emissions as a function of temperature and of excitation energy in the UV range [**M. Leone *et al.*, 1997** and **1999a**], has shown that $S_1$ lifetime and the ISC rate, $k_{ISC}$, are quite sensitive to the local dynamics and disorder of the host matrix [**M. Leone, *et al.*, 1999a**]. In Chapter 4 we will discuss in more details these aspects.

Concerning the surface variants of the $=T^{\bullet\bullet}$ centers, much less attention has been devoted to their optical properties [**Skuja *et al.*, 1984, Bagratashvili *et al.*, 1995, Radzig, 1995a**], and the surface $=Sn^{\bullet\bullet}$ variant has not been so far observed. Furthermore, at our knowledge, only few detailed works in un-doped [**Skuja *et al.*, 1984, Bagratashvili *et al.*, 1995**] and no one on Ge-doped silica have been so far performed. The main differences with respect to the bulk activity consist in a grater efficiency of the ISC process and in a 0.2 eV blue-shift of the OA bands. Regarding the $S_1$ and the $T_1$ radiative decay times, **Bagratashvili *et al.***, in **1995**, reported the values of 12.2 ns and 18 ms, respectively; for the surface $=Si^{\bullet\bullet}$, while, at our knowledge, no analogous data on the surface $=Ge^{\bullet\bullet}$ are known.

The occurrence of an iso-structural and iso-electronic series, both in the bulk and in the surface variant, supplies a powerful tools in order to investigate the effective role of the host matrix in affecting the optical features of these defects, but no work with this aim has been so far performed. This thesis tries to fill this lack.

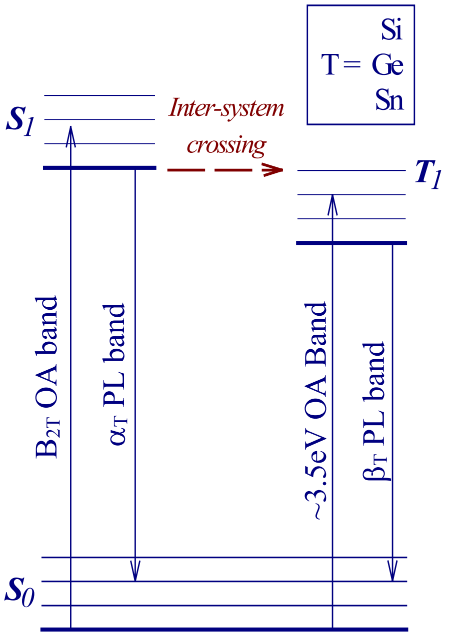

| | $=\mathrm{Si}^{\bullet\bullet}$ | $=\mathrm{Ge}^{\bullet\bullet}$ | $=\mathrm{Sn}^{\bullet\bullet}$ |
|---|---|---|---|
| $S_0 \rightarrow S_1$ | 5.0 | 5.1 | 4.9 |
| $S_1 \rightarrow S_0$ | 4.45 | 4.3 | 4.1 |
| $S_0 \rightarrow T_1$ | 3.3 | 3.7 | 3.7 |
| $T_1 \rightarrow S_0$ | 2.7 | 3.15 | 3.1 |
| $S_1$ radiative decay time | 4 ns$^{(a)}$ | 7 ns$^{(b)}$ | 10 ns$^{(c)}$ |
| $T_1$ radiative decay time | 10 ms | 110 μs | 10 μs |

Figure 1.4. (left) Energy levels scheme of the two-fold coordinated Si, Ge and Sn atoms in a-$SiO_2$; the solid and dashed lines represent the radiative transitions and the inter-system crossing process, respectively. (right) The observed values of the transition energies, given in eV, for the bulk activities. $^{(a)}$From **Boscaino *et al.*, 1996**; $^{(b)}$From **Leone *et al.*, 1999a**; $^{(c)}$From **Chiodini *et al.*, 2000**; the other data from **Skuja 1992** and **1994a**.

### *1.2.2 History of B-type activity*

The first works on the absorption and emission bands in a-$SiO_2$ were done in the fifties [**Garino-Canina, 1954** and **1956, Cohen, 1957**]. **Garino-Canina** observed several luminescence bands under excitation energy at 5 eV and, in particular, three emission bands centered at ~4.3, ~3.2 and ~2.7 eV, that he named $\alpha$, $\beta$ and $\gamma$ bands, respectively (see note 4). **Cohen** reported the presence of an OA band at ~5.1 eV both in natural glassy silica and neutron irradiated one. **Mitchell and Piage** in **1957** termed *$B_2$ band* the OA band found by Cohen. Since this activity is induced by neutrons, **Garino-Canina** and **Cohen** proposed that the related defect is an intrinsic ODC. Furthermore, **Garino-Canina** observed an increasing of the $B_2$ related activity in Ge doped silica. In **1973**, **Arnold** reported the increasing of the $B_2$ band after $H^+$ implantation and proposed, as a structural model, the neutral oxygen vacancy, assuming a knock-on process where an O atom is displaced by a $H^+$ ion.

In **1978**, **Skuja *et al.*** estimated a value of 10 ns as an upper limit for the ~4.3 eV emission lifetime and, in agreement with an allowed character of the $B_2$ band, suggested a related singlet-singlet transition. In **1984**, **Skuja *et al.*** affirmed that the $B_2$ band is centered at 5.03 eV (what we call $B_{2Si}$ band) and it is associated with two emission bands at 4.3 and at 2.7 eV. The two-fold coordinated silicon model was proposed, for the first time, in this paper, also in comparison with the corresponding surface optical activity, and the α and γ emissions were associated with an $\boldsymbol{S_1 \rightarrow S_0}$ and $\boldsymbol{T_1 \rightarrow S_0}$ transition, respectively. In this paper, the authors assigned the β band to a triplet emission of the substitutional $=Ge^{\bullet\bullet}$.

In **1988**, **Imai *et al.*** reported the growing of the E' related activity with an opposite behavior of the $B_2$ and α bands under laser irradiation at 6.4 eV, supporting the neutral oxygen vacancy model of **Arnold, 1973**. In the same year, **Nagasawa *at al.*, 1988** corroborated this model by asserting that the E' defect generation under UV light happens only in a-$SiO_2$ specimens characterized by a relevant $B_2$ band.

In **1989**, **Kohketzu *et al.*** and **Tohmon *et al.*** wrote that the $B_2$ band is due to two different contributions which overlap around ~5 eV; they observed a composite nature also for the α band. In the paper of **Tohmon *et al.***, the two components of the $B_2$ band are named for the first time $B_{2\alpha}$ and $B_{2\beta}$ (in the following $B_{2Si}$ and $B_{2Ge}$). The former is centered at 5.02 eV (FWHM = 0.35 eV) and is associated with a strong emission at 4.42 eV and a very weak one at 2.7 eV. The $B_{2Ge}$ band is centered at 5.15 eV (FWHM = 0.48 eV) and it is characterized by two strong emissions at 4.24 and 3.16 eV. The authors termed this activity A and B, respectively, and suggested that they are related to two different defects. Adopting the notation previously introduced, the 4.42 and the 4.24 eV band are named $\alpha_{Si}$ and $\alpha_{Ge}$.

In **1992** and **1994**, **Skuja** proposed the existence of the iso-electronic and iso-structural $=T^{\bullet\bullet}$ model, as reported in the previous section. In the paper of **1994**, this author reported that the thermal behavior of the ISC efficiency for the Si related activity is in agreement with a thermally activated process governed by an activation barrier of 0.13 eV. In the same year, **Hosono and Abe** observed that the $B_{2Si}$ is significantly reduced by UV irradiation, with the simultaneous growing of Ge related E' center, whereas the $B_{2Ge}$ does not change. The authors rationalized these results suggesting the $B_{2Si}$ band is related to a neutral oxygen vacancy involving two Ge atoms, while defect accounting for the $B_{2Ge}$ band is still the $=Ge^{\bullet\bullet}$.

In **1994**, **Tsai *et al.*** reported a root square growing of the $B_{2Ge}$ band with the Ge content, proposing an extensive defect involving more Ge atoms.

In **1995**, **Bagratashvili *et al.*** pointed out the inhomogeneous nature of the Si related B-type activity in vitreous silica by photochemical and photoluminescence studies. They suggested that the inhomogeneous character of the ODC optical properties is due to small geometrical differences of the centers. They reported also that the non radiative channels from $S_1$ and $T_1$ toward $S_0$ are negligible. In this year, **Skuja *et al.*** showed the presence of an inhomogeneous broadening of ~0.1 eV in the so-called R band, a luminescence band centered at 1.9 eV and excitable at 2.0 and 4.8 eV.

In **1997**, **Leone *et al.*** reported measurements on the Ge related B-type activity as a function of temperature, corroborating the $=Ge^{\bullet\bullet}$ model and the absence of non radiative relaxation channels toward $S_0$. The authors observed that the $k_{ISC}$ is spread by the conformational heterogeneity of the silica matrix. They also found that its efficiency is strongly thermally dependent, decreasing of two orders on lowering the temperature from

300 K down to 120 K, with a subsequent freezing of the ISC mechanisms below 100 K. A typical activation barrier of 70 meV was found to govern the thermal activation of the ISC process. In the same year, **Zang and Raghavachari** corroborated the $=T^{\bullet\bullet}$ model obtaining an excellent agreement with the experimental data of the absorption and luminescence activity for the Si and Ge related defects, using first-principle quantum-chemical simulation techniques.

In **1998**, **Pacchioni and Ferrario** extended successfully their *ab initio* calculations, based on the $=T^{\bullet\bullet}$ model, to the Sn activity, and to evaluate the radiative decay time for all the three activities. In this year, **Martini *et al.*** reported a detailed mapping of the excitation-emission UV pattern of the Ge related B-type activity, corroborating the results of **Leone *et al.*, 1997,** and revealing the presence of cross-correlation effects.

**Agnello *at al.*, 1998** and **2000**, observed the growing of Ge related paramagnetic defects under $\gamma$ irradiation and a simultaneous decreasing of Ge related B-type activity. The linear correlation between the final content of paramagnetic defects and the $\beta_{Ge}$ band intensity before the irradiation was rationalized assuming an interconversion mechanism based on the $=Ge^{\bullet\bullet}$ model for the Ge related B-type activity. In this respect, **Essid *et al.*, 1999,** reported a linear relation between the initial $B_{2Ge}$ band intensity and the Ge related paramagnetic centers content, obtained by laser irradiation at 5 eV.

**Leone *et al.*, 1999a** and **1999b**, reported the time decay of the $\alpha_{Ge}$ at low and room temperature. At 10 K the behavior is well described by a single exponential decay law with a decay time of $7.3 \pm 0.1$ ns, whereas a non exponential behavior is observed at room temperature. The authors ascribed this result to the dispersion of $k_{ISC}$ which affects the $\boldsymbol{S_1}$ lifetime, this effect been negligible at low temperature due to the poor efficiency of the ISC processes. Furthermore, the authors discussed the presence of conformational disorder in vitreous systems, investigating the luminescence activity on Ge doped silica. They observed that the effect of the conformational heterogeneity is not only to modulate the optical properties of each single defect, with a subsequent inhomogeneous broadening of the bands, but also to point out the microscopic relations among the different spectral properties.

In **2000**, **Sakurai** resumed an idea of **Anedda *et al.*, 1996,** which suggested a composite nature of the $\beta_{Ge}$ band, while **Bagratashvili *et al.*, 2000,** reported several experimental evidences of the inhomogeneous nature of the optical bands associated with the B-type activity. Even if the $=T^{\bullet\bullet}$ model is almost universally accepted, **Uchino *et al.*, 2000,** proposed a new model derived from the neutral oxygen vacancy based on ab initio computations.

In **2001**, **Sakurai and Nagasawa** investigated the Si related B-type activity by a fine tuning of excitation energy at different temperatures from 300 K down to 20 K. The authors observed a different dependence on excitation energy varying the temperature and rationalized these results by assuming a narrowing of the excited levels with the cooling.

In the last years more attention has been devoted to the Sn related ODCs. In **2000**, **Chiodini *et al.*** reported luminescence measurements on Sn doped silica that confirmed the results of **Skuja, 1992,** corroborating the iso-structural model. More recently, **Rybaltovskii *et al.*, 2002,** studied in details the optical activity associated with the $=Sn^{\bullet\bullet}$ center. In particular, they observed a dispersion of the ISC rates and evaluated a mean activation barrier of 50 meV.

Regarding the surface activity, previous experimental works were performed on highly dispersed powder-like samples, whose surfaces were activated by mechanical and thermochemical techniques (see the review paper of **Radzig, 1995a** and references therein, see also chapter 3). The main interest of these works was about the processes involved in solids surface reactivity and no particular attention was devoted to their optical properties. The first experimental investigation on the optical properties of activated surface defects in silica was performed, at our knowledge, by **Skuja *et al.*, 1984**. In this work the authors observed an optical activity characterized by two related emission bands at 4.3 and 2.65 eV upon excitation at 5 eV. By lifetime measurements, the latter was related to a forbidden transition. The authors associated this activity with the surface two-fold coordinated silicon. In **1995**, **Bagratashvili *et al.*** performed a comparative study on bulk and surface Si-ODC; they found small but significant differences in the spectroscopic properties. In particular, the authors observed a blue shift of 0.2 eV and a widening of surface related absorption band with respect to the bulk one and a relevant increasing in the ISC efficiency for the surface activity. Furthermore, they showed that a common feature of both systems is a significant inhomogeneous dispersion of their optical properties and of the activation barrier governing the ISC process. They rationalized this result assuming small geometrical changes in the defect structure.

Regarding surface variant of the $=\mathrm{Ge}^{\bullet\bullet}$, no detailed investigation has been performed so far, at our knowledge. The only results on the optical properties of this center was reported by **Radzig, 1995a**. The author investigated the optical response of activated surface ODC involving Ge atoms. He observed an intense OA band centered at 5.39 eV and two related emissions: a singlet-singlet band at 4.28 eV and a triplet-singlet band 3.18 eV. The author assigned this optical activity to the surface variant of the two-fold coordinated germanium.

# Chapter 2

# Theoretical background

The comprehension of the optical properties of molecular systems interacting with an external matrix has been the subject of several works [**Huang and Rhys, 1950; Markhan, 1959; Pryce, 1966; Cupane *et al.*, 1995; Sanfratello *et al.*, 2000**], books (see for example **Herzberg, 1966,** and **Rebane, 1970**) and, in particular regarding the theoretical treatment of point defects in silica, it has been recently reviewed by **Skuja, 2000,** and by **Leone *et al.*, 2001**. We refer to them for a detailed discussion, while in this chapter we will supply the basic theoretical background to describe the optical properties of a single point defect embedded in a solid matrix.

## 2.1 Energy levels and electronic transitions of a point defect

Since a point defect strongly interacts via covalent bonds with the matrix and it does not exist as a separate entity, it can not be studied apart from the surrounding. The electronic structure of the system is indeed greatly affected by its vibrational modes (*electron-phonon coupling*) and, in this respect, it is more proper to speak in terms of defect-matrix complex and of its optical properties. The theoretical approach is to consider a cluster of the matrix containing a single defect and to treat it as a molecular system. This approach is, indeed, usually adopted in all the computational works, where a particular attention is devoted to obtain an estimate of the right size of the cluster [**Stefanov and Raghavachari**, **1997**].

The computation of eigenfunctions and the treatment of optical properties related to a molecular system is a many-body problem and so it can not be exactly carried out. For this purpose, it is usual to adopt the *Born-Oppenheimer* or *adiabatic approximation* [**Rebane, 1970, Weissbluth, 1978, Bransden and Joachain, 1983**], which assumes that the total eigenfunctions $\Psi(\boldsymbol{r}, \boldsymbol{R})$ of a molecular system can be factorized in two terms: an electronic wave function $\chi(\boldsymbol{r}, \boldsymbol{R})$, depending on both nuclear, $\boldsymbol{R}$, and electronic, $\boldsymbol{r}$, coordinates, and a wave function $\varphi(\boldsymbol{R})$ associated to the nuclei and depending only on their coordinates:

$$\Psi(\boldsymbol{r},\boldsymbol{R}) = \chi(\boldsymbol{r},\boldsymbol{R})\varphi(\boldsymbol{R}). \tag{2.1}$$

It is worth to note that the electronic wave function $\chi(\boldsymbol{r}, \boldsymbol{R})$ contains also the electronic spin variables $\boldsymbol{s}$ and must be antisymmetric with respect to the electronic coordinates permutations. Since in the following of this section we will not deal with the spin variables, we do not explicitly indicate the spin states. In agreement with the adiabatic approximation, $\chi(\boldsymbol{r}, \boldsymbol{R})$ can be thought as the eigenfunction of the electronic subsystem with the nuclei fixed at the positions $\boldsymbol{R}$.

Assuming the system in a stable configuration (i.e. in a energy local minimum) and in the case of small nuclear motions (*harmonic approximation*), we can express the cartesian coordinates $\boldsymbol{R}$ in terms of the normal vibrational modes $\boldsymbol{Q}$ of the defect-matrix complex and factorize the nuclear wave function as a product of $N$ single harmonic oscillator eigenfunctions $\varphi_t(Q_i)$, characterized by the equilibrium position $Q_{0i}$ and vibrational energy $E_i=h\nu_t$

$$\varphi(\boldsymbol{Q}) = \prod_{i=1}^{N} \varphi_i(Q_i). \tag{2.2}$$

In this framework, the energy eigenvalue associated with a $\Psi(\boldsymbol{r}, \boldsymbol{R})$ is

$$E = E_0 + \sum_{i=1}^{N} E_i \left( ½ + m_i \right) \qquad m_i = 0, 1, 2, \ldots \tag{2.3}$$

where $E_0$ is the energy of the system considering all the nuclei fixed in the equilibrium position, $N$ is the number of the normal modes, and $m_i$ is the occupation number of the $i$-th mode $Q_i$, respectively.

In the zero-th order approximation, the main contribution to a radiative transition rises from the electric dipole moment between the involved states, which are usually the ground electronic state $g$ and the first excited electronic state $u$ ⁽¹⁾. In the following, we will indicate the two states with $\Psi_g(\boldsymbol{r},\boldsymbol{Q}) = \chi_g(\boldsymbol{r},\boldsymbol{Q})\varphi_g(\boldsymbol{Q})$ and $\Psi_u(\boldsymbol{r},\boldsymbol{Q}) = \chi_u(\boldsymbol{r},\boldsymbol{Q})\varphi_u(\boldsymbol{Q})$, respectively, while the corresponding energy eigenvalues are

$$E_g = E_{0g} + \sum_{i=1}^{N} E_{ig} \left( ½ + n_i \right) \qquad n_i = 0, 1, 2, \ldots \tag{2.4}$$

$$E_u = E_{0u} + \sum_{i=1}^{N} E_{iu} \left( ½ + m_i \right) \qquad m_i = 0, 1, 2, \ldots \tag{2.5}$$

A convenient way to visualize the energy levels scheme associated with the equations (2.4) and (2.5), and the related optical transitions, is the configurational diagram shown in figure 2.1 (a). The energy of the defect-matrix complex in the ground and excited electronic states is reported as a function of nuclear displacements, which are symbolized by a single generalized normal coordinate, $Q_i$. Furthermore, in agreement with the harmonic approximation, we have drawn parabolic wells both for the ground and the excited states. When the system is excited to the upper state by the absorption of a photon, some configurational relaxation occurs, changing the equilibrium position and decreasing the total electronic energy. To picture this process, the lower and upper wells in figure 2.1 (a) are

---

(1) In agreement with a common spectroscopic notation, these state are also named HOMO (Higher Occupied Molecular Orbital) and LUMO (Lower Unoccupied Molecular Orbital), respectively.

indeed shifted and centered in different equilibrium positions ($\Delta_i$ represent their relative shift), while the energy decreasing immediately after the excitation is indicated by dashed arrows toward the new equilibrium position. Even if a relaxation in a system implies a changing in the normal mode set, this effect is usually negligible and it is mostly correct to assume the same vibrational frequencies in both states, i.e. $E_{ig} = E_{iu}$ (*linear coupling approximation*). Furthermore, as that electronic wave function $\chi(\boldsymbol{r}, \boldsymbol{Q})$ is expected to be only a weak function of the nuclear coordinates [**Rebane, 1970**], it is generally correct to suppose, in zero-th order approximation, that it depends only on the equilibrium positions $\boldsymbol{Q_0}$ of the nuclei in the related

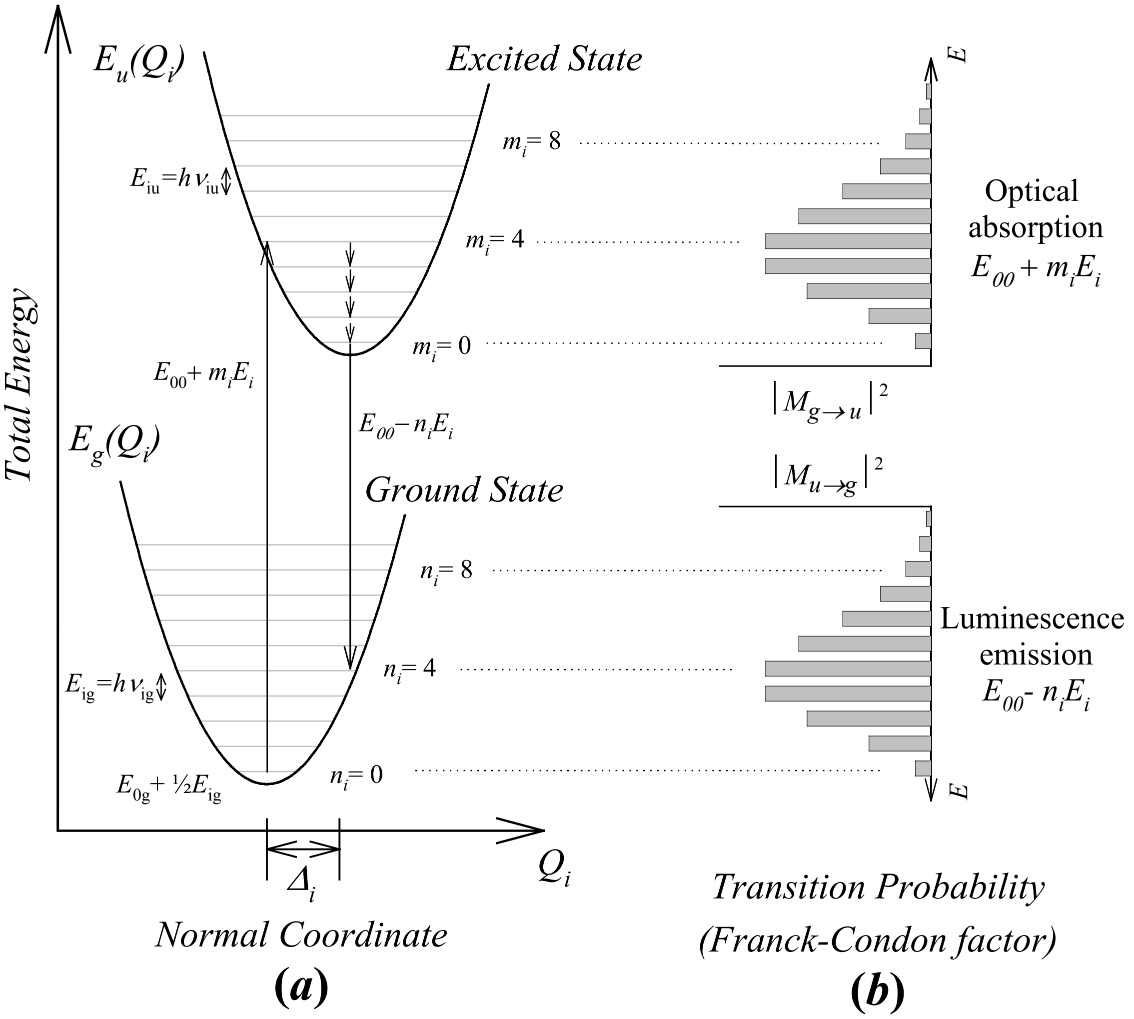

Figure 2.1. (*a*) Configurational diagram of the potential energies of the ground (*g*) and excited (*u*) states as a function of a generalized normal mode in harmonic approximation. (*b*) Energy dependence of the transition probabilities for absorption and emission. See text for details (figure from **Skuja, 2000**).

electronic state (*Condon approximation*). Since an electronic transition occurs in a time scale of $10^{-15}$ sec and the typical nuclear dynamics are ~$10^{-12}$ sec, and considering that the electronic subsystem is much lighter than the nuclear one, it is reasonable to assume that: i) the nuclei do not move during the electronic transition (solid arrows in figure 2 (a) must be vertical), ii) no changes in their momenta must be considered (i.e. the slowest subsystem does not react). The supposition of both conditions is the simplest formulation of the *Franck-Condon Principle* and, in this framework, the electric dipole matrix element $M_{g\to u}$ for a transition from the ground to the excited state is:

$$M_{g\to u} = M_e \int \varphi^*_{u\{m_i\}}(\boldsymbol{Q})\varphi_{g\{n_i\}}(\boldsymbol{Q})d\tau_N \ , \tag{2.6}$$

where, accordingly to the Condon approximation,

$$M_e = e\vec{\varepsilon}\cdot\int \chi^*_u(\boldsymbol{r},\boldsymbol{Q}_{0u})\left(\sum_{i=1}^{n}\vec{\boldsymbol{r}}_i\right)\chi_g(\boldsymbol{r},\boldsymbol{Q}_{0g})d\tau_e \ , \tag{2.7}$$

$\{m_i\}$ and $\{n_i\}$ are the occupation numbers of the excited and ground vibrational levels, respectively, $e$ is the electron charge, $n$ is the number of electrons and $\vec{\varepsilon}$ is the electromagnetic field polarization vector; the integrals in equations (2.6) and (2.7) are calculated on the nuclear and electronic variables, respectively. In agreement with the Franck-Condon principle, the nuclear coordinates of the excited state in equation (2.6) were set equal to the ground state's ones. Regarding the factor $M_{\{n_i\}\{m_i\}} = \int \varphi^*_{u\{m_i\}}(\boldsymbol{Q})\varphi_{g\{n_i\}}(\boldsymbol{Q})d\tau_N$ , it is named *Franck-Condon integral* or *Franck-Condon factor*. It depends on the starting vibrational levels of the ground state, $\{n_i\}$, and on the arrival vibrational levels of the excited state, $\{m_i\}$. In the following, we will consider as a starting level only the vibrational ground one (i.e. $\{n_i\} = \{0\}$), assuming the system at 0 K. Regarding the electronic matrix element $M_e$, with the assumption of the Condon approximation, it is a constant factor which depends only on the involved electronic states.

The transition rate for an allowed optical transition between the ground and the excited states of the defect-matrix complex is proportional to the square of the electric dipole matrix [**Bransden and Joachain, 1983**], $\left|M_{g \to u}\right|^2 = \left|M_e\right|^2 \cdot \left|M_{\{0\}\{m_i\}}\right|^2$. The Franck-Condon factor gives the transition probability between the ground vibrational level of the electronic ground state ($\{n_i\} = \{0\}$) and the vibrational level of the excited state characterized by the vibrational occupation numbers $\{m_i\}$. It is worth to note that, being the vibrational wave functions orthogonal, the summation of $\left|M_{\{0\}\{m_i\}}\right|^2$ over all the arrival vibrational levels is always equal to unity. Then, the overall probability of a electronic promotion from the ground to an excited state, regardless the arrival vibrational level, depends only on the electronic term, which is indeed proportional to the oscillator strength of the transition. In this respect, the allowed or forbidden nature of an electronic transition lies only in the value of $M_e$ or, in other words, of the associated electronic dipole moment: we will speak of *symmetry forbidden transition* if $M_e$ is zero because of the spatial symmetries of the function involved in the integral (2.7); in our case, since the investigated system lacks any symmetry, all the optical transitions (apart unlikely cases by coincidence) are symmetry allowed. In the next section we will consider the case of zero value of $M_e$ by reason of selection rules between the spin variables (*spin forbidden transition*) of the starting and arrival states.

Regarding the Franck-Condon factor, since the total nuclear wave function is factorised in single oscillator eigenfunctions (see equation (2.2)) we can write

$$M_{\{0\}\{m_i\}} = \prod_{i=1}^{N} M_{0m_i} \,. \tag{2.8}$$

where $M_{0m_i}$ is the Franck-Condon factor associated with the $i$-th vibrational normal mode and calculated accordingly to the integral in equation (2.6), using $\varphi_i(Q_i)$ instead of the total $\varphi(\boldsymbol{Q})$. Considering the normal modes in the ground and in the excited states, some ones will be characterized by a conformational rearrangement, and correspond to harmonic wells centered in different positions, the remainders correspond to the case $\Delta_i = 0$ (see figure 2.1 (a)). In the latter case, $\varphi_l(Q_i)$ of the $i$-th mode in the ground and excited states are orthogonal, being associated to the same harmonic well, and so obey the usual selection rule $m_i = n_i$. In our case it implies $m_i$=0 and the only contribution to the total Frank-Condon factor in equation (2.8) is $M_{0,m_i=0} = 1$; furthermore, no relaxation and subsequent dynamics are induced. In this respect, these vibrational modes, termed *uncoupled modes*, are not relevant to the optical line profiles and the internal conversion dynamics. At the variance, the vibrational normal modes characterized by a conformational rearrangement, and named *coupled modes* or *Franck-Condon active modes*, are described by harmonic eigenfunctions in the ground and excited states which do not obey $m_i = n_i$, being non orthogonal. The most probable transitions correspond to the vibrational functions with the greatest spatial overlapping, which at 0 K occurs at the turning points of the excited well vertically placed over the lowest vibrational level of the ground state [**Rebane, 1970, Skuja, 2000**]. So, their contributions to the total Franck-Condon factor depend on the arrival vibrational level, which is depicted in figure 2.1 (b) for a single coupled mode. In the last two sections we will discuss how the Franck-Condon factor shapes the absorption and luminescence bands profiles.

## 2.2 Inter-system crossing and spin-orbit coupling

In the previous section we adopted the common theoretical framework, where only the spatial coordinates of the system are taken into account and the only care over the electronic spin variables ***s*** is regarding the antisymmetry and the multiplicity of the eigenfunctions [**Weissbluth, 1978, Bransden and Joachain, 1983**]. The main reason is that in the zeroth order approximation a molecular system is described by the Hamiltonian

$$H_C = T_N + T_e + V_C(\boldsymbol{r}, \boldsymbol{R}) \tag{2.9}$$

where $T_N$ and $T_e$ are the kinetic energy operators of the nuclei and of the electrons, respectively; $V_C(\boldsymbol{r}, \boldsymbol{R})$ is the potential energy operator due only to the terms of coulombian origin (nucleus-nucleus and electron-electron repulsion, nucleus-electron attraction) so depending only on the spatial coordinates of nuclei and electrons. Equation (2.9) represents the non relativistic Hamiltonian associated with a molecular system and it is widely used, since it is able to supply reliable results with respect to the main aspects of the investigated system (optimization of ground state geometry, characterization of energy level structure, spatial distribution of molecular orbitals, etc.).

In this framework, since $H_C$ commutes with the total electronic spin angular momentum operators $S^2$ and $\boldsymbol{S} = (S_x, S_y, S_z)$ [**Weissbluth, 1978**], the eigenfunctions of the equation (2.9) (2) $\Psi_\alpha(\boldsymbol{r}, \boldsymbol{R})$ are eigenstates of $S^2$ and $S_z$, this feature lying in the fact that $V_C(\boldsymbol{r}, \boldsymbol{R})$ depends only on the spatial coordinates and not on the spin variables. We note that this characteristic is not due to any particular approximation or to the size of the defect-matrix cluster.

A common notation in atomic and molecular physics identifies $s$ and $m_S$ (3), the eigenvalues of the operators $S^2$ and $S_z$, explicitly labeling the eigenfunctions ${}^s\Psi_{\alpha,m_S}(\boldsymbol{r}, \boldsymbol{R})$. In the case of different spin states, the orthonormality condition implies

$$\left\langle {}^p\Psi_{\alpha,m_p} \middle| {}^q\Psi_{\beta,m_q} \right\rangle = 0 \qquad (p \neq q \text{ or } m_p \neq m_q), \tag{2.10}$$

and, considering any operator $G(\boldsymbol{r}, \boldsymbol{R})$ depending only on the spatial coordinates, it occurs that [**Hameka, 1967, Weissbluth, 1978**]

---

(2) For the sake of clearness, we labeled the different $\Psi$ with $\alpha$. In the framework of the previous section $\alpha$ accounts for the electronic state and the occupation numbers of the vibrational levels.

(3) For a diamagnetic system (thus, with an even number of electrons), the possible values of $s$ are 0, 1, 2, … and of $m_S$ are $\pm s$, $\pm(s-1)$, …, 0,

$$\left\langle {}^{p}\Psi_{\alpha,m_p} \left| G(\boldsymbol{r},\boldsymbol{R}) \right| {}^{q}\Psi_{\beta,m_q} \right\rangle = 0 \qquad (p \neq q \text{ or } m_p \neq m_q). \tag{2.11}$$

So, regarding the transition probability between two states with different spins, the last equation implies that it is exactly zero (i.e. it is zero not only the electric dipole moment but also any other higher transition moment [**Bransden and Joachain, 1983**]). Concerning the intersystem crossing, it is a near-resonant radiationless transition which is proportional to the mixing of the starting and arrival states [**Siebrand, 1967, Weissbluth, 1978**]; thus, accordingly to the equation (2.10), it should not occur.

In the light of this discussion, we obtain that the theoretical framework derived from the Hamiltonian (2.9) can not account for the energy levels scheme of the B-type activity outlined in the first chapter (see figure 1.4), since it is able to treat neither the $\beta_T$ emission nor the ISC process, being due to $\boldsymbol{T_1}\rightarrow\boldsymbol{S_0}$ and $\boldsymbol{S_1}\rightarrow\boldsymbol{T_1}$ transitions, respectively. To understand the finite probability of spin forbidden transitions, we need a more accurate Hamiltonian and, in particular, we have to consider those terms which depend on the electron spins. These spin interaction contributions are due to relativistic effects rising from the motion of the electrons in the electrostatic field generated by the nuclei and by the electrons themselves of the molecular system. The derivation of this correction is a straightforward problem and we will only report the final expression [**Hamera, 1967**]:

$$H_{s.o.} = \frac{e}{mc}\sum_i \boldsymbol{S}_i \times \boldsymbol{B}_i\ , \tag{2.12}$$

with

$$\boldsymbol{B}_i = \frac{1}{2m_e c}\left(\boldsymbol{E}_i \wedge \boldsymbol{p}_i\right) + \frac{e}{mc}\sum_{k\neq i}\frac{1}{\left|\boldsymbol{r}_i - \boldsymbol{r}_k\right|^3}\left[\left(\boldsymbol{p}_k - \tfrac{1}{2}\boldsymbol{p}_i\right)\wedge\left(\boldsymbol{r}_i - \boldsymbol{r}_k\right)\right]. \tag{2.13}$$

where the symbols × and ∧ represent a scalar and a vector product, respectively; both the summations run over the number of the electrons, which are characterized by coordinates $\boldsymbol{r}_i$ and momenta $\boldsymbol{p}_i$; in agreement with the adiabatic approximation, we assumed that the nuclei are at rest so they give rise to an electrostatic field $\boldsymbol{E}$ only, and we indicated with $\boldsymbol{E}_i$ the field experienced by the *i*-th electron. So, since the vector $\boldsymbol{B}_i$ is mostly due to the orbital momentum operators of the electrons, the main consequence of the relativistic correction is to mix, in the Hamiltonian (2.12), the electron spins and orbital momenta and this effect is indeed called *spin-orbit coupling*. A further correction, due to mutual interaction between different electron spins (named indeed *spin-spin coupling*), exists but we will not consider it, being its contribution usually negligible with respect to the spin-orbit term (see **Hamera, 1967,** and **Bransden and Joachain, 1983** for a more detailed discussion). These corrections are very small with respect to the non relativistic Hamiltonian $H_C$, and their effect is to perturb the pure singlet and triplet functions, mixing small amounts of triplet functions with the singlet ones, and vice versa. The orthonormality condition (2.10) is no more fulfilled and electric dipole moment can be different from zero, so obtaining finite $\boldsymbol{T_1 \rightarrow S_0}$ and $\boldsymbol{S_1 \rightarrow T_1}$ transition probabilities.

A quantitative theoretical derivation of these transition probabilities is out from the aims of this thesis (see for example **Hamera, 1967,** and **Siebrand, 1966** and **1967,** and references therein), and we will qualitatively discuss the implications of equations (2.12) and (2.13) considering the B-type activity energy levels scheme. The contribution, rising from the perturbing singlet states$^{(4)}$ $\boldsymbol{S_n}$ to the triplet state $\boldsymbol{T_1}$, will be superposition of terms proportional to the matrix elements $\langle \boldsymbol{S_n} | H_{s.o.} | \boldsymbol{T_1} \rangle$, and both the $\boldsymbol{T_1 \rightarrow S_0}$ emission and the $\boldsymbol{S_1 \rightarrow T_1}$ ISC process rates are expect to be proportional to the superposition of terms linearly depending on $\left| \langle \boldsymbol{S_n} | H_{s.o.} | \boldsymbol{T_1} \rangle \right|^2$.

---

(4) Even if in the B-type energy levels scheme we consider only the first excited single state $\boldsymbol{S_1}$ and the $\boldsymbol{S_1 \rightarrow T_1}$ transition, the singlet character of $\boldsymbol{T_1}$ could be due to a mixing with higher excited singlet states.

An important role in the spin-orbit Hamiltonian is played by $\boldsymbol{E}_i$, the nuclear electrostatic field experienced by the *i*-th electron:

$$E_i = e\sum_n \left[ Z_n \cdot \left| \boldsymbol{r}_i - \boldsymbol{R}_n \right|^{-3} \cdot \left( \boldsymbol{r}_i - \boldsymbol{R}_n \right) \right] , \qquad (2.14)$$

where the summation is over the number of nuclei of the defect-matrix complex, $Z_n$ and $\boldsymbol{R}_n$ are the atomic number and the position vector of the *n*-th nucleus, respectively.

One of the main aspects is that $E_i$ induces a dependence of the spin-orbit term on the configuration of the nuclei. This result means that in an amorphous system, as vitreous silica, an effect of the conformational heterogeneity on the ISC rate is expected, as already pointed out in the previous chapter. Since the ISC process is a near-resonant transition or, in other words, occurring between almost degenerate states, the effects of a geometrical perturbation are expected to affect more the ISC rates than the $\boldsymbol{T_1 \rightarrow S_0}$ transition rates. All the three variants of the B-type activity show indeed a single exponential time decay of the $\boldsymbol{T_1}$ state and a dispersion of the ISC rates.

An other important implication is a dependence on the atomic number of the involved atomic species. In particular, the spin-orbit term increases by substituting a light atom with an heavier one (*heavy atom effect*). At our knowledge, this dependence does not obey a general law but in the case of very localized transitions, as it occurs for the B-type activity [**Skuja, 1992**]. In this case, indeed, the electron involved in the transition (or more properly the wave function in the excited state) is localized mainly on an atom, which is the T atom in the case of the B-type activity, and it can be assumed as a rough approximation that $E_i$ is due mainly to this atom. In this atomic-like field the spin-orbit coupling increases with the forth power of $Z$ [**Hamera, 1967, Weissbluth, 1978**]. With this assumption, **Skuja** in **1992** was able to rationalize quantitatively the shortening of the $\boldsymbol{T_1}$ lifetime increasing the atomic number in the isoelectronic series $=\mathrm{T}^{\bullet\bullet}$. In this approximation, the substitution of one of the near atoms with an heavier one is expected to induce a small enhancement of local electric field, so increasing the spin-orbit coupling (*external heavy atom effect*). This effect on the $\beta_{Si}$ lifetime was indeed observed by implantation of increasingly heavier ions in silica [**Seol *et al.*, 1996**].

Since the spin-orbit correction (2.12) discussed so far is related to the electrostatic filed due to fixed nuclei, a temperature independent contribution to ISC process is, in principle, expected and is due to the spin-orbit Hamiltonian corresponding to the nuclei in their equilibrium positions.

Concerning the role of temperature on the spin-orbit coupling, different contributions are expected. Since the electric field $\boldsymbol{E_i}$ brings on a dependence of the spin-orbit term on the nuclear coordinates, a dependence of the spin-orbit matrix elements on the vibrational occupation numbers of $\boldsymbol{S_1}$ and $\boldsymbol{T_1}$ (5) is expected. As a consequence, an increase of the ISC efficiency accordingly with temperature is induced because of the rise of matrix phonon population. It is indeed worth to note that, on the contrary of the optical transitions described in the previous paragraph, all the vibrational modes of the defect-matrix complex contribute to the spin-orbit interaction, even if some modes could be more effective than others. Further contributions are, in principle, expected as the appearance of a random magnetic field, $\boldsymbol{H_i}$, generated by the local electric field fluctuations induced by the nuclear vibrations. As a consequence, an additional term $\frac{e}{mc}\sum_i \boldsymbol{S}_i \times \boldsymbol{H}_i$ [**Hamera, 1967**], whose intensity is expected to increase with temperature, has to be added to the spin-orbit Hamiltonian (2.12).

All these effects depend on the phonon population of the whole matrix and, to stress this aspect, they are also named *spin-lattice coupling*. So, in agreement with this discussion, we can state that the ISC process is expected to have thermally activated contributions depending on the phonon population of the matrix. We are not able to derivate a law accounting for

---

(5) In the same framework of the previous section, we can indeed write $M_{\{n_i\}\{m_i\}} = \langle \boldsymbol{S_1} | H_{s.o.}(\boldsymbol{r},\boldsymbol{Q}) | \boldsymbol{T_1} \rangle$ $= \int \varphi^*_{\boldsymbol{S_1}\{n_i\}}(\boldsymbol{Q}) \cdot M_{s.o.}(\boldsymbol{Q}) \cdot \varphi_{\boldsymbol{T_1}\{m_i\}}(\boldsymbol{Q}) d\tau_N$, where $M_{s.o.}(\boldsymbol{Q}) = \int \chi^*_{\boldsymbol{S_1}}(\boldsymbol{r},\boldsymbol{Q}_{0\boldsymbol{S_1}}) H_{s.o.}(\boldsymbol{r},\boldsymbol{Q}) \chi_{\boldsymbol{T_1}}(\boldsymbol{r},\boldsymbol{Q}_{0\boldsymbol{T_1}}) d\tau_e$.

them, but, in order to describe thermally activated processes involved not only with point defects in solid systems but with many other fields (chemical reactions, diffusion processes, etc.), it has been revealed to be adequate the following phenomenological law, named Arrhenius law

$$k_{ISC} = k_0 e^{-\frac{\Delta G}{k_B T}}, \tag{2.15}$$

which describes the thermal dependence of the ISC rate $k_{ISC}$ accordingly to a free energy barrier $\Delta G$ between $\boldsymbol{S_1}$ and $\boldsymbol{T_1}$. In this equation, $k_B$ is the Boltzmann constant and $k_0$ is a pre-exponential factor. Considering explicitly the entropy and the enthalpy terms of $\Delta G = \Delta H - T\Delta S$, we obtain

$$k_{ISC} = k_0 e^{\frac{\Delta S}{k_B}} e^{-\frac{\Delta H}{k_B T}}. \tag{2.16}$$

In this picture, $k_0$ is the typical rate of the system in order to perform the $\boldsymbol{S_1 \rightarrow T_1}$ transition, the entropy factor accounts for the degeneration of the transition and the enthalpy factor gives the dependence on the temperature, assuming a thermally activated process governed by an enthalpy activation barrier $\Delta H$. In the light of the discussion in this section, $k_0$ is related to the strength of the spin-orbit coupling and to structural effects as the heavy atom effect; regarding the entropy and enthalpy factor they are linked with the effects of the matrix dynamics on the spin-orbit coupling. In particular, the former takes account of the number of mostly effective low frequency vibrational modes, while the latter describes the sensitivity to the matrix phonon population.

## 2.3 Absorption spectroscopy

The number of centers making per unit time the g→u optical transition by absorbing radiation is

$$n_0 \cdot B_{g\to u} \cdot \rho(E) \cdot \delta(E - E_{ug}), \tag{2.17}$$

where $n_0$ is the centers volume density in the g state, $\rho(E)$ is the energy density of the radiation field at the energy $E$, $E_{ug} = E_u - E_g$, and $B_{g\to u}$ is the transition probability, or the *Einstein coefficient, for absorption*, defined as [**Bransden and Joachain, 1983**]

$$B_{g\to u} = \frac{16\pi^4}{3h^2} \cdot \frac{1}{4\pi\varepsilon_0} \cdot \left|M_{g\to u}\right|^2. \tag{2.18}$$

Since the energy lost by the field after each promotion is $E$, the light intensity $I(E)$ decreases going through the sample, in agreement with the following differential equation

$$-\frac{dI}{dl} = n_0 \cdot B_{g\to u} \cdot E \cdot \frac{I(E)}{c} \cdot \delta(E - E_{ug}), \tag{2.19}$$

where we substituted $\rho(E)$ with $I(E)/c$ and neglected the stimulated emission term (*weak field regime*). By integration of the equation (2.19) over the sample thickness $d$, we obtain the well-known Lambert-Beer law [**Jaffé and Orchin, 1970, Harris and Bertolucci, 1978**], which empirically links the light intensity outgoing from the sample with the incident light intensity, $I_0(E)$

$$I(E) = I_0(E) \cdot e^{-\alpha(E) \cdot d}, \tag{2.20}$$

where we set

$$\alpha(E) = n_0 \cdot B_{g\to u} \cdot E \cdot c^{-1} \cdot \delta(E - E_{ug}), \tag{2.21}$$

which is termed *absorption coefficient.* The adimensional quantity experimentally measurable is the *absorbance*, $A(E) = \log_{10}(I_0(E)/I(E))$, and it is related to $\alpha(E)$ by the formula

$$\alpha(E) = 2.303 \cdot A(E)/d. \tag{2.22}$$

To write explicitly the spectral shape of $\alpha(E)$, firstly we have to take account of the homogeneous broadening, rising from the finite lifetime $\tau$ of the excited state, by substituting the δ-function with a Lorentzian spectral distribution

$$\alpha(E) = n_0 \cdot B_{g\to u} \cdot \frac{E}{c} \cdot \frac{\Gamma}{\left(E - E_{ug}\right)^2 - \Gamma^2}, \qquad (2.23)$$

where $2\cdot\Gamma = h/\tau$. Others and more important contributions in vitreous systems are due to the Franck-Condon factor, included in the Einstein coefficient $B_{g\to u}$. Since the computation of the related integral is not trivial (see for example **Cupane *et al.*, 1995**) and out to the aims of this thesis, we report only the final expression for $\alpha(E)$:

$$\alpha(E, T=0) = \frac{4\pi^3}{3ch^2\varepsilon_0} \cdot n_0 \cdot E \cdot \left|M_e\right|^2 \cdot \sum\nolimits_{\{m_i\}} \left[ \left( \prod\nolimits_{i=1}^{N} e^{-S_i} \frac{S_i^{m_i}}{m_i!} \right) \cdot \frac{\Gamma}{\left(E - E_{00} - \sum_{i=1}^{N} m_i E_i\right)^2 - \Gamma^2} \right], \qquad (2.24)$$

where the main summation runs over all the possible N-dimensional set of occupation numbers $\{m_i\}$ of the vibrational levels of the excited state. $E_{00}$ is the energy associated with the transition between lowest vibrational levels of the ground and excite states and is equal to $E_{00} = E_{0u} - E_{0g}$ (corresponding to the $n_i$=0 and $m_i$=0 levels of figure 2 (a), respectively), while the related transition is usually termed *zero phonon*, or *pure electronic*, *transition*. The parameters $S_i$ are *the linear coupling*, or *Huang-Rhys*, *constants* [**Huang and Rhys, 1950**] and can be defined as $S_i = ½\cdot E_i\cdot \Delta_i^2$ .The term

$$E_{00} + \sum\nolimits_{1=1}^{N} m_i E_i \qquad (2.25)$$

describes the energies where the Lorentzian lines, associated with the transition from the lowest level of the g state (being T = 0 K) to the vibrational levels of the u state characterized by the numbers $\{m_i\}$, are centered.

Increasing the temperature, the thermal dependence of the optical bands shapes should be obtained considering the superposition of the Frank-Condon factors for the transition from the vibrational levels of the ground state ($\{n\}_i \neq \{0\}$) populated according to the Boltzmann law. This approach can not be applied in practice if all the vibrational modes and the related Huang-Rhys constants are not known, which is the common case. A convenient way to analyzed the effect of temperature is to divide the normal modes in high and low frequency modes which are characterized by the condition $E_i > k_B T_{Max}$ and $E_i \leq k_B T_{Max}$, respectively; where $T_{Max}$ is the highest temperature reached during the measurements, and $k_B$ is the Boltzmann factor. The latter ones are responsible of the thermal effects being characterized by a thermal distribution of the vibrational levels population in the ground state, which depends on temperature. On the other hands, the contribution of high frequency modes to the band shape is not affected by the temperature, being their population always on the lowest vibrational levels. To treat in a simplified way the low frequency modes, it is usually assumed the *Einstein model*, which considers the coupling with these modes as due to a single mode characterized by a mean vibrational energy $\langle E_l \rangle$, a mean linear coupling constant $S_l$ and degeneration $N_l$, which equals the number of the low frequency modes. In this framework, the absorption coefficient can be so expressed [**Cupane *et al.*, 1995**]:

$$\alpha(E,T) = \alpha(E,T=0) \otimes \frac{1}{w(T)} \cdot e^{-\frac{1}{2} \cdot \frac{E^2}{w(T)^2}}, \tag{2.26}$$

where the symbol ⊗ indicates the convolution operator and

$$w(T)^2 = N_l \cdot S_l \cdot \langle E_l \rangle^2 \cdot \coth\left( \frac{\langle E_l \rangle}{2k_B T} \right). \tag{2.27}$$

So, in the case of linear coupling (i.e. $E_{ig} = E_{iu}$), the only effect of the temperature is an homogeneous broadening of the Lorentzian lines, accordingly to equation (2.27).

If the linear coupling approximation is not completely fulfilled, further thermal effects on the band shapes are expected. In particular, if the vibrational energies of the two states are slightly different, $0 < \left| E_{u_g}^2 - E_{i_g}^2 \right| << E_{i_g}^2$ (*quadratic coupling approximation*), a shift of the zero phonon energy, and then of absorption band, with temperature is expected accordingly to the following equation:

$$E_{00}(T) = E_{00}^{*} - \frac{1}{4} \cdot N_l \cdot (1 - R_l) \cdot \langle E_l \rangle \cdot \coth\left( \frac{\langle E_l \rangle}{2k_B T} \right), \tag{2.28}$$

where, indicating with $R_i = \frac{E_{ig}^2}{E_{iu}^2}$ (*quadratic coupling constant* of the *i*-th mode), $R_l = \langle R_{il} \rangle$ is the mean of low frequency modes constants. In equation (2.28), $E_{00}^{*}$ indicates the zero phonon energy in the case of linear coupling only (i.e. $R_i$=1).

In order to point out the effective role and the physical meaning of the parameters in equation (2.24), we will consider in the following the case of the coupling with a single vibrational mode characterized by a vibrational energy $E_h$. With this assumption equation (2.24) becomes:

$$\alpha(E, T = 0) = \frac{4\pi^3}{3ch^2\varepsilon_0} \cdot n_0 \cdot E \cdot |M_e|^2 \cdot \sum_m \left[ e^{-S} \frac{S^m}{m!} \cdot \frac{\Gamma}{(E - E_{00} - m \cdot E_h)^2 - \Gamma^2} \right]. \tag{2.29}$$

So, the absorption band shape consists of a series of Lorentzian lines enveloped with a Poisson function. The maximum of the absorption band occurs at $E_A = E_{00} + S \cdot E_h$; thus, the value of Huang-Rhys constant $S$ indicates the vibrational level in the excited state with the highest transition probability. As an example, figure 2.1 (b) shows the transition probability in the case of S = 4. It is worth to note that, in agreement with a Poisson function shape, absorption spectra affected by electron-phonon coupling are intrinsically asymmetric, being more broadened toward the higher energies (figure 2.1 (b)). But, increasing the value of S, this feature becomes less and less remarkable, being the Poisson shape more and more symmetric.

For the sake of clarity, in the following we will express the absorption coefficient (see equations (2.24) and (2.26)) explicitly separating the contribution of Franck-Condon factor:

$$\alpha(E, T) = \alpha_0 \cdot E \cdot f(E - E_A, T), \tag{2.30}$$

where we set

$$\alpha_0 = \frac{4\pi^3}{3ch^2\varepsilon_0} \cdot n_0 \cdot \left|M_e\right|^2 . \tag{2.31}$$

The function $f(E-E_A, T)$ is, indeed, the square of Franck-Condon factor referred to the mean absorption energy $E_A$ [6] and, as previously discussed, it is a unitary area function.

When the optical spectra do not have a clearly resolved vibrational structure, which is the common case in vitreous systems, the analysis of the experimental spectra in terms of equations (2.24) and (2.26) do not provide reliable results. However, it is possible to investigate the vibrational dynamics of the system analyzing the spectral first ($M_1$) and second ($M_2$) moments of the absorption band (moments method analysis [**Markham, 1959**]), whose definitions are

$$M_1 = \int_0^{+\infty} E \cdot f(E-E_A, T) dE , \tag{2.32}$$

$$M_2 = \int_0^{+\infty} E^2 \cdot f(E-E_A, T) dE - M_1^{\,2} . \tag{2.33}$$

In agreement with these definitions, $M_1$ and $M_2$ are the mean value and the variance of the function $f(E-E_A, T)$, respectively. In the same theoretical background depicted in this chapter, **Markham, 1959,** showed that also $M_1$ and $M_2$ are affected by temperature in a similar way of the zero phonon energy and the homogeneous broadening, respectively (equations (2.27) and (2.28)):

$$M_1(T) = M_1^0 - \frac{1}{4} \cdot N_l \cdot (1 - R_l) \cdot \langle E_l \rangle \cdot \coth\left( \frac{\langle E_l \rangle}{2k_B T} \right) , \tag{2.34}$$

$$M_2(T) = M_2^{\,0} + N_l \cdot S_l \cdot \langle E_l \rangle^2 \cdot \coth\left( \frac{\langle E_l \rangle}{2k_B T} \right) . \tag{2.35}$$

---

(6) It is worth to note that, being the Franck-Condon factors asymmetric, $E_A$ is in principle different from the maximum absorption energy. In the case of great linear coupling constants ($S > 5$), the Franck-Condon factor is almost symmetric and then the two values tend to coincide. This is indeed our case, as we will see later.

In these equations $M_1^0$ is a measure of the most probable electronic transition from the ground vibrational levels of $\boldsymbol{S_0}$ state to the $\boldsymbol{S_1}$ state, in the case of linear coupling only (i.d. $R = 1$); $M_2^0$ accounts for the homogeneous broadening due to the lifetime of excited states and to the spectral distribution of high frequency normal modes, whose vibrational levels cannot be populated in the investigated temperature range [**Cupane *et al.*, 1995**].

In the case of centers in a glassy matrix, $M_1^0$and $M_2^0$ account also for the inhomogeneous dispersion due to site-to-site non-equivalences among the point defects.

## 2.4 Luminescence spectroscopy

In this section we will analyze the emission bands of a point defect characterized by the energy level scheme depicted in figure 2.2. All the electronic states are coupled with the vibrational normal modes of the system. Due to the absorption of a photon, the system is promoted from $\boldsymbol{S_0}$ to an excited vibrational state of $\boldsymbol{S_1}$ ($\boldsymbol{S_1}_{\{\mathrm{mi}\}}$) in a very short time ($\sim10^{15}$ sec$^{-1}$). Then, it relaxes toward the lowest vibrational level of $\boldsymbol{S_1}$ ($\boldsymbol{S_1}_{\{0\}}$) with a typical rate of $\sim10^{12}$ sec$^{-1}$ by giving energy to the host matrix. This radiationless process, termed internal conversion or vibrational relaxation, competes with the $\boldsymbol{S_1 \rightarrow S_0}$ emission rate $k_S$ and with the ISC rate $k_{ISC}$. In the case of B-type activity, at room temperature, both rates are less than $10^9$ sec$^{-1}$ [**Bagratashvili *et al.*, 1995, Leone *et al.*, 1997, Chiodini *et al.*, 2000, Rybaltovskii, 2002**], so it is reasonable to assume that the system is completely relaxed to $\boldsymbol{S_1}_{\{0\}}$ before these empting processes could be effective. After the system reaches the lowest vibrational level of $\boldsymbol{S_1}$, it can relax or towards $\boldsymbol{T_1}$, via the ISC process with rate $k_{ISC}$, or towards $\boldsymbol{S_0}$ by emission of a photon with rate $k_{S,}$ or by giving energy to the host matrix via non radiative processes with rate $k_{nr}^S$. The system which transfers to $\boldsymbol{T_1}$ undergoes a vibrational relaxation down to the lowest vibrational level and then reaches $\boldsymbol{S_0}$, or radiatively with a rate

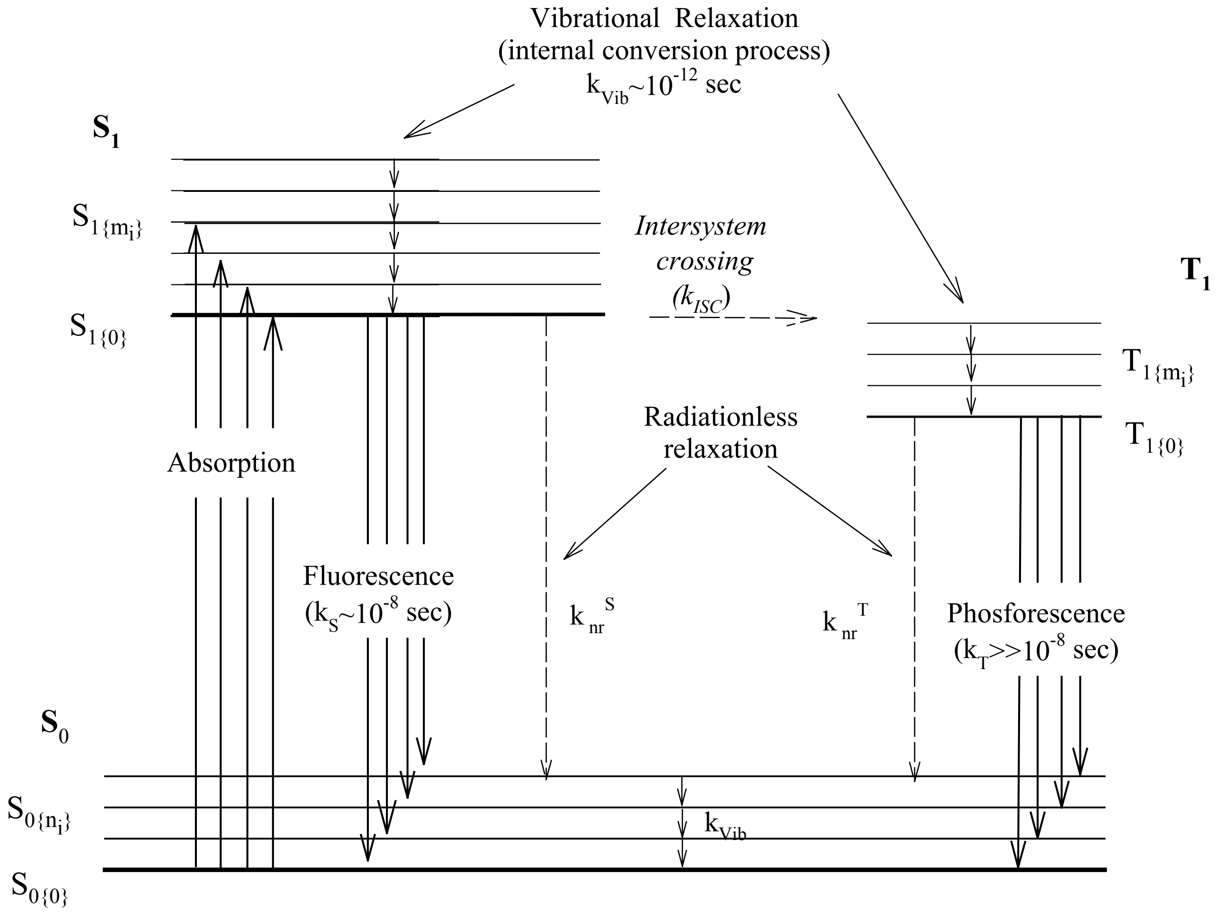

Figure 2.2. Scheme of the first three energy levels for a point defect. The possible transitions and the respective typical rates are reported.

$k_T$, or non radiatively with a rate $k_{nr}^T$. In agreement with the features of the B-type activity, in the following we will assume $k_{nr}^S$ and $k_{nr}^T$ negligible; thus, each excited center will relax to the ground state by emitting a photon. A system with this feature is said to be characterized by an *unitary emission quantum yield* (7). The number of emitted photons corresponding to the transitions $\boldsymbol{S_1} \rightarrow \boldsymbol{S_0}$ and $\boldsymbol{T_1} \rightarrow \boldsymbol{S_0}$ are, in the same order, $n_S \cdot k_S$ and $n_T \cdot k_T$, where $n_S$ and $n_T$ are the respective number of centers in $\boldsymbol{S_1}$ and $\boldsymbol{T_1}$. With the previous assumption on $k_{nr}^S$ and $k_{nr}^T$, the rate equations associated with the energy level scheme in figure 2.2 are

---

(7) The quantum yield of a photo-induced process is defined as the ratio of the number of molecules undergoing the process to the number of absorbed photons [**Harris and Bertolucci, 1978**].

$$\begin{cases} \dfrac{dn_S}{dt} = p_{Abs}(E_{ex}) - (k_S + k_{ISC}) \cdot n_S \\ \dfrac{dn_T}{dt} = k_{ISC} \cdot n_S - k_T \cdot n_T \end{cases}, \tag{2.36}$$

where $p_{Abs}(E_{ex})$ is the pumping rate, i.e. the number of centers excited to $\boldsymbol{S_1}$ in the time unit, and it depends on the energy of the exciting photons $E_{ex}$ being

$$p_{Abs}(E_{ex}) = n_0 \cdot B_{g\to u} \cdot \frac{\Gamma}{(E_{ex} - E_{ug})^2 - \Gamma^2} \cdot \frac{I_0}{c} = I_0 \cdot \alpha_0 \cdot f(E_{ex} - E_A). \tag{2.37}$$

This equation is derived with the same assumptions of previous section (see equations (2.23) and (2.30)) considering, for the sake of handiness, an uniform excitation spectrum.

In the case of steady state conditions ($dn_S/dt = dn_S/dt = 0$), we obtain

$$\begin{aligned} n_S &= \frac{I_0 \cdot \alpha_0 \cdot f(E_{ex} - E_A)}{k_S + k_{ISC}} \\ n_T &= \frac{k_{ISC}}{k_T} \cdot n_s = \frac{k_{ISC}}{k_S + k_{ISC}} \cdot \frac{I_0 \cdot \alpha_0 \cdot f(E_{ex} - E_A)}{k_T} \end{aligned}. \tag{2.38}$$

Regarding the spectral distribution of emitted photons, the same theoretical treatment of absorption can be applied to the luminescence, being also the transition probability for the emission governed by the corresponding Franck-Condon factor (see also figure 2.1 (a) and (b))

$$M_{u\to \boldsymbol{S_0}} = M_e^u \int \varphi^*_{\boldsymbol{S_0}\, n_i}(\boldsymbol{Q}) \varphi_{u\, m_i}(\boldsymbol{Q}) d\tau_N \qquad (u = \boldsymbol{S_1}, \boldsymbol{T_1}). \tag{2.39}$$

So, the spectral dependence of the $\boldsymbol{S_1}$ and $\boldsymbol{T_1}$ emissions are affected by an homogeneous broadening due to both the excited states lifetime and the electron-phonon coupling

$$\begin{aligned} S(E_{em}, E_{ex}) &= k_S \cdot n_S = \frac{k_S}{k_S + k_{ISC}} \cdot I_0 \cdot \alpha_0 \cdot f(E_{ex} - E_A) \cdot g(E_{em} - E_S) \\ T(E_{em}, E_{ex}) &= k_T \cdot n_T = \frac{k_{ISC}}{k_S + k_{ISC}} \cdot I_0 \cdot \alpha_0 \cdot f(E_{ex} - E_A) \cdot h(E_{em} - E_S) \end{aligned}, \tag{2.40}$$

where $S(E_{em}, E_{ex})$ and $T(E_{em}, E_{ex})$ are the spectral distributions of the emitted photons due to the transitions $\boldsymbol{S_1} \rightarrow \boldsymbol{S_0}$ and $\boldsymbol{T_1} \rightarrow \boldsymbol{S_0}$, respectively. The functions $g(E_{em}$-$E_S)$ and $h(E_{em}$-$E_T)$

account for the respective line shapes and are equal to the square of the corresponding Franck-Condon integral in equation (2.39). As the function $f(E_{ex}-E_A)$, they are unitary area functions and centered in $E_S$ and $E_T$, respectively.

An other important quantity is the emission intensity, i.e. the energy emitted in the unit time; it is related to the spectral density of emitted photons by the following equations:

$$\begin{aligned} I_S(E_{em},E_{ex}) &= E_{em}\cdot S(E_{em},E_{ex}) \\ I_T(E_{em},E_{ex}) &= E_{em}\cdot T(E_{em},E_{ex}) \end{aligned} . \qquad (2.41)$$

It is worth to note that both the quantities defined by equations (2.40) and (2.41) are experimentally measurable and, at a fixed excitation energy $E_{ex}$, we obtain functions of the emission energy $E_{em}$ which are generally named photoluminescence (PL) bands. Since the experimental set-up used for the measurements of this thesis directly gives the number of emitted photons instead of the emission intensity (see next chapter), we will refer in the following as PL bands (or spectra) to the functions (2.40).

Concerning the shape of the $\boldsymbol{S_1}\rightarrow\boldsymbol{S_0}$ PL band, it is interesting to note some general features and its relation with the inverse transition, the $\boldsymbol{S_0}\rightarrow\boldsymbol{S_1}$ OA band. As already discussed and with the notation of figure 2.2, after the promotion from $\boldsymbol{S_0}$ to $\boldsymbol{S_1}$, the system relaxes to the lowest vibrational level of $\boldsymbol{S_1}$, $\boldsymbol{S_1}_{\{0\}}$. So, in the emission process (at 0 K) the starting level is $\boldsymbol{S_1}_{\{0\}}$ while the arrival state $\boldsymbol{S_0}_{\{ni\}}$ is a generic excited vibrational level of $\boldsymbol{S_0}$, with occupation number $\{n_i\}$. So, the transition moment is not computed between the same states involved in the absorption. As discussed in the previous section, the electronic part of the transition moment is only a constant term which does not affect the shapes and furthermore, in agreement with the Condon approximation, since it has a small dependence on the nuclear coordinates, it is usually assumed the same for the absorption and luminescence. Regarding the energies associated with the involved transition, the energy of the states $\boldsymbol{S_1}_{\{0\}}$ and $\boldsymbol{S_0}_{\{ni\}}$ are $E_{0\boldsymbol{S_1}}+\sum_{i=1}^{N}\frac{1}{2}\cdot E_i$ and $E_{0\boldsymbol{S_0}}+\sum_{i=1}^{N}E_i\cdot(\frac{1}{2}+n_i)$, respectively, so the transition energies are

$$E_{00} - \sum_{i=1}^{N} n_i \cdot E_i \ . \tag{2.42}$$

The comparison with the respective expression for the absorption (2.25) reveals that the emission energies are shifted toward lower values with respect to the absorption ones and are specular with respect to the zero-phonon energy $E_{00}$. This fact is known as *Stokes shift*.

Regarding the Franck-Condon factor, since in the linear approximation the vibrational wave functions of the excited and ground states are the same and shifted of the same amount $\Delta_i$, the amplitude of the Franck-Condon factors associated with the $\boldsymbol{S_1}_{\{0\}} \rightarrow \boldsymbol{S_0}_{\{\mathrm{ni}\}}$ and the $\boldsymbol{S_0}_{\{0\}} \rightarrow \boldsymbol{S_1}_{\{\mathrm{mi}\}}$ transitions, in the case of $\{n_i\} = \{m_i\}$, are the same. This results reveals that the absorption and emission Franck-Condon factors obey a mirror symmetry law with respect to the pure electron transition $\boldsymbol{S_0}_{\{0\}} \leftrightarrow \boldsymbol{S_1}_{\{0\}}$ and the zero phonon energy, which can thus be calculated as the mean value between the maxima of PL and OA bands. In the case of the coupling with a single vibrational mode (*single effective vibrational mode approximation*) with vibrational energy $E_h$ and Huang-Rhys constant $S$, the PL band profile $g(E_{\mathrm{em}}\text{-}E_A)$ is centered at $E_S = E_{00}\text{-}SE_h$ and, considering the respective result for the absorption, the Stokes shift is directly related to $S$

$$\Delta E_{Stokes} = E_A - E_S = 2 \cdot S \cdot E_h \, . \tag{2.43}$$

All these features are schematically depicted in figure 2.1 (a) and (b).

It worth to note that, in this homogeneous framework, where all the defects are assumed equal, the only effect of varying the excitation energy is on the overall intensity of PL bands, and none on their shape. Regarding the excitation photo-luminescence (PLE) spectra, obtained varying $E_{ex}$ at a fixed $E_{em}$, and in the case of a constant spectral distribution of the light source intensity, they should have the same shape of $f(E_{ex}-E_A)$, the absorption coefficient divided by $E_{ex}$ (see next chapter for a discussion on the experimental PLE spectra) (8).

As discussed about the absorption bands, since the optical spectra in vitreous systems have not a clearly resolved vibrational structure, a more reliable analysis consists in studying the spectral moments. The singlet ($M_{0S}$) and triplet ($M_{0T}$) zeroth moments are

$$\begin{aligned} M_{0S}(E_{ex}) &= \int_0^\infty S(E_{em},E_{ex})dE_{em} = \frac{k_S}{k_S+k_{ISC}}\cdot I_0\cdot\alpha_0\cdot f(E_{ex}-E_A) \\ M_{0T}(E_{ex}) &= \int_0^\infty T(E_{em},E_{ex})dE_{em} = \frac{k_{ISC}}{k_S+k_{ISC}}\cdot I_0\cdot\alpha_0\cdot f(E_{ex}-E_A) \end{aligned} . \qquad (2.44)$$

Both depend only on the excitation energy accordingly with $f(E_{ex}-E_A)$, while their ratio $\zeta$

$$\zeta = \frac{M_{0S}(E_{ex})}{M_{0T}(E_{ex})} = \frac{k_{ISC}}{k_S} \qquad (2.45)$$

does not depend on the excitation and it is a measure of the ISC rate with respect to the radiative $\boldsymbol{S_1}\rightarrow\boldsymbol{S_0}$ emission rate. We previously observed that the excitation energy only affects the amplitude but not the profile of the PL bands and the last two results are an obvious consequence. For the same reason, the singlet ($M_{1S}$) and triplet ($M_{1T}$) first moments are expected to be independent on $E_{ex}$. Considering the properties of the functions $g(E_{em}-E_S)$ and $h(E_{em}-E_T)$, we indeed obtain

$$\begin{aligned} M_{1S} &= \frac{1}{M_{0S}(E_{ex})}\cdot\int_0^\infty E_{em}\cdot S(E_{em},E_{ex})dE_{em} = E_S \\ M_{1T} &= \frac{1}{M_{0T}(E_{ex})}\cdot\int_0^\infty E_{em}\cdot T(E_{em},E_{ex})dE_{em} = E_T \end{aligned} . \qquad (2.46)$$

Concerning the effects of the temperature, they lie in the ISC rate $k_{ISC}$ (see equation (2.16)) and in the electron-phonon coupling with the coupled low frequency vibrational modes of the $\boldsymbol{S_1}$ state.

---

(8) It is worth to note that, in the case of great absorption ($\alpha_0 \cdot d$>0.1), experimental artifacts occur which hide this expected behavior [**Lakowicz, 1983, Skuja, 2000**].

The thermal dependence of $k_{ISC}$ induces an opposite behavior of the singlet and triplet bands: lowering the temperature, it is expected an increase of the singlet band and a decrease of the triplet band. The respective zeroth moments show of course the same behavior and their ratio $\zeta$, in this homogenous framework, follows a pure Arrhenius law accordingly with $k_{ISC}$

$$\zeta = \frac{k_{ISC}}{k_S} = \frac{k_E}{k_S} \cdot e^{-\frac{\Delta H}{k_B T}} , \tag{2.47}$$

where we indicated, for the sake of clarity, the product of $k_0$ and the entropy factor with a total pre-exponential factor $k_E$. The second effect of the temperature is related to the Boltzmann distribution of the vibrational levels in the excited states, under equilibrium conditions. It can be described by the equations (2.34) and (2.35), valid also for the moments of the emission bands, both of the singlet and triplet excited states.

In the case of pulsed excitation, we can obtain the time resolved spectra considering the rate equations (2.36). When the excitation light is shut off (t=0), the temporal behavior of the $\boldsymbol{S_1}$ population is a pure exponential time decay with decay rate $k_S+k_{ISC}$, and the time resolved spectra for singlet emission is given by

$$S(E_{em}, E_{ex}, t) = S(E_{em}, E_{ex}, t=0) \cdot e^{-(k_S + k_{ISC}) \cdot t} . \tag{2.48}$$

If the time duration of the excitation pulse is longer than the thermalization (vibrational) time (~$10^{-12}$ sec), $S(E_{em}, E_{em}, t=0)$ is given by the first equation of (2.40). The triplet time resolved emission depends by the transient time behavior of the singlet population, but after a time $t_0 >> (k_S+k_{ISC})^{-1}$, when $\boldsymbol{S_1}$ is almost empty, it is described by the following expression

$$T(E_{em}, E_{ex}, t) = T(E_{em}, E_{ex}, t_0) \cdot e^{-k_T \cdot t} . \tag{2.49}$$

## 2.5 Transient Absorption spectroscopy

As discussed in the previous section, when a center is excited to $\boldsymbol{S_1}$, it is brought in a non equilibrium position and so it relaxes toward the $\boldsymbol{S_1}$ equilibrium configuration under the effects of internal conversion. Then, in agreement with the B-type activity scheme, the $\boldsymbol{S_1}$ state will decay by radiative emission in a nsec time scale. Concerning the relaxation dynamics, they occur in a sub-psec time domain.

A more complete scheme of the electronic levels of point defects responsible of the B-type activity, have to include also the higher excited states and, in particular, the second excited singlet and triplet states $\boldsymbol{S_2}$ and $\boldsymbol{T_2}$, respectively, as reported in figure 2.3 (a).

If we consider the $\boldsymbol{S_2}$ state of the system, an $\boldsymbol{S_1 \rightarrow S_2}$ transition could be induced before the $\boldsymbol{S_1}$ decay. A *transient absorption* (TA) is an absorption process between excited states and the ideal experiment to measure a TA is characterized by two steps: i) an intense light pulse (termed *pump*) excites a significant number of centers from $\boldsymbol{S_0}$ to $\boldsymbol{S_1}$ in order to have enough population in $\boldsymbol{S_1}$, the starting state; ii) a second pulse (named *probe*) induces the $\boldsymbol{S_1 \rightarrow S_2}$ transition. In figure 2.3(b) a schematic picture of a TA is reported. The observed quantity is the depletion of the probe intensity $\Delta I$ with respect to the probe intensity $I_0$ without the pump pulse. The theoretical treatment is the same of an usual absorption and, with the care of working in linear regime, we can assume $I_{probe} = I_0 \cdot e^{-\alpha \cdot d}$ obtaining

$$\frac{\Delta I}{I_0} = \frac{I_0 - I_{probe}}{I_0} = 1 - e^{-\alpha \cdot d}, \qquad (2.50)$$

where $I_{probe}$ is the probe intensity coming out from the sample, $\alpha$ is the absorption coefficient for the $\boldsymbol{S_1 \rightarrow S_2}$ transition, $d$ is the thickness of the sample. Furthermore, in the case of low absorption, we can approximate the equation (2.50) with:

$$\frac{\Delta I}{I_0} \cong \alpha \cdot d \tag{2.51}$$

So the experimentally detectable ratio $\Delta I/I_0$ is a direct measure of the absorption coefficient for the $S_1 \rightarrow S_2$ transition. It is worth to note that, with respect to the usual absorption, the time is introduced as a new parameter: the probe can indeed be deliberately

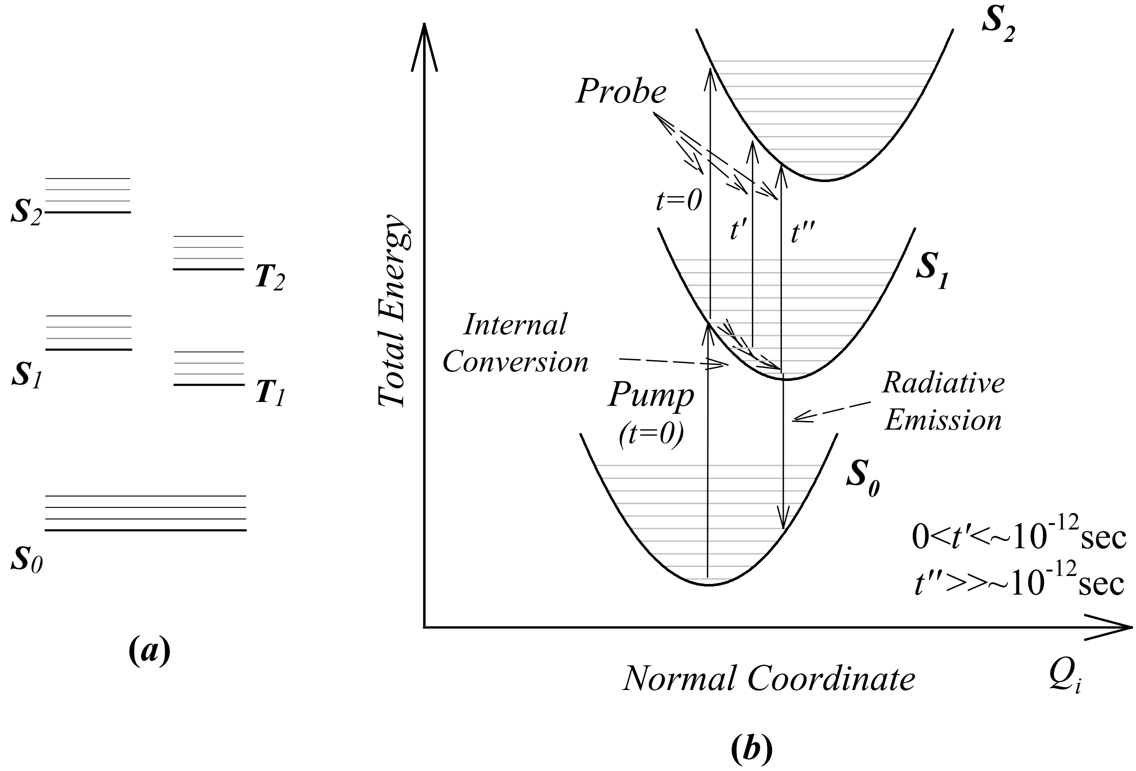

Figure 2.3. (a) B-type energy levels scheme considering also $S_2$ and $T_2$, the second excited singlet and triplet states, respectively. (b) Schematic picture of a transient absorption from $S_1$ to $S_2$ (see text). The internal conversion and the $S_1 \rightarrow S_0$ emission are also shown. Three cases are depicted: the probe and the pump pulses are simultaneous ($t$=0); the probe induces the transition during the internal conversion ($t'$); the probe arrives after the thermalization to $S_1$ minimum ($t''$).

delayed with respect to the pump, in order to explore the $S_1$ state at different times after the excitation. We can recognized two regimes (see figure 2.3(b)), if the $S_1 \rightarrow S_2$ transition occurs before or after the complete internal relaxation. In the first case, the atoms will be not in the $S_1$ equilibrium position, the $S_1 \rightarrow S_2$ absorption coefficient could be different in this configuration and, during the relaxation, a time dependence of $\alpha$ is expected (9). In the second case, the absorption process is analogous to the $\boldsymbol{S_0 \rightarrow S_1}$ transition previously described. The main difference lies in the dependence of $\alpha$ on the $\boldsymbol{S_1}$ population $n_S$ (see equation (2.23)), which is time dependent, accordingly to a pure exponential time decay with decay rate $k_S+k_{ISC}$ (see equation (2.48) and related discussion). So, the probe depletion signal is expected to decrease with the same time constant of the luminescence signal.

It is worth to note that since the value of $n_S$ depends on the pump intensity, the probe absorption is not an absolute measurement.

---

(9) We want to note that, even in this non equilibrium case, the $\boldsymbol{S_1 \rightarrow S_2}$ transition has to be thought instantaneous (vertical transition), occurring in $\sim 10^{-15}$ sec.

# Chapter 3

# Materials and Methods

In this chapter we will report the main details on the sample employed in this thesis and the experimental techniques adopted.

## 3.1 Samples: Synthesis techniques

### ***3.1.1 Bulk samples***

Several manufacturing techniques exist and, as pointed out in the first chapter, they can differs for an unbelievable numbers of parameters (the adopted physicochemical process, the purity of the starting material, the thermal history, the synthesis atmosphere, doping, etc.). The main methods used for industrial manufacturing are characterized by high temperatures (~2000 °C), apart from the sintering of silicon and germanium oxides by way of very high pressure ($\sim 10^{10}$ Pa), since they resort to the fusion of $SiO_2$ quartz powders (natural silica) or to the oxidation of $SiCl_4$ vapors (synthetic silica). The doping with Ge atoms is obtained, in the former case, by mixing silica quartz powders with $GeO_2$ quartz powders or, in the latter case by introducing $GeCl_4$ vapors. Similar methods are adopted to dope samples with Sn atoms.

An other synthesis method is the *Sol-Gel method* which, even if it is still not usually adopted for commercial applications, is particularly powerful for research purposes, being even itself subject of an intense investigation [**Grandi, 1998, Brinker *et al.*, 2000, Grandi *et al.,* 2002** and references therein]. The scheme of synthesis of silica specimens with Sol-Gel method is shown in figure 3.1. The synthesis of undoped $SiO_2$ is usually performed starting from a aqueous solution of alkoxides like silicon tetramethoxide (TMOS) and silicon tetraethoxide (TEOS). The so obtained sol (a suspension of colloidal solid particles) condenses, reaching the gel phase. The gelation occurs when a network is created that spans the entire solution volume. In the gel state, the system is highly porous and it is characterized by a great amount of solvent and reaction products inside the pores.

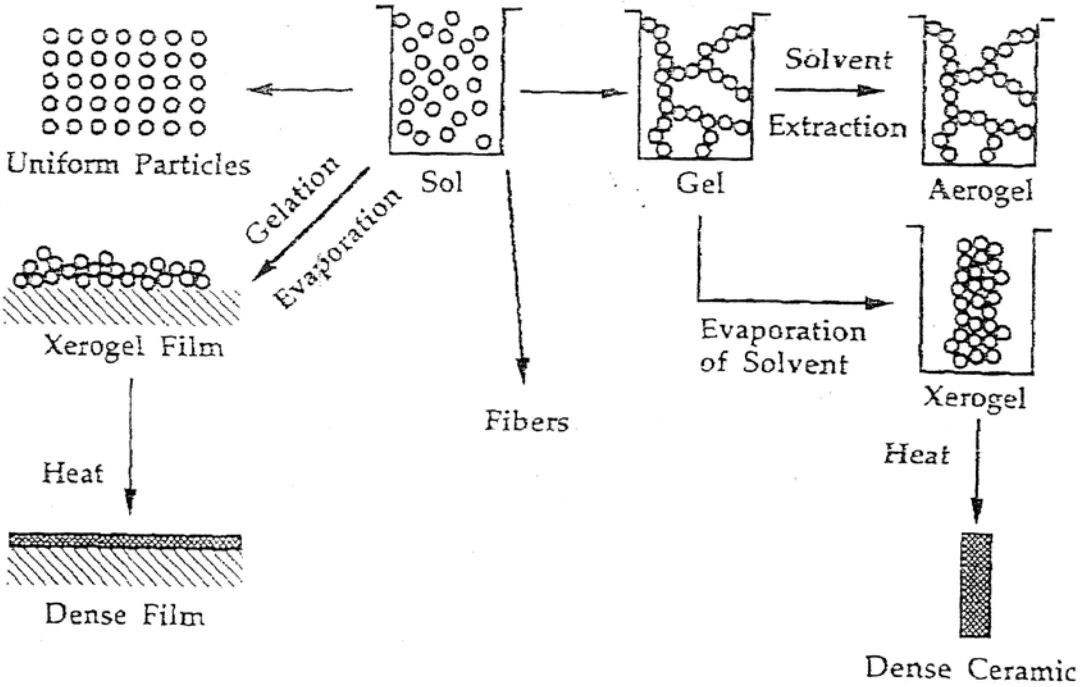

Figure 3.1: Scheme of synthesis with Sol-Gel method. Also the synthesis methods directly from the sol are reported [**Grandi,1998**]

The methods to extract the solvent (gel drying) are *evaporation* or *supercritical solvent extraction*. In the former case, the samples are allowed to dry slowly, at room temperature, typically in some weeks. The sample so obtained (*xerogel*) is characterized by a final size which is remarkable smaller than the initial one and by a density similar to the glassy silica. In the latter case, the gel is heated up to a temperature higher than critical temperature of the solvent, which can be so extracted without boiling and consequent cracking of the sample. The specimens obtained accordingly with this procedure are termed *aereogels*; they are very porous systems with low density and almost the same size of the initial gel. At the variance of the xerogels, they are characterized by the absence of solvent residues because of high porousness.

The last step consists of a thermal treatment to eliminate the inner porousness (*densification* or *sintering process*). Concerning the xerogels, the densification temperature is rather low (900-1000°C) but it must be reached very slowly ($\leq 0.1\,{}^{°C}/_{min}$), in order to avoid that the embedded solvent residues could crack the samples by boiling. Regarding the aerogels, the densification temperature is 1000-1400°C and can be reached ten times more quickly. After this treatment the porousness is eliminated and a glassy silica sample is obtained.

In order to dope the final sample, a proper chemical compound containing the wanted impurity can be added in the initial aqueous solution, or by mixing the undoped sol with a sol obtained by alkoxides of the impurity.

The features that make the Sol-Gel method so suitable for research purposes are the high reproducibility and the possibility to control the content of various compounds. This is a useful and actually investigated characteristic for the preparation of high performance materials for electronic and optical devices [**Shen *et al.*, 1998, Chiodini *et al.*, 1999, Mezza *et al.*, 1999, Brinker *et al.*, 2000, Grandi *et al.*, 2003**].

The Ge doped bulk samples used for this thesis are obtained starting from a aqueous solution of TEOS and germanium tetraethoxide (TEOG). The aerogel, obtained in agreement with the previous discussion, is heated up to 1150 °C at $0.3\,{}^{\mathrm{°C}}/_{\mathrm{min}}$ and then maintained at this temperature for 24 hours. The atmosphere is oxygen up to 700 °C and then vacuum, to stimulate the formation of ODCs. A detailed description of the synthesis protocol is reported by **Grandi *et al.*, 2002** and **2003**. The samples used for this thesis have a nominal concentration of 1000 and 10000 molar ppm and, after an optical polish treatment, their thickness was reduced to 1 mm. The formation of $=\mathrm{Ge}^{\bullet\bullet}$ centers is proved by the presence of a Ge related B-type activity proportional to the Ge content [**Grandi *et al.*, 2003**].

Concerning the Sn doped bulk sample, Sol-Gel synthesis from hydrolysis of TEOS and dibutyl-tin-diacetate (DBTDA) was employed to obtain Sn-doped silica containing up to 0.5 mol% of dispersed tin in substitutional position for silicon atoms, avoiding Sn segregation. In fact, tin shows a much lower solubility in silica than Ge, and it easily segregates in its own oxide phase $SnO_2$, six-fold coordinated in a rutile lattice. After the gelation and the drying process (15 days at 40°C), a xerogel was obtained. The glassy silica samples were obtained by heating the xerogels up to 1050 °C at $0.07 - 0.1\,{}^{\mathrm{°C}}/_{\mathrm{min}}$ and maintained at this temperature for 20 hours. The atmosphere was $O_2$ up to 450°C, vacuum from 450°C and 950°C, $O_2$ again up to 1050°C. See **Chiodini *et al.*,1999** and **2001** for a more detailed discussion. We used two specimens with a nominal concentration of 100 and 2000 molar ppm and a thickness of 1.4 mm. The presence of a clear Sn related B-type activity in both samples confirms the stabilization of $=\mathrm{Sn}^{\bullet\bullet}$ centers after the synthesis process.

It is worth to note that, even if many properties of silica depends on the manufacturing process and the thermal history (see chapter 1), it has been observed that both the Ge and the Sn related activity in Sol-Gel samples do not show significant differences with respect to the case of samples from the melt [**Chiodini *et al.*, 2000, Cannizzo *et al.*, 2003**].

### *3.1.2 Microporous samples with surface activity*

Point defects can be stabilized on silica surface by different methods. One of them is the mechanical treatment of the material in a controlled atmosphere. In this case, the formation of defects is due to the cleavage and rearrangement of chemical bonds in a solid matrix under the action of mechanical strains [**Radzig, 2000** and references therein]. Another method is the thermochemical one [**Morterra and Low, 1973**], where the silica surface is chemically modified in order to induce defect precursors which are subsequently activated by a thermal treatment at high temperature (> 1000 K). Both methods induce typically a defect surface concentration of $10^{12}$ $cm^{-2}$ [**Radzig, 2000**].

In the case of a bulk sample with a thickness of 1 mm, the surface defect content is then $2 \cdot 10^{11}$ $cm^{-3}$, which is much less than the minimum amount detectable with non site-selective spectroscopy ($>10^{15}$ $cm^{-3}$). To increase the number of centers per $cm^3$ it has been successfully employed silica powders and microporous silica samples. Since the powders can not be employed for optical absorption measurements in the UV-Vis range because of remarkable scattering [**Radzig, 1995**], at the variance of microporous silica, we will focus only on the latter one. This kind of silica is characterized by a relevant presence of pores whose size can vary from few tens of Angstrom to microns. Due to the internal surface of these pores, these samples are characterized by an effective surface much wider than the macroscopic external surface (or, in other word, the surface of a bulk sample with the same shape). The effective surface per mass unit is termed *specific surface*. Microporous silica can be characterized by a specific surface area more than $10^6$ $cm^2/g$ and a corresponding defect concentration per gram of material more than $10^{18}$ can be reached, which is sufficient for reliable experimental detection. A method to synthesize microporous silica is to press high dispersed silica powder in order to obtain semitransparent films which are suitable for quantitative optical measurements [**Radzig, 2000**].

The samples used for this thesis work are indeed pressed transparent films and have the size of 10x3.5x<0.1mm. They were obtained by pressing a highly disperse Aerosil®-300, a hydrofilic fumed silica with an average particle size of 7 nm (1). They are characterized by a microporous structure with a micropore size of 30-60 Å and a specific surface of $10^6$ $cm^2/g$ [**Bagratashvili *et al.*, 1995, Radzig, 1998**].

In order to stabilize $=Si^{\bullet\bullet}$ on the pore surfaces, a thermochemical methods was adopted: the superficial ≡Si-O-H groups were converted to the $\equiv Si\text{-}O\text{-}CH_3$ groups and the sample was activated by vacuum pyrolysis at 1200 K, which is accompanied by formation of $=Si^{\bullet\bullet}$ centers with a surface concentration of $\sim 1 \cdot 10^{13}$ $cm^{-2}$. This sample is indeed characterized by a relevant OA band around 5.2 and two related emissions at 4.4 eV and 2.7 eV, in agreement with previous results [**Skuja *et al.*, 1984**] and the discussion in the first chapter.

To synthesize the sample with surface $=Ge^{\bullet\bullet}$ centers, Ge atoms where chemically deposited on the surface of disperse Aerosil®-300 before pressing [**Radzig, 1995a**]. After a treatment in $O_2$ atmosphere at 850 K, to remove organic impurities on surface, and a subsequent high vacuum pyrolisis treatment at 1200 K, the formation of surface $=Ge^{\bullet\bullet}$ centers with a concentration of $\sim 1 \cdot 10^{13}$ $cm^{-2}$ is achieved (2). The stabilization of these defects is proved by the appearance of a clear OA band at 5.4 and two related emissions at 4.3 eV and 3.2 eV.

Since the surface centers are highly reactive, the samples were placed in a conventional suprasil silica container with residual He atmosphere of 3-4 mbar. Even if the container is characterized by a negligible optical activity (≤ 5 % of the observed signals), we used an

---

(1) General Aerosil brochure, Company Publication, Degussa AG, Düsseldorf.

(2) V.A. Radzig, private communication.

empty sample container as a reference for the background subtraction from the experimental measurements.

## 3.2 Experimental set-up and data analysis

### *3.2.1 Absorption measurements*

The absorption measurements were carried out with a JASCO V-570 double-beam spectrophotometer. It is equipped with two light sources: a deuterium discharge tube for the UV range 190-340 nm (6.5-3.6 eV) and a tungsten iodine lamp in the visible and near-IR range 340-2500 nm (3.6-0.5 eV). The monochromator is based on a Czerny-Turner mount grating with 1200 $^{\text{lines}}/_{\text{mm}}$ and with 300 $^{\text{lines}}/_{\text{mm}}$ for use in the UV-Vis range and in the near-IR region, respectively. The monochromatic beam is then 50%:50% split into two light paths by a beam splitter mirror: one goes through sample, while the other is considered as a reference beam. Finally, the two beams are alternately detected by a photomultiplier tube (UV, Vis) or a PbS photoconductive cell (near-IR).

The absorption spectra reported in this thesis were detected in the UV range 200-500 nm (2.5 ÷ 6.2 eV), with a bandwidth value of 0.5 nm, a time constant value of 1 sec, a scan speed of 20 $^{\text{nm}}/_{\text{min}}$ and a data step of 0.5 nm. All the spectra were subtracted of the zero signal, i.e. the absorption spectrum in the same respective experimental conditions (included the mounting of the sample-holder), apart from the sample. In the case of a non negligible background, the absorption bands were isolated subtracting the tangent to the minima as a baseline.

For optical measurements as a function of temperature in the range 300 ÷ 20 K, we used an Oxford-Optistat$^{\text{CF}}$ continuous-flow helium cryostat, equipped with four optical windows.

Temperature was controlled by an Oxford-ITC503 instrument. At each temperature, the spectra were recorded after 20 min for thermal equilibrium.

In agreement with the theoretical background reported in the previous chapter, the analysis of the thermal behavior of the absorption band, $\alpha(E)$, was done in terms of the first ($M_1$) and second ($M_2$) moments of its spectral profile $B(E)=\alpha(E)/E$, according to the following equations:

$$M_1 = \frac{1}{M_0}\int_0^{+\infty} E \cdot B(E)\, dE\,, \tag{3.1}$$

$$M_2 = \frac{1}{M_0}\left(\int_0^{+\infty} E^2 \cdot B(E)\, dE - M_1^{\,2}\right), \tag{3.2}$$

where $M_0$, the zero moment, is given by:

$$M_0 = \int_0^{+\infty} B(E)\, dE\,. \tag{3.3}$$

### *3.2.2 Luminescence measurements*

The steady-state luminescence measurements were carried out with a JASCO PF-770 spectrofluorimeter equipped with a 150 W Xenon arc lamp and operating in the spectral range 200-750 nm (6.2-1.7 eV). Both the excitation and emission monochromators are based on holographic concave gratings with 1800 $^{\text{lines}}/_{\text{mm}}$. The emitted light is finally detected by a photomultiplier tube (PMT). Since the two monochromators can be separately and simultaneously driven, the light emitted from the sample under continuous wave (c.w.) excitation can be detected in different ways and in particular: i) as a function of emission wavelength $\lambda_{em}$, at a fixed excitation wavelength $\lambda_{ex}$ shorter than $\lambda_{em}$ (PL spectrum), or ii) as a function of $\lambda_{ex}$, at a fixed $\lambda_{em}$ longer than $\lambda_{ex}$ (PLE spectrum). A feedback circuit is present, which monitors the light outgoing from the excitation monochromator and adjusts the PMT gain to balance the effects of the time fluctuations and the spectral distribution of the light source and the spectral response of the excitation monochromator on the measurements. Since this circuit employs a Rhodamine B quantum counter, the final effects is equivalent to use an ideal excitation monochromator and a very stable light source with a constant spectral photon density. The advantages are: i) the PLE spectra, as collected by the spectrofluorimeter, are already corrected for the spectral distribution of the light source and for the spectral response of the excitation monochromator, so they need no other corrections, ii) PL spectra collected under different excitation wavelengths and in different days can be not only qualitatively (i.e. the profiles) but also quantitatively (i.e. the intensities) compared.

It is worth to note that, since the feedback circuit normalizes to the number of photons emitted by the light source $n_{source}$ and the incident intensity is proportional to $E_{ex} \cdot n_{source}$, the PLE spectra result to be multiplied by $E_{ex}$. So they have to be compared directly with the absorption coefficient.

Regarding the PL spectra, they need one more correction due to the spectral response of the detection system (emission monochromator and PMT). To measure this response the excitation light is scatter by a MgO diffuser plate and then collected by the detection system during a synchronous spanning of $\lambda_{ex}$ and $\lambda_{em}$ (the emission is revealed at the same wavelength of the excitation). This spectrum $R(\lambda)$ is proportional only to the spectral response of the detection system, being the fluctuations and the spectral dependence of the excitation light balanced by the feedback circuit. After that all the PL spectra were divided by $R(\lambda)$, they need no other correction.

Concerning the mounting of the sample, a 45°-backscattering geometry was adopted: one of the optical surfaces of the sample is placed a 45° with respect to the excitation light, while the light emitted from the other face is collected at 90° with respect to the excitation light. This geometry avoids that the excitation light can be directly reflected towards the detector, decreasing the signal-to-noise ratio.

It is worth to note that since a PMT is a photon-counter, the emission signal is proportional to the photons emitted at a given $\lambda_{em}$, instead of the emitted energy and, as anticipated in paragraph 2.4, the PL band will be the spectral distribution of the emitted photons.

For a more detailed discussion on the several aspects associated with a fluorescence measurement and with spectrofluorimeters (monochromators, spectrum correction, sample geometry, etc) see **Lakowicz, 1983**.

The PL spectra reported in this thesis were collected in the emission range 250 ÷ 550 nm (4.96 ÷ 2.25 eV), under excitation in the range 220 ÷ 274 nm (5.64 ÷ 4.53 eV) and in the range 305 ÷ 335 nm (4.07 ÷ 3.70 eV). Both excitation and emission bandwidths were chosen to be 3 nm, and a scan speed value of 50 nm/min, a time constant value of 2 sec and a data step of 0.5 nm were used.

The PLE spectra were detected varying the excitation wavelength in the range 200 ÷ 400 nm (6.2 ÷ 3.1 eV), being all the other experimental parameters the same. The emission wavelength interval were 275 ÷ 320 nm (4.5 ÷ 3.8 eV) and 360 ÷ 440 nm (3.4 ÷ 2.8 eV) for the $\alpha_T$ and $\beta_T$ bands, respectively.

PL and PLE spectra as a function of temperature in the range 330 ÷ 3 K were carried out with the same set-up and the same thermalization procedure used for the absorption measurements.

Measurements of the $\alpha_T$ time decay were carried out as a function of temperature and of excitation energy in the UV range. The excitation energies explored were around the maximum of the $B_{2T}$ band (~ 5.0 eV). Lifetime measurements of the emission at the maximum of the $\alpha_T$ were carried out by pulsed excitation in the range 275 ÷ 218 nm (4.5-5.7 eV), with a spectral resolution of 0.23 nm, using synchrotron radiation light with a pulse FWHM of 130 psec, at the SUPERLUMI station on the I-beamline of HASYLAB at

DESY, Hamburg (Germany). The wavelength of excitation beam was selected by a primary monochromator consisting in a 2 m unit in 15 ° McPherson mounting, while the wavelength of the emitted light was selected by a 0.5 m monochromator (Czerny-Turner mounting) and detected by a photomultiplier (Hamamatsu R2059 model). The dead time of the overall detection system was evaluated as 2.3 ns, so that only data for times longer than 2.3 ns were considered for the time decay analysis. For each measurement, the PL time decay was detected with high time resolution using 1024 memory channels to scan an interval of 192 ns between adjacent pulses. A sample chamber, equipped with a continuous-flow liquid-helium cryostat, was used to vary the temperature from 6 up to 295 K, with an accuracy of ±1 K. The experimental apparatus used at DESY is described with more details by **Zimmerer, 1991**.

### *3.2.3 Pump-probe transient absorption measurements*

In figure 3.2 it is reported a flow-chart of the pump-probe set-up used for the transient absorption measurements for this thesis which was used to investigate the time domain from fsec up to hundreds of psec. These experiments were carried out in the laboratories of Prof. M. Chergui at the Laboratoire de Spectroscopie Ultrarapide, Ecole Polytechnique Fédérale de Lausanne, Lausanne (Switzerland). As discussed in the previous chapter, the probe pulse reaches the sample after a time delay $\Delta t$ with respect to the pulse. To synchronize the two pulses, they were generated by the same output of an high power laser centered at 1.6 eV which was split into two beams, being used to produce the pump at 4.7 eV and the probe at 3.1 eV through non linear crystals (in figure, the 4.7 eV and the 3.1 eV generators, respectively). It was possible to control the pump and pulse beams intensity by placing proper O.D. filters in the respective optical paths. To induce a controlled time delay with a resolution of ~fsec, a mirror mounted on a micrometric translation stage (delay stage) is used to change the probe optical path. After the probe pulse passed through the sample, it is detected by a photo-diode, while the pump is terminated by a beam dump. To measure the initial probe intensity $I_0$, a probe pulse is detected without pump, afterward the pump pulse was generated and the intensity of the subsequent probe pulse $I_{probe}$ was measured. The probe depletion is calculated as $\Delta I = I_0 - I_{Probe}$. In order to work with the same initial conditions, the time between the two consecutive probe pulses was chosen longer enough to have all the centers in the $\boldsymbol{S_0}$ state in both cases. Considering the two investigated systems (the =Ge$^{\bullet\bullet}$ and =Sn$^{\bullet\bullet}$ centers) the longest time is the Ge related triplet lifetime $\tau$=110 μsec and we used a probe repetition rate of $2 \cdot \nu_p$ = 1000 Hz (> $(5 \cdot \tau)^{-1}$) and consequently a pump repetition rate of $\nu_p$ = 500 Hz. It is worth to note that, if we indicate with $I_{avr} = (I_0 + I_{Probe})/2$, the signal detected has a component which oscillates at $2 \cdot \nu_p$ with amplitude $I_{avr}$, superimposed to a signal at $\nu_p$ and amplitude $\Delta I$. This feature allows a study in the frequency domain in order to increase the signal-to-noise ratio (lock-in technique): the Fourier transform of the probe signal is calculated and the amplitude at $\nu_p$ and $2 \cdot \nu_p$ are proportional to $\Delta I$ and $I_{avr}$, respectively. Both the lock-in set-up and the micrometric translator are controlled by computer.

Since the pump pulse is very intense it is possible that the investigated centers are burned or converted during the experiment due to extensive irradiation. To monitor the number of centers and the possible deterioration of the samples, it was observed *in situ* the intensity of the $\alpha_T$ and $\beta_T$ emission induced by the pump pulse.

Since we used an homemade set-up, which we developed on the purpose for these measurements, we report more technical details on it. The set-up is capable of recording the probe depletion as function of the time delay of the probe pulse with respect to the pump pulse in the range up to 500 psec, with a resolution of 3 fsec. The experimental set-up consisted of a 1 kHz Ti: sapphire laser/regenerative amplifier system producing ~100 fsec, 0.85 mJ pulses centered at ~800 nm (1.6 eV). The amplified output was 90%:10% split. The 10% part was attenuated and focused into a 1 mm thick BBO crystal to produce the second harmonics of the fundamental wavelength namely 400 nm (3.1 eV) probe light. This light, after being variably time-delayed using translation stage, was focused into the sample, using a thin lens with a focal length of 150 mm, to a spot of ca. 30 μm size. After the sample, it was re-collimated again by another lens and focused onto a suitably fast photodetector (here a Si photodiode Hamamatsu S3279 model). The 90% part of the fundamental beam served as the pump beam. Its wavelength was set to 266 nm by tripling the frequency of the fundamental beam in a set of two subsequent BBO crystals (first doubling the frequency of the fundamental beam and later mixing the remaining part of the fundamental with newly produced second harmonics in another nonlinear crystal). The cut angles of both nonlinear crystals were adjust for the optimum conversion of the parametric process and the polarization states of wavelength. The pump was then focused onto the sample using a thin UV-coated lens with 200mm focal length to obtain a spot of ca. 70 μm. At the sample position, the excitation and probe beams were overlap at the angle of approx. $15^o$. The relative polarization of the excitation and probe beams was $90^o$. The temporal resolution of both pump and probe pulses was estimated to amount to the FWHM of 200 fsec. In addition, to halve the repetition rate of the pump beam, its beam was chopped with a mechanical chopper at 500 Hz frequency (HMS-221 model), whereas the probe pulse was set to the nominal repetition rate of the laser source at 1 kHz. This combination, together with lock-in amplifier detection (Stanford Research System lock-in amplifier SR830 DSP model), allowed us to record signals originating from the photoexcited sample only. The time constant used in these experiments was 1 sec. Concerning the intensity of both pulses, we took a special care to work in a linear regime for the transient absorption signal. In particular, pump power density per pulse was chosen to be $9\times10^{12}$ and $2\times10^{13}$ $(\mathrm{mW/cm^2})_{\mathrm{pulse}}$ for the measurements on the Ge and Sn related activity, respectively. Regarding the probe pulse, we set the value of $3\times10^{11}$ $(\mathrm{mW/cm^2})_{\mathrm{pulse}}$ for both experiments. With these values, no remarkable bleaching was observed in hours time domain. In this respect, measures up to 500 psec were the longest with a duration of 20 min, however we changed the spot on the sample after each measure.

For a more detailed discussion on the several aspects associated with measurements in femto and picosecond time domain and with the related experimental techniques see **Diels and Rudolph, 1996** or **Rullière, 1998**.

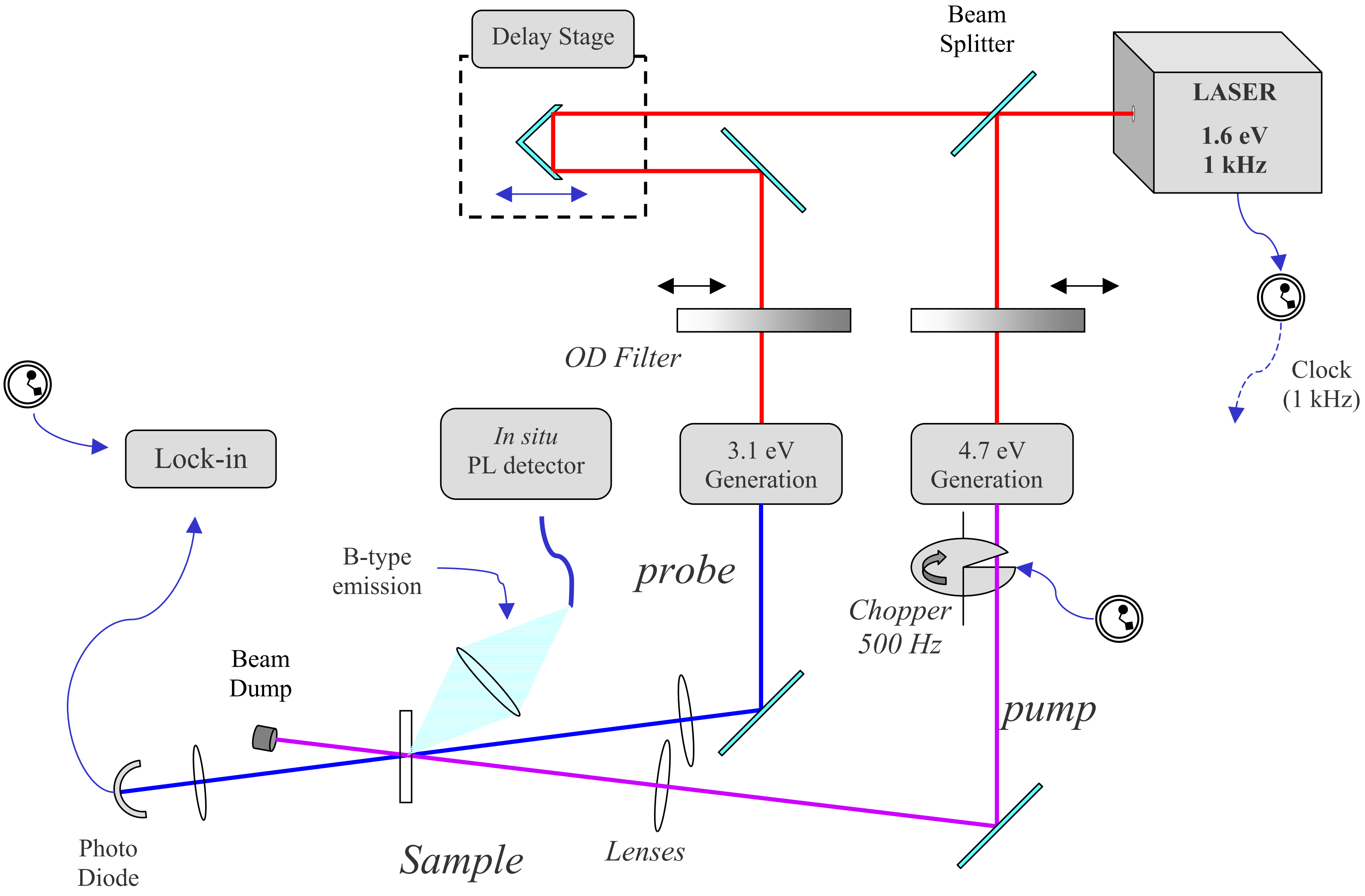

Figure 3.2. Flow-chart of the femtosecond transient absorption set-up (see text for details).

# Chapter 4

# Optical properties of two-fold coordinated germanium and their relation with the conformational disorder of vitreous matrix

4.1 Experimental results and discussion
  4.1.1 Room temperature measurements
  4.1.2 Temperature effects on the absorption band profile: the defect-matrix coupling
  4.1.3 Temperature dependence of the emission bands: the intersystem crossing process
  4.1.4 Temperature effects on lifetimes
4.2 The theoretical model
  4.2.1 Introduction to the model
  4.2.2 Results and discussion
4.3 Conclusions

As discussed in the first chapter, the iso-electronic series =Si$^{\bullet\bullet}$, =Ge$^{\bullet\bullet}$ and =Sn$^{\bullet\bullet}$ supplies a good system to study the structural and dynamic properties of silica matrix and to point out the role of the conformational disorder [**Skuja, 1992, Skuja *et al.*,1995, Leone *et al.*, 1997** and **1999a, Radzig, 1995a, Bagratashvili *et al.*, 1995**]. Since the most studied is the Ge related bulk activity, we have focused our attention on this activity to point out the relation between the optical activity of =Ge$^{\bullet\bullet}$ center and the dynamic properties and the conformational heterogeneity of vitreous silica.

In the first section of this chapter, we will discuss our experimental results on the Ge related B-type activity; in the second part we will propose a theoretical model able to rationalize in a unitary framework the experimental results.

## 4.1 Experimental results and discussion

All the experimental results reported in this chapter were obtained on a silica specimen having a nominal Ge content of 1000 molar ppm.

### *4.1.1. Room temperature measurements*

In figure 4.1 the UV absorption spectrum of the Ge-doped sample at room temperature in the range 3.6-6.2 eV is reported. It is dominated by the presence of the $B_{2Ge}$ band at 5.15 eV, whose intensity at room temperature is $\alpha_{max} \approx 20$ cm$^{-1}$. On the basis of the cross section value $\sigma = 1.0 \pm 0.5\ 10^{-16}$ cm$^2$ [**Agnello *et al.*, 2000**], we can estimate the concentration of $=\text{Ge}^{\bullet\bullet}$ centers as $\approx 2\times10^{17}$ /cm$^3$.

The luminescence activity excited within this band is reported in figure 4.2, where the emission spectra at room temperature under continuous wave (c.w.) excitation at 5.00 eV are shown. We observe two emission bands: the greater one is centered at 3.19 ± 0.01 eV and with a FWHM of 0.43±0.01 eV; the other one, which is ~4 times smaller, is characterized by a peak position of 4.31 ± 0.02 eV and a FWHM of 0.48 ± 0.01 eV. In agreement with the discussion in chapter 1, the former is the $\beta_{Ge}$ band and the latter is the $\alpha_{Ge}$ band. In the light of the energy levels scheme for the B-type activity, the occurrence of a triplet band greater than the singlet band indicates the presence of a very effective ISC rate, ~4 times greater than the $S_1$ radiative rate.

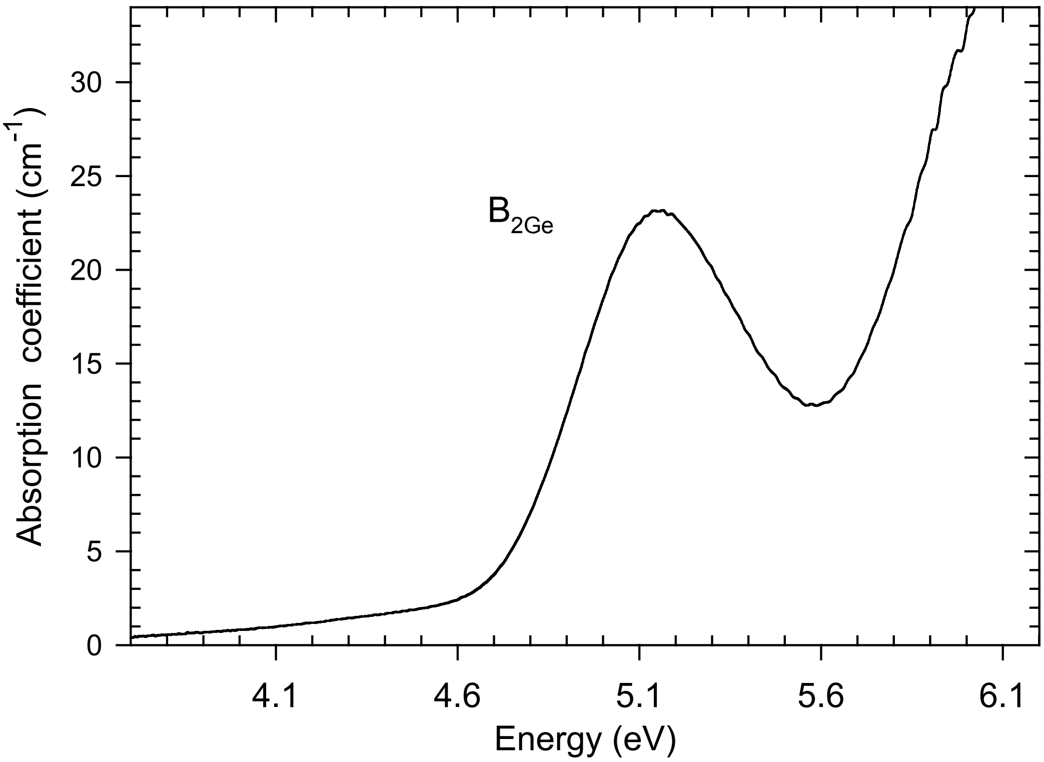

Figure 4.1. Optical absorption $B_{2Ge}$ band detected at room temperature in a 1000 ppm Ge-doped sol-gel sample.

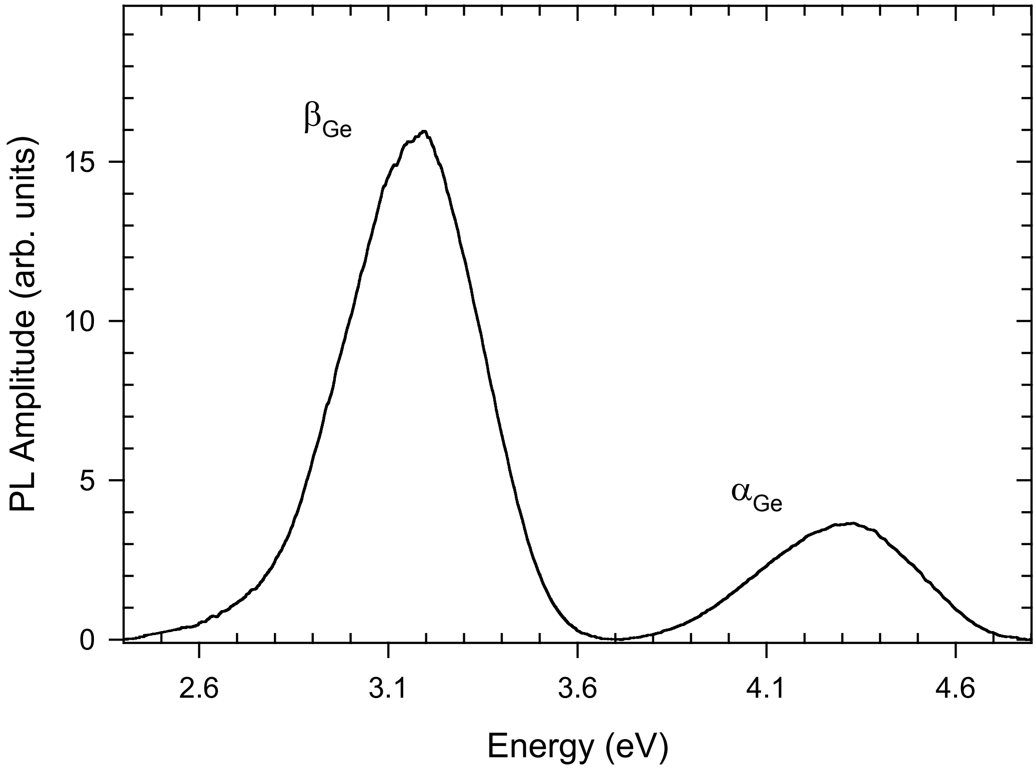

Figure 4.2. Emission spectrum obtained at room temperature, under excitation at 5.00 eV.

The excitation spectra at 3.16 and 4.25 eV are reported in figure 4.3 together with the $B_{2Ge}$ OA band. Both excitation spectra show a clear band centered at 5.1 eV and almost overlapping with the $B_{2Ge}$ band spectrum. This result is in agreement with the B-type level scheme and confirms the previous assignment of both emissions to the $B_{2Ge}$ band. The comparison of the PLE spectra with the OA band reveals small but significant differences not expected in the framework of chapter 2, which speak for a inhomogeneous broadening of the B-type activity (see discussion below). Furthermore, since the two PLE spectra are not coincident, a dependence on the excitation energy of the relative amplitudes for the two PL bands is expected.

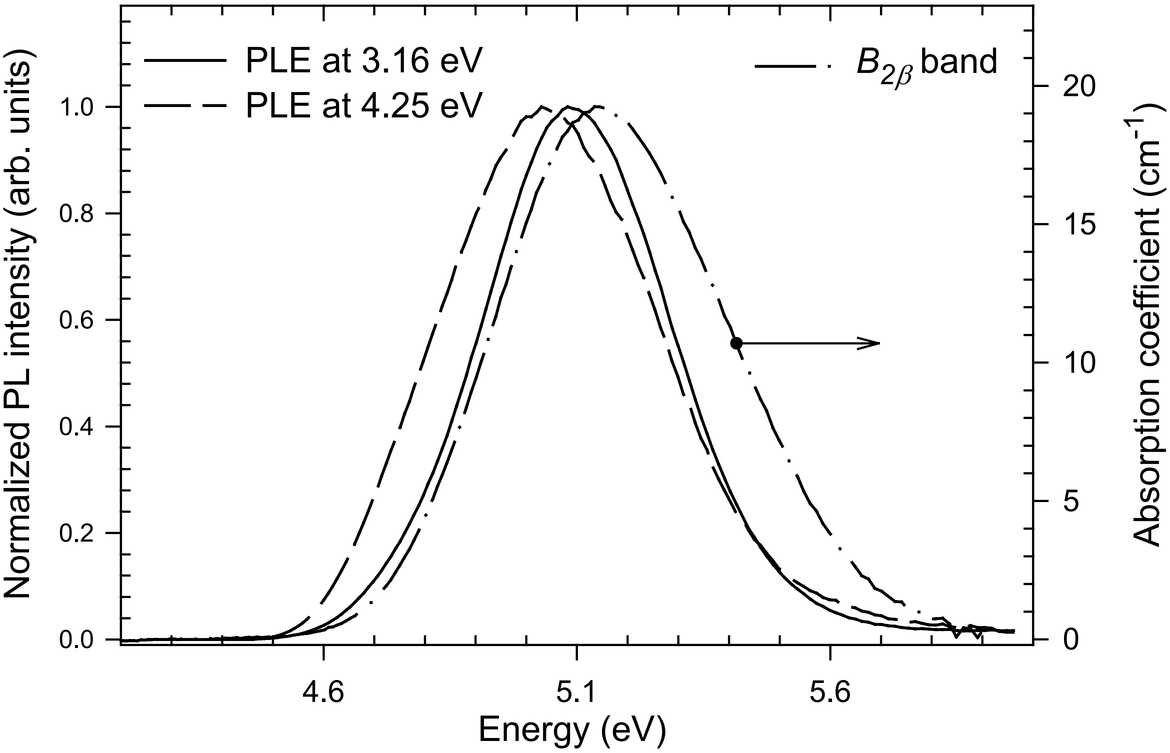

Figure 4.3. PLE spectra at 3.16 eV (solid line) and at 4.07 eV (dashed line) compared with the Ge related $B_{2Ge}$ band (dash-dot line). Both PLE bands are normalized to the maximum.

The comparison of OA band in figure 4.3 and the PL bands in figure 4.2 shows that no distortion of $\alpha_{Ge}$ band due to re-absorption by the $B_{2Ge}$ band is present, being the overlapping of the two bands negligible. In other words, the amplitude of the absorption band at the

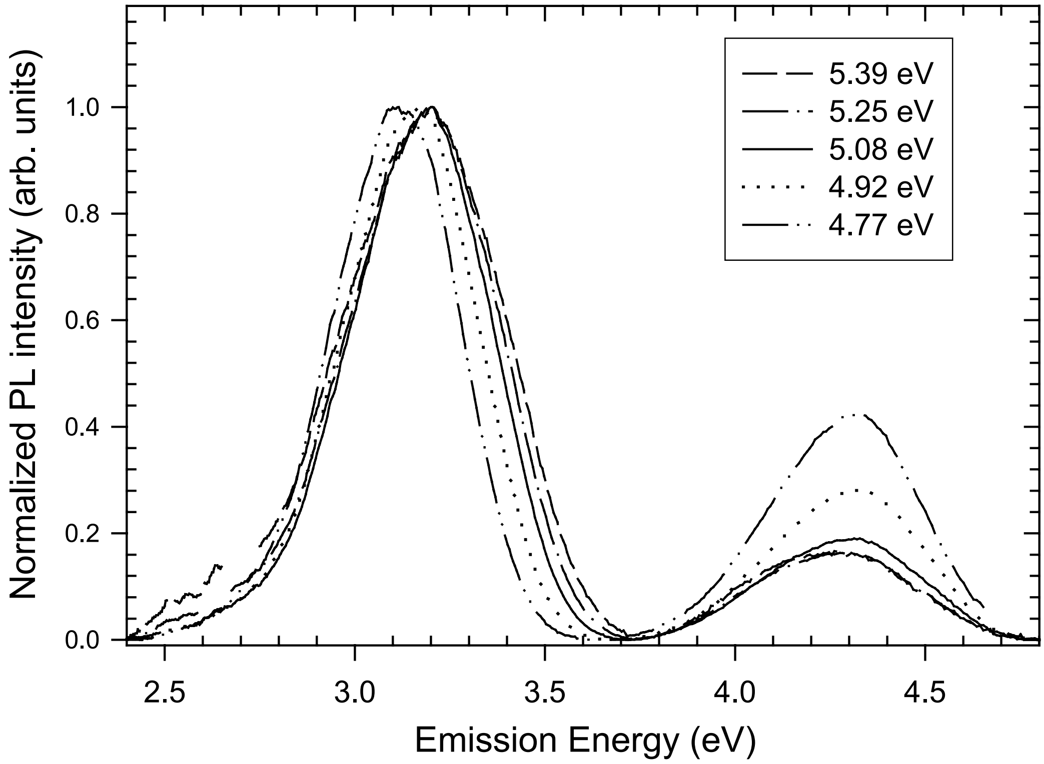

Figure 4.4. Photoluminescence spectra at room temperature, under excitation energy from 4.77 to 5.39 eV for Ge related bulk B-type activity. The spectra are normalized at the maximum of the $\beta_{\mathrm{Ge}}$ band, around 3.1 eV.

zero-phonon energy is very low and, together with a significant Stokes shift of 0.8 eV and a good symmetry of all the bands, it speaks for a relevant electron-phonon coupling and for Huang-Rhys constants of high frequencies modes greater than unity.

To point out the correlations between the emission and absorption spectra, we observed the luminescence activity finely tuning the excitation energy within the absorption band. In figure 4.4, the PL bands obtained varying the excitation energy from 4.77 to 5.59 eV are reported. For the sake of evidencing the differences in the spectral profiles, the data in figure 4.4 are normalized at the maximum of the $\beta_{\mathrm{Ge}}$ band, around 3.1 eV. It is immediate to note that the spectral profile of both bands are dramatically affected by the excitation energy. In particular, on increasing the excitation, the $\beta_{\mathrm{Ge}}$ band undergoes a blue-shift and an evident broadening. Regarding the $\alpha_{\mathrm{Ge}}$ band, even if not so remarkable changes in the spectral profile are found, an undoubted dependence of the amplitude with respect to the $\beta_{\mathrm{Ge}}$ band one is detected: we observe, indeed, a decreasing from 0.42 to 0.16, varying the excitation energy from the red to the blue tail of the OA band. To point out more evidences of a correlation between the observed optical properties, we collected PLE spectra with a fine tuning of the emission energy (data not reported), obtaining slight but clear dependence of the spectral profiles on the emission energy. We quantitatively analyzed the emission bands in terms of their first ($M_1$) spectral moments calculated according to the equations (2.46). Furthermore, to evidence the dependence of ISC efficiency on the excitation energy, we calculated $\zeta = k_{ISC}/k_S$ as defined by the equation (2.45). It is worth to note that, as we will show further, $k_S$ is temperature independent and homogeneous, so the ratio $\zeta$ has to be considered proportional to the ISC efficiency. The outcomes of this analysis are reported in figure 4.5: the ratio of the $\beta_{Ge}$ band area to the $\alpha_{Ge}$ band area ($\zeta$) in the panel (a) and the first spectral moment of the $\alpha_{Ge}$ and $\beta_{Ge}$ bands in the panel (b) and (c), respectively. We note in all the three panels a clear dependence on excitation in agreement with the qualitative analysis of figure 4.4.

To investigate directly the relaxation processes from $\boldsymbol{S_1}$, we studied the time decay of the emission at 4.2 eV. In figure 4.6 the time decay under excitation energy at 5.0 eV is reported, while the comparison of time decays varying the excitation energy from 4.7 to 5.0 eV are shown in the inset. In agreement with the allowed nature of the $\alpha_{Ge}$ emission, we observe that the relaxation process occurs in the nsec time domain, but this process does not obey a single exponential decay law. Considering that the observed relaxation is a single step process, the obtained result speaks definitely for a distribution of decay rates. Furthermore, we note, in the inset, an unexpected dependence on the excitation energy of the decay kinetics.

It is worth to note that all the results reported in figures 4.3-4.6 do not agree with the hypothesis of an homogenous optical activity, since a pure exponential empting of $\boldsymbol{S_1}$ and no dependence on the excitation energy of the spectral profiles and of the decay rates is expected (see chapter 2). Furthermore, we note that also the usual simplified model, discussed in

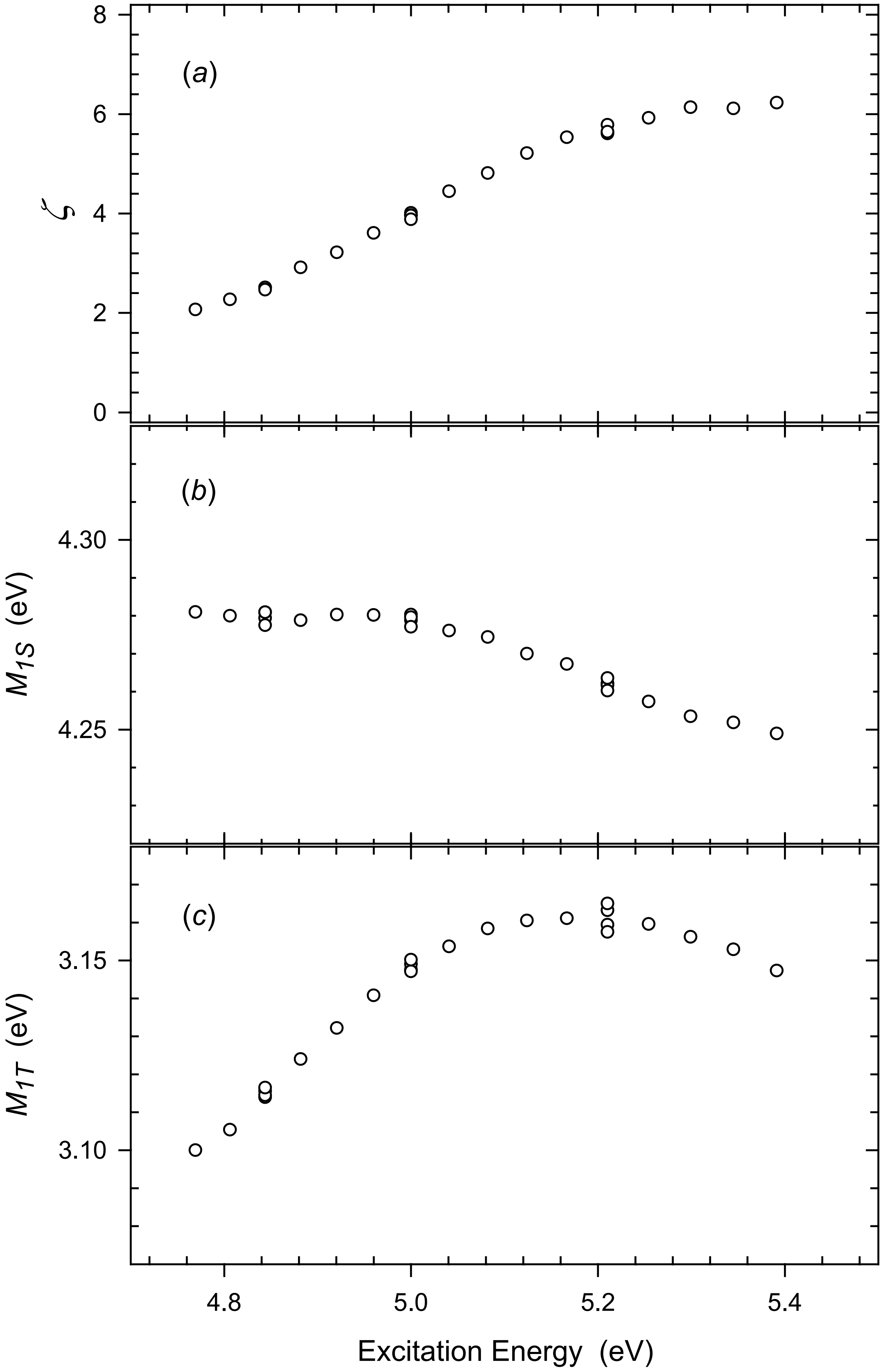

Figure 4.5. Results of the analysis in terms of spectral moments of emission bands as a function of excitation energy: (*a*) ratio of $\beta_{Ge}$ band area to the $\alpha_{Ge}$ one ($\zeta$); (*b*) first moment, $M_1$, of $\alpha_{Ge}$ and (*c*) $\beta_{Ge}$ bands.

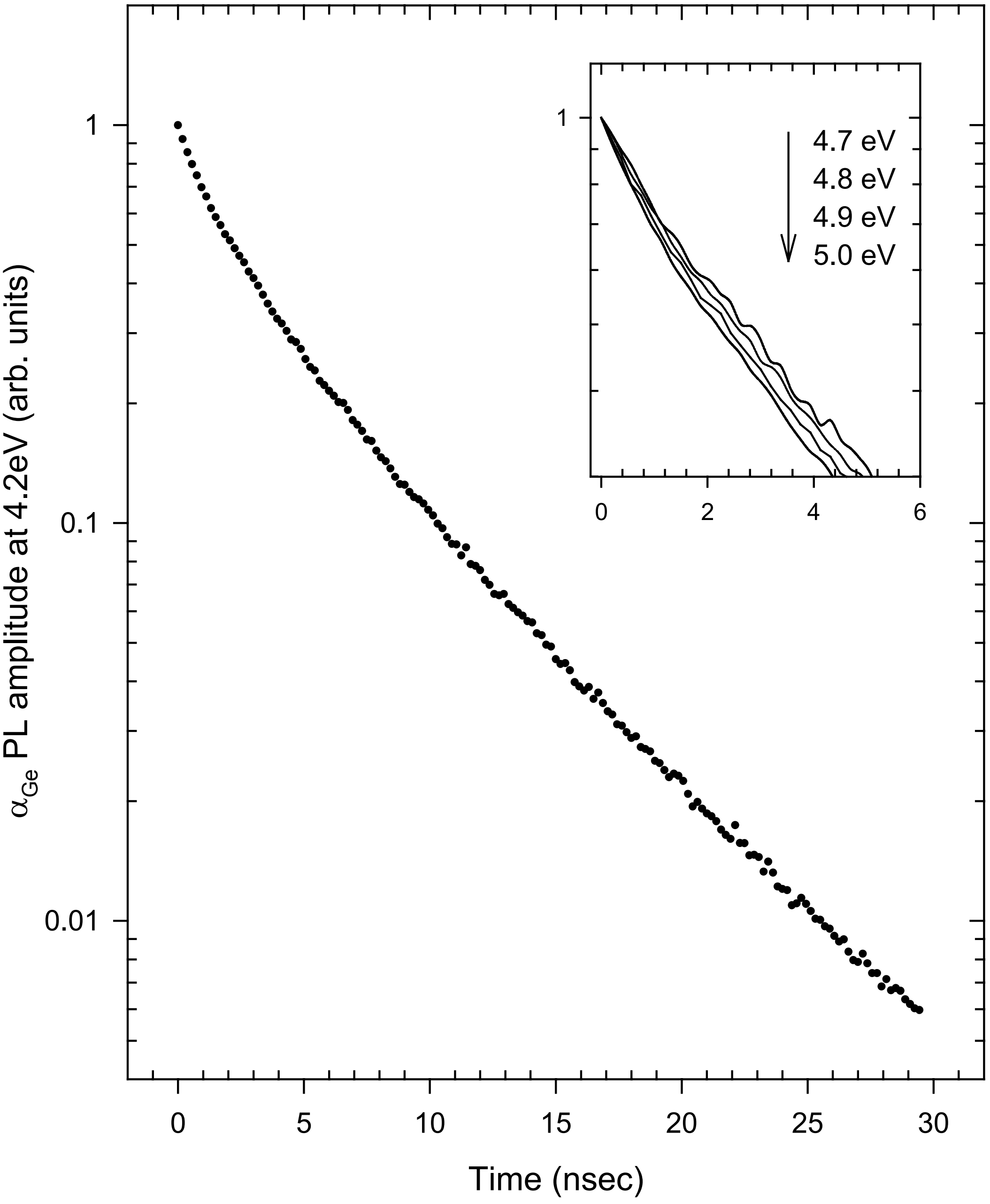

Figure 4.6. Decay kinetics of 4.2 eV emission detected under pulsed excitation at 5.0 eV, at room temperature. The inset shows the comparison of time decays normalized to the maximum at different excitation energies from 4.7 to 5.0 eV

chapter 2, is inadequate to treat these results. In particular, $\zeta$ shows a remarkable variability from 2 to 6, revealing a distribution of the ISC rates $k_{ISC}$ evidenced by the fine tuning within the OA band. This results is analog with the behavior observed for the time decay which speaks for a dispersion of the $\boldsymbol{S_1}$ relaxation rates $k$ and a dependence of this dispersion on the excitation energy. We can roughly characterize this distribution considering the greatest and the smallest slope of the decay curve of figure 4.6, in a *ln* scale for the PL intensity, as an evaluation of the upper and lower limit for the $\boldsymbol{S_1}$ decay rates. We obtain that the slope of the curve decreases from $5\cdot10^8$ to $1.3\cdot10^8$ sec$^{-1}$, suggesting a lifetime distribution form 2 to 8 nsec. It is worth to note that both $k_{ISC}$ and $k$ show the same variability. In the light of the energy levels scheme for B-type activity, this result is not surprising since the total $\boldsymbol{S_1}$ decay rate $k$ is expected to be due to the competition between the pure radiative rate $k_S$ and the ISC one $k_{ISC}$. A wider discussion of the role of $k_S$ and $k_{ISC}$ on the $\boldsymbol{S_1}$ time kinetics will be presented in the following.

It is universally accepted that all these results, usually named *spectral heterogeneity*, prove definitely an inhomogeneous nature of the B-type optical activity. In this respect, some authors [**Leone *et al.*, 1997** and **1999a, Bagratashvili *et al.*, 1995**] suggest that the observed optical activity is associated with a set of point defects that are structurally the same (i.e. =Ge$^{\bullet\bullet}$ centers) but with slightly differences in the spectroscopic properties (monomodal distribution hypothesis). They propose that the inhomogeneous nature of the =Ge$^{\bullet\bullet}$ centers is due to a small dispersion in the geometrical configurations induced by the conformational heterogeneity of the silica matrix. Other authors [**Anedda *et al.*, 2002, Sakurai, 2000, Nishikawa *et al.*, 1994,**] suggest a composite nature of the B-type activity rationalizing the observed behavior as the occurrence of at least two different optical activity in the same spectral range associated to different types of point defects. We think that the results here reported strongly support the first scenario since the continuous dependence on excitation energy of all the spectroscopic features are in contrast with the expected step behavior of the second scenario. In particular, in the latter case the expected behavior for the time kinetics should be a bi-exponential decay on the contrary of the observed continuously dispersed kinetics. In this respect, the presence of small and not dramatic dependence of the time decay (see inset in figure 4.6) corroborate more the hypothesis of a unique defect with small differences, instead of different defects with different decay rates. Further proofs will come out from the measurements varying the temperature.

### *4.1.2. Temperature effects on the absorption band profile: the defect-matrix coupling*

Figure 4.7 shows the $B_{2Ge}$ band as measured in our sample on varying the temperature in the interval 300 ÷ 30 K. The inspection of the raw data evidences that, on lowering the temperature, the OA band undergoes a blue-shift and a narrowing. At variance, no dramatic change in the amplitude is induced in this temperature range.

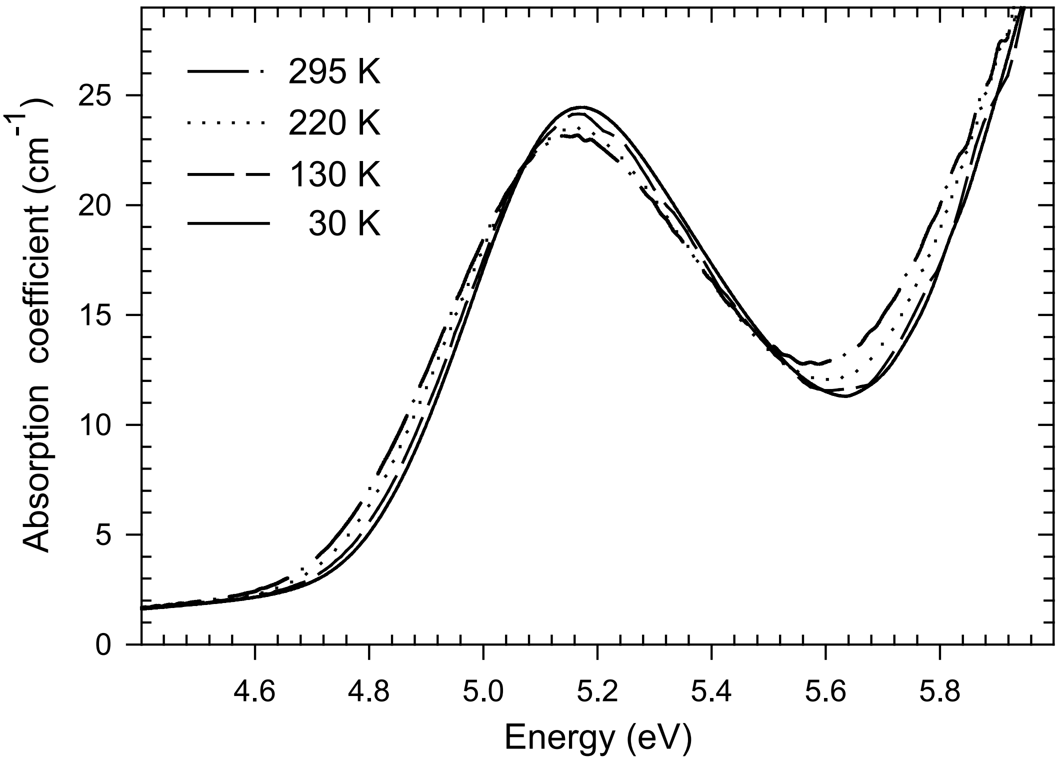

Figure 4.7. Optical absorption $B_{2Ge}$ band detected at various temperatures in a 1000 ppm Ge-doped sol-gel sample.

The analysis of the thermal behavior of $B_{2Ge}$ band is done in terms of the zeroth ($M_0$), first ($M_1$) and second ($M_2$) moment, calculated according to the equations (3.1)-(3.3) and reported in figure 4.8. In the panel (*a*), we note that almost constant values of $M_0$ as a function of

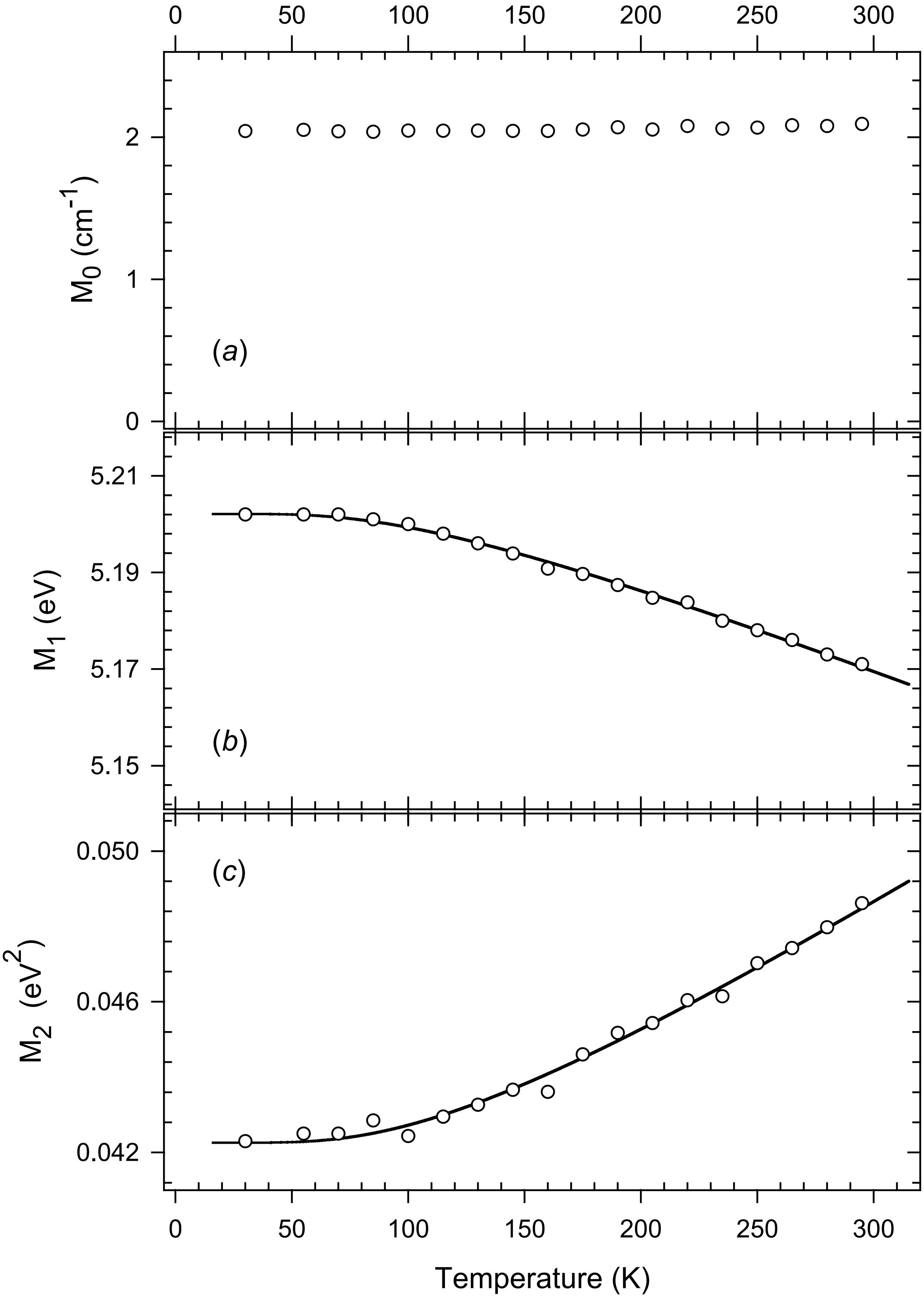

Figure 4.8. Temperature dependence of zeroth (*a*) first (*b*) and second (*c*) spectral moments of $B_{2Ge}$ band. Continuous lines represent the best fit of the data in (*b*) and (*c*) in terms of equations (2.34) and (2.35) (see chap.2), respectively.

temperature are found, suggesting that no quenching effects occur on this band on varying the temperature.

Table 4.1. Values of the parameters obtained by fitting of equations (2.34) and (2.35) to the thermal behavior of second and first moment of $B_{2Ge}$ band (figure 4.8(b) and (c)), respectively.

| $N_l \cdot S_l$ | $N_l \cdot (1-R_l)$ | $\langle E_l \rangle$ (meV) | $M_2^0$ ($eV^2$) | $M_1^0$ (eV) |
|---|---|---|---|---|
| 10 ± 2 | 4.5 ± 0.2 | 26 ± 2 | 0.036 ± 0.005 | 5.23 ± 0.01 |

The thermal behavior of $M_1$ and $M_2$ emphasizes the changes of $B_{2Ge}$ profile shown in figure 4.7: on lowering the temperature, $M_1$ increases from ~5.17 to ~5.20 eV and $M_2$ decreases from ~0.049 to ~0.042 $eV^2$. As discussed in paragraph 2.3, the analysis of these data in terms of equations (2.34) and (2.35) gives a quantitative measure of the interaction between $=Ge^{\bullet\bullet}$ related electronic states involved in the absorption transition and the local coupled vibrational modes of the defect-matrix complex.

Continuous lines in figures 4.8 (*b*) and 4.8 (*c*) represent the best fit of equations (2.34) and (2.35), respectively, to the experimental data, the relative parameters being reported in table 4.1. From these data, we can infer that the $=Ge^{\bullet\bullet}$ in interaction with its environment has access to low-frequency dynamics ($\langle E_l \rangle = 26$ meV). It is worth noting that, at room temperature, the broadening of $B_{2Ge}$ absorption due to the electron-phonon coupling is about 0.5 times the $\sqrt{M_2^0}$ term, associated with the spectral contributions of the high frequency modes and the inhomogeneous width. Moreover, as $N_l \geq 1$, the Huang-Rys factor $S_l$ for this coupling is less than 10. Finally, the blue shift observed on lowering the temperature agrees with values of $R_l<1$, suggesting that the vibrational frequency in the excited state is higher than that of the ground state.

### *4.1.3. Temperature dependence of the emission bands: the intersystem crossing process*

In figure 4.9 we report the emission spectra under excitation at 5.00 eV varying the temperature from 329 K down to 22 K. On cooling the system, an impressive decreasing of

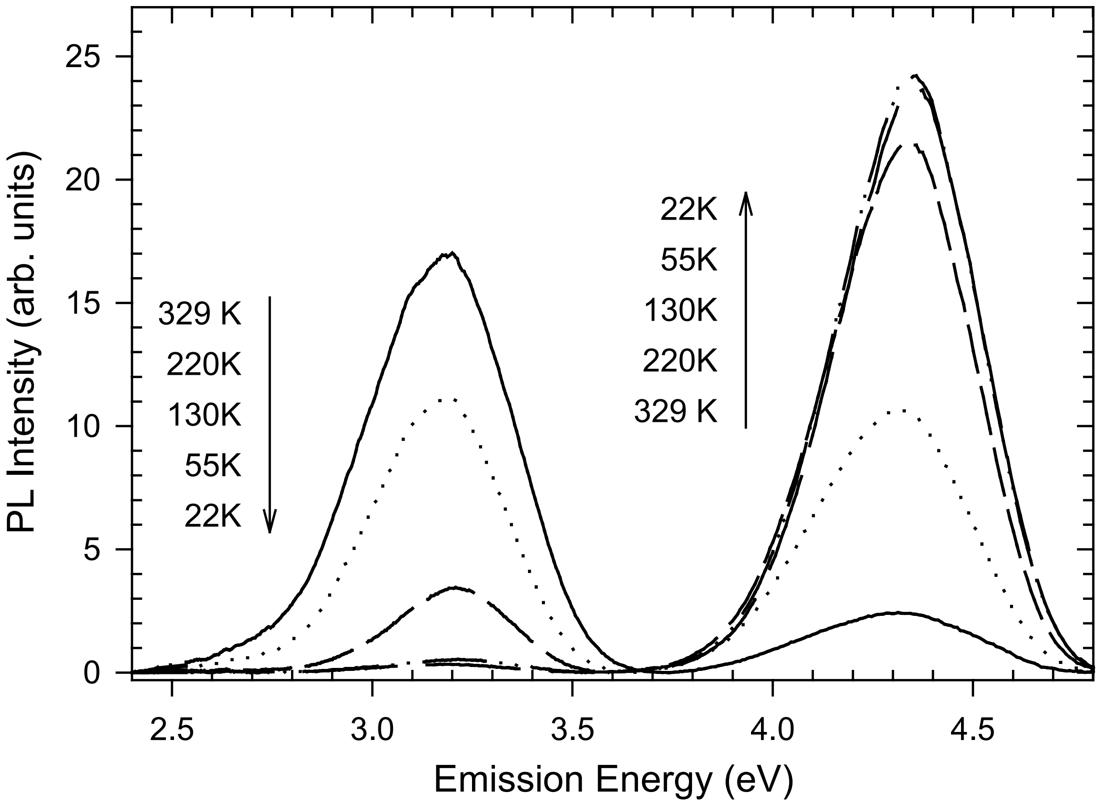

Figure 4.9. Emission spectra for the Ge related B-type activity as a function of temperature under excitation energy at 5.00 eV. Arrows indicate the evolution of relative bands decreasing the temperature from 329 to 22 K.

the $\beta_{Ge}$ intensity with an opposite behavior of the $\alpha_{Ge}$ band is found. Furthermore, we note that these thermal kinetics are frozen below 50 K where a small but detectable $\beta_{Ge}$ band still remains. This results speaks for an active ISC process also at low temperature. To point out the effects of the temperature decreasing on the excitation energy dependence of the ISC process and of the optical features, we investigated the emission activity by a fine excitation tuning at low temperature. In figure 4.10, the luminescence spectra at 22 K, normalized at the maximum of the $\alpha_{Ge}$ band, are reported as a function of excitation energy. As observed at room temperature, we find a significant dependence of the spectral profiles, in particular of the $\alpha_{Ge}$ band. The analysis in terms of spectral moments reveals that, on increasing the excitation energy, the first moment of the $\alpha_{Ge}$ band performs a non monotonic behavior between 4.24 and 4.34 eV (data not reported), whereas the $\beta_{Ge}$ band $M_1$ assumes the value of

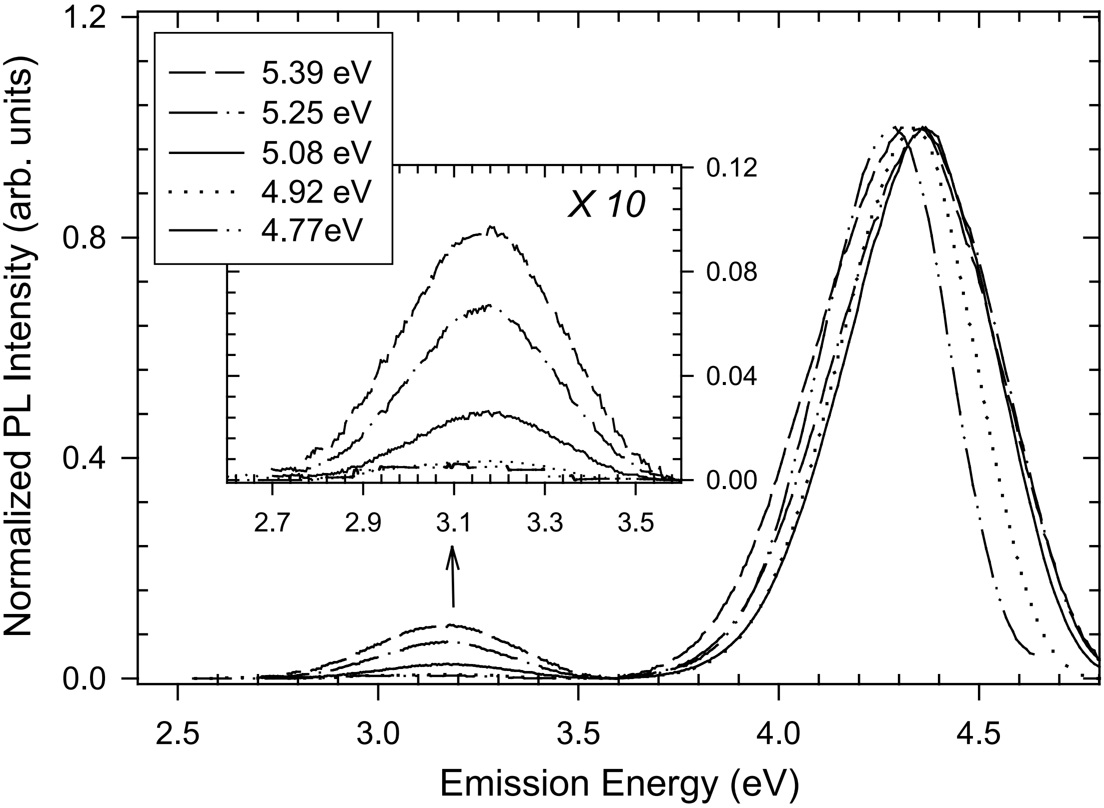

Figure 4.10: Photoluminescence spectra at 22 K, under excitation energy from 4.77 to 5.39 eV, for bulk Ge related B-type activity. The PL spectra are normalized to the maximum of the $\alpha_{\mathrm{Ge}}$ band, around 4.3 eV. The inset shows the spectral range 2.6-3.6 eV in a magnified scale.

3.15 ± 0.08 eV regardless the excitation. We also note a great broadening of the $\alpha_{\mathrm{Ge}}$ band. The behavior of the ISC efficiency will be discussed after the dependence on temperature.

The thermal behavior of the two emissions (see discussion in paragraph 2.4) is related to the competition between the two decay rates from the $\boldsymbol{S_1}$ state: the radiative one $k_S$, temperature independent, and the thermally activated non-radiative $k_{ISC}$ towards $\boldsymbol{T_1}$. In agreement with the absence of any non radiative channels from $\boldsymbol{S_1}$ and $\boldsymbol{T_1}$ toward $\boldsymbol{S_0}$, we observed an almost constant value of the total area of the two emission band ($M_{0S}$+$M_{0T}$), within an uncertainty of 10 %. It is worth to note that this result corroborates one more time the assignment of the overall B-type activity to a unique structural defect.

The thermal behavior of the PL emissions in figure 4.9 is qualitatively accountable by the expected Arrhenius behavior of the ISC rate (see equations (2.40) and (2.47)). For a quantitative analysis of the ISC process, we need to have an estimation of $k_S$. In the next section we will estimate a value of $(1.28 \pm 0.03)\times10^8$ $sec^{-1}$ for $k_S$. Using this value, we determine the $k_{ISC}$ values accordingly to equation (2.45) and to the experimental values of $\zeta$, measured under c.w. excitation at three different energies, 5.00, 4.84 and 5.21 eV. The results are reported in figure 4.11 and clearly evidence that the expected Arrhenius behavior of $k_{ISC}$ is not obeyed in the whole temperature range. We also note that, at the three excitations, $k_{ISC}$ decreases on lowering the temperature down to 50 K and tends to a constant value at lower temperatures. Moreover, both at $T>250$ K (see also the inset) and at $T<50$ K the slopes of the curves are almost constants. Then, in these temperature ranges we can compare the $k_{ISC}$ behavior with the Arrhenius one; the corresponding parameters being reported in table 4.2. We note that an excitation dependence over the whole temperature range is observed: $k_{ISC}$ increases on increasing excitation energy, this effect being more pronounced on lowering the temperature. To evidence the influence of the excitation energy on ISC process, we report, in figure 4.12, $k_{ISC}$ values under different excitation energies from 4.77 to 5.39 eV at two temperatures, where the ISC effectiveness changes by two orders of magnitude.

The above reported results point out the interplay between the enthalpy and entropy factor in governing the overall behavior of phonon assisted ISC. On the one hand, both $\Delta H$ and $k_E$ exhibit a temperature dependence, decreasing by three-four orders of magnitude in the investigated range 330 down to 4.5 K. On the other hand, the $k_{ISC}$ dependence on the excitation energy involves only the entropy factor $k_E$. We underline that these features support the hypothesis that ISC occurrence is strictly related to the amorphous nature of $SiO_2$ matrix [**Martini *et al.*, 1998, Leone *et al.*, 1999a**]. Indeed, this process arises from the interaction between the twofold coordinated Ge and its environment: the complex configurational landscape of the a-$SiO_2$ matrix reflects on a significant role played by the entropy factor and on the inhomogeneous distribution both of $\Delta H$ and of $k_E$.

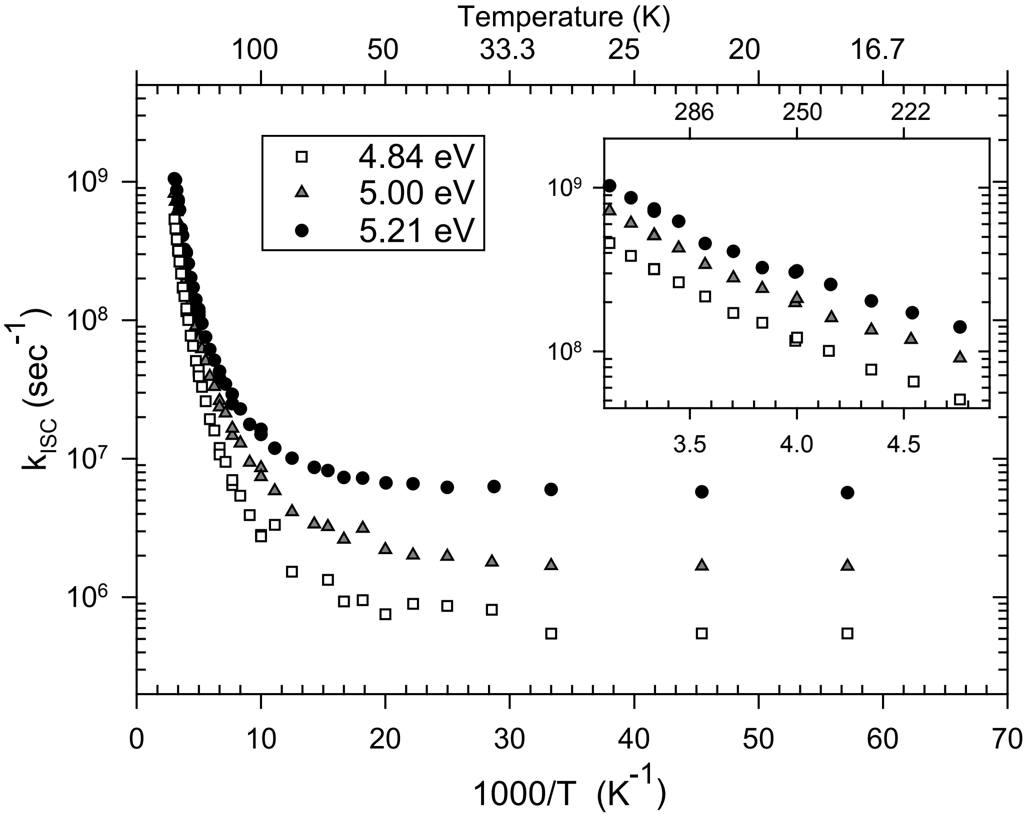

Figure 4.11. Thermal behavior of ISC rate measured according to equation (2.45) under c.w. excitation at 4.84, 5.00 and 5.21 eV. The inset shows the ISC rate in the high temperature range (T > 200 K).

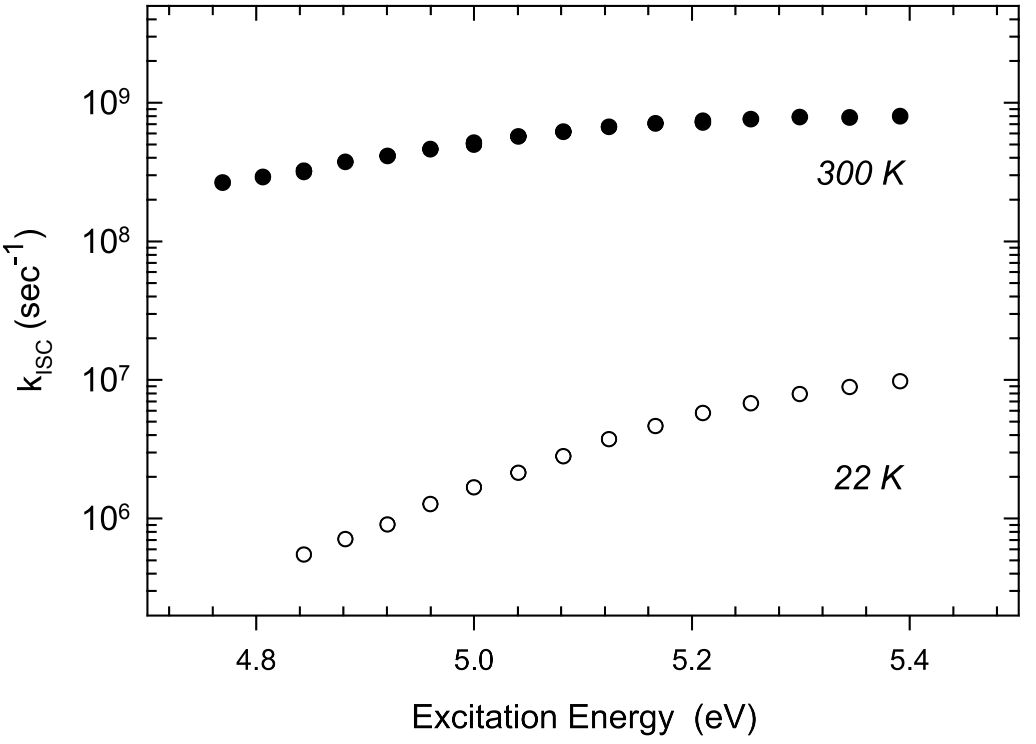

Figure 4.12. Efficiency of ISC process as a function of the excitation energy, measured according to equation (2.45), at 300 K (full marks) and 22 K (open marks).

Table 4.2. Values of decay rates from $\boldsymbol{S_1}$ and of thermodynamic parameters of ISC process obtained at three different excitation energies.

|  | $k_BT > 20$ meV |  |  |  | $k_BT < 2$ meV |  |  |  |
|---|---|---|---|---|---|---|---|---|
| $E_{ex}$ (eV) | $k_s$ ($10^6$ s$^{-1}$) | $k_{ISC}$[a] ($10^6$ s$^{-1}$) | $k_E$ ($10^6$ s$^{-1}$) | $\Delta H$ (meV) | $k_s$ ($10^6$ s$^{-1}$) | $k_{ISC}$[b] ($10^6$ s$^{-1}$) | $k_E$ ($10^6$ s$^{-1}$) | $\Delta H$ (meV) |
| 4.84 | 128±3 | 318±1 | $(4\pm1)\times10^4$ | 125±8 | 128±3 | 0.5±0.1 | 0.7±0.5 | <0.3 |
| 5.00 | 128±3 | 509±3 | $(7\pm2)\times10^4$ | 125±8 | 128±3 | 1.6±0.3 | 1.7±0.1 | <0.3 |
| 5.21 | 128±3 | 727±10 | $(9\pm3)\times10^4$ | 125±8 | 128±3 | 5.6±0.9 | 5.8±0.1 | <0.3 |

[a] $k_{ISC}$ values as obtained at 300 K
[b] $k_{ISC}$ values as obtained at 22 K.

We could also rationalize these features via an alternative explanation that takes into account the presence of different local environment (conformational substates) in the neighborhood of a given single point defect, each substate being related to a specific value of $k_E$ and $\Delta H$. As the transitions among the substates are expected to occur via a phonon-assisted process, the number of substates that a single defect explores increases on increasing the temperature, so determining a temperature dependence of both entropy and enthalpy factors. In particular, as $k_E$ is a measure of the rate at which the defect in the excited state $\boldsymbol{S_1}$ tries to convert towards $\boldsymbol{T_1}$, one can assume that, at a given temperature, it is related to the number of populated substates. In this respect an increasing of $k_E$ with temperature is expected regardless the previous assumption of different values of $k_E$ in different substates.

A particular remark must be deserved to the results in the low temperature range. As discussed in chapter 2, the presence of a plateau can be ascribed to temperature independent mechanisms but we are not able to distinguish them from ISC rates characterized by very low activation barriers. So, in the absence of a quantitative data on the ISC rates associated with these mechanisms, we preferred to adopt an unique analysis comparing the ISC rates in the low temperature range with an Arrhenius law. It is worth to note that the $k_{ISC}$ values in figure 4.11 subtracted of the plateau value, still have a clear non Arrhenius behavior, showing that the dispersion of $k_E$ and $\Delta H$ is not an artifact, as proved by the excitation energy dependence and the experimental evidences at room temperature. In this respect the wide “elbow” range is a consequence of this dispersion.

### *4.1.4. Temperature effects on lifetimes*

To investigate the relaxation channels from the $\boldsymbol{S_1}$ state and to single out their weight, we measured the $\alpha_{Ge}$ decay by detecting the transient 4.2 eV emission under pulsed excitation at 5.0 eV on varying the temperature. Figure 4.13 reports the time decay of the PL at 4.2 eV under excitation energy of 5.0 eV at various temperatures, from 10 to 295 K. The PL data cover a dynamic range of about three orders of magnitude, enabling a fair characterization of the decay profile. As evidenced by the semi-logarithmic scale, the decay kinetics are a single exponential for $T < 145$ K and become non exponential on increasing the temperature. As already observed about data in figure 4.6, the non single exponential decay of the PL emission observed at room temperature suggests that a distribution of relaxation rates affects the decay process. The inset in figure 4.13 reports the time decay of the PL at 4.2 eV at 10 K, under excitation energy 4.84 eV, 5.00 eV and 5.21 eV. The comparison with the results obtained at $T = 295$ K reveals that the non exponential decay rate is more and more pronounced on increasing the excitation energy. At variance, at low temperature no dependence on the excitation energy is found.

The quantitative analysis of the time decay of the PL at 4.2 eV was carried out by fitting the experimental decay profile for $t > 2.3$ nsec (see chapter 3) with a *stretched exponential* law [**Kohlrausch, 1847**]:

$$I \propto exp[-(t/\tau)^{\gamma}], \tag{4.1}$$

where $I$ is the PL amplitude, $\tau$ is a characteristic decay time and $\gamma$ is the stretching parameter, which describes the deviation from a single exponential law. The full lines in figure 4.13 plot the best fit curves of the PL decay at 10 K and at 295 K with the stretched exponential of equation (4.1).

The results of the fitting procedure applied to the PL decay data at various temperatures

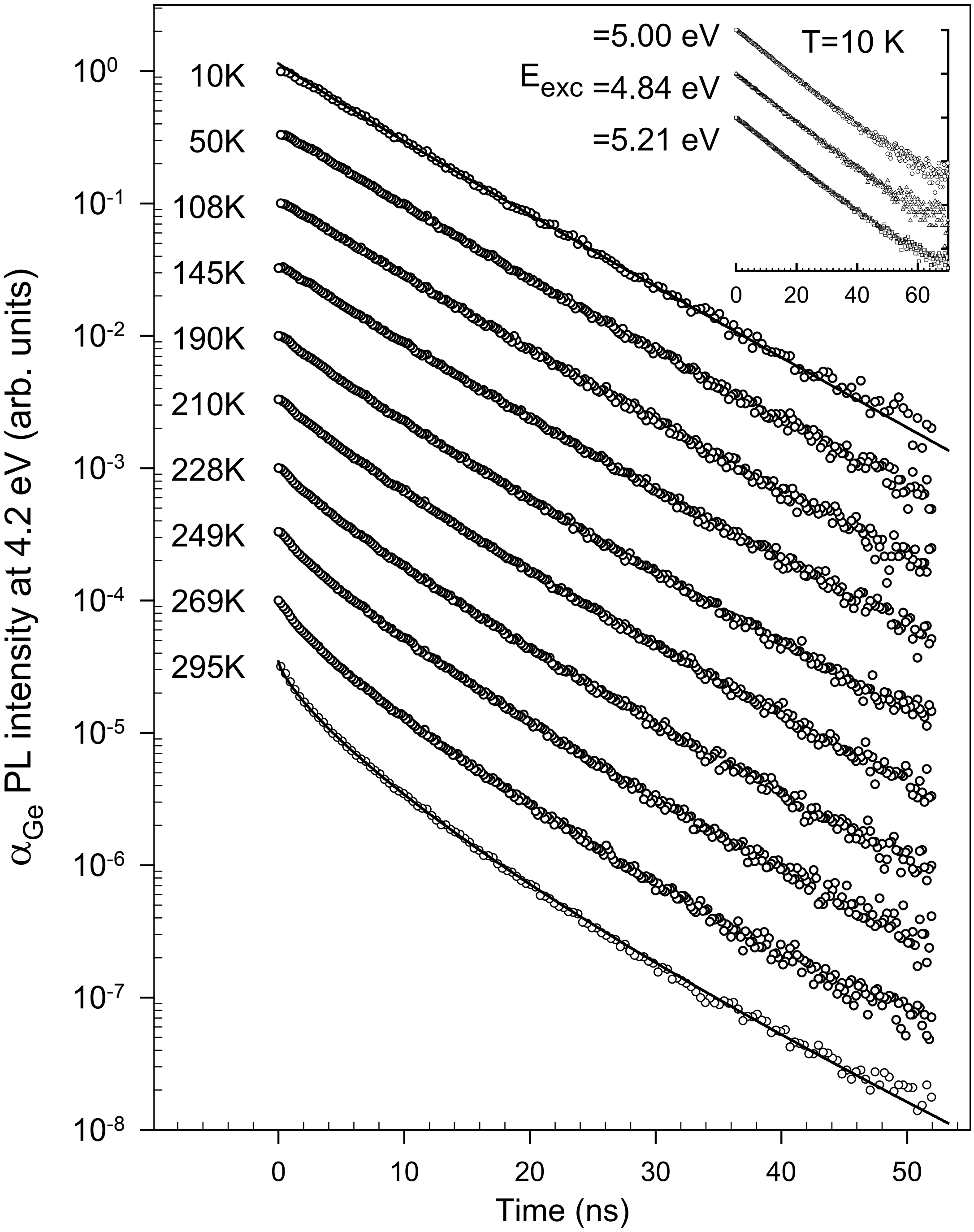

Figure 4.13. Decay kinetics of emission at 4.2 eV detected under pulsed excitation at 5.0 eV as a function of temperature from 10 up to 293 K. In the inset is reported the comparison among the time decays at T = 10 K for three excitation energies: 5.00, 4.84 and 5.21 eV. For viewing purposes, the decay curves are arbitrary scaled. The solid line are a representative selection of fitting outicomes in terms of a stretched exponential decay (equation (4.1)).

are reported in figure 4.14 as a function of temperature, under excitation energy at 5.0 eV. As shown in figure 4.14 (a), for $T < 130$ K a constant value of 7.8 ± 0.2 ns for the PL characteristic decay time $\tau$ is obtained; at higher temperature the decay time is gradually shortened to the value $\tau = 1.9 \pm 0.2$ ns. Figure 4.14 (b) reports the temperature dependence of the stretching parameter $\gamma$. The dependence is similar to that of the decay time: below 130 K, $\gamma$ has the constant value 1.00 ± 0.02 (tending to a single exponential law) and at higher temperature it decreases down to the value 0.64 ± 0.02.

In figure 4.15, we report the results of the fitting procedure applied to the data of the PL decay measurements as a function of the excitation energy at $T = 10$ K and at $T = 295$ K. As shown in figure 4.15 (a), at $T = 10$ K the lifetime does not depend on the excitation energy and we find a decay time $\tau = 7.8 \pm 0.2$ nsec. The stretching parameter in this temperature range is $\gamma = 1.00 \pm 0.02$ and does not change with the excitation energy in accordance, with the observed single exponential decay. As shown in the bottom side of figure 4.15 (a), a different dependence is found at $T = 295$ K. The decay time decreases gradually from 2.6 ± 0.2 nsec at excitation energy 4.6 eV down to 1.6 ± 0.2 nsec at excitation energy 5.5 eV, with a variation of about 38%. As reported in figure 4.15 (b), at the same temperature the stretching parameter changes from 0.70 ± 0.02 down to 0.61 ± 0.02 increasing the excitation energy from 4.6 to 5.5 eV.

The reported results evidence that the time decay of the PL at 4.2 eV, above 130 K, is characterized by a non exponential law that depends on the temperature and on the excitation energy. The analysis with the stretched exponential of equation (4.1) enables us to characterize the time decay more quantitatively. In particular, we have determined a characteristic decay time $\tau$ and a stretching parameter $\gamma$. Here we assume that $\tau^{-1}$ is an estimate of the mean decay rate of the relaxation process even in presence of the non single exponential decay.

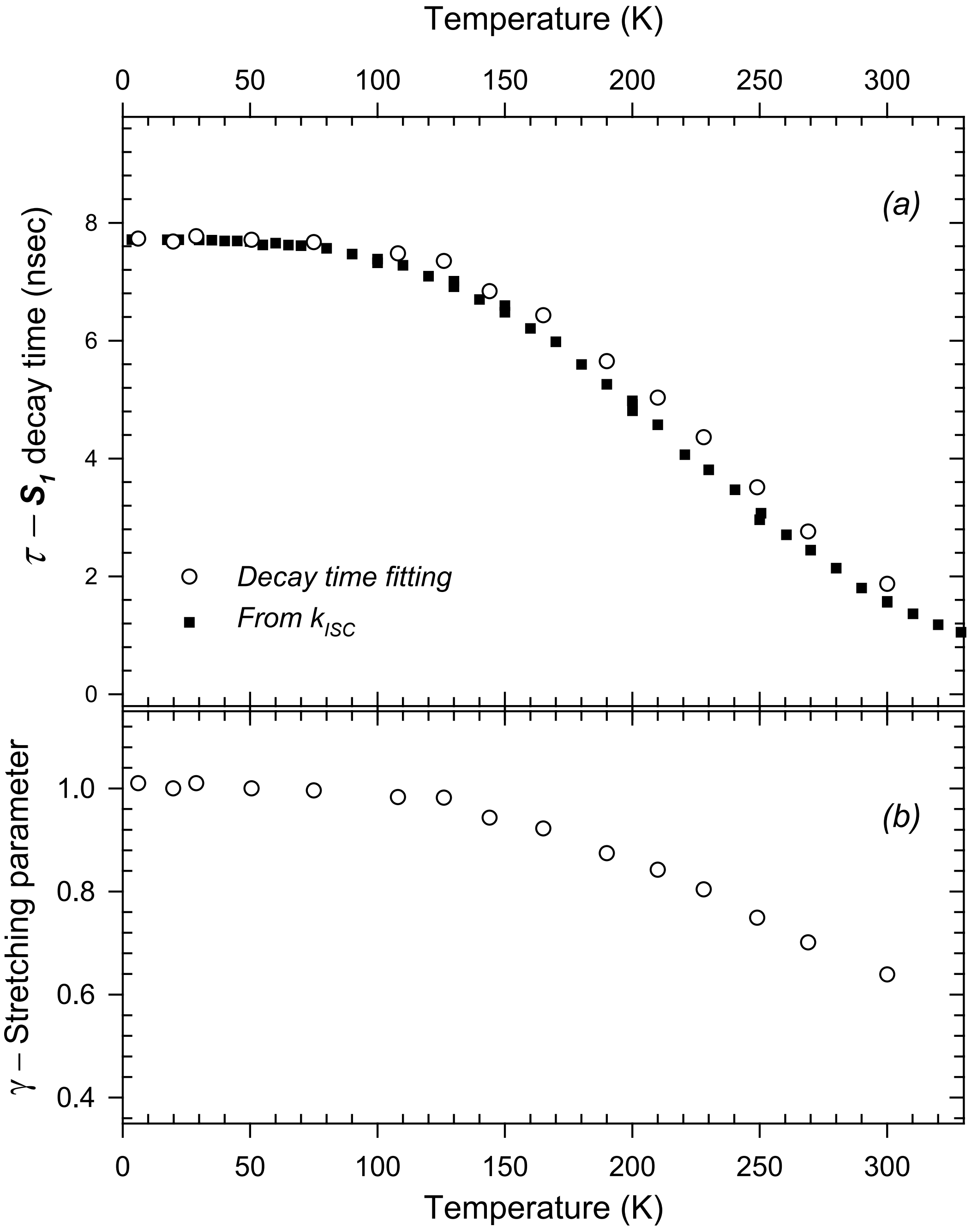

Figure 4.14. (*a*) $\boldsymbol{S_1}$ decay time $\tau$ and (*b*) stretching parameter, $\gamma$, varying temperature, as obtained by fitting data in figure 4.13 in terms of eq. 4.1 (open circles). For comparison purpose, the expected values of $\tau$ from the values of $k_{ISC}$ (full squares) are reported in (*a*) (see text for details).

The temperature dependence of the lifetime reported in figure 4.14 (a) can be rationalized on the basis of the B-type energy level scheme. Indeed, the lifetime of $\boldsymbol{S_1}$ is governed by the radiative decay rate, $k_S$, and by the ISC one, $k_{ISC}$, according to the law:

$$\tau = (k_S + k_{ISC})^{-1}, \tag{4.2}$$

so that, the dependence of $\tau$ on the temperature is only due to $k_{ISC}$, i.e to the thermal behavior of the efficiency of ISC process. Accordingly to previous discussions and to **Leone *et al.*, 2001,** no other relaxation rate is required, as the sum of the PL amplitudes integrated over the $\alpha_{Ge}$ and $\beta_{Ge}$ bands keeps a constant value on varying the temperature. At low temperature, the radiative decay is predominating with respect to $k_{ISC}$, as can be seen considering the values of $\zeta$ at low temperature. The analysis of data in figures 4.9 and 4.10 reveals, indeed, that, under excitation at 5.00 eV, $k_{ISC}$ is 0.01 times $k_S$. So, the constant value $\tau = 7.8 \pm 0.2$ ns for $T < 130$ K enables us to estimate the radiative decay rate $k_S$ as $(1.28 \pm 0.03) \times 10^8$ sec$^{-1}$. On the other hand, the ISC process is intensified on increasing the temperature and, when $k_{ISC}$ becomes competitive with $k_S$, the decay time is reduced.

As shown in figure 4.15 (a), the PL lifetime values at low temperature show no variation by tuning finely the excitation at T = 10 K. This results suggest that the inhomogeneity, arising from the glassy matrix, poorly affects the radiative relaxation rate $k_S$.

As reported in figure 4.6 and 4.13, for T = 295 K the PL decay is not a single exponential, and the decay time depends on the excitation energy, as shown in figure 4.15 (a). These features suggest that at high temperature the decay process from the excited state is affected by the inhomogeneous distribution of centers. This result is in agreement with the hypothesis that the overall behavior of the total $\boldsymbol{S_1}$ lifetime is due to the competition between $k_S$ and $k_{ISC}$: the ISC efficiency increases accordingly with temperature and, above 130 K, becomes competitive with $k_S$. So, above this temperature, the inhomogeneous distribution of the ISC rates is able to affect the total $\boldsymbol{S_1}$ lifetime both for the time behavior (non single exponential decay) and for the excitation dependence. In this respect, this picture is supported by the behavior observed for the parameter $\gamma$ as found by the fitting procedure, recalling that this parameter represents the deviation from the single exponential decay.

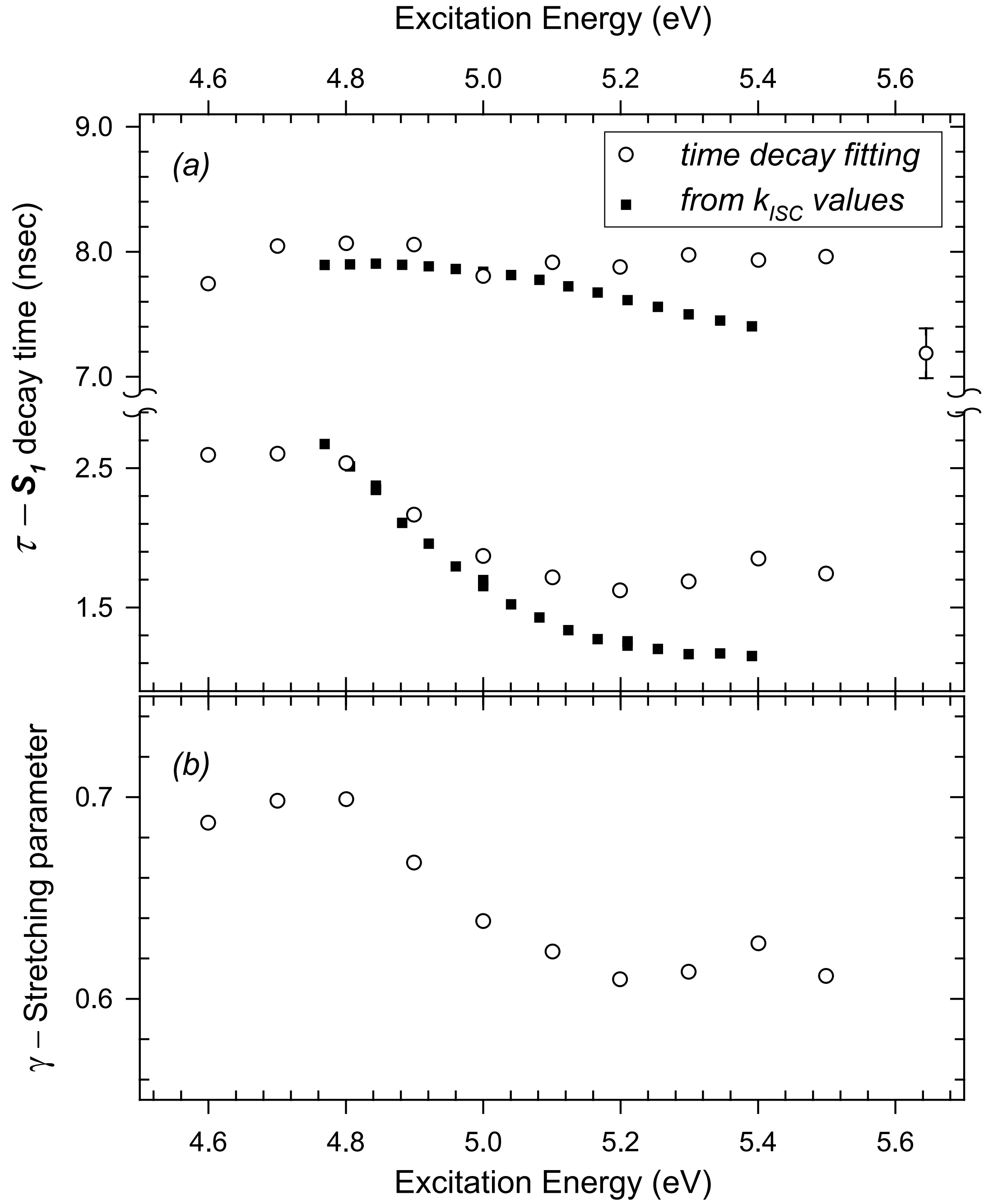

Figure 4.15. Photoluminescence decay parameters (open circles), determined by fitting the data using eq. (4.1), are reported as a function of excitation energy: (a) decay time at 10 K (top) and 295 K (bottom); (b) stretching parameter $\gamma$ at T = 295 K. For comparison purpose, the expected values of $\tau$ from the values of $k_{ISC}$ (full squares) are reported in (*a*) (see text for details).

In order to verify the goodness of this rationalization, we compare in figure 4.14 (*a*) the values of $\tau$, as found by the fitting procedure, with the expected values calculated with the equation (4.2) and the values of $k_{ISC}$ of figure 4.11. We obtain an excellent agreement that proves definitely that the thermal behavior of the $\boldsymbol{S_1}$ relaxation dynamics are due only to the competition between $k_S$ and $k_{ISC}$. With an analog analysis we compared the excitation dependence of the values of $\tau$ obtained by fitting and by data in figure 4.12. This comparison is reported in figure 4.15 (a), where we find a good accordance, within the experimental uncertainties, between the two set of data. The excitation dependence of the stretching parameter $\gamma$ suggests that, by changing the excitation energy, a different population of centers are excited, each of them with a different ratio between the ISC and the radiative rate.

## 4.2 The theoretical model

In the previous paragraph we reported several data that shows unmistakably the presence of a spectral heterogeneity affecting the experimental data. In particular, the occurrence of mutual dependences speak for microscopic links and point out the inadequacy of the simplified approach discussed in chapter 1. Even if some authors [**Leone *et al.*, 1997** and **1999a, Bagratashvili *et al.*, 1995, Skuja, 1998**] suggested a fundamental role of the matrix's amorphous nature on the observed spectral heterogeneity, and in particular on the correlation among different spectroscopic properties, no concrete effort has been done, at our knowledge, in order to explain in a unified picture all these effects. The aim of the next section is to present and discuss a theoretical model able to frame the anomalous results previously detected.

In this respect, the first part will be dedicated to the development of the model in the light of the main incongruities evidenced between the expected behavior and the experimental results on the Ge related bulk B-type activity. In the second section, we will apply the model to the experimental data and some remarks on the reliability of the stated assumptions will be discussed.

### *4.2.1 Introduction to the model*

In this section we are going to outline the optical activity in a glassy matrix arising from embedded defects characterized by a B-type like activity, whose energy levels scheme is described in figure 1.4.

As discussed in chapter 2, for a single defect, or for an homogeneous collection of defect, the expected OA band and the singlet and triplet emission are described by equations (2.30) and (2.40). As observed in the previous paragraph, the main effect of the temperature is due to the thermally activated ISC rate $k_{ISC}$, in agreement with equation (2.16). The other effects, the band narrowing and energy shift linked to the phonon coupling, are much less relevant and will not be considered in first approximation.

Regarding the excitation energy dependence, neither $k_{ISC}$ nor the first moments of singlet and triplet emissions (see equations (2.46)) are expected to be affected. These results have to be compared with the relative experimental data. In particular, the dependences of $k_{ISC}$ on temperature and on the excitation energy are shown in figures 4.16 and 4.17 (from figures 4.11 and 4.12), respectively, and the behaviors at 300 and 22 K of $M_{1S}$ and $M_{1T}$ are reported in figures 4.18 and 4.19 as a function of the excitation energy, respectively.

As widely underlined in the previous paragraph, the experimental data are not consistent with expected behavior, assuming that the investigated optical activity rises from a homogeneous collection of point defects. The weak spot of this treatment is to have studied defects apart from the surrounding environment. The following treatment is based on the idea that each single center interacts with a particular local rearrangement of matrix, which is different point by point inside the sample. Each center will be brought in a topological configuration (lengths and angles of bonds) different each from others. As the electronic eigenfunctions and energy eigenvalues are strictly dependent on special arrangement of defect, they will get different values defect by defect. This dependence of all the electronic features on the configurational coordinates of the defect-matrix complex is expected to induce mutual cross-correlations between different properties of centers [**Skuja *et al.*, 1998** and **2000**]. For sake of simplicity one may think of a simplified model where the system geometry is described by a single generalized coordinate $X$. In this framework, some optical properties can be function of $X$ (they map in $X$), and the presence of this mapping induces a cross-correlation among the different optical properties. If we indeed consider, for example, $E_A$ and $E_S$, since they are function of the same variable $X$, they will be also each a function of the other (i.d. $E_S=f(E_A)$ or $E_A=f(E_S)$). Similar considerations can be applied to all the properties of the point defect which are expected to depend on its geometry. In particular, to rationalize the cross-correlations evidenced in figures 4.16 – 4.19, the optical properties that will be considered in this model are the absorption energy ($E_A$), the singlet emission energy ($E_S$), the triplet emission energy ($E_T$) and, to rationalize the ISC rate, the enthalpy ($\Delta H$) and entropy ($\Delta S$) of the ISC process. Even if, from a theoretical point of view, these properties are all equivalent, from the experimental one the quantity $E_A$ is more suitable to be considered as the independent variable because it is immediately linked by equation (2.30) to the excitation energy, which is, together with the temperature, directly settable. In other words, we will treat, in the following, $E_S$ , $E_T$, $\Delta H$ and $\Delta S$ as function of $E_A$. In this respect, it is worth to note that this assumption implies that equations (2.16) and (2.40) have to be considered as depending on $E_A$.

As wrote before, due to the matrix disorder, the configuration coordinate $X$ is different from defect to defect. It means that also $E_A$ it is not the same in different centers. To describe such situation, we have to introduce the probability $P(E_A)dE_A$ of finding a defect with a value of $E_A$ between $E_A$ and $E_A + dE_A$. The presence of this distribution, due to the mapping, brings to a dispersion also for the other optical properties, and then to the observed spectral inhomogeneity.

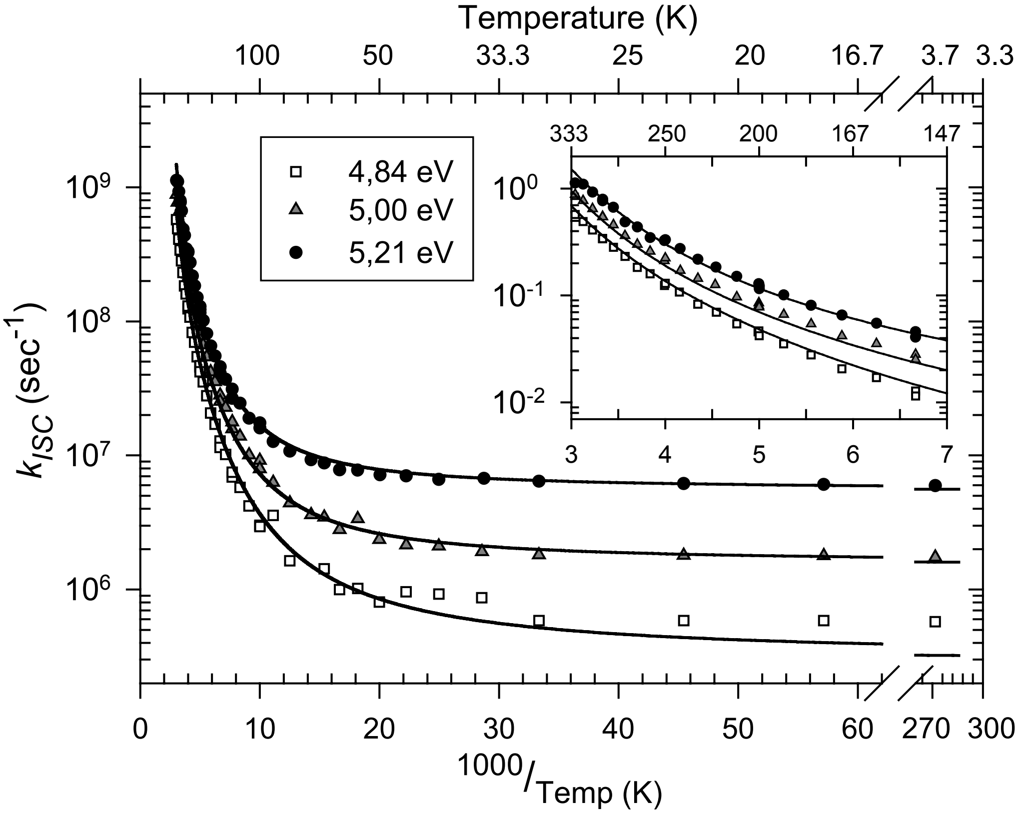

Figure 4.16. ISC rate as a function of temperature at three different excitation energies. In the inset we report the high temperature zone. The continuous lines are the results of fitting procedure (see text for details).

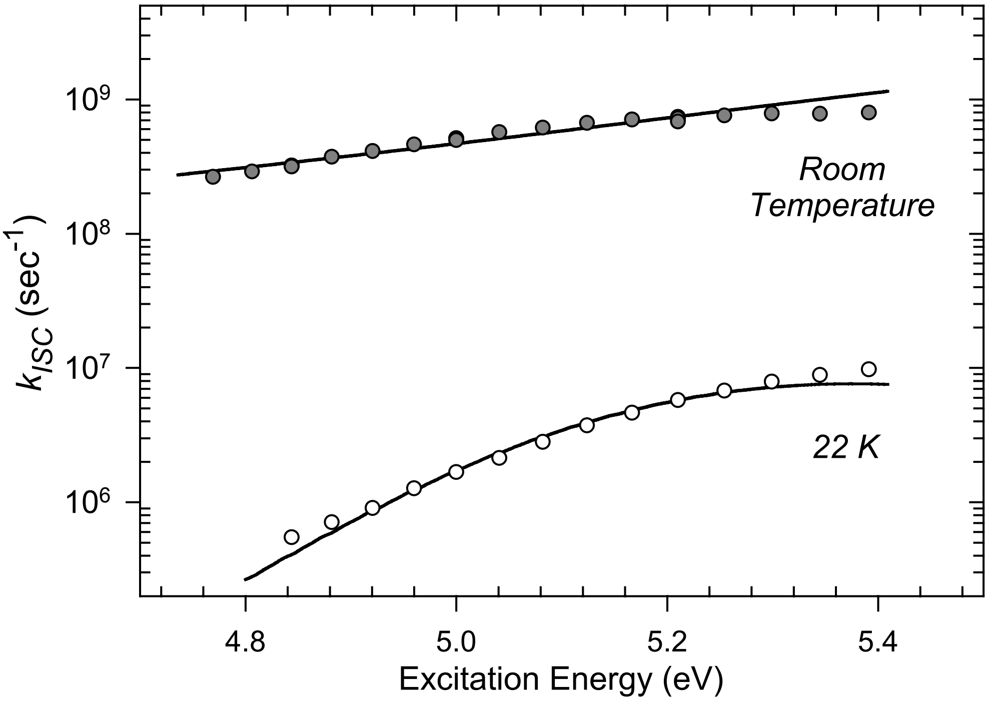

Figure 4.17. ISC rate as a function of excitation energy at room temperature (full marks) and at 22 K (open marks). The continuous lines are the results of fitting procedure (see text for details).

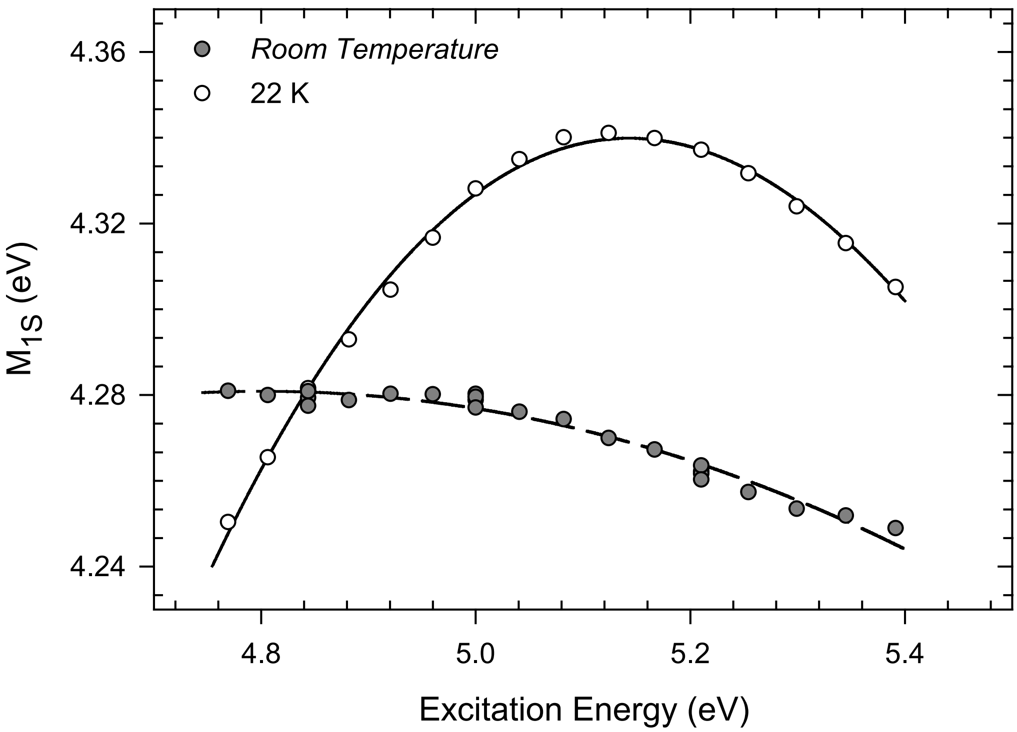

Figure 4.18. First moment of the singlet band as a function of excitation energy at room temperature (full marks) and at 22 K (open marks). The continuous lines are the results of fitting procedure (see text for details).

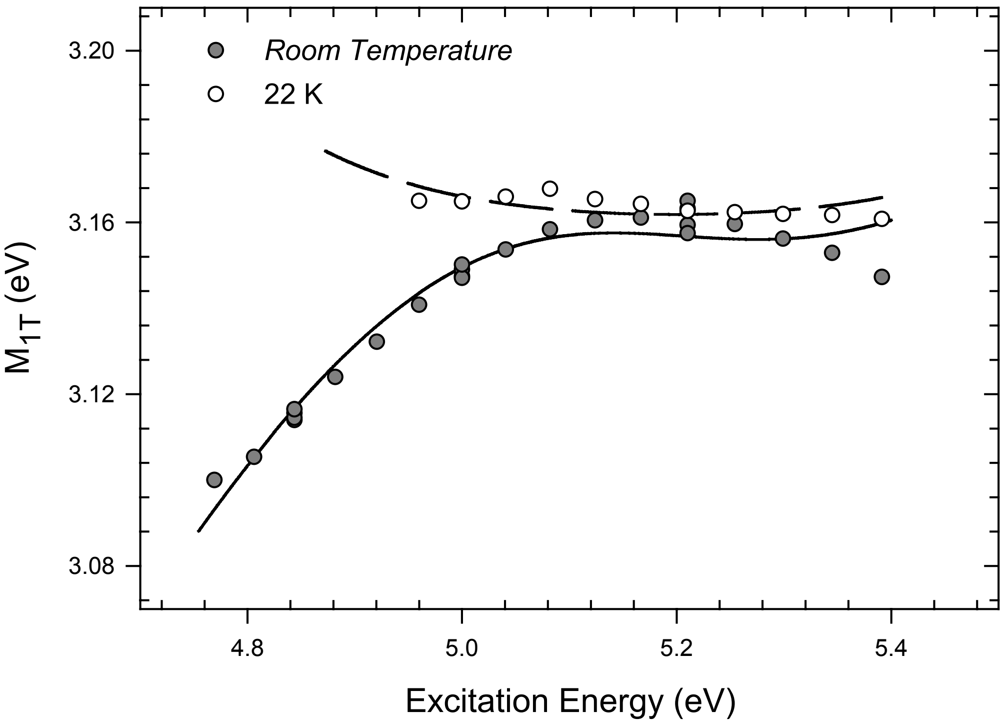

Figure 4.19. First moment of the triplet band as a function of excitation energy at room temperature (full marks) and at 22 K (open marks). The continuous lines are the results of fitting procedure (see text for details).

From a general point of view, this distribution could be depending on temperature, but we will assume the easiest frame where a temperature independent distribution is supposed. We will reconsider this assumption during the discussion.

The observed bands (labeled with the subscript *IN*, standing for inhomogeneous) are now given by single center bands (see equations (2.30) and (2.40)) weighted with a distribution:

$$\alpha_{IN}(E_{Ex})=\int_0^\infty \alpha(E_{Ex})P(E_A)dE_A = E_{Ex}\cdot\int_0^\infty f(E_{Ex}-E_A)\cdot P(E_A)dE_A \tag{4.3}$$

$$S_{IN}(E_{Em},E_{Ex},T)=\int_0^\infty S(E_{Em},E_{Ex},T,E_A)\cdot P(E_A)dE_A \tag{4.4}$$

$$T_{IN}(E_{Em},E_{Ex},T)=\int_0^\infty T(E_{Em},E_{Ex},T,E_A)\cdot P(E_A)dE_A\,. \tag{4.5}$$

In the above equations, we wrote manifestly the $T$ and the $E_A$ dependence and we omitted $\alpha_0$ (see equation (2.30)) because is only a scaling factor common to all equations; for the same reason we will omit the $I_0\cdot\alpha_0$ factor in the PL band equations (see equations (2.40)). In the following we will refer to the integral of equation (4.3) as the “spectral profile” of the OA band, and it has to be compared with the experimental OA band divided by energy, $E_{Ex}$ (the function $B(E)$ of equations (3.1)-(3.3)).

Regarding the experimental values of ISC rates reported in figures 4.16 and 4.17, they were calculated as the triplet to singlet areas ratio multiplied by the pure radiative $\boldsymbol{S_1}$ decay rate, $k_S$. So, considering that $g(E_{Em}-E_S)$ and $h(E_{Em}-E_T)$ are unity area functions, the expression for the expected $k_{ISC}$ is the following:

$$k_{ISC}=k_S\cdot\frac{\int_0^\infty T_{IN}dE_{Em}}{\int_0^\infty S_{IN}dE_{Em}}=k_S\cdot\frac{\int_0^\infty \frac{k_{ISC}^{E_A}(T)}{k_S+k_{ISC}^{E_A}(T)}f(E_{Ex}-E_A)\cdot P(E_A)dE_A}{\int_0^\infty \frac{k_S}{k_S+k_{ISC}^{E_A}(T)}f(E_{Ex}-E_A)\cdot P(E_A)dE_A} \tag{4.6}$$

where the superscript $E_A$ stresses, now and in the following, the dependence on $E_A$. This new expression deserves some attention: even if it is easy to realize why this expression is able to explain the multi-exponential behavior as a function of temperature, it is less immediate to appreciate the dependence on the excitation energy. Since $f(E_{Ex}-E_A)$ is a bell-like function, it selects the $E_A$ range which really contributes to the integral. In this respect, a changing of $E_{Ex}$ is equivalent to a shift of the effective $E_A$ integration range. The dependence of $k_{ISC}$ on $E_A$ induces, in equation (4.6), a change of the upper integral different from the lower one. In agreement with this argumentation, we rationalize also why we found, under different excitation energies, different dependence of $k_{ISC}$ on the temperature.

About the singlet ($M_{1S}$) and triplet ($M_{1T}$) first moments shown in figures 4.18 and 4.19, the proper expressions to describe them are respectively:

$$M_{1S} = \frac{\int_0^\infty E_{Em}\cdot S_{IN}\, dE_{Em}}{\int_0^\infty S_{IN}\, dE_{Em}} = \frac{\int_0^\infty \frac{k_S}{k_S + k_{ISC}^{E_A}(T)} E_S^{E_A} f(E_{Ex}-E_A)\cdot P(E_A)\, dE_A}{\int_0^\infty S_{IN}\, dE_{Em}} \tag{4.7}$$

$$M_{1T} = \frac{\int_0^\infty E_{Em}\cdot T_{IN}\, dE_{Em}}{\int_0^\infty T_{IN}\, dE_{Em}} = \frac{\int_0^\infty \frac{k_{ISC}^{E_A}(T)}{k_S + k_{ISC}^{E_A}(T)} E_T^{E_A} f(E_{Ex}-E_A)\cdot P(E_A)\, dE_A}{\int_0^\infty T_{IN}\, dE_{Em}}. \tag{4.8}$$

The right side of both expressions was written since the average positions of $g(E_{Em}-E_S)$ and $h(E_{Em}-E_T)$ are $E_S$ and $E_T$, respectively. Identical considerations discussed about equation (4.6) show that equations (4.7) and (4.8) predict a dependence on excitation and on temperature of the first moment of relative band.

Until now, the proposed model is quite general and potentially able to be applied to any inhomogeneous system (provided the reasonability of temperature independent distribution); in the following, we will concern ourselves with our system.

Regarding the functions $f(E_{Ex}-E_A)$, $g(E_{Em}-E_S)$ and $h(E_{Em}-E_T)$, we will assume that they are unitary area gaussian functions, since we observed that B-type activity is characterized by almost symmetric band and Huang-Rhys constants of high frequency modes significantly greater that unity. Regarding the assumptions on the distribution function $P(E_A)$ and on the mapping among optical properties, we will state them in the light of experimental results of figures 4.16-4.19.

The behavior in figure 4.16 has two main features: a broad elbow-shape behavior in the temperature range $T > 50K$, and a constant one for $T < 30K$. The former speaks for a continuous distribution of $k_{ISC}$ (and than of $\Delta H$ and $\Delta S$) and, in agreement with the previous theory, we will describe such condition introducing a $P(E_A)$. We will suppose it to be gaussian for simplicity, in agreement with the idea that defect distortions are due to cumulative effects of large number of different causes, as widely used to describe successfully other complex system like proteins [**Frauenfelder *et al.*, 1988, McMahon *et al.*, 1998**]. With this assumption, the integral in equation (4.3), the OA band spectral profile, is a convolution between two gaussians and its result is a gaussian centered in $E_A^0$ and standard deviation $\sigma = \sqrt{\sigma_A + \sigma_{Ex}}$ ; here, $E_A^0$ is the center of $P(E_A)$, while $\sigma_A$ and $\sigma_{Ex}$ are the standard deviations of $P(E_A)$ and $f(E_{Ex}-E_A)$, respectively. The comparison with the experimental OA band spectral profile allows a direct estimation of $E_A^0$ and $\sigma$. It worth to note that, in this frame, the defects with the related OA band centered at $E_A^0$ have to be thought as those centers characterized by the most common geometrical configuration.

Regarding the expected values for $\sigma_A$ and $\sigma_{Ex}$, experimental results reported in figures 4.16-4.19 strongly suggest that they should be comparable. Indeed, to explain in our framework the observed strong dependence on $E_{Ex}$, $\sigma_A$ can not be negligible, but also $\sigma_{Ex}$ can not be small, in agreement with behavior showed in figures 4.16 and 4.17. These data speak, indeed, for a big overlapping of single center OA bands because the observed $k_{ISC}$ *Vs* $T$ can be explained, in our framework, only if we suppose to excite a lot of different centers subgroup at the same time; otherwise, we should observe only an almost exponential behavior as a function of $T$ (we say that excitation energy is not site-selective).

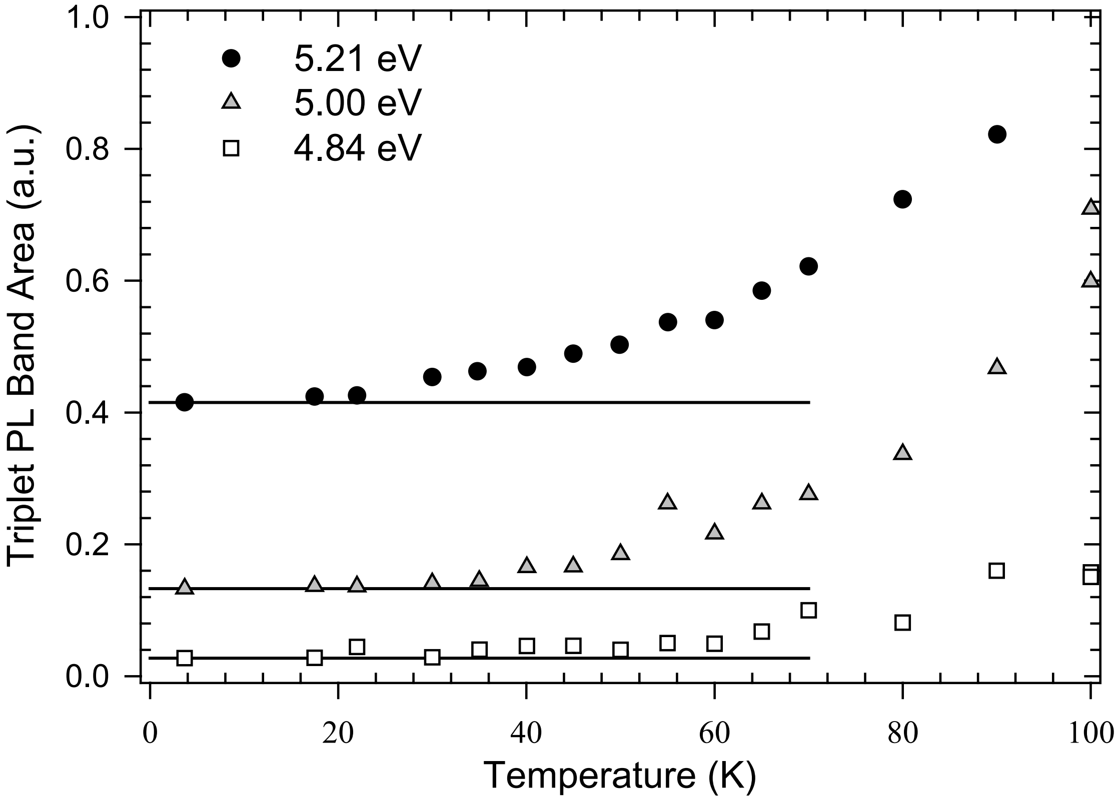

Figure 4.20. Triplet band area as a function of temperature at three different excitation energies. The solid lines show the relative expected values a 0 K.

The constant behavior in the lower temperature range deserves more attention: the observed plateau argues for a small number of centers (~ 1 %)[(1)] able to covert from $\boldsymbol{S_1}$ to $\boldsymbol{T_1}$ which do not show a thermal dependence below 30 K. This feature is shown unmistakable in figure 4.20, where the triplet band area, which is proportional to the $\boldsymbol{T_1}$ population, is reported as a function of temperature at the same three excitation energies of figure 4.16. On lowering the temperature, we observe, indeed, that the triplet state population does converge to a non zero value, which it is nearly reached still at 30K, as evidenced by solid lines in figure 4.20. The presence of non thermally activated ISC mechanisms is not surprising in the light of discussion in paragraph 2.2 and, to include them in the previous theoretical framework, we will assume that they have $\Delta H = 0$. These centers, which will be named $\beta_0$ centers, are then

---

[(1)] Considering the value of $1.28 \cdot 10^8$ sec$^{-1}$ for $k_S$, the typical value of $10^6$ sec$^{-1}$ for $k_{ISC}$ at low temperature (see figs. 4.16 and 4.17) corresponds to a concentration of ~1 % of defect in $\boldsymbol{T_1}$ (see eq. (4.6) and relative discussion).

characterized by the $E_A$ value ($E_A^{\beta_0}$) which verifies $\Delta H\left(E_A^{\beta_0}\right)=0$. Together with the gaussian term, we have to consider a δ-function contribution to the total distribution *P($E_A$)*. In agreement with the previous discussion, it is centered at $E_A^{\beta_0}$ and is proportional to the $R_{\beta_0}$, the ratio between the density of $\beta_0$ centers to the density of non zero enthalpy centers.

The second step is to find a suitable mapping of the other optical properties ($\Delta H$, $\Delta S$, $E_S$, $E_T$) with respect to $E_A$. The leading idea is that the effects of environment on defect's structure are perturbing; for this reason we suppose that, in first approximation, the $E_A$ dependence should be linear or, at the most, quadratic. If the experimental behavior of an optical property as a function of $E_{ex}$ is monotonic, we will describe it with a linear mapping, otherwise with a quadratic one. It is worth to note that, in agreement with a gaussian dispersion due to a perturbation, the geometrical configuration of the defects with the related OA band centered at $E_A^0$ assumes the double reading not only of the most common one but also of the unperturbed one.

From figure 4.17 we deduce a monotonic behavior for $k_{ISC}$ and then we will hypothesize a linear mapping for $\Delta S$ and $\Delta H$:

$$\Delta S = \widetilde{S}_0 + a_E \cdot \left(E_A - E_A^0\right) \tag{4.9}$$

$$\Delta H = H_0 + a_H \cdot \left(E_A - E_A^0\right) \tag{4.10}$$

where $\widetilde{S}_0$ and $H_0$ are the entropic and enthalpic barriers, respectively, of unperturbed centers and $a_E$ and $a_H$ are the linear coefficient of entropy and enthalpy mapping, respectively.

Regarding the $E_S$ and $E_T$ mapping, we have to consider figures 4.18 and 4.19, respectively. About $E_S$, the behavior in figure 4.18 is ambiguous because, at 22K, we find a clearly non monotonic dependence on $E_{Ex}$, at the variance of data at room temperature. We observe in equation (4.7) that the factor involving $k_{ISC}$ is a term depending on $E_A$ which alters the effect, on the integral value, of the dependence on $E_A$ of $E_S$ ($E_S^{E_A}$). As $k_{ISC}$ becomes more and more negligible with respect to $k_S$ by lowering the temperature, the behavior at 22 K is more representative of the $E_S$ mapping. Regarding $E_T$, we have the opposite situation: a non monotonic behavior at high $T$ and a monotonic one at low $T$. Considering the equation (4.8), we realize that now, to minimize the effect of $k_{ISC}$, we have to make it greater as possible, so the most representative curve is now the one at room temperature.

We will then state a quadratic mapping as a function of $E_A$ both for $E_S$ and $E_T$:

$$E_S^{E_A} = E_S^0 + a_S \cdot \left(E_A - E_A^0\right) + b_S \cdot \left(E_A - E_A^0\right)^2 \tag{4.11}$$

$$E_T^{E_A} = E_T^0 + a_T \cdot \left(E_A - E_A^0\right) + b_T \cdot \left(E_A - E_A^0\right)^2 \tag{4.12}$$

where $E_S^0$ and $E_T^0$ are the centers of the singlet and triplet emission bands, respectively, of the unperturbed center, $a_S$ ($b_S$) and $a_T$ ($b_S$) are the linear (quadratic) coefficients of singlet and triplet emission mapping, respectively.

### *4.2.2 Results and discussion*

The details of the fitting procedure of equations (4.6) - (4.8) to the data in figures 4.16 - 4.19 are reported in appendix A. In this section we will concern with the related outcomes. The resulting parameters are reported in table 4.3, while the corresponding theoretical behavior is represented in figure 4.16-4.19 with solids lines. The comparison with the experimental values shows that the quality of fitting is excellent and confirms the goodness of this approach. Two aspects are, in our opinion, particularly relevant. Firstly, we have been able to frame in a unified picture both the optical and the thermodynamic properties of the investigated center. This result is quite stimulating because they are usually studied apart, since the former is commonly considered a peculiarity of the defect structure, whereas the latter is generally thought to be matter related to the matrix physics. In this respect, the key point characterizing the proposed model is to have treated the defect-matrix complex as a whole. The second aspect is that, for the first time, we have been able to account for a variation of $k_{ISC}$ for more then three magnitude orders in a wide temperature range (330-3.7 K) and as a function of excitation energy, using simple and general hypotheses and a few number of parameters. In this respect, we want, indeed, to stress that the parameters involved in $k_{ISC}$ equations are only the first 6 in table 4.3, reveling the result concerning $k_{ISC}$ behavior to be particularly appreciable.

In the following we will consider in details the results in table 4.3 and their implications.

In agreement with the value of $\alpha$ in table 4.3, the value of $\sigma^2$ and the constraint $\sigma^2 = o_A^2 + \sigma_{Ex}^2$, we obtain for the homogenous and inhomogeneous width respectively:

$$\sigma_A = 0.0657 \pm 0.0029 \text{ eV}$$

$$\sigma_{Ex} = 0.2026 \pm 0.0067 \text{ eV}$$

At our knowledge this is the first time that both widths are evaluated. These values speak for an optical activity characterized by homogeneous and inhomogeneous widths of the same order, in agreement with the previous discussion on the experimental data. In particular, the information of $\sigma_{Ex}$ allows us to isolate for the first time the single center OA band which is an useful datum for comparison with computational works. Furthermore, regarding the estimation of the spread of the absorption energies $\sigma_A$, it is worth to note that **Skuja, 1994b,** and **Skuja *et al.*, 1995,** observed experimentally an inhomogeneous gaussian dispersion of optical activity related with an other point defect in silica, the so-called non bridging oxygen hole center (NBOHC). In particular, it was found a gaussian distribution of the zero-phonon line, and so of the absorption energies, characterized by a standard deviation of 0.037 eV. Bearing in mind the different centers and the different experimental methods, we can consider this value to be in good agreement with $\sigma_A$, suggesting that 0.01-0.1 eV is the typical spread induced by silica matrix on energy levels spacing.

Table 4.3. Values of the parameters obtained by fitting the equations (4.6) - (4.8) to the data in figure 4.16-4.19 (see also appendix A), except $M_{1S}$ at room temperature and $M_{1T}$ at 22K.

<table>
<tr><td colspan="6">$\alpha = \sigma_A/\sigma_{Ex} = 0.324 \pm 0.014$</td></tr>
<tr><td colspan="6">$R_{\beta_0} = 0.01348 \pm 0.00047$</td></tr>
<tr><td colspan="3">$S_0/k_B = 9.7 \pm 1.1$</td><td colspan="3">$a_E/k_B = (-7.8 \pm 2.2)\ \mathrm{eV}^{-1}$</td></tr>
<tr><td colspan="3">$H_0 = (0.180 \pm 0.020)\ \mathrm{eV}$</td><td colspan="3">$a_H = -1.09 \pm 0.13$</td></tr>
<tr><td colspan="2">$E_S^0 = (4.634 \pm 0.016)\ \mathrm{eV}$</td><td colspan="2">$a_S = -1.39 \pm 0.13$</td><td colspan="2">$b_S = (-78.6 \pm 4.1)\ \mathrm{eV}^{-1}$</td></tr>
<tr><td colspan="2">$E_T^0 = (3.349 \pm 0.018)\ \mathrm{eV}$</td><td colspan="2">$a_T = 3.66 \pm 0.23$</td><td colspan="2">$b_T = (-62.5 \pm 5.3)\ \mathrm{eV}^{-1}$</td></tr>
</table>

An other result in agreement with the experimental data is the value of $R_{\beta_0}$, which speaks for a very small number of $\beta_0$ centers with respect to the temperature depending ones, as we argued from the experimental value of $k_{ISC}$ at very low temperature.

Regarding $\Delta S$ and $\Delta H$ mapping, since we have not found neither experimental nor computational works to compare the mapping coefficients reported in table 4.3, we will discuss mainly the respective distributions, as obtained considering the $E_A$ distribution, $P(E_A)$, and the mapping equations (4.9) and (4.10) (see also equation (A.4)). We firstly analyze the temperature dependent centers, which are described by the gaussian term of $P(E_A)$ distribution.

Thanks to equation (4.10), we can derive their enthalpy distribution, which results to be centered in $H_0 = (0.180 \pm 0.020)$ eV with width $\sigma_H = (0.0713 \pm 0.0091)$ eV. We firstly observe that the typical value of 0.125 eV, previously obtained as a fitting of an Arrhenius law to data of figure 4.16 (see table 4.2 and discussion on figure 4.11), is consistent with this distribution. We note secondly that also for the enthalpies, as for the absorption energies, the obtained value for the distribution width is near 0.1 eV.

Concerning the entropy distribution, we derive from equation (4.9) (see also eq. (A.4)) that it is centered in $S_0 = (9.7 \pm 1.1) \cdot k_B$ (2) and its width is $\sigma_E = (0.51 \pm 0.15) \cdot k_B$. In order to discuss these results, it is important to bring in mind that we do not know the real absolute value of $S_0$ since, as discussed regarding equation (A.3), we included in it also the contribution of the pre-exponential factor, $k_0$. However, it is worth to note that this assumption does not affect the value of $\sigma_E$. We will consider deeply this aspect later but, for the present discussion, the main point is that the results of this model confirms the picture found in the previous paragraph, i.e. that ISC process is mainly driven by the temperature independent factors. The obtained value of $H_0$ corresponds, indeed, to a very low enthalpy factor $\exp\left(-{\Delta H}/{k_B T}\right) \sim 0.001$ also at room temperature which is balanced by a total pre-exponential factor equal to 16000, inducing the observed inversion of the **S**$_1$ and **T**$_1$ population. A stimulating way to compare the experimental behavior with the model is to consider the thermal behavior in terms of free energy barriers $\Delta G$. We can obtain, indeed, the same result calculating the $\Delta G$ distribution ($P(\Delta G)$) and bearing in mind that, if a center has a negative value of $\Delta G$, it has a very high conversion probability, because $k_{ISC}$ is greater than $k_S$ (see equations (2.16) and (A.3)); on the contrary, a center with $\Delta G > 0$ prefers to remain in the singlet state. So, the position of $P(\Delta G)$ with respect to $\Delta G=0$ indicates the relative number of centers relaxing via the $\boldsymbol{S_1} \to \boldsymbol{S_0}$ or the $\boldsymbol{T_1} \to \boldsymbol{S_0}$ transition. In this framework, the thermal behavior of the ISC process is due to the temperature dependence of $\Delta G$, which reflects in a shift of the $P(\Delta G)$. A representative selection of $P(\Delta G)$ is reported in figure 4.21, at different temperatures from 300 to 3.7 K. All curves are trucked because of condition $\Delta H(E_A) \geq 0$ (see equation (A.1) and relative discussion). On lowering the temperature, we observe a monotonic shift of the $P(\Delta G)$ distribution from negative to positive $\Delta G$ values. In particular, at 300K the most part of

---

(2) To compare with the enthalpy term, it can be useful to remember that $k_B = 86.1735\ {}^{\mu eV}/_{K}$

centers has a negative *ΔG* value, explaining the population inversion experimentally observed. Since at 215K there are as centers with $\Delta G < 0$ as centers with $\Delta G > 0$, we should have triplet and singlet state equally populated; such situation corresponds to $k_{ISC} = k_S$, which experimentally occurs indeed at 210-240K (see figure 4.16). Furthermore, we explain a so broad elbow-region because, as far as 50 K, a non negligible number of centers still remains in negative *ΔG* range. Regarding the excitation dependence, we found that the obtained *ΔH* and *ΔS* mapping coefficients correspond, in the investigated temperature range, to negative *ΔG* mapping coefficient, explaining the observed $k_{ISC}$ monotonic decreasing with $E_{Ex}$ (see figure 4.17). Furthermore, in agreement with this mapping, centers with higher *ΔG* values are characterized by higher *ΔH* values, and vice versa. For this reason, centers with greater $k_{ISC}$ (i.e. greater *ΔG*) at the same temperature, show a stronger thermal dependence, as proved

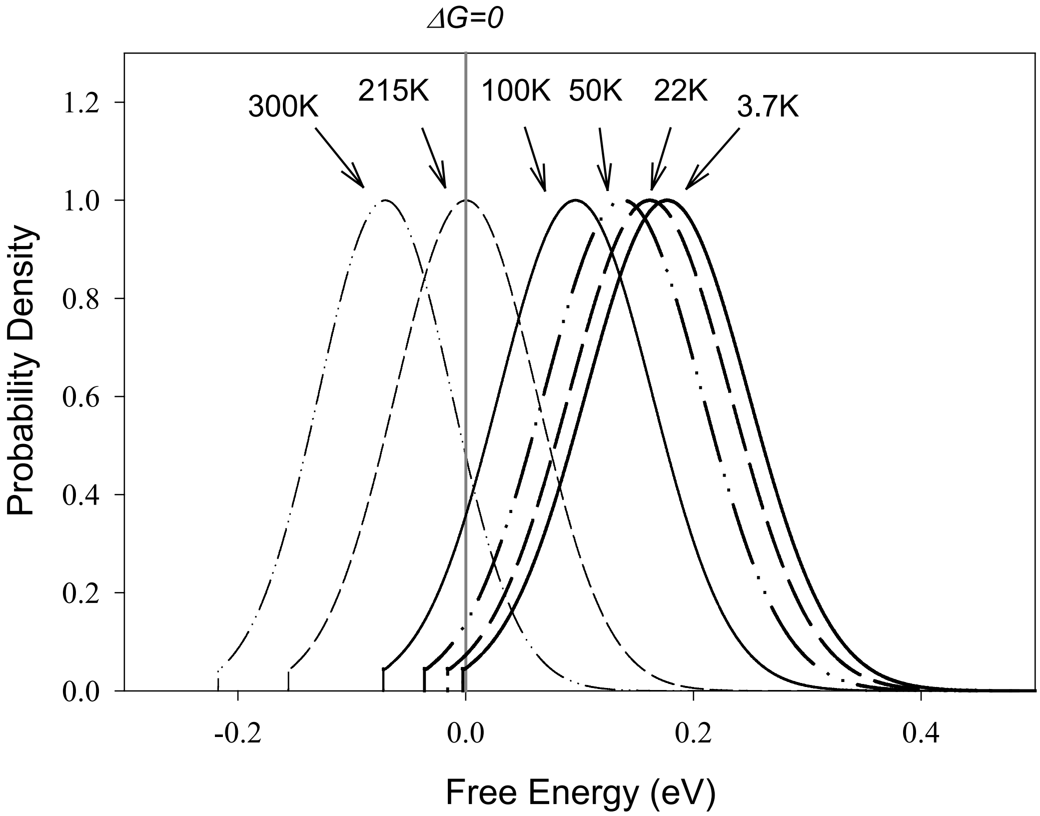

Figure 4.21. Free energy distribution function at different temperatures. The curves are normalized at the maximum.

experimentally in figure 4.16.

We consider now the $\beta_0$ centers. For these centers, that are characterized by $\Delta H = 0$ eV, we obtain $E_A^{\beta_0} = (5.350 \pm 0.031)$ eV and $\Delta S^{\beta_0} = (8.4 \pm 1.2)\cdot k_B$. They have then $k_{ISC}$ always ~4000 times greater then $k_S$, and so they contribute only to triplet state. The value of $E_A^{\beta_0}$ means that these defects are centered in the high energy tail of OA band, this result taking into account for the flatting of $k_{ISC}$ as a function of $E_{Ex}$, at 22 K, near 5.3 eV, where we excite more $\beta_0$ centers, giving a greater constant contribution to $M_{0T}$ which slows down the $k_{ISC}$ decreasing. This effect is absent at high temperature because of their low relative density. Regarding their $\Delta G$ values at different temperatures, they correspond to the cut-off of $\Delta G$ in figure 4.21.

We consider now the fitting results for first moment mapping $M_{1S}$ and $M_{1T}$. For both mapping coefficients we observe that the quadratic ones are much greater than the corresponding linear ones, corroborating the quadratic mapping hypothesis both for singlet and triplet first moments. Another consequence of the high value of $b_S$ and $b_T$ is a great variability of $E_S$ and of $E_T$ among centers.

It is worth to note that the values found for the unperturbed centers are quite different from experimental results. This is a warning for comparison between experimental and computational works on disordered systems, because the former measure mean values but the latter analyze a particular configuration. In this respect, a non monotonic mapping can induce experimental mean values of the spectroscopic parameters which do not correspond to the same configuration. For example, the fitting results in table 4.3 suggest that, to text the results of a computational work, the proper values of the absorption and of the related singlet and triplet emissions for the comparison are 5.2, 4.6 and 3.3 eV instead of 5.2, 4.2 and 3.1 eV. In our case, and considering the usual uncertainty of computational works (5÷10 %), this correction has not practical effects. Nevertheless for future, more detailed, computational

Table 4.4. Values of the parameters for $E_S$ and $E_T$ mapping obtained by fitting $M_{1S}$ at room temperature and $M_{1T}$ at 22 K. in figure 4.18 and 4.19 (see also appendix A).

| | | |
|---|---|---|
| $E_S^0 = (4.102 \pm 0.013)$ eV | $a_S = -5.09 \pm 0.58$ | $b_S = (-26.7 \pm 3.8)$ eV$^{-1}$ |
| $E_T^0 = (3.59 \pm 0.51)$ eV | $a_T = 5.4 \pm 3.7$ | $b_T = (-49 \pm 18)$ eV$^{-1}$ |

works or for system characterized by more remarkable non linear mapping, one should care about it.

As before reported, we compared the calculated behavior for $M_{1S}$ at 300 K and $M_{1T}$ at 22 K with the experimental ones but the result is quite unsatisfactory (3). To verify if there is an insufficiency in the whole model or the problem regards only the first moment mapping, we decided to fit $M_{1S}$ at 300 K and $M_{1T}$ at 22 K with all coefficients fixed except those for first moment mapping. The results are listed in table 4.4 and the new calculated plots are showed in figure 4.18 and 4.19 with dashed lines.

Since the results are again satisfying, we believe that the whole model is still good but there are some other not considered effects that are not negligible for the first moments mapping. We could suppose, for example, that the hypothesis of $T$-independent mapping coefficients is wrong for emission energy. As corroboration, we recall that PL bands, as the OA ones, can undergo small energy shifts with temperature, which could modify dramatically the dependence on $E_A$ because they could be different in different centers.

In conclusion of this paragraph, we want to deserve some comments about two points. The first concerns the assumption of a distribution and mapping coefficients independent on temperature. In this respect, in the investigated thermal range, silica does not perform any phase transition or structural changing (as proved by the volume density independent on temperature), so corroborating that all the nuclei move in harmonic approximation. In this

---

(3) We do not report them because are out of scale in figure 4.18 and 4.19.

case it is reasonable to assume that the defect-matrix complex geometry is not affected by the temperature, being consequently independent both the distribution and the mapping. The other point is maybe more basilar of the first one: why to develop such model? The answer is that the requirement of a model based on a distribution such this is more than a "theoretical exercise" because all attempts to fit data on figure 4.16 using exponential functions (stretched or not) are failed. In this respect, the good agreement with these data confirms the goodness of assuming an Arrhenius law for the single defect, despite the first impression of the thermal behavior of the ISC rate.

## 4.3 Conclusions

The analysis of the thermal behavior of some optical features of absorption and luminescence bands, associated with the twofold coordinated Ge embedded in silica, allows us to quantitatively characterize the coupling of this defect with the dynamics of its environment. Indeed, the vibrational modes populated in the temperature range extending below 330 K affect both the shape and the peak of optical bands and the relaxation kinetics from the excited states. In this framework, this Ge-ODC center reveals to be a probe to experience low frequency ($\langle E_l \rangle = 26$ meV) dynamics of host amorphous $SiO_2$ matrix, so allowing the phonon assisted ISC process to be efficient in spite of large values of enthalpy factor even at room temperature. Investigation of its optical properties corroborates previous computational works devoted to calculate the vibrational density of states for this energy range [**Uchino and Yoko, 1997, Pasquarello and Car, 1998, Zotov *et al.*,1999**]. The experimental approach here adopted allows quantifying the relaxation rates $k_S$ and $k_{ISC}$ from the excited state $S_1$. In particular, we found a non-Arrhenius behavior of ISC process and a non-exponential decay of fluorescence emission at 4.2 eV in the temperature range T≥ 210 K.

We stress that such a $k_{ISC}$ temperature dependence agrees with previous results obtained in natural silica [**Leone *et al.*, 1997** and **1999b**], so indicating that it is a =Ge$^{\bullet\bullet}$ related feature regardless the sample [**Grandi *et al.*, 2003**]. Photoluminescence time decay measurements as a function of the temperature and of the excitation energy has enabled an investigation of the competition between the radiative decay and the phonon assisted ISC process in the relaxation from the first excited singlet state of the defect. The non single exponential PL decay at room temperature and the dependence of decay time on the excitation energy are explained as a consequence of the ISC process able to experience the vitreous disorder at variance with the radiative process.

These results fit into a wide range of relaxation phenomena both in silica [**Griscom, 2001**] and in other disordered systems like proteins [**Frauenfelder *et al.*, 1988**], so they can be taken into account by considering the common amorphous nature. They show a relevant inhomogeneous broadening of all the measured quantities and the presence of cross-correlations between optical properties and between these and thermodynamics features. Particularly remarkable is the behavior of the ISC rate and the $S_1$ lifetime (figure 4.15 and 4.12). These mutual dependences reveal the presence of microscopic links and point out the inadequacy of the simplified approach discussed in chapter 1.

On this basis, we developed a theoretical model able to describe an ensemble of optically active point defect embedded in a disordered matrix. The model supposes a functional dependence (mapping) of the optical properties of the centers and of their phonon coupling with the matrix on a conformational coordinate. Via the mapping, the conformational disorder of amorphous matrix reflects itself in inhomogeneous broadening of the optical properties and coupling parameters, while the mapping induces a mutual dependence of the properties themselves which leads to the experimental cross-correlations.

We applied this model, with minimal and reasonable hypothesis, to describe the Ge related B-type activity in bulk silica, explaining satisfactorily, on the one hand, the temperature and excitation energy dependence of the ISC process and, on the other, the behavior of singlet and triplet first moments as a function of excitation energy at a fixed T. The good agreement between theory and experiment leads to the determination of important parameters such as the homogeneous width of absorption band, the inhomogeneous spectral width, the entropy and enthalpy distribution. In this respect, the good accordance with the parameters determined by comparison of the data in the linear behavior ranges (see in table 4.2 and related discussion) with an Arrhenius law corroborates the goodness of this analysis method to obtain a reliable typical value of the enthalpy barriers.

In conclusion of this chapter we want to note that both the optical properties and the activation barriers show a similar spread, supporting the previous remark of a typical value of 0.01-0.1 eV for the matrix perturbation on the energy terms. As pointed out by **Skuja, 1998**, if this fluctuation can be negligible, in first approximation, on the optical features of the absorption and luminescence band, it is comparable with the ISC activation barriers inducing the observed dramatic consequences on thermal dependence of ISC rates.

It is indeed worth to note that obtained parameters picture a matrix disorder able to modulate in a impressive way the enthalpy barriers causing a spread from 0 to 400 meV. Furthermore, it is stimulating to note that similar values of energy and free energy per atom has been found to be typical of the silica matrix in computational works on the glass transition from melting state [**Yuhai Tu *et al.*, 1998**].

# Chapter 5

# Defect-matrix coupling and heavy atom effect: iso-electronic Sn-Ge substitution

In this chapter, we report a study of the Sn related B-type activity to investigate the effects of the iso-electronic and iso-structural substitution on the defect-matrix complex. The comparison with the data relative to Ge-doped silica allows us to separate the effective role of conformational disorder and of local low frequencies dynamics of the matrix from the effects due to the particular atomic structure of defects, such as heavy atom effects and spin-orbit interaction or short-range organization effects.

## 5.1 Experimental results and discussion

The optical absorption measurements reported in this chapter were carried out with a sample doped with a nominal Sn content of 100 molar ppm, while both the steady state luminescence measurements and the time decays were detected on a sample with a nominal Sn content of 2000 molar ppm.

UV absorption spectra of the 100 ppm Sn-doped sample are dominated by the presence of the $B_{2Sn}$ band centered at about 4.9 eV, whose intensity at room temperature is $\alpha_{max} \approx 9$ cm$^{-1}$. As discussed in chapter 1, this band was assigned to an electronic promotion from the singlet ground state $\boldsymbol{S_0}$ to the first excited one $\boldsymbol{S_1}$ of the =Sn$^{\bullet\bullet}$ center (see figure 1.4) [**Skuja 1992**]. Figure 5.1 shows the $B_{2Sn}$ band as measured in our sample on varying the temperature in the

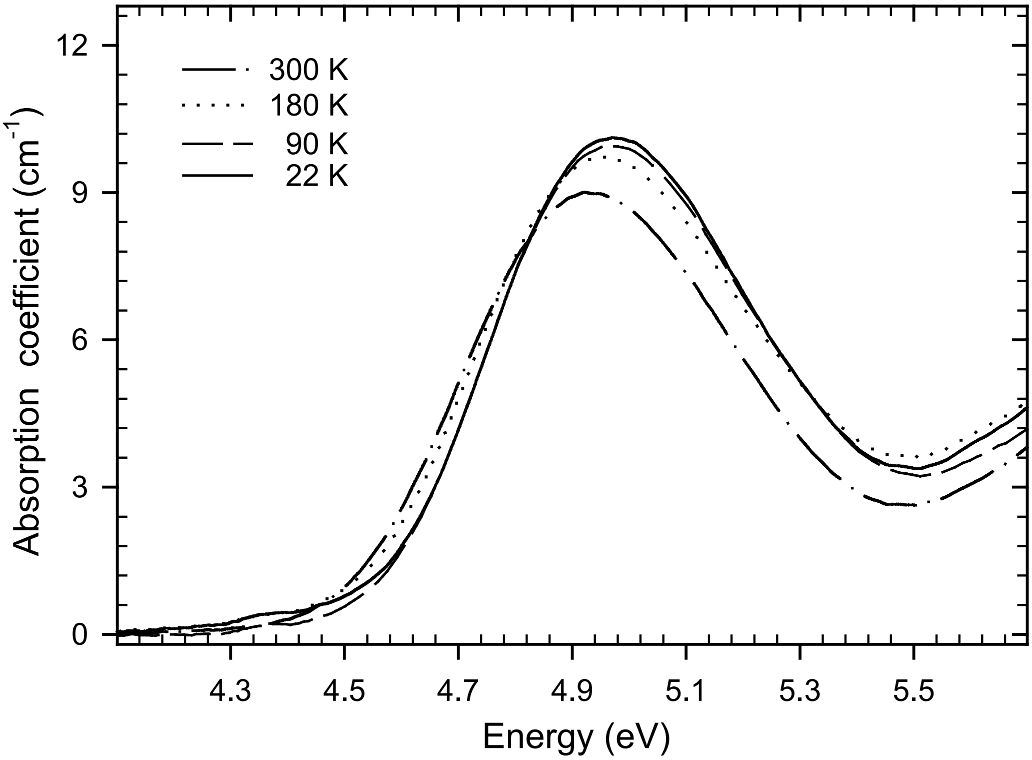

Figure 5.1. Sn related optical absorption $B_{2Sn}$ band detected at various temperatures

range 300 ÷ 22 K. In analogy with the behavior found for the Ge related $B_{2Ge}$ band in the previous chapter, the raw data evidences that, on lowering the temperature, OA band undergoes a blue-shift and a narrowing.

As described in the third chapter, we analyzed the thermal behavior of the $B_{2Sn}$ band in terms of the moments of its spectral profile. In figure 5.2 the temperature dependence of the $M_0$, $M_1$ and $M_2$ values for the Sn-doped sample are reported and compared with data of the Ge-doped sample of the previous chapter,. No significant variations of $M_0$ are found in the panel (a), in accordance with the behavior of the Ge related $B_{2Ge}$ band. In agreement with the changes observed in the $B_{2Sn}$ band profile (figure 5.1), on lowering the temperature $M_1$ increases from ~4.95 to ~4.99 eV. We observe almost the same dependence in the Ge related data, apart from a constant shift. In order to investigate the coupling of the electronic transition of the $=Sn^{\bullet\bullet}$ with low frequency normal modes of the defect-matrix complex, we

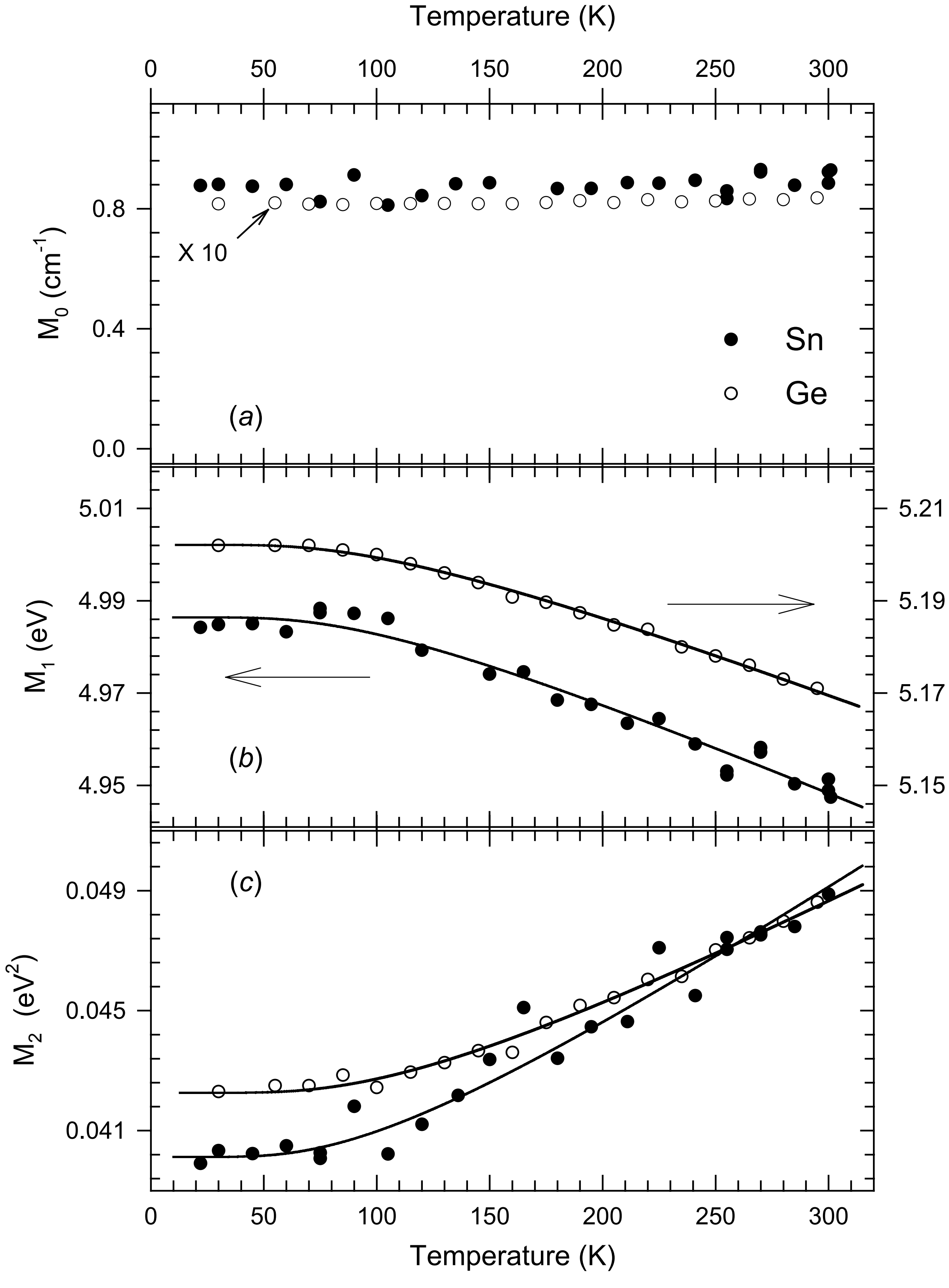

Figure 5.2. Temperature dependence of zero (a), first (b) and second (c) spectral moments of Sn related $B_{2Sn}$ band (filled marks). For comparison porpouse, the first and second moments of the Ge related $B_{2Ge}$ band (open marks) are reported. Continuous lines represent the best fit of the data in (*b*) and (*c*) in terms of equations (2.34) and (2.35), respectively. Note that in (b) the left scale refers to Sn-doped sample, the right scale to Ge-doped sample

fitted data in figure 5.2(b) and (c) with the equations (2.34) and (2.35). Continuous lines in figure 5.2 represent the results of the fitting procedure and the relative parameters are reported in table 5.1. Data show that the iso-structural substitution Sn-Ge does not change significantly the mean vibrational energy value of the “bath” of low-frequency modes, suggesting that the local dynamics coupled with the electronic transition is essentially determined by the vitreous silica matrix, embedding both the two ODC centers. At the contrary, the substitution influences the $M_1^0$ and $N_l(1\text{-}R_l)$ values, both related to the different electronic properties of the two defects.

Figure 5.3 shows the steady state PL spectra at 300 K (a) and 22 K (b) under different excitation energies (4.71, 5.00 and 5.21 eV). The comparison of the (a) and (b) panels reveals an opposite thermal behavior of the two bands: on lowering the temperature, the $\alpha_{Sn}$ intensity increases whereas $\beta_{Sn}$ one decreases, this decrease being more pronounced on lowering the excitation energy.

In agreement with the B-type activity level scheme, the thermal behavior of the two emissions is due to the competition between the two decay rates from the $\boldsymbol{S_1}$ state: the radiative one $k_S$, temperature independent, and the thermally activated, non-radiative, $k_{ISC}$ towards $\boldsymbol{T_1}$. As discussed in chapter 2, we will consider the ratio between the areas of the two integrated PL bands as a measure of the ratio $\zeta=k_{ISC}/k_S$ (see equation (2.45)), if radiationless relaxation processes from $\boldsymbol{S_1}$ and $\boldsymbol{T_1}$ toward $\boldsymbol{S_0}$ are negligible. To prove this condition, we

Table 5.1. Values of the parameters obtained by fitting eqs. (2.34) and (2.35) to the thermal behavior of the first and second moments of Sn related $B_{2Ge}$ band. The same parameters relative to the Ge related activity are also reported in the second row, for comparison (table 4.1).

| B-type activity | $N_l S_l$ | $N_{l'}(1\text{-}R_l)$ | $\langle E_l \rangle$ (meV) | $M_2^0$ (eV$^2$) | $M_1^0$ (Ev) |
|---|---|---|---|---|---|
| Sn related | 12 ± 1 | 5.0 ± 0.6 | 25 ± 5 | 0.033 ± 0.001 | 5.02 ± 0.01 |
| Ge related | 10 ± 2 | 4.5 ± 0.2 | 26 ± 2 | 0.036 ± 0.005 | 5.23 ± 0.01 |

verified that the total area $M_{0S}+M_{0T}$ is constant regardless the temperature (data not reported). As done for the Ge related activity, we will compare the thermal behavior of the ISC process with the Arrhenius law (2.47). For the aim of this chapter, we note that, as shown in equation (2.16), the total pre-exponential factor $k_E$ can be thought as factorized in two terms,

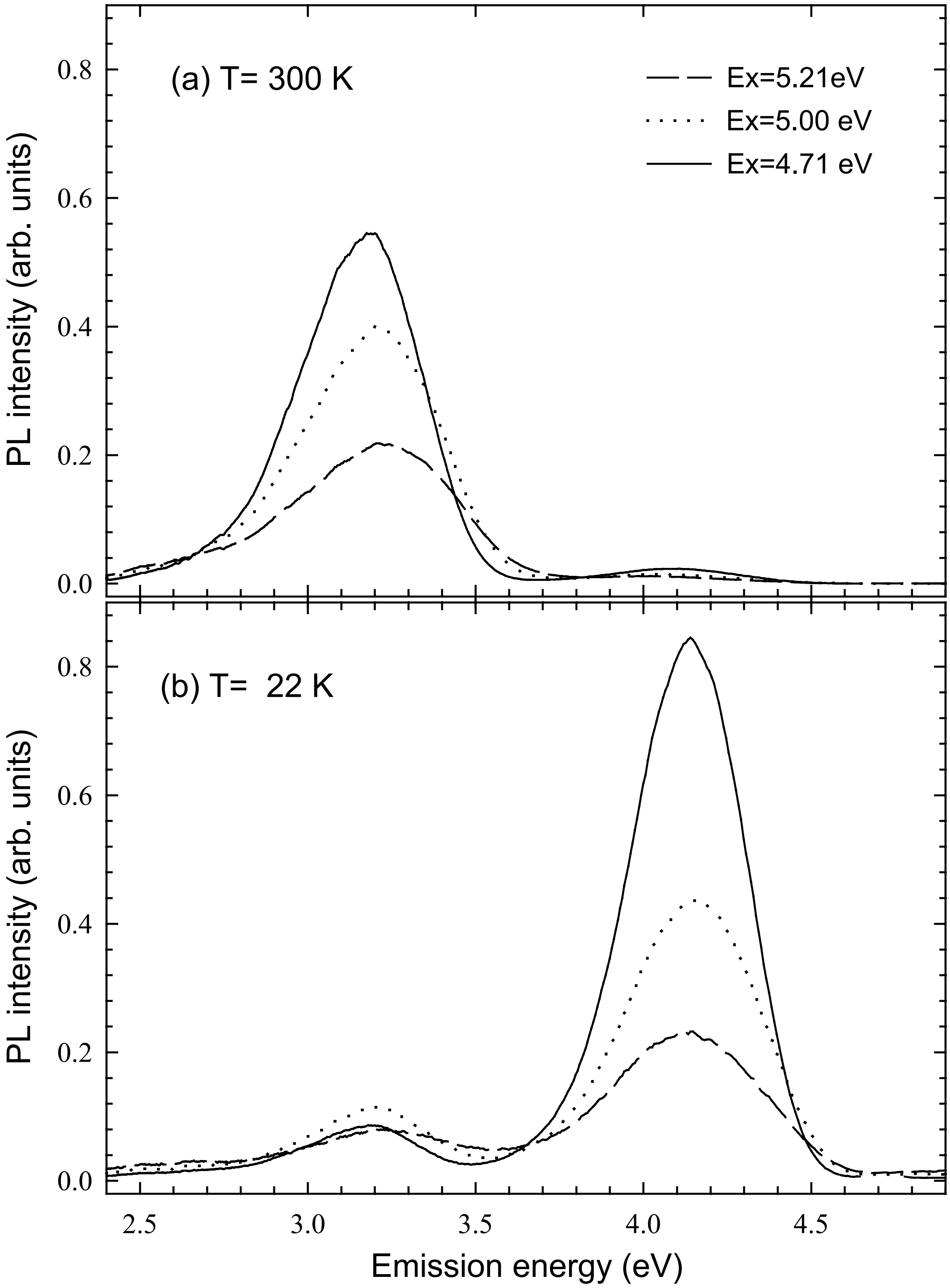

Figure 5.3. Emission spectra centered at ~3.2 eV ($\beta_{Sn}$ band) and ~4.2 eV ($\alpha_{Sn}$ band), obtained under excitation at 4.71, 5.00 and 5.21 eV. (a) T = 300 K; (b) T = 22 K.

to point out the different role of entropy contribution ($\Delta S$) and of the contribution due to other effect, like spin-orbit coupling. From these equations, the thermal behavior of the emission spectra (figure 5.3) can be rationalized. Firstly, we characterized the weight of the two relaxation channels from $\boldsymbol{S_1}$ with time decay measurement on the $\alpha_{Sn}$ band, by detecting the transient 4.1 eV emission under pulsed excitation at 5.0 eV and varying the temperature from 18 to 300 K. Figure 5.4 shows the dependence of $\alpha_{Sn}$ kinetics on the temperature, which can be rationalized by considering the competition between the radiative channel $k_S$ and the thermally activated ISC process, the total $\boldsymbol{S_1}$ lifetime being $\tau = (k_S + k_{ISC})^{-1}$. As it can be seen, the emission decay occurs in the ns scale and, on increasing the temperature, the decay time decreases and the kinetics deviate from a single exponential law. In particular, the lifetime shortening becomes more and more evident above 100 K, so indicating that at this temperature $k_{ISC}$ is comparable with $k_S$. Finally, the deviation from single exponential law suggests that $k_{ISC}$ rates are characterized by a relevant spread. Regarding the fine tuning of the excitation energy, no clear dependence was found on the emission time decay measurements at room temperature and at 22 K.

We quantitatively analyzed the ISC process associated with the $=\mathrm{Sn}^{\bullet\bullet}$ center by comparing the data relative to the steady state PL bands and to the lifetime measurements. The low temperature data in figure 5.4 show a single exponential behavior, corresponding to a $(k_S + k_{ISC})$ value of $(1.19 \pm 0.03)\times10^{8}$ sec$^{-1}$. Analyzing the data at low temperatures in figure 5.3, we can calculate the ratio $\zeta$, obtaining a value of $0.23 \pm 0.08$. These results, according to equation (2.45), give $k_S = (0.91 \pm 0.09)\times10^{8}$ sec$^{-1}$, in agreement with data already reported by **Chiodini *et al.*** in **2000**. Before of the analysis of time decays at higher temperature, we will use this value of $k_S$, to determine the $k_{ISC}$ values according to equation (2.45) and to the experimental data of the ratios $\zeta$, measured under c.w. excitation at three different energies. The obtained values of $k_{ISC}$ are reported in figure 5.5 and clearly

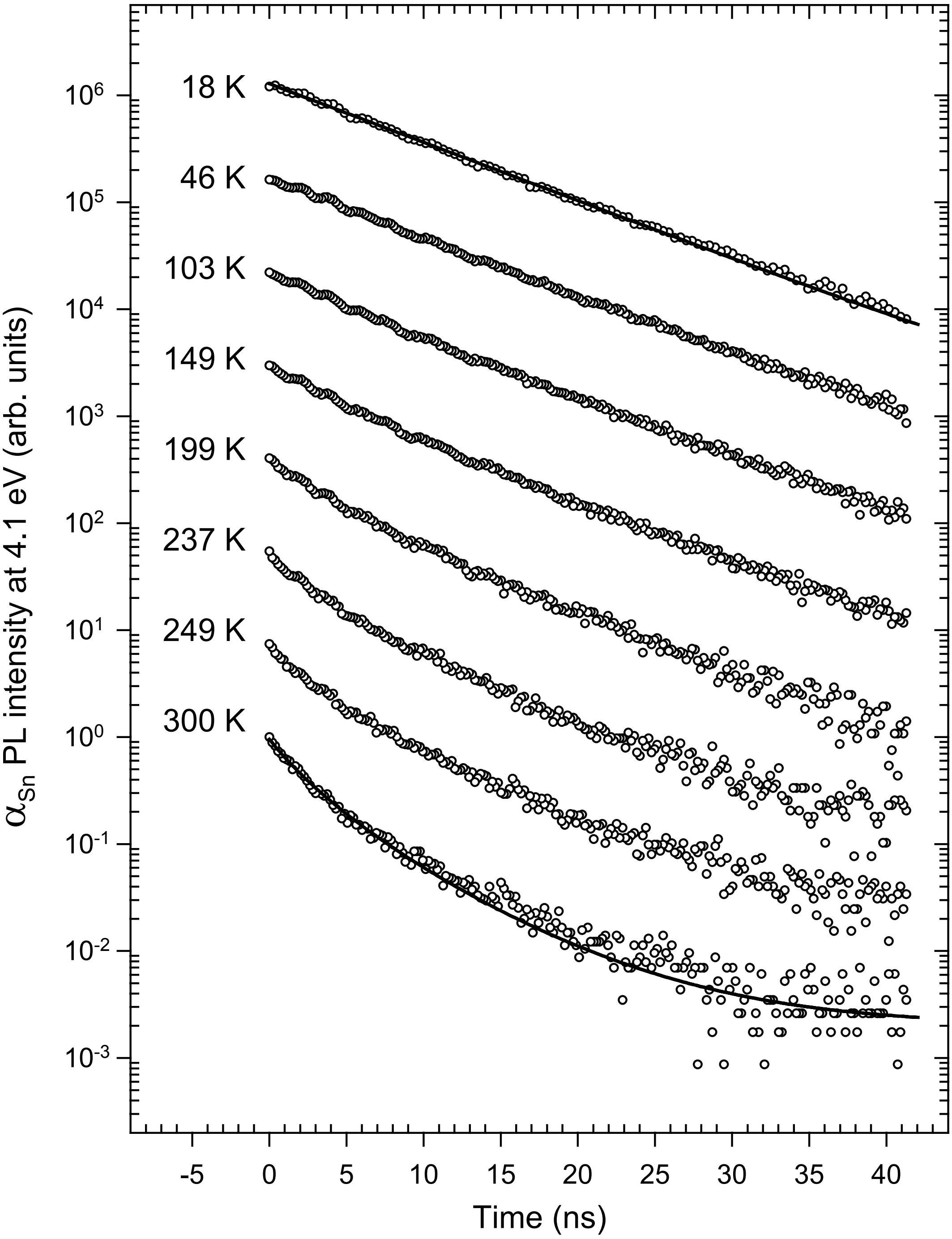

Figure 5.4. Decay kinetics of 4.1 eV emission detected under pulsed excitation at 5.0 eV, as a function of temperature from 18 up to 300 K. For viewing purposes, the decay curves are arbitrary scaled. The solid line are representative selection of fitting the data in terms of a stretched exponential decay (equation 4.1).

show a non-Arrhenius behavior (see equation (2.16) or (2.47)) in the whole temperature range. Regarding the dependence on the excitation energy, in the low temperature range $k_{ISC}$ exhibits a monotonic dependence whereas, at high temperatures, no dependence is observed (see also the inset). We also note that, at the three excitations, $k_{ISC}$ decreases on lowering the temperature down to 50 K and tends to a constant value at lower temperatures. Moreover, both at T > 250 K (see once more the inset) and at T < 50 K the curve slopes are almost constants. Then, in these temperature ranges, we can compare the $k_{ISC}$ behavior with an Arrhenius law, the relative parameters being reported in table 5.2.

The above reported results reveal the interplay between the enthalpy and the pre-exponential factor in governing the overall behavior of phonon assisted ISC. On the one hand, both $\Delta H$ and $k_E$ show a remarkable spread, decreasing by three-four orders of magnitude on lowering the temperature from 300 down to 3 K. On the other hand, the behavior of $k_{ISC}$ varying the excitation energy reflects the mapping of the entropy and

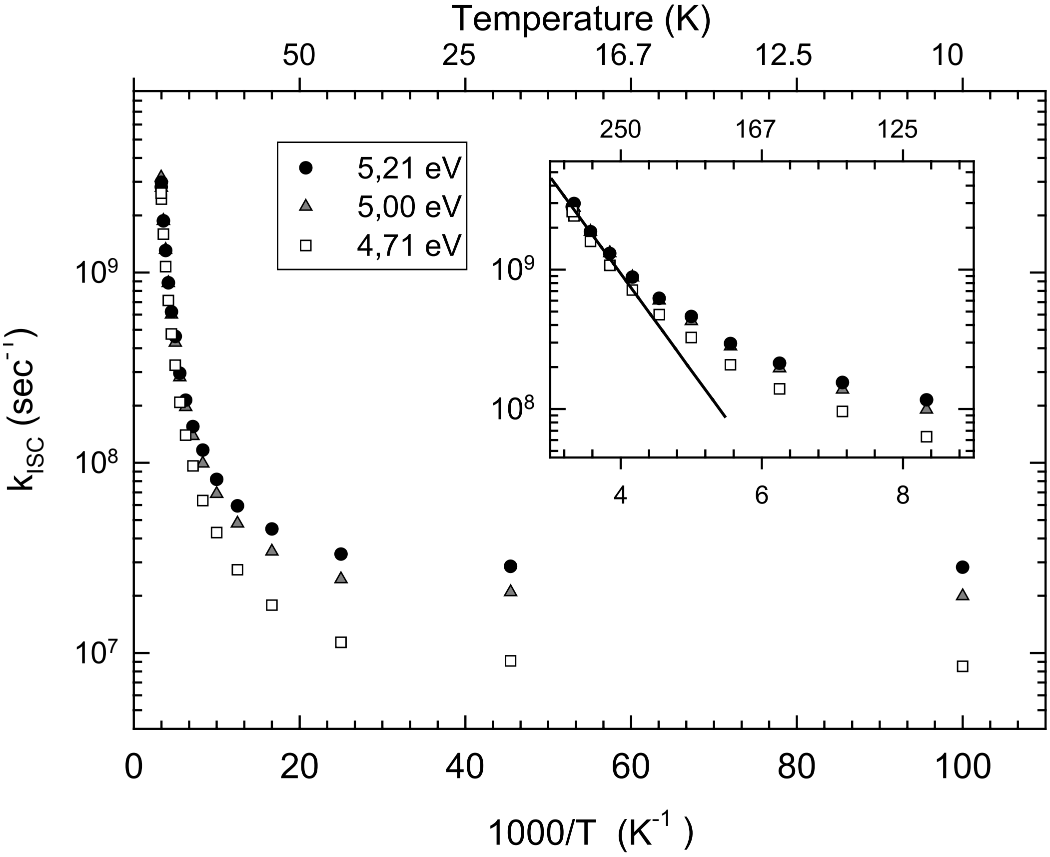

Figure 5.5. Thermal behavior of ISC rate measured according to eq. (2.45) under c.w. excitation at 4.71, 5.00 and 5.21 eV. The inset shows the ISC rate in the high temperature range (T > 100 K). The straight line in the inset shows the fitting in the high T range in terms of an Arrhenius law (eq (2.47)).

Table 5.2. Values of decay rates from $\mathbf{S_1}$ and of the thermodynamic parameters of ISC process obtained at three different excitation energies for the Sn related activity.

| | $k_BT > 20$ meV | | | | $k_BT < 2$ meV | | | |
|---|---|---|---|---|---|---|---|---|
| $E_{exc}$ (eV) | $k_s$ ($10^6$ s$^{-1}$) | $k_{ISC}{}^a$ ($10^6$ s$^{-1}$) | $k_E$ ($10^6$ s$^{-1}$) | $\Delta H$ (meV) | $k_s$ ($10^6$ s$^{-1}$) | $k_{ISC}{}^b$ ($10^6$ s$^{-1}$) | $k_E$ ($10^6$ s$^{-1}$) | $\Delta H$ (meV) |
| 4.71 | 91±9 | 2070±40 | $(5\pm2)\times10^5$ | 130±10 | 91±9 | 9.0±0.2 | 9.1±0.3 | <0.3 |
| 5.00 | | 2720±50 | | | | 20.8±0.4 | 21 ± 1 | |
| 5.21 | | 2210±40 | | | | 29.5±0.9 | 29 ± 1 | |

$^a k_{ISC}$ values as obtained at 300 K

$^b k_{ISC}$ values as obtained at 22 K.

enthalpy energies on the defect configuration.

Concerning the quantitative analysis of the thermal behavior of the time decays in figure 5.4, it was carried out by fitting the experimental data with a stretched exponential law (see equation (4.1)). We recall that the analysis is made for times longer than 2.3 ns (see chapter 3). Full lines in figure 5.4 represent the best fit curves of the PL decay at 18 and at 300 K, under excitation at 5.00 eV, in terms of equation (4.1). The results of the fitting procedure applied to the PL decay data are reported in figure 5.6, as a function of the temperature. We observe in the panel (*a*) that, rising the temperature, $\tau$ decreases from 8.4 ns down to 1.0 ns and exhibits a temperature dependence typical of a thermally activated process. Similar dependence is also found for the parameter $\gamma$, as can be seen in the panel (*b*). Analogously with the results of the Ge related B-type activity, these results can be rationalized assuming that, increasing the temperature, the ISC process become more and more effective. It implies, indeed, a shortening of the $\boldsymbol{S_1}$ lifetime and, in agreement with previous discussions on the $k_{ISC}$ spread, a deviation from a single exponential behavior. To check the reliability of this rationalization, we compare the values of $\tau$ obtained by fitting with the ones calculated from the values of $k_{ISC}$ in figure 5.5, using the equation $\tau = (k_S+K_{ISC})^{-1}$ and $k_S = (0.91 \pm 0.09)\times10^8$ sec$^{-1}$. The expected values of $\tau$ thus obtained are reported in figure 5.6(*a*) and are in good agreement with the values obtained by direct fitting. So, the whole observed thermal behavior of $\boldsymbol{S_1}$ for the Sn related B-type activity can be ascribed to the temperature dependence of the competition between $k_S$ and $k_{ISC}$..

As discussed in the previous chapter and in several works [**Martini *et al.*, 1998, Leone *et***

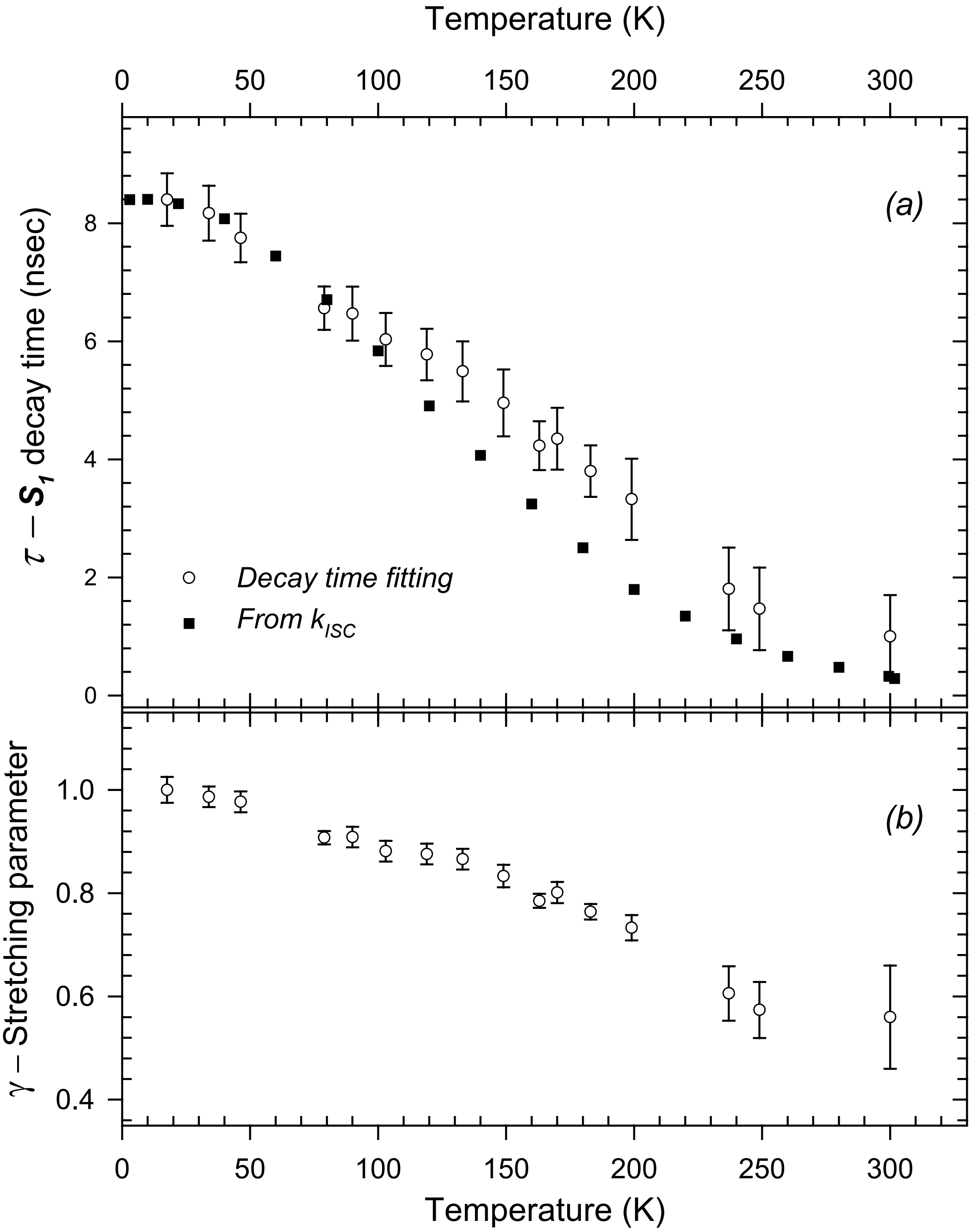

Figure 5.6. (*a*) $\boldsymbol{S_1}$ decay time $\tau$ and (*b*) stretching parameter, $\gamma$, varying temperature, as obtained by fitting data in figure 5.4 in terms of eq.(4.1) (open circles). For comparison purpose, the expected values of $\tau$ from the values of $k_{ISC}$ (full squares) are reported in (*a*) (see text for details).

***al.*, 1999a, 1999b** and **2001**], and in agreement with the model previously proposed for the Ge related defects, these results support the hypothesis that ISC occurrence is strictly related to the amorphous nature of $SiO_2$ matrix; since the site-to-site non-equivalence of the centers causes the inhomogeneous distribution of both the activation energies and the entropy factors.

The alternative explanation suggested in chapter 4 (see subsection 4.1.3) is, of course, still valid for the Sn related B-type activity.

In figure 5.7, we compare the thermal behavior of the Sn and the Ge related ISC rates under excitation at 5.00 and 5.21 eV, respectively, i.e. at about the maximum of their corresponding $B_{2T}$ bands. In table 5.3, we report the relative thermodynamic parameters for the ISC process.

As it can be seen, the efficiency of the Sn related ISC process is one order of magnitude

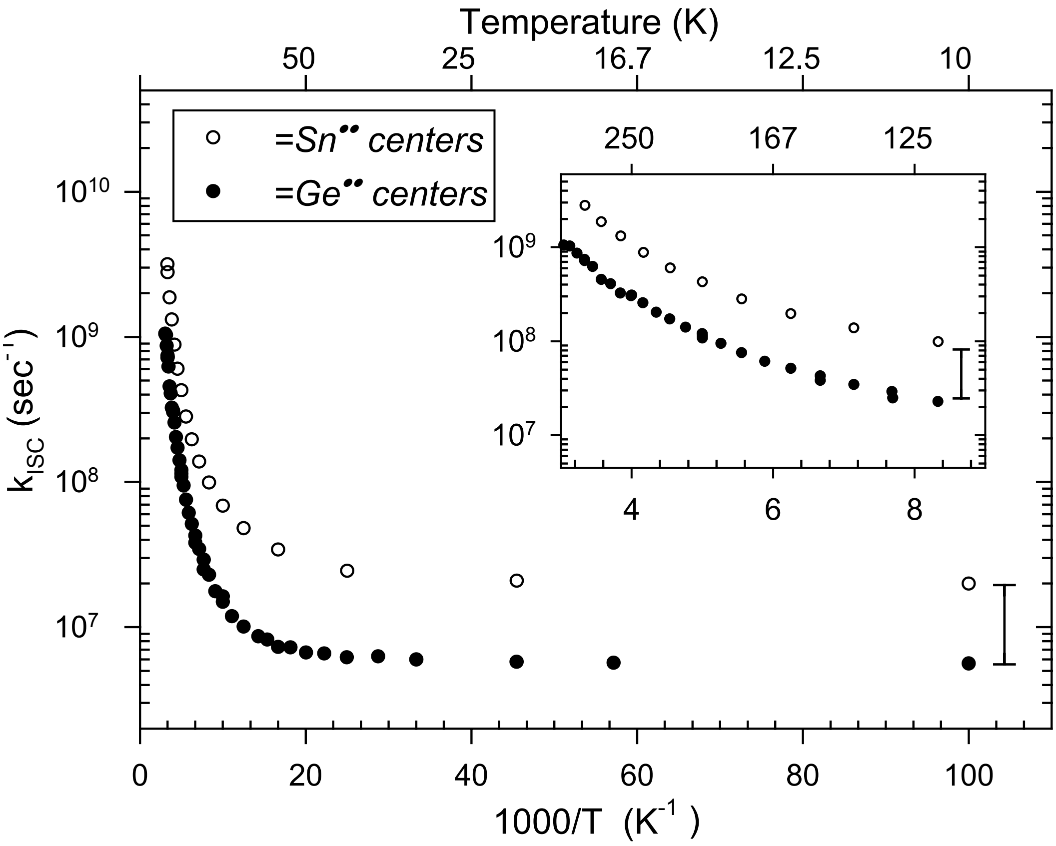

Figure 5.7. Comparison of the thermal behavior of ISC rate, according to eq. (2.45), for the Sn (open symbols) and Ge (full symbols) related activities. The inset shows the ISC rate in the high temperature range (T > 100 K).

greater than the Ge related one. We note that data in figure 5.7 and the $k_{ISC}$ and $k_E$ values in table 5.3 are scaled one respect to the other in the whole temperature range. This suggests that the Sn-Ge substitution induces an increasing of the ISC efficiency, which involves only the pre-exponential factor $k_E$.

Regarding the enthalpy barriers, in agreement with the scaling effect both the temperature dependence of the data reported in figure 5.7 and the values of $\Delta H$ in table 5.3 are the same in both systems, suggesting that the enthalpy barrier values and their distribution are poorly affected by the iso-electronic substitution. This result is corroborated by the value of 130 meV reported by **Skuja** in **1994** for the activation barriers governing the ISC processes in the =Si$^{\bullet\bullet}$. It is worth to note that also the mean vibrational energy of the "bath" of low frequency modes (table 5.1) are almost the same in both the systems. We can rationalize these results assuming that the Sn-Ge substitution does not substantially modify the local dynamics in the surrounding of the two defects and that the only effect is to induce an homogeneous temperature-independent scaling factor of the ISC efficiency.

Since the dynamics of the host matrix are the same in both systems, the changes in ISC efficiency is expected to be related to some property of the Ge and Sn atoms. In this respect, it is worth to note that these results agree with the shortening of the Sn related triplet state

Table 5.3. Comparison of the thermodynamic parameters of ISC process for Sn and Ge related activities, under excitation energy near the maximum of the respective $B_{2T}$ bands.

| | $k_BT > 20$ meV | | | $k_BT < 2$ meV | | |
|---|---|---|---|---|---|---|
| B-type activity | $k_{ISC}$ [a] ($10^6$ s$^{-1}$) | $k_E$ ($10^6$ s$^{-1}$) | $\Delta H$ (meV) | $k_{ISC}$ [b] ($10^6$ s$^{-1}$) | $k_E$ ($10^6$ s$^{-1}$) | $\Delta H$ (meV) |
| Sn related | 2720±50 | $(5\pm2)\times10^5$ | 130±10 | 20.8±0.4 | 21 ± 1 | <0.3 |
| Ge related [c] | 727±10 | $(9\pm3)\times10^4$ | 125±8 | 5.6±0.9 | 5.8±0.1 | <0.3 |

[a] $k_{ISC}$ values as obtained at 300 K

[b] $k_{ISC}$ values as obtained at 22 K.

[c] From table 4.2.

lifetime (~10 μsec) respect to the Ge related one (~110 μsec), which was shown to be proportional to the spin-orbit coupling, regardless the temperature and the excitation energy (see paragraphs 1.2 and 2.2). Therefore, these data suggest that the observed enhancement in the Sn related ISC rates is due to the spin-orbits terms that reveal themselves to play a significant role in the coupling of the vibrational modes of the lattice with electronic transitions between states of different multiplicity. Accordingly to equation (2.16) and the related discussion, the total pre-exponential factor $k_E$ implicitly contains two different contributions. The $k_0$ factor accounts for the typical time of a single $\boldsymbol{S_1} \rightarrow \boldsymbol{T_1}$ process and it is expected to be dependent on the atomic structure of the defect. At the contrary, the entropy term depends on the interaction with the local lattice. Since the heavy atom effect has been found to be homogenous and independent on temperature, the previous considerations suggest that the substitution concerns essentially the $k_0$ factor. Accordingly to the shortening of the $\boldsymbol{T_1}$ lifetime by a factor $10^2$ and $10^3$ passing from the $=\mathrm{Si}^{\bullet\bullet}$ to $=\mathrm{Ge}^{\bullet\bullet}$ and to $=\mathrm{Sn}^{\bullet\bullet}$ centers, respectively, we distinguish in the experimental values of Ge and Sn related $k_E$ (see table 5.3) an homogeneous factor at least of $10^2$ and $10^3$, respectively. In the light of this result, we note that the value of $(9.7 \pm 1.1) \cdot k_B$ for the mean entropy $S_0$ associated with the $=\mathrm{Ge}^{\bullet\bullet}$ centers (table 4.3), obtained accordingly to the model in paragraph 4.2, contains also the contribution $ln(k_0/k_S)$ (see equation (A.3) and following discussion), being the entropy distribution centered, at most, in 5 $k_B$ .

We want to stress that, even if $k_{ISC}$ is found to involve a homogenous process, the non exponential time decays at high temperatures and observed dependence on the excitation energy (see figures. 5.4 and 5.5) still speak for an inhomogeneous spread. Further information on the effect of the Sn-Ge substitution can be indeed achieved studying the dependence of $k_{ISC}$ on the excitation energy at different temperatures and comparing the thermal behavior of the $\boldsymbol{S_1}$ time decay in both the systems. In figure 5.8 we report $k_{ISC}$ values under different

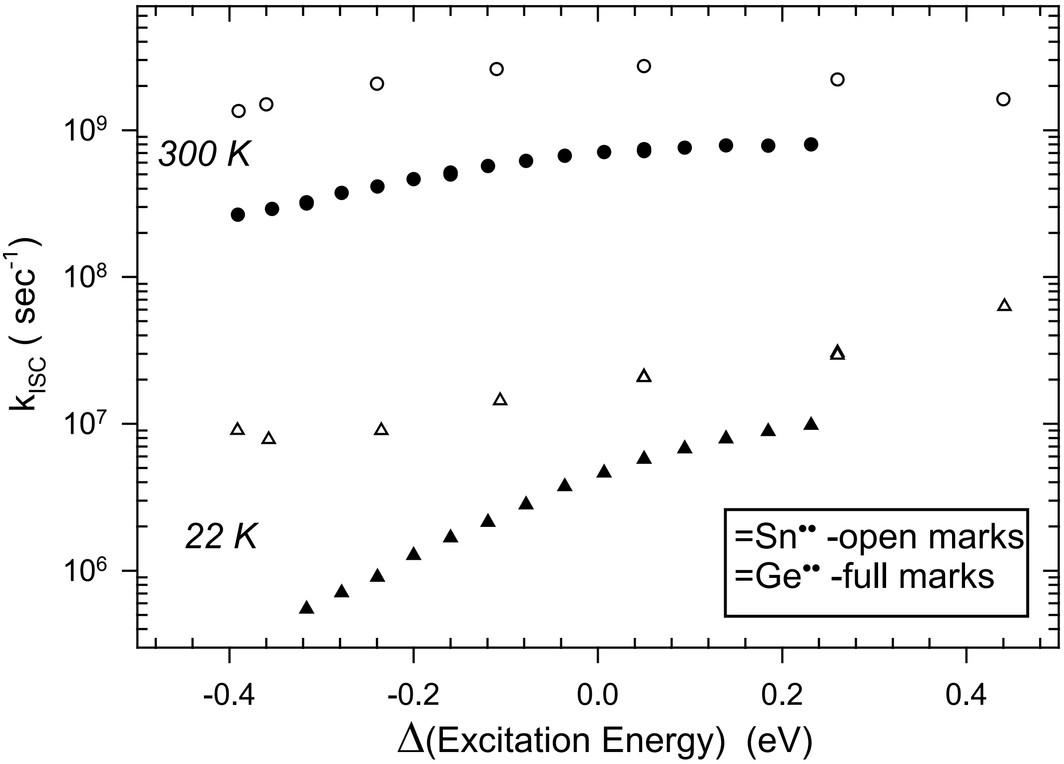

Figure 5.8. ISC rates, according to equation (2.45), as a function of the differen in excitation energy with respect to the maximum of the relative $B_{2T}$ bands (4.95 eV and 5.16 eV respectively). Circles: 300 K; triangles: 22 K. Open marks refer to $=Sn^{\bullet\bullet}$ centers; full marks refer to $=Ge^{\bullet\bullet}$ centers.

excitation energies within the respective $B_{2T}$ bands at two temperatures, where the ISC effectiveness changes by two orders of magnitude. In order to compare the Sn and the Ge related $k_{ISC}$ behavior, the data are reported as a function of the difference in the excitation energy with respect to the maximum of the respective $B_{2T}$ bands (4.95 and 5.16 eV respectively). At both temperatures, the observed dependence is almost the same in both systems, even if they are not perfectly scaled and, in particular, the Ge related ISC rate shows a variability greater than the Sn related one. This result is in agreement with the poorer dependence on the excitation of the Sn related $S_1$ lifetime with respect to the Ge related one. This comparison confirms that the previous picture about the influence of the substitution is basically right, even if there are some other smaller consequences. In particular, this suggests two different effects: i) the substitution with a Sn atom induces a partial decreasing of the

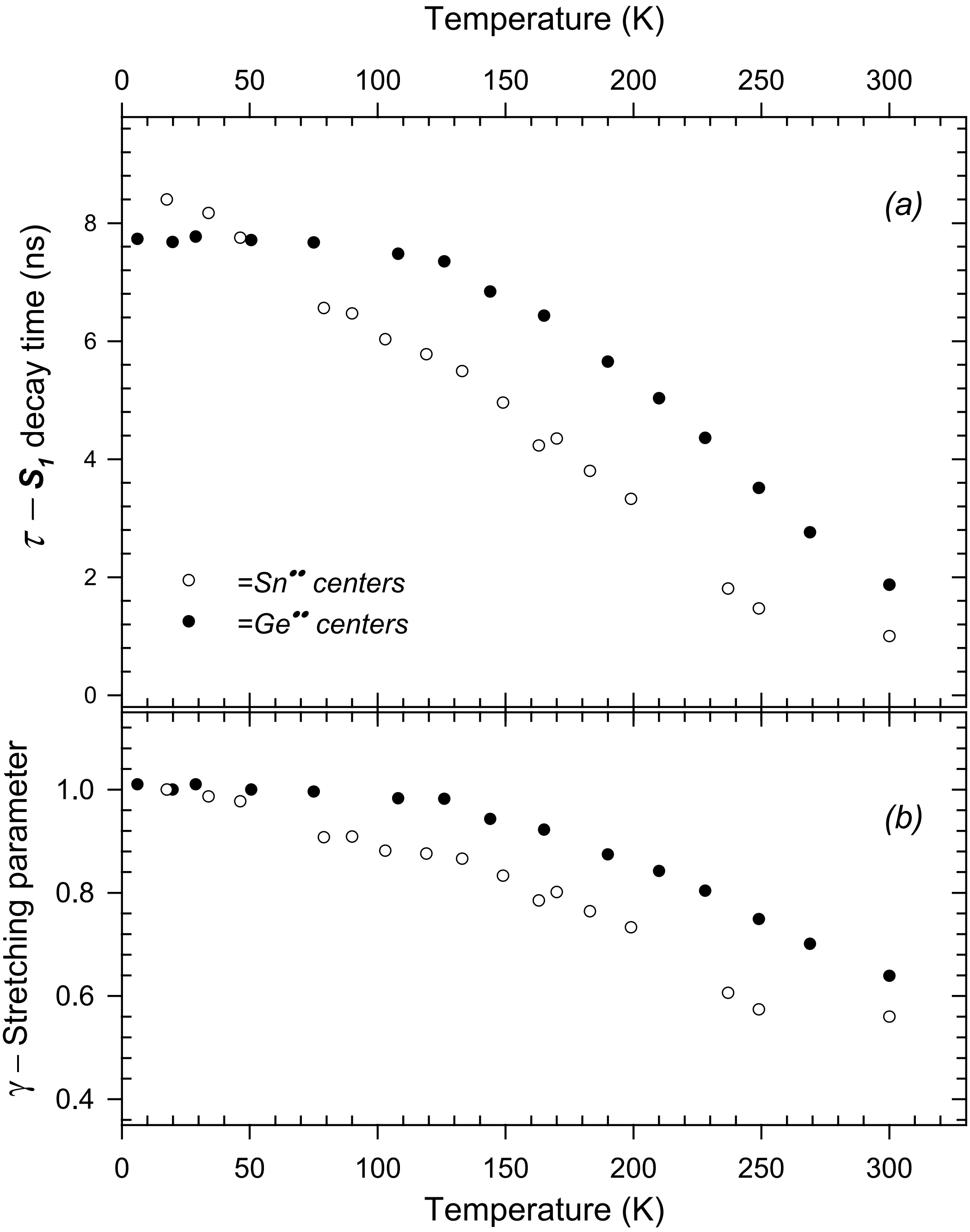

Figure 5.9. (*a*) $S_1$ decay time $\tau$ and (*b*) stretching parameter, $\gamma$, varying temperature, as obtained by fitting data in figure 5.4 in terms of eq.(4.1) (open marks). For comparison purpose, the values of $\tau$ and $\gamma$ for the Ge related B-type actitivy (full marks) are reported (from figure 4.14).

local disorder or ii) the optical properties of the two-fold coordinates Sn are less sensitive to the local conformations.

In conclusion of this section we show the effect of Sn-Ge substitution on the thermal behavior of the $S_1$ time decays. At this aim we report in figure 5.9 the results for both systems, previously obtained by fitting the time decays in terms of a stretched exponential (equation (4.1)). The comparison reveals a quite different behavior increasing the temperature: the $\boldsymbol{S_1}$ lifetime for the Ge related activity assume a constant value and a single exponential decay ($\gamma$=1) below 150 K diverging from this behavior at higher temperature; whereas the $\boldsymbol{S_1}$ time decays of the Sn related ODC show immediately a decrease of $\tau$ and a deviation from the pure exponential behavior. This differences can be rationalized as an effect of the Sn-Ge substitution on the ISC efficiency. We have already shown that the shortening of $\tau$ and the deviation from a single exponential behavior can be, indeed, explained for both systems as an effect of the competition between $k_{ISC}$ and $k_S$: the shortening is due to the enhancing of the $k_{ISC}$ efficiency rising of temperature, the non exponential behavior is due to the dispersion of the activation barriers governing the ISC process. In agreement with this picture, the Ge related $k_{ISC}$ starts to be comparable with $k_S$ only over 150 K, where $k_{ISC}$ is 0.2 times $k_S$ (see figure 5.7). Such analysis on the Sn related ISC rates shows that $k_{ISC}$ is never negligible with respect to $k_S$ since, also at 10 K, it is 0.2 times $k_S$ (see one more time figure 5.7), in agreement with the behavior observed in figure 5.9.

## 5.2 Conclusions

With the same methodological approach adopted for the Ge related B-type activity, we have analyzed the coupling of the $=\mathrm{Sn}^{\bullet\bullet}$ center with the low frequency dynamics of the host amorphous silica matrix. By comparing the data relative to the stationary emission activity and to the time decay measurements, we are able to separate the relaxation rates $k_S$ and $k_{ISC}$. Concerning the phonon coupling, the $=\mathrm{Sn}^{\bullet\bullet}$ centers experience the same low frequency ($\langle E_l \rangle = 25$ meV) dynamics of the $=\mathrm{Ge}^{\bullet\bullet}$ while, analogously with the Ge related activity, the

ISC process shows a non-Arrhenius behavior and the fluorescence emission at 4.1 eV follows a non-exponential decay in the temperature range $T \geq 100$ K.

The comparison of the optical activity associated with the two fold coordinated Ge suggests a significant role played by the spin-orbit term in the coupling of the vibrational modes of the lattice with the electronic transitions between states of different multiplicity, and shows that the dynamics and the disorder of the local environment is poorly affected by the iso-structural and iso-electronic substitution Sn-Ge. These results prove that the ISC processes in the B-type activity are not only related to the thermodynamic of the matrix-defect systems but involve also contributions depending on the structure of the defect.

# Chapter 6

# Role of the matrix: comparison between bulk and surface activity

In this chapter, we report a study on the surface variant of the Ge and Si related B-type activity to investigate the effects of local environment on the optical and dynamical features of the defect-matrix complex. For this aim, we compare in the fist section the surface and bulk Ge related activities, while, in the second section, the role of the environment on the heavy atom effect is investigated by comparing the surface Si and Ge activities.

## 6.1 Optical activity of surface two-fold coordinated germanium

Since a detailed investigation on the surface Ge related B-type activity has never been reported at our knowledge, we will deal in the first part of this section mostly with the experimental results on the surface $=Ge^{\bullet\bullet}$. The comparison with the bulk Ge related activity will be discussed in the second part.

### *6.1.1 Experimental results and discussion*

Figure 6.1 shows the optical activity of the Ge doped microporous silica specimen. The UV absorption at room temperature (panel (a)) is characterized by a clear OA band around

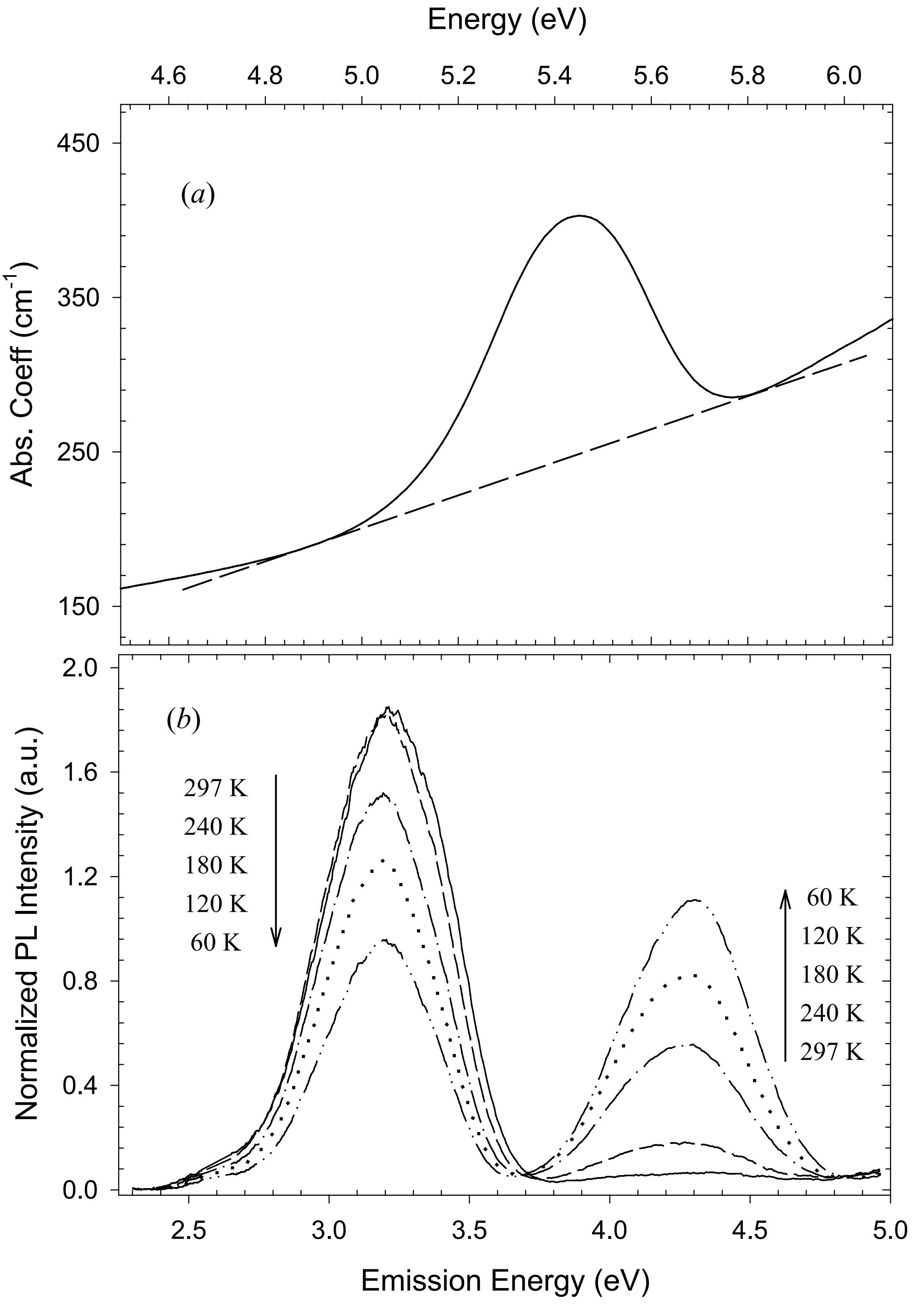

Figure 6.1. Optical activity of the surface =Ge$^{\bullet\bullet}$ centers. (a) Optical absorption spectrum at room temperature (the dashed line show the tangent to the minima). (b) Photoluminescence spectra varying the temperature from 297 K down to 60 K, under excitation energy at 5.21 eV. Arrows indicate the changes induced by decreasing the temperature. The spectra are normalized to the total area.

5.4 eV. By the subtraction of the tangent to the minima (see dashed line in figure), we isolated this band from the background obtaining the value of 155±5 $cm^{-1}$ for the band amplitude, 5.43 ± 0.01 eV for the peak position and 0.37 ± 0.01 eV for the FWHM. Excitation within this OA induces the two emissions reported in figure 6.1(b), which are peaked around 3.2 eV and 4.3 eV and characterized by a typical FWHM of 0.48. As reported by **Radzig**, **1995a**, this activity is related to the surface variant of the $=\mathrm{Ge}^{\bullet\bullet}$ center and it is described by the B-type energy level scheme in figure 1.4. In order to explore the excitation pathway of these emissions, we detected the PLE spectra at the maximum of both PL bands, obtaining in both cases, a single band around 5.4 eV, definitely distorted by excessive absorption (data not reported), which confirms the previous assignment.

We investigated the effect of temperature on the emission activity in the range 300 - 5 K, and a representative selection, under excitation at 5.21 eV, down to 60 K is reported in figure 6.1(b). No remarkable changing at lower temperature has been detected. As it occurs for the bulk activity, we have obtained that the sum of integrated intensities of the two PL bands is almost constant (data not reported), proving this result that also the surface activity is characterized by an unitary total quantum yield for the emission [**Skuja, 1992; Leone *et al.*, 2001**]. According with this result, the PL spectra in figure 6.1(b) are normalized to the total area, $M_{0S}+M_{0T}$. The opposite thermal behavior of the two emissions agrees with a thermally activated ISC process (see equation (2.16)). The temperature lowering induces on the spectral profile of the $\alpha_{\mathrm{Ge}}$ band a remarkable increasing of the amplitude with not significant changing in the peak position and in the width. The overall behavior of the $\beta_{\mathrm{Ge}}$ band, cooling the sample, is an halving of the amplitude down to 60 K with an initial red shift and a narrowing in the range 300-180 K. Below 60 K the $\alpha_{\mathrm{Ge}}$ and $\beta_{\mathrm{Ge}}$ band amplitudes are almost the same and temperature independent.

Following the usual methodological approach, we measured the PL bands performing a fine tuning of the excitation energy within the absorption band, to point out the presence of

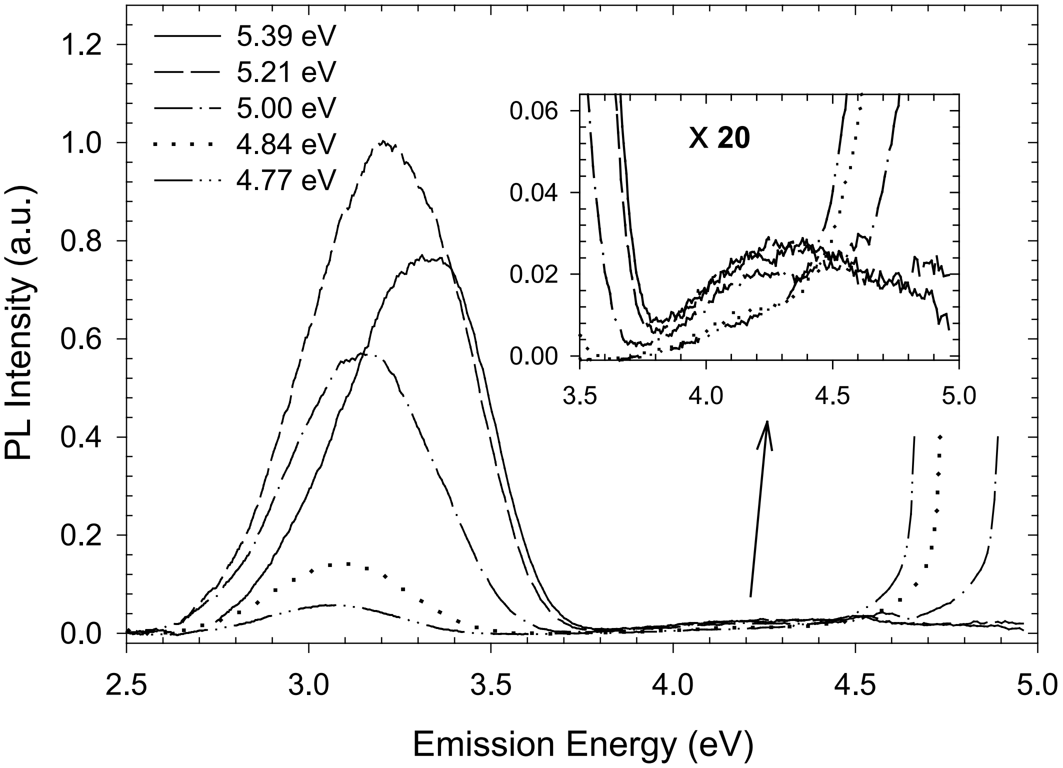

Figure 6.2. PL spectra as a function of excitation energy at room temperature for surface =Ge•• centers. The inset shows the range 3.5-5.0 eV in a magnified scale.

spectral heterogeneity in this sample. These measurements were collected at room temperature and 20 K. In figure 6.2 we show a representative selection of the observed luminescence spectra varying the excitation energy from 4.77 to 5.64 eV at room temperature. Regarding the singlet band, it is always almost 100 times smaller and, with excitation energies lower than 5.00 eV, it is nearly absent (see the inset in figure 6.2). On the other hand, we observe that the triplet band is characterized by a great blue shift increasing the excitation energy. Not so marked behavior for the band width is found. A more quantitative analysis, performed in terms of first and second(1) band moments, confirms these impressions reveling a monotonic increase of the triplet first moment from 3.05 to 3.30 eV and of the second moment from 0.033 to 0.049 eV$^2$, varying the excitation energy from 4.77 to 5.64 eV. We performed such analysis also for the singlet band obtaining 4.3 ± 0.1 eV for the first moment

---

(1) The second band moment is the variance of the corresponding PL band (see equation (7.1))

and 0.06 ± 0.02 $eV^2$ for the second moment. A typical value of 60 is found for the ratio of the triplet band area to the singlet one. The remarkable indetermination on the singlet band analysis results, due to the low intensity of the band, does not allow to appreciate any dependence on the excitation energy. However, the significant dependence of the triplet features reveals definitively that the surface $=Ge^{\bullet\bullet}$ is greatly affected by the local matrix, comparably with the bulk variant activity (see chapter 4). This results is not obvious if we consider that the expected more freedom degrees for the surface species could balance the conformational distortion induced by the local surroundings. Furthermore, the role of the matrix for the Ge related surface B-type activity is evidenced by a relevant coupling with the local surroundings, as proved by a huge Stoke shift of 1.1 eV, being this feature common to the bulk variant.

To corroborate the assignment of the emission bands at 4.3 and 3.2 to a singlet-singlet and triplet-singlet transition, respectively, we recorded the time decay of both emissions. We performed these measurements at cryogenic temperatures to freeze any thermally activated non radiative channel and to have a significant $\alpha_{Ge}$ band amplitude. In figure 6.3(*a*) and (*b*) we report the time decay of the $\alpha_{Ge}$ and $\beta_{Ge}$ band maxima, respectively, at 8.5 K under excitation at 5.21 eV. Both decays show an almost single exponential behavior as evidenced by the straight lines in figure, which are the results of a fitting procedure in terms of a single exponential decay law. The obtained lifetime values for the $\alpha_{Ge}$ and $\beta_{Ge}$ emissions are 2.0 ± 0.1 nsec and 69 ± 3 μsec, respectively. These results prove definitively the previous associations of the $\alpha_{Ge}$ and $\beta_{Ge}$ bands to a singlet-singlet and a triplet-singlet transition, respectively. We performed the same measurement on the $\beta_{Ge}$ band at room temperature, obtaining the same behavior, i.e. a single exponential decay with a value of 72 ± 3 μsec for the $\boldsymbol{T_1}$ lifetime. This result proves certainly the absence of any (thermally activated) non radiative relaxation process from $\boldsymbol{T_1}$ to $\boldsymbol{S_0}$; in agreement with the previous comments about the

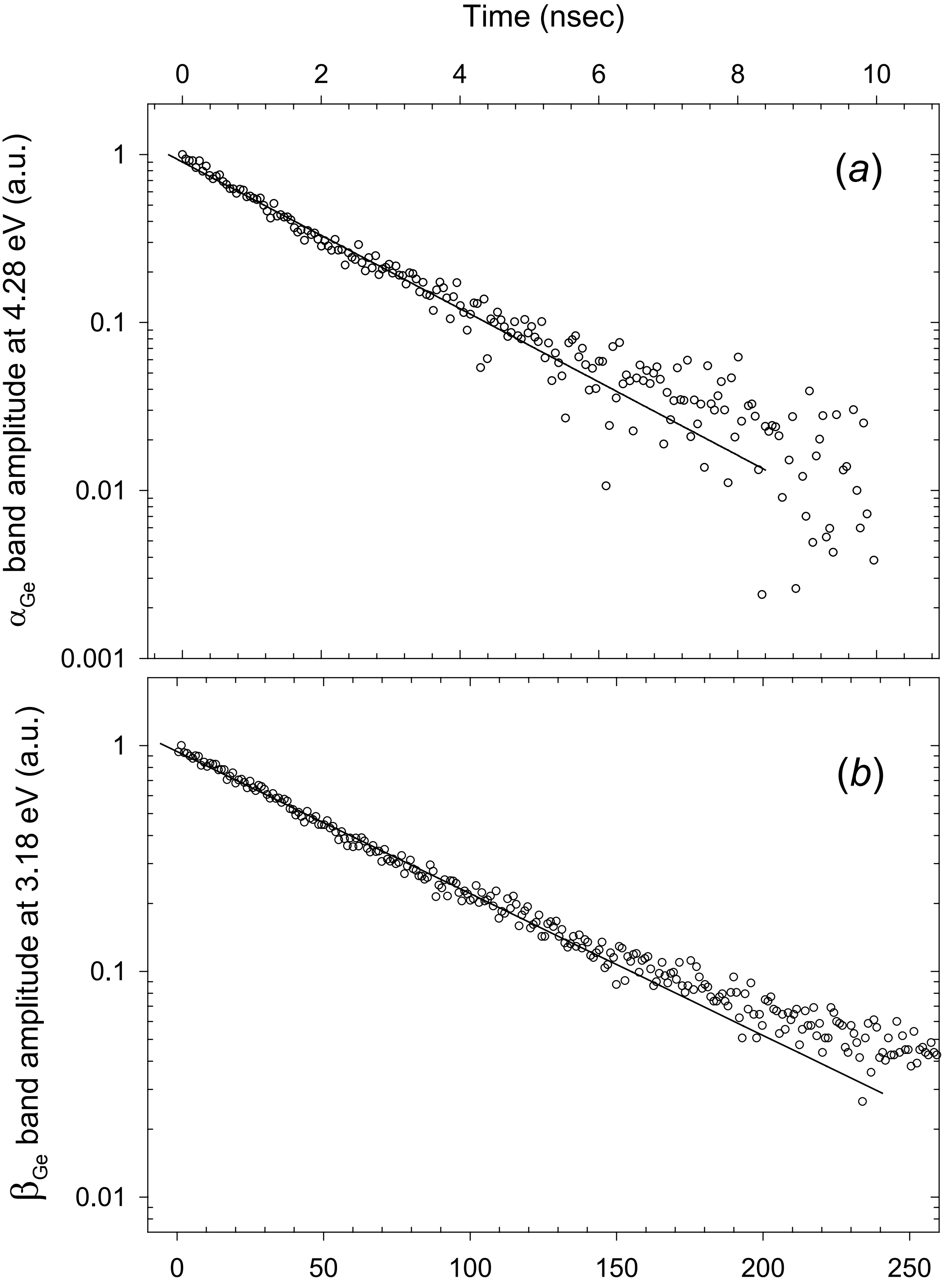

Figure 6.3. Time decay of PL emissions at 4.28 eV (*a*) and 3.18 eV (*b*) at 8.5 K, under excitation at 5.21 eV. The straight lines are the fitting of a single exponential decay law to the data in the first decade of the decay range

temperature effects on total area of the two emissions. As a consequence of these two results also the absence for $\boldsymbol{S_1}$ of any (thermally activated) non radiative relaxation channel to $\boldsymbol{S_0}$ is indirectly confirmed. Regarding the $\alpha_{Ge}$ time decay at room temperature, we were not able to detect any clear signal. A final remark on the obtained value of 2.0 ± 0.1 nsec for the $\boldsymbol{S_1} \rightarrow \boldsymbol{S_0}$ transition: considering the huge efficiency of the ISC process also at cryogenic temperature, the respective value of $(0.50 \pm 0.03)\times10^9$ sec$^{-1}$ for the decay rate $k$ of $\boldsymbol{S_1}$ has not to be considered as a good measurement for the radiative rate $k_S$ of the $\boldsymbol{S_1}\rightarrow\boldsymbol{S_0}$ transition. Assuming the relation $k = k_S + k_{ISC} = k_S(1+\zeta)$ (see equation (2.45)) valid, a better estimation can be achieved by correcting with the factor $(1+\zeta)$ calculated with the value of $\zeta$ at 10 K and excitation energy of 5.21 eV, found from the analysis of PL emission in figure 6.1(b). The obtained estimation for $k_S$ is $(0.26 \pm 0.02)\times10^9$ sec, corresponding to a value of 3.8 ± 0.4 nsec for the radiative decay time. We note that, also after the correction, it still remain smaller than the respective value of 7.8 ± 0.2 nsec for the bulk activity. It is worth to note that, in our experience, this correction is not usually exact. The value obtained by correction, even if closer to the real one, has to be considered more as typical value. Since a good estimation of $k_S$ is essential to calculate the ISC rate $k_{ISC}$ from the ISC relative efficiency, $\zeta$, we preferred to show the data in this chapter as $\zeta$ instead of $k_{ISC}$.

In figure 6.4 the dependence of $\zeta$ on temperature under excitation at 5.21, 5.00 and 4.84 eV is reported on a Arrhenius plot. These results, in agreement with the observed behavior of bulk activity, do not obey the expected Arrhenius behavior in the whole temperature range. Accordingly with data in figure 6.1(b), we observe that, at the three excitations, $\zeta$ decreases on lowering the temperature down to 60 K and tends to a constant value at lower temperatures. It is worth to note that this constant behavior, close to the unity below 60 K, reveals the presence of effective temperature independent ISC processes (see paragraph 2.2 and chapter 5). The presence of a linear regime in the range 300-220 K allows a quantitative analysis of the thermodynamic parameters of the ISC process by fitting the data in this range with an Arrhenius law (see equation (2.47)). Since the data at different

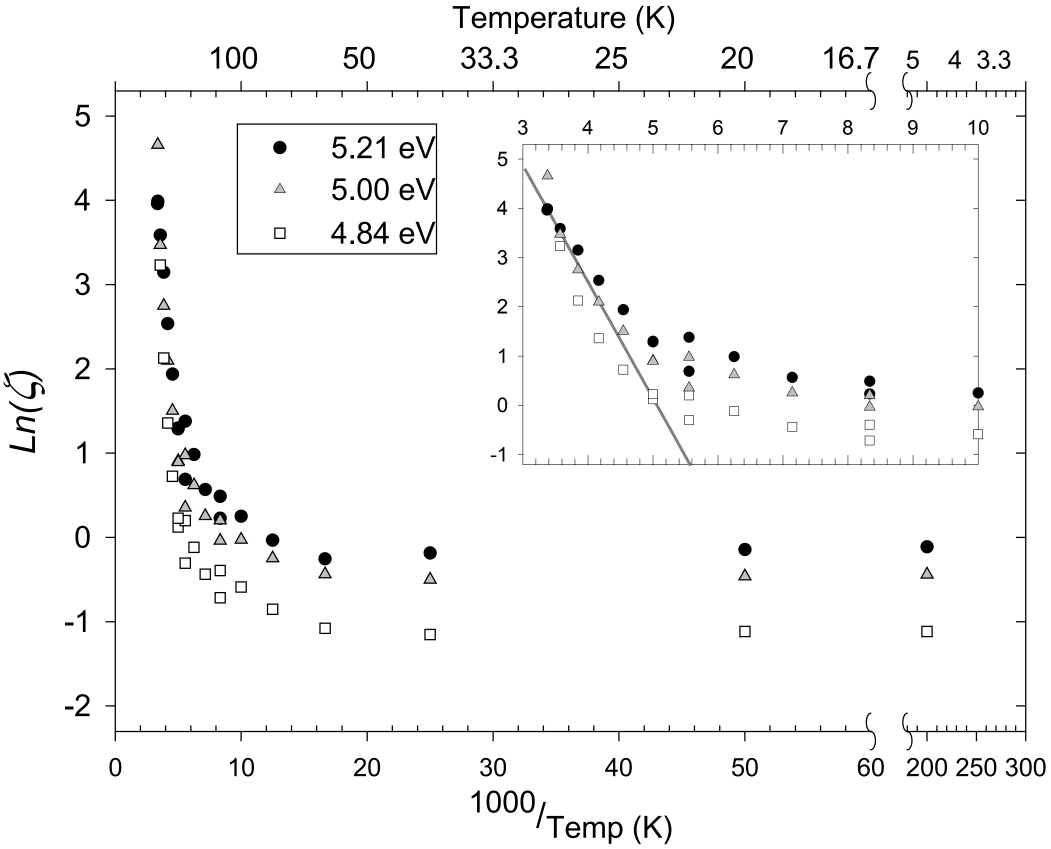

Figure 6.4. ISC relative efficiency ζ as a function of temperature, exciting at 5.21, 5.00 and 4.84 eV, for surface =Ge•• centers. In the inset the range 333 -100K is shown. The solid line is obtained by fitting an Arrhenius law (see equation (2.47)) to data in the range 300-220 K.

excitations are significantly overlapping, we will consider them as a unique set during the fitting procedure, obtaining $\Delta H = 0.23\pm0.05$ eV and $Ln(K_E) = 13\pm3$. The straight line in figure 6.4 is the fitting outcome. These results reveal that, as for the bulk activity, the main role in the ISC process is played by the total pre-exponential factor $k_E$. How the local matrix affects these parameters will be discussed by comparison with the bulk activity related ones. We note that a small excitation dependence is observed: ζ increases on increasing excitation energy, this effect being less pronounced on raising the temperature.

The comparison with the bulk activity is reported in figure 6.5, where we show the observed luminescence activity at room temperature, under excitation at 5.21 eV and normalized at the maximum of triplet band, in both samples. A relevant difference regards the relative amplitudes of the two bands: in the case of bulk activity the singlet band is 5 times

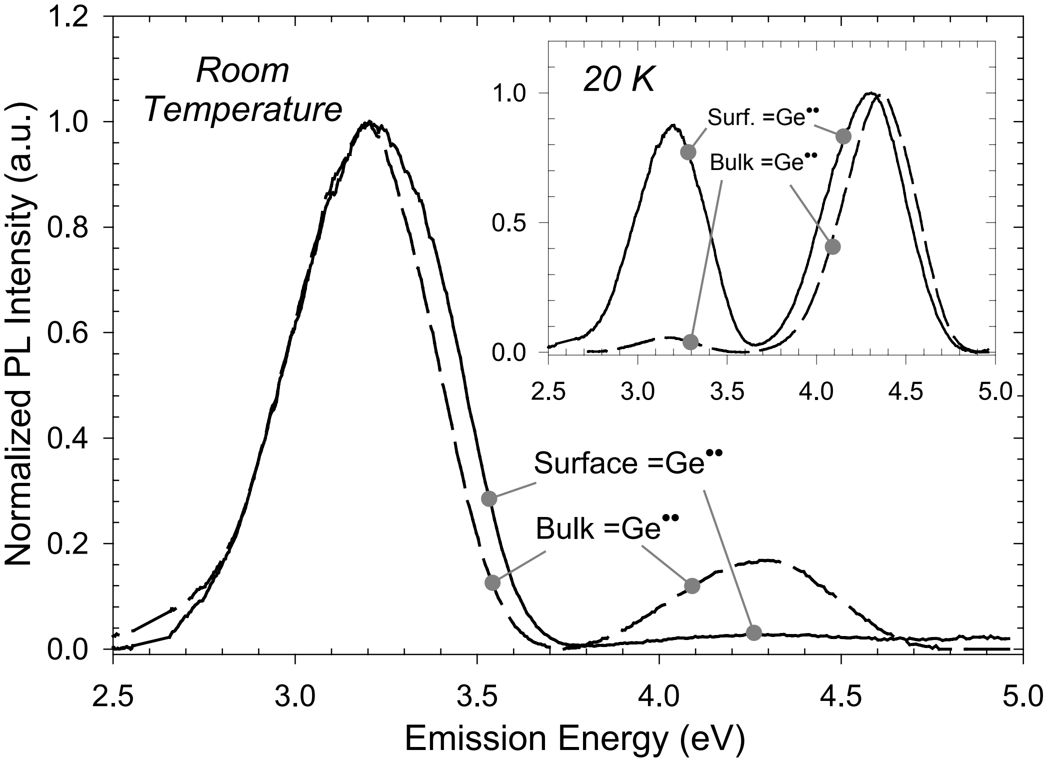

Figure 6.5. PL spectra at room temperature under excitation at 5.21 eV for surface (straight line) and bulk (dashed line) B-type activity. The spectra are normalized at 3.2 eV. The inset shows the same measurements at 20K and normalized at 4.3 eV.

smaller than the triplet one; for the surface activity the singlet band is 70 times smaller (see inset in figure 6.2). We observe also a relative red-shift and a narrowing of the triplet band in the bulk activity. The inset in figure 6.5 shows the same spectra at 20 K, where the ratio of the $\beta_{Ge}$ band amplitude to the $\alpha_{Ge}$ one for the bulk and surface activity are 0.05 and 0.9, respectively. So, in agreement with equation (2.45) and assuming similar values of $k_S$ for the two activities, the surface defects related ISC process is found ~15 more efficient than bulk ones, both at room and at cryogenic temperature. Concerning the OA band at room temperature, the comparison with data in figures 4.1 and 6.1(a) reveals a significant blue shift of the surface activity band, respect to the bulk one, of 0.28 ± 0.02 eV and a clear narrowing, from FWHM = 0.49 ± 0.01 eV to 0.37 ± 0.01 eV, for the surface activity.

The comparison of the ISC efficiency varying the temperature in the range 300-3 K and under excitation at 5.21 eV, is reported in figure 6.6 on a Arrhenius plot. In agreement with data in figure 6.5, we observe that the surface related ISC efficiency is one order of magnitude greater than the bulk related one in the whole investigated range, this effect being more pronounced on lowering the temperature. It is remarkable that both systems show the similar behavior on cooling the system, with a initial strong decrease followed by a plateau. As already discussed, a non Arrhenius behavior speaks for the presence of an inhomogeneous spread of activation barriers. In this respect, we observe that the two set of data are not simply scaled but show different behaviors. In particular, $\zeta$ for the surface activity shows a faster decrease and reaches the constant value already below 100 K. The decrease of $\zeta$ for the bulk activity is slower and continues down to 40 K. This behavior suggests that the distribution of activation barriers for the bulk center is characterized by a relevant contribution toward low value of $\Delta H$ ~3 meV (corresponding to 40 K), instead of the surface activity which looks to

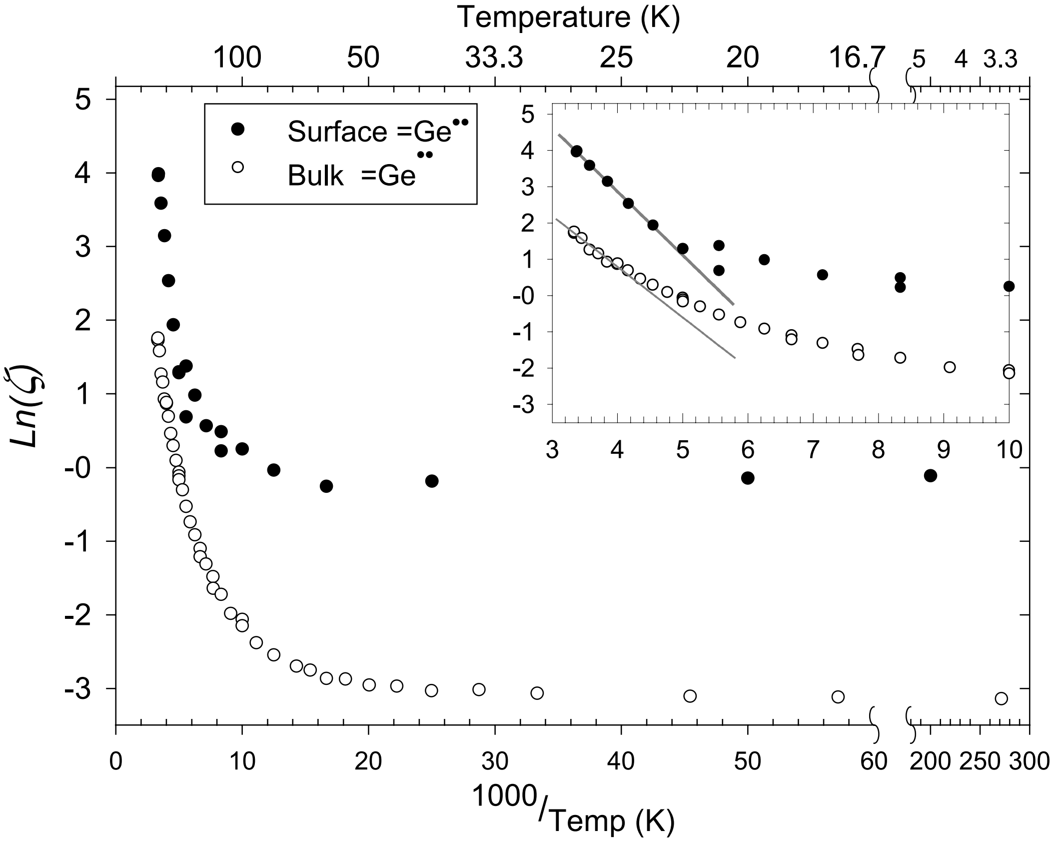

Figure 6.6. ISC relative efficincy $\zeta$ as a function of temperature, for surface (full marks) and bulk (open marks) $=Ge^{\bullet\bullet}$ centers, under excitation at 5.21 eV. In the inset the range 333-100 K is shown. The solid lines are the results of fitting an Arrhenius law (eq.(2.47)) to data in the range 300-220 K.

be constituted by centers with activation barriers greater than ~10 meV (corresponding to 120 K).

In table 6.1 we report the outcomes of the analyses of the linear behavior in the high temperature range in terms of an Arrhenius law (equation (2.47)) for both systems (see table 4.2). In the inset of figure 6.6 we show the related results of these fittings. These parameters indicate that the primary role in the ISC process for both activities is played by the total pre-exponential factor $k_E$. In the case of the surface activity, it increases so much, with respect to the bulk one, to balance, and even to exceed, the rising of the activation barrier. Furthermore, the comparison corroborates a shift toward higher barriers for the surface activity. This result suggests that the thermally activated ISC rates are competitive with the temperature independent one down to 40 K, whereas the surface activity looks to be dominated by the latter ones still at 100 K. It worth to note that a thermal behavior, which is not simply scaled, strongly suggests that the barrier distribution governing the ISC process is not the same in the two systems.

In the light of the results on bulk activity, it is not surprising the presence of a plateau zone also for the surface activity. The data in figure 6.6 indicate, indeed, the presence of temperature independent contributions to the ISC rate related to the surface activity, which are almost two orders of magnitude more effective than the bulk related ones. It is less

Table 6.1. Activation barrier $\Delta H$ and ratio of the total pre-exponential factor $k_E$ to the pure radiative $\boldsymbol{S_1}$ decay rate $k_S$, obtained by fitting the data of figure 6.4 in the range 300-220 K with an Arrhenius law (equation (2.47)). $\zeta_{T\approx 0K}$: value of $\zeta$ in the plateau zone (T < 30 K). For comparison purpose, the respective data for the bulk $=\mathrm{Ge}^{\bullet\bullet}$ centers are reported.

| B-type Activity | $k_BT > 20$ meV | | $k_BT < 3$ meV |
|---|---|---|---|
| | $\Delta H$ (eV) | $Ln(k_E/k_S)$ | $\zeta_{T\approx 0K}$ |
| Surface $=\mathrm{Ge}^{\bullet\bullet}$ | $0.23 \pm 0.05$ | $13 \pm 3$ | $0.65 \pm 0.03$ |
| Bulk $=\mathrm{Ge}^{\bullet\bullet}$ [a] | $0.125 \pm 0.008$ | $6.5 \pm 0.4$ | $0.044 \pm 0.008$ |

[a] from table 4.2 and $\zeta = k_{ISC}/k_S$.

foreseeable why non thermally activated processes should be so dramatically affected by modification of the local matrix. It is also more surprising that not so much remarkable alterations are found in the other features of the luminescence activity as the spectral positions and the shapes of the PL bands. To point out how the local matrix affects the different spectroscopic features, we compared the energy excitation dependence of both activities at room temperature and 20 K.

In figure 6.7 we report the relative ISC efficiency $\zeta$ for the surface and the bulk activity as a function of excitation energy at room temperature and 20 K. We observe that the latter activity shows an evident dependence on excitation energy at variance to the former one, this difference being more pronounced on lowering the temperature. As previously underlined, the analysis of the luminescence spectra at room temperature revealed that the poor dependence of surface related $\zeta$ on excitation energy does not correspond with the behavior of the $\alpha_{Ge}$ and

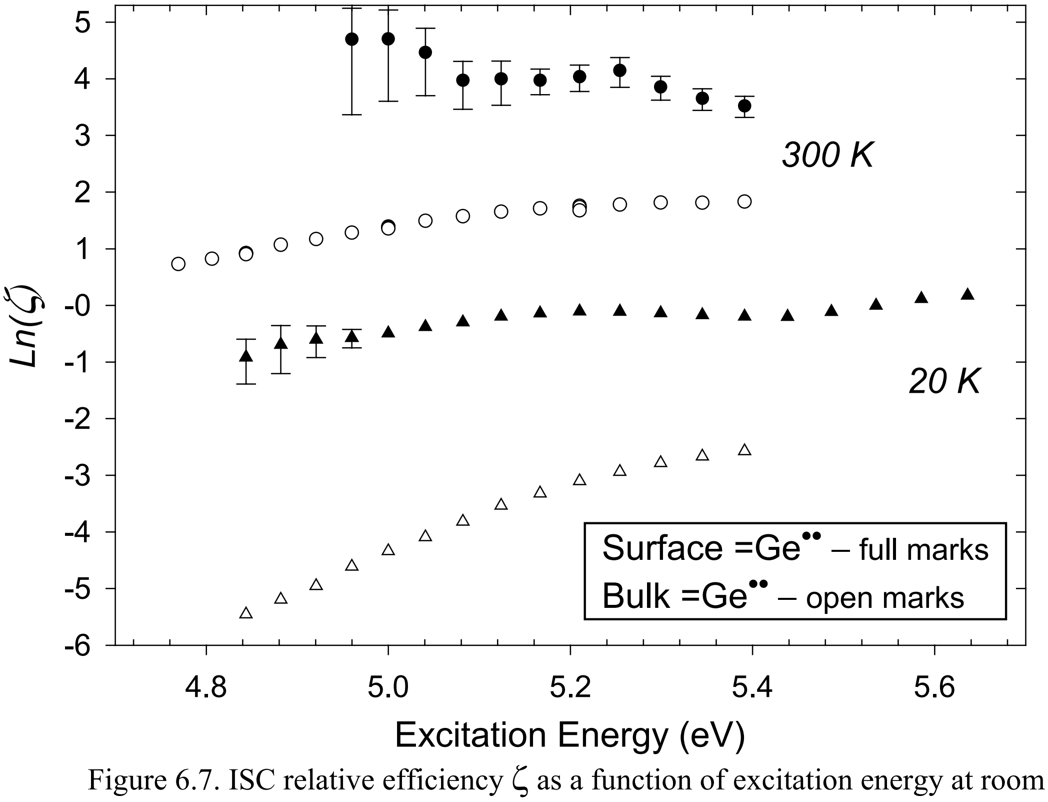

Figure 6.7. ISC relative efficiency $\zeta$ as a function of excitation energy at room temperature and 20 K, for Ge related surface and bulk B-type activity. Circles: 300 K; triangles: 20 K. Open marks refer to the surface activity; full marks refer to the bulk one. Error bars are reported only if greater than mark size.

$\beta_{Ge}$ band optical properties. We observed the same behavior also at low temperature (20 K), where both the singlet and the triplet bands show a sizeable and comparable dependence on excitation energy both in bulk and surface activities (data not reported), in contrast with the nearly independent behavior of the surface related ISC efficiency $\zeta$.

## 6.2 Optical activity of surface two-fold coordinated silicon

### *6.2.1 Experimental results and discussion*

In figure 6.8 we report the optical activity in the un-doped microporous silica sample. In the panel (a) the UV absorption spectrum in the range 4.5-6.1 eV at room temperature shows a relevant OA band around 5.2 eV. As it is distorted by excessive absorption, no further analysis can be done. We compare it with the OA spectrum for the bulk activity measured on a commercial specimen of natural dry silica (QC by Starna Ltd, Romford, England). It is clearly shifted ~0.2 eV toward smaller energy, in agreement with **Skuja *et al.*, 1984**. In the panel (b) we show the observed luminescence activity normalized at the maximum of the singlet band and excited at 5.21 eV. Two evident emissions are detected at 4.42 ± 0.02 eV and at 2.75 ± 0.02 eV and with a FWHM of 0.58 ± 0.01 eV and 0.35 ± 0.02 eV, respectively. As reported by **Skuja *et al.*,1984**, and **Radzig, 1995a**, this optical activity is associated with the surface variant of the $=\mathrm{Si}^{\bullet\bullet}$ center and it is properly described by the general B-type activity energy levels scheme. The comparison with the bulk related emission activity, excited in the same commercial specimen of panel (a) at 4.80 eV, reveals that the more evident difference consists in the amplitude of the triplet band, which is clearly detectable in the case of surface activity, whereas in the bulk activity it is nearly absent. The analysis of spectra in figure 6.8(b) shows that, the area of the surface $\beta_{Si}$ band is 7 times smaller than the related $\alpha_{Si}$ band one, whereas the bulk $\beta_{Si}$ band is 90 times smaller that the respective $\alpha_{Si}$ band. It means

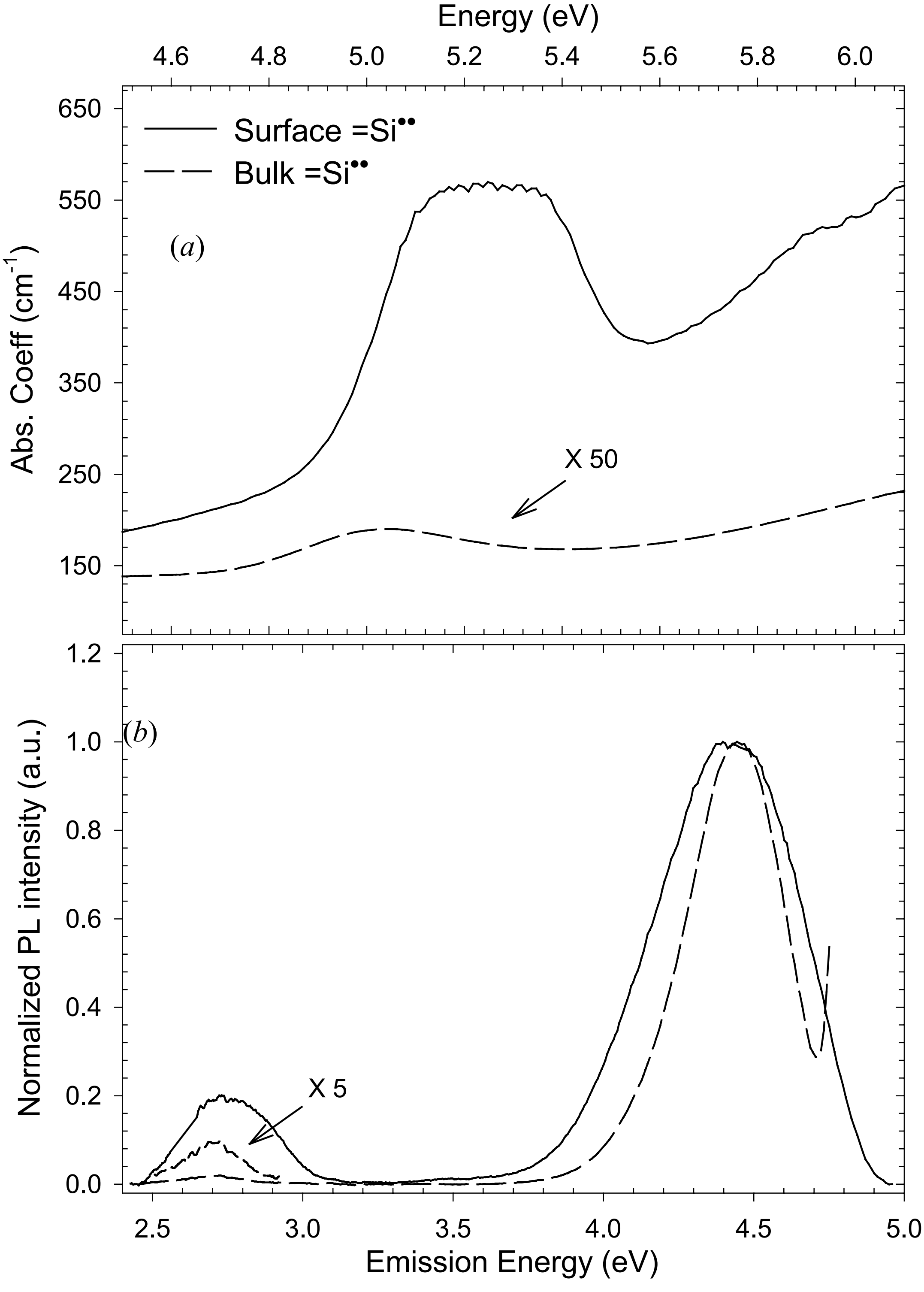

Figure 6.8. (a) Optical absorption spectrum at room temperature for the surface =Si•• centers. The spectrum is distorted by excessive absorption in the range 5.1-5.4 eV. (b) Related luminescence spectrum under excitation at 5.21 eV. For comparison purpose, the $B_{2Si}$ band and the PL bands exciting at 4.80 eV for bulk activity are reported. The PL spectra are normalized at 4.4 eV.

that the surface variant is characterized by a ISC relative efficiency one order of magnitude more effective that the bulk one, in agreement with the results on the Ge related activity.

Other sizeable differences are found in the width both of the $\alpha_{Si}$ and of the $\beta_{Si}$ bands. We observe, indeed, that the overall bulk activity is significantly narrower than the surface one, as already noted for the comparison of the bulk and surface =Ge•• centers (see figure 6.5 and relative comments).

The role of the local disorder is investigated by a detailed analysis of the emission bands with a fine tuning of the excitation energy within the OA band. In figure 6.9 a representative selection of the observed luminescence spectra, varying the excitation energy from 5.38 to 4.77 eV at room temperature, is shown. The singlet band does not show a monotonic behavior, whereas the triplet band is characterized by a blue shift on increasing the excitation energy. A less marked behavior for the band width is found. Regarding the relative amplitude of the $\beta_{Si}$ band with respect to the $\alpha_{Si}$ band, it decreases from ~1 down to ~0.1 heightening the excitation energy.

We investigated also the thermal behavior of the emission spectra in the range

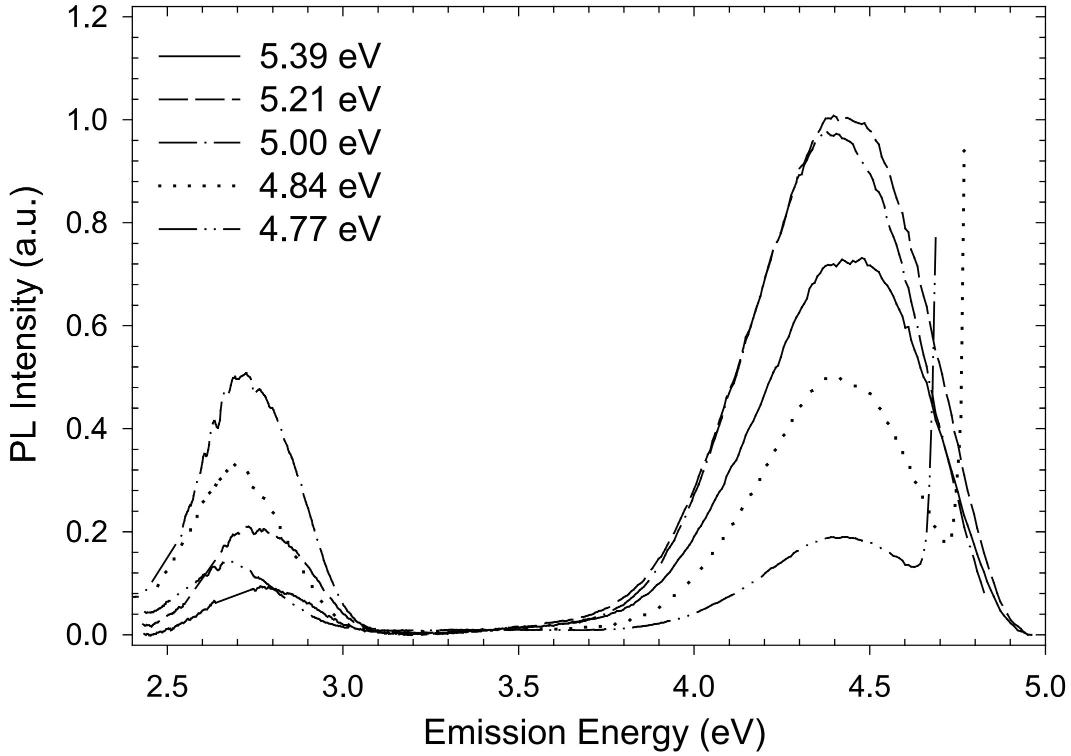

Figure 6.9. Luminescence spectra at room temperature under excitation at different energies for surface two-fold coordinated silicon.

296 K ÷ 5 K. A representative selection of PL spectra down to 60 K is reported in figure 6.10, taken exciting at 5.00 eV and normalized for the total area. No more changes are induced at lower temperatures. As expected, on cooling the system, the singlet band increases and the triplet one decreases, maintaining an almost constant total area in the whole temperature range. This results corroborate definitely that the feature of a total emission quantum yield close to the unity is a general characteristic of the B-type activity, regardless the particular iso-electronic defect and the local matrix. Concerning other effects on the optical properties, no clear dependence on the temperature of the spectral profiles of both emissions was found.

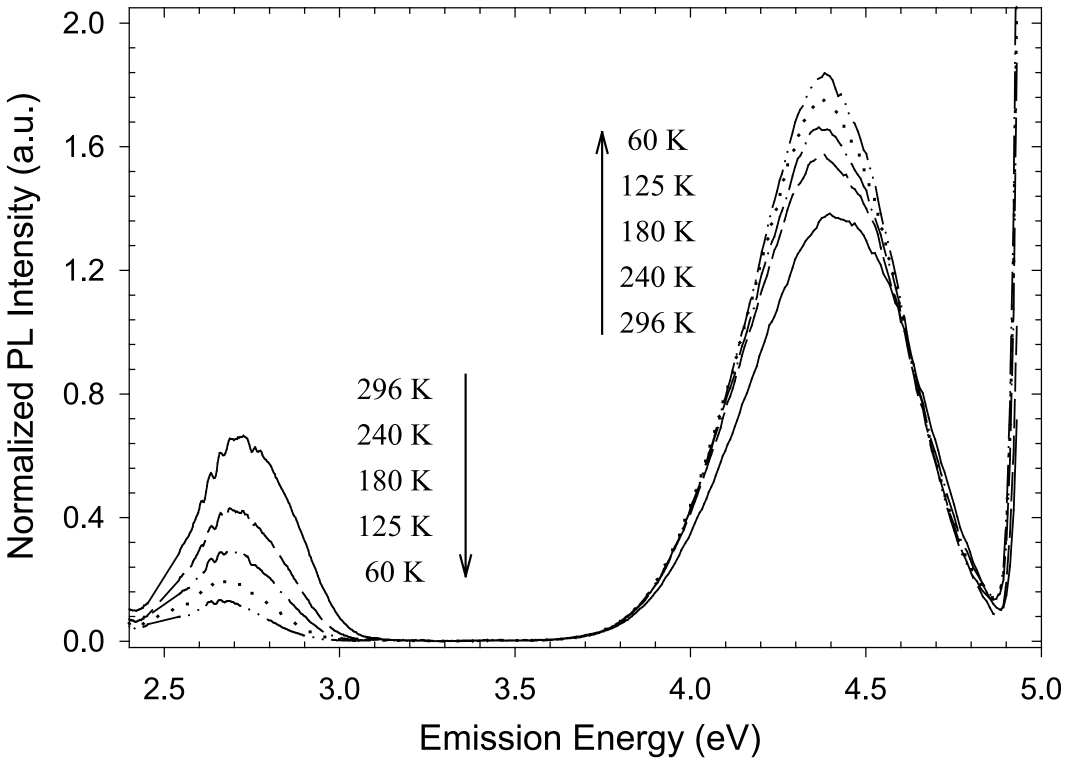

Figure 6.10. Photoluminescence spectra varying temperature from 296 K down to 60 K, under excitation energy at 5.00 eV, for surface Si related B-type activity. Arrows indicate the changes induced by decreasing the temperature. The spectra are normalized to the total area.

In figure 6.11 it is reported, on an Arrhenius plot, the ratio of the triplet area to the singlet one $\zeta$ varying the temperature from 300 K to 5 K and exciting at 4.84, 5.00 and 5.21 eV (in the inset we show, in details, the high temperature range). We observe an initial decrease of $\zeta$ on lowering the temperature and, finally, a constant value below 120 K. This non Arrhenius

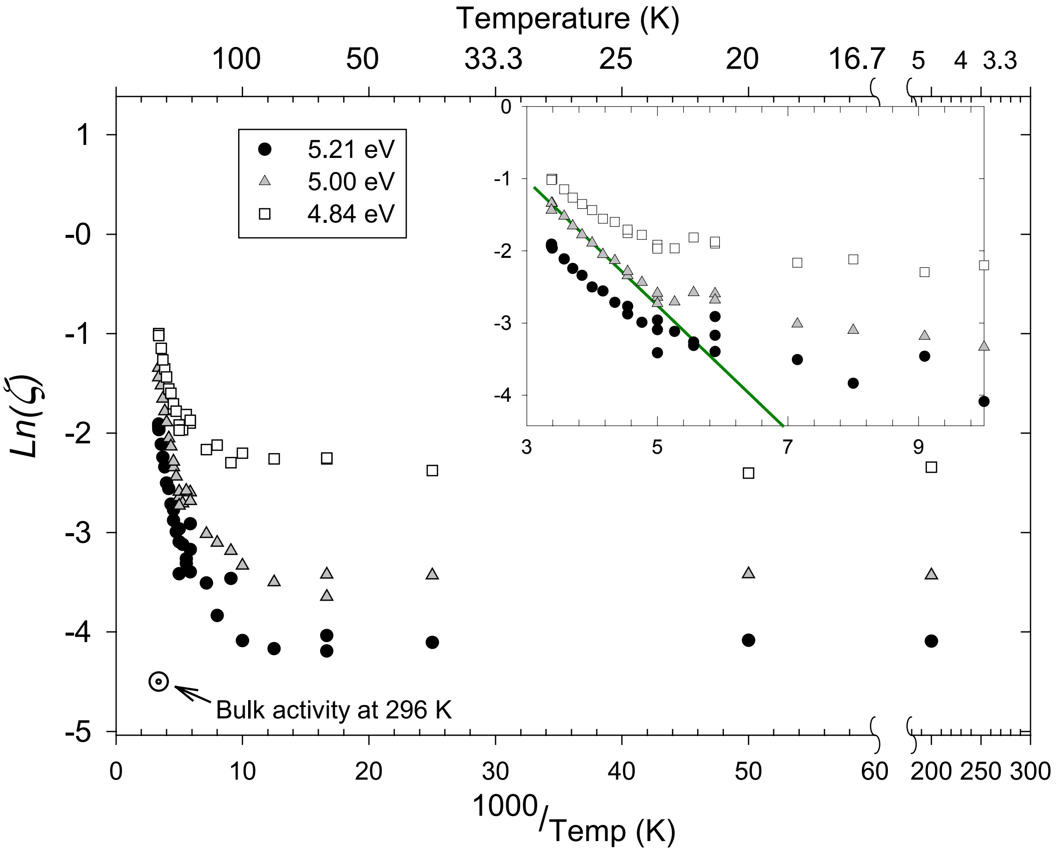

Figure 6.11. ISC relative efficiency ζ as a function of temperature, exciting at 5.21, 5.00 and 4.84 eV for surface =Si•• centers. The value for the bulk =Si•• centers at room temperature is reported. In the inset it is shown the range 333-100 K. The solid line is a rappresentative fitting of an Arrheius law (equation (2.47)) to the data in the range 300-220 K.

behavior confirms the presence of inhomogeneous spread of the activation barriers in these systems, as pointed out by **Radzig, 1995a**. On the basis of the linear behavior observed in the range 300-220K, we estimate the activation barrier $\Delta H$ and the ratio $k_E/k_S$ accordingly to the Arrhenius law in equation (2.47). We obtain $\Delta H = 0.07 \pm 0.01$ eV, regardless the excitation energy, and $ln(k_E/k_S)$ varying from 2 to 1 on increasing the excitation energy. So, we can state that also for this variant of the B-type activity the ISC process is mainly driven by the pre-exponential factor, which reveals itself to be more sensitive to the excitation energy with respect to the activation barrier.

It is worth to note that a clear decreasing of the ISC efficiency with the energy is observed, being this behavior maintained in the whole investigate temperature range. A more detailed analysis on the excitation dependence of the ISC relative efficiency is reported in

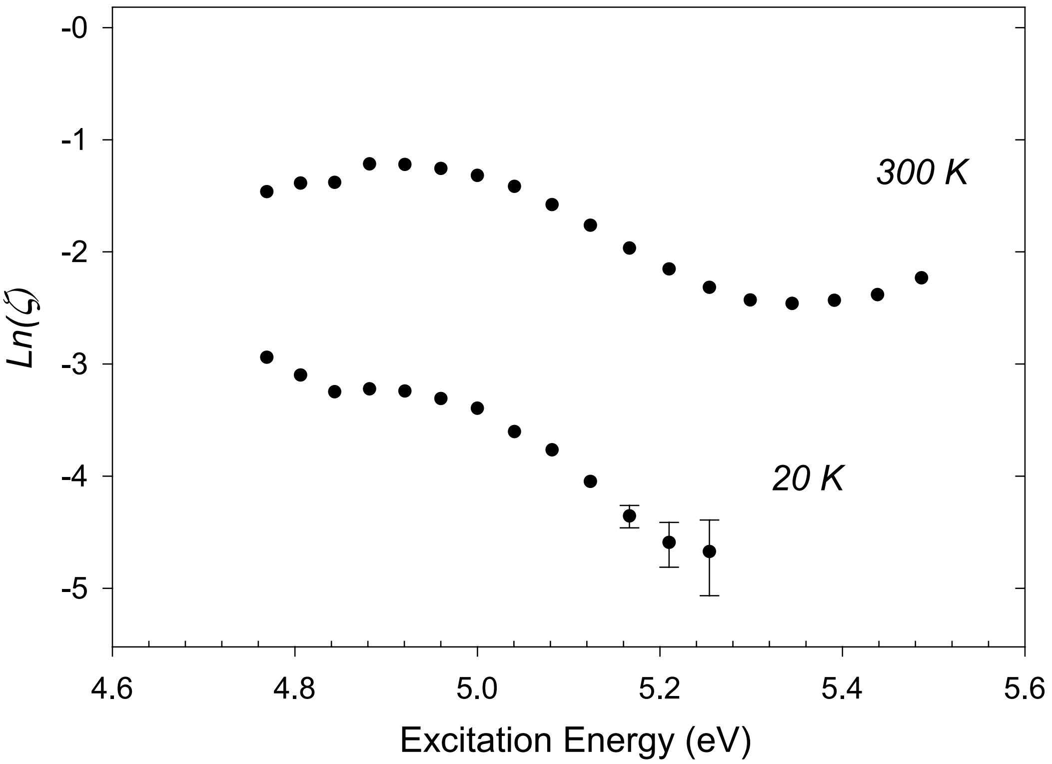

Figure 6.12. ISC relative efficiency ζ as a function of excitation energy at room temperature and 20 K for Si related surface B-type activity. Error bars are displayed only if greater than mark size.

figure 6.12, where the values of ζ are reported at room temperature and at 20 K, finely varying the excitation energy within the absorption band. The observed opposite behavior of the ISC efficiency with the excitation energy is confirmed in the whole range. We want to stress that this result is quite unexpected if we consider that not only both surface and bulk Ge related activities but also the Sn related bulk one have an opposite behavior. Furthermore, we observe that the two sets of data follow the same behavior almost scaled for a constant factor. This result suggests that the main difference, exploring the defect distribution by fine excitation energy tuning, occurs more in the pre-exponential factor than in the activation barriers. This hypothesis agrees with the outcomes for $\Delta H$ and $k_E/k_S$ by fitting the data in the range 300-220 K, where a clear dependence on excitation energy was found only for the pre-exponential factor. It is worth to note that, as observed for the Ge related surface activity, the different local surrounding affects not only the thermally activated ISC mechanisms but also the temperature independent ones.

The effects of the temperature on the $S_1$ time decays are shown in figure 6.13, where the time dependence of the PL intensity at 4.28 eV under excitation at 5.2 eV is reported as a function of temperature from 8.5 to 300 K. The small fluctuation around 17 nsec, and present in all the curves, is a meaningless artifact of the experimental set-up. As evidenced by the semi-logarithmic scale, the decay kinetics obey to a single exponential law (2) for almost all the temperature range with a small decreasing of the slope over 260 K. A slight non exponential character can be observed only at room temperature. To point out if a distribution of relaxation rates affects the decay process, we detected the emission decays at different excitation energies. A representative selection of these measurements are reported in the insets of figure 6.13: in the upper one the data a 8.5 K are reported, in the lower one the decay curves at room temperature are shown. In the latter case a small but clear decrease of the slope increasing the excitation energy is observed. At variance, at low temperature, no significant dependence on the excitation energy is found. To make a quantitative analysis, we calculated the lifetime $\tau$ of each decay curve as the time to have a reduction to $e^{-1}$ of the initial signal. In figure 6.14 we report the data for the temperature dependence. We observe an initial increase of the decay time value down to 200 K and then, below this temperature, we have no more changes. It is worth to note that such behavior is not found for the Si related bulk activity, where $\tau$ is almost constant in all this temperature range [**Boscaino *at al.*, 1996**]. Similar considerations can be done for the excitation dependence reported in figure 6.15 at 300 and 8.5 K. We find, indeed, a significant dependence at room temperature on the contrary

---

(2) The small decrease of the slope at $t > 20$ nsec is imputable to a small contribution due to the presence of a small Ge related B-type activity in the sample container, as evidenced by measurements on the empty container.

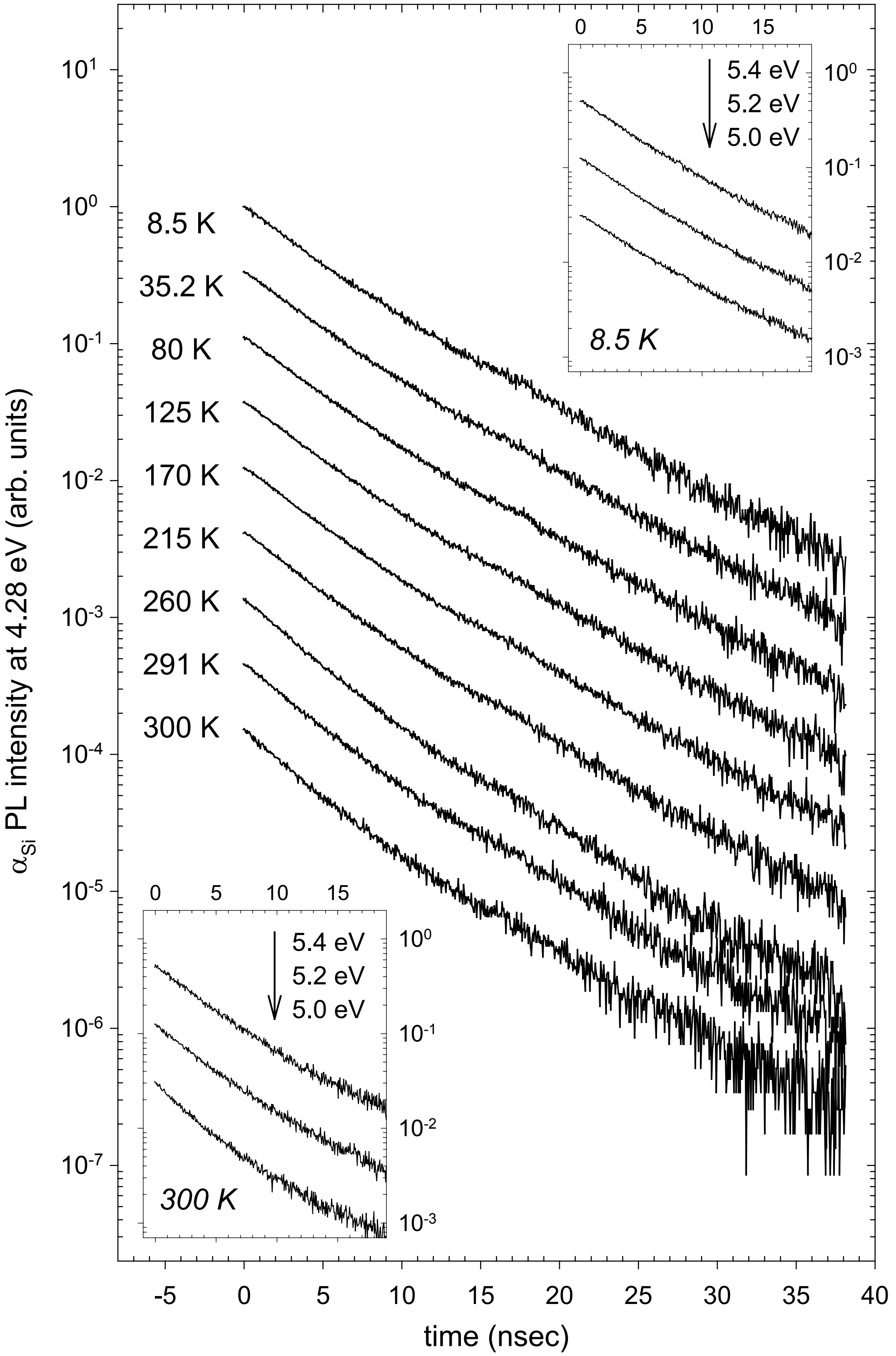

Figure 6.13. Decay kinetics of 4.28 eV emission for the Si surface activity detected under pulsed excitation at 5.2 eV as a function of temperature from 8.5 up to 300 K. In the upper and lower insets it is reported the comparison among the time decays at T = 8.5 K and 300 K, respectively, for three excitation energies: 5.00, 5.21 and 5.39 eV. For viewing purposes, the decay curves are arbitrary scaled.

of the bulk activity [**Nishikawa *et al.*, 1997**], while an almost constant behavior is recovered at low temperature. It is remarkable that, as for the ISC behavior in figure 6.12, the $\tau$ dependence on the excitation energy is opposite to the dependence found for the Ge and Sn related activities, where the significant dependence on temperature and excitation energy was rationalized as an effect of the ISC rate $k_{ISC}$ that, increasing the temperature, becomes competitive with the radiative $\boldsymbol{S_1}$ lifetime $k_s$. The comparison of the Si related bulk and surface activities prove definitely the goodness of this explanation. Furthermore, this result is corroborated by the excitation dependence at room temperature of $\tau$ which, accordingly with $k = k_{ISC} + k_S$ and with the ISC behavior at room temperature (see figure 6.12), decreases with the excitation energy. In agreement with the previous picture, this result is an effect of the opposite behavior of the Si surface ISC process respect to the Ge and Sn related ones. A further proof is that the value of 5.15 ± 0.05 nsec for $\tau$ at low temperature is consistent with

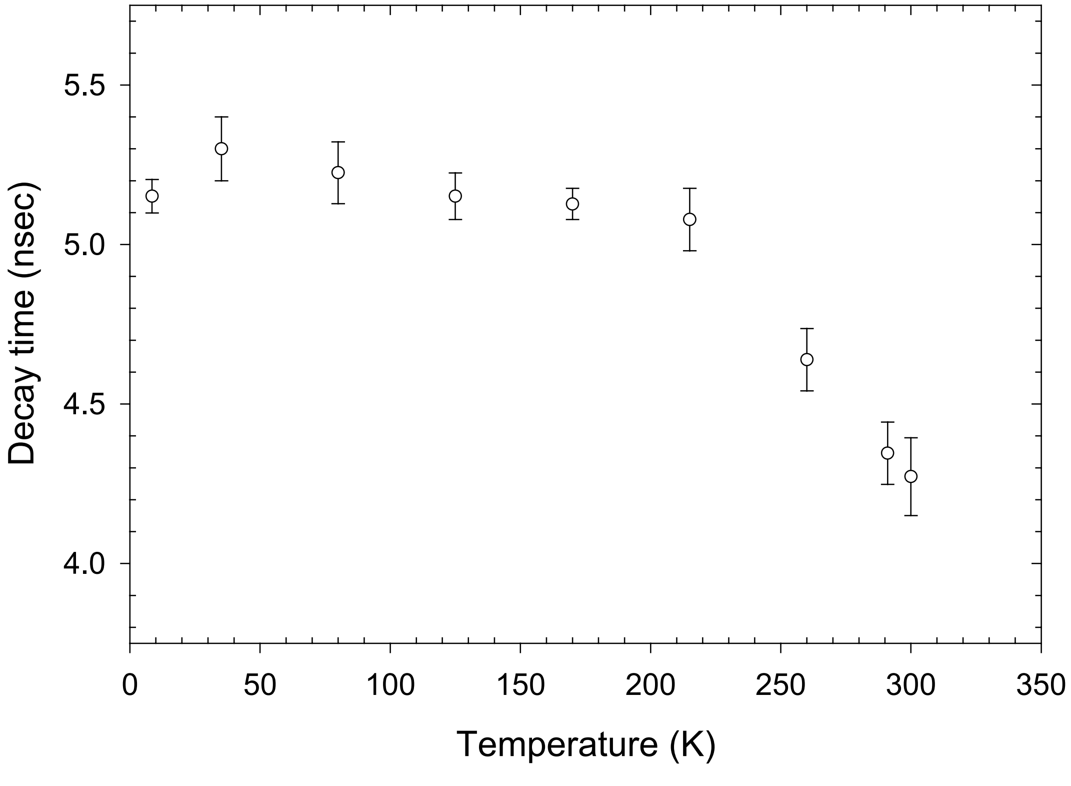

Figure 6.14. Surface related $\alpha_{Si}$ emission decay time, determined as the time needed to reduce the amplitude to 1/e of its initial value, as a function of temperature upon excitation energy at 5.2 eV

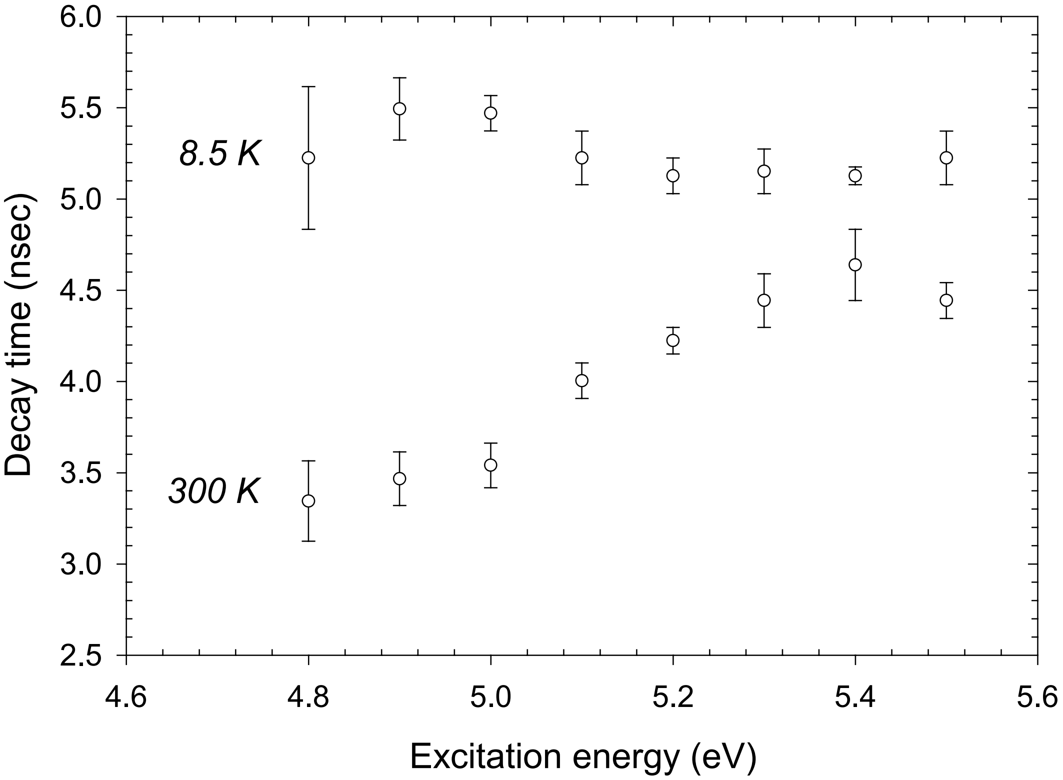

Figure 6.15. Surface related $\alpha_{\mathrm{Si}}$ emission decay time, determined as the time needed to reduce the amplitude to 1/e of its initial value, as a function of excitation energy at room temperature and 8.5 K.

the value of 4.8 ± 0.1 nsec for the Si related bulk one [**Boscaino *et al.*,1996**]

The effects of the iso-electronic Si-Ge substitution for surface activity are shown in figure 6.16, where the ISC relative efficiency $\zeta$ for the Si and Ge related B-type activity as a function of temperature under excitation at 5.00 and 5.21 eV, respectively, are reported. Likewise the comparison of Ge and Sn related bulk activity, we compare data obtained exciting in the same relative position respect to the absorption band. We observe that the Si related efficiency is smaller than the Ge related one in the whole temperature range, proving the increasing of $k_{ISC}$ with the atomic number also for the surface activity. In this respect, the Sn related surface activity is expected above the Ge related one and with a similar behavior in this temperature interval. It is worth to note that, on the contrary of the Sn-Ge substitution for the bulk activity, here we do not observe only a relative shift of the two curves. With respect to the Ge activity, we find indeed a much smaller variation with temperature: the Si related efficiency decreases 8 times cooling the system, while the Ge related one undergoes a variation of 60 times. This difference can be observed in figure 6.16, where Si related $\zeta$, with respect to the Ge related one, is 200 times smaller at room temperature and 30 times at 5 K. The different temperature dependence reflects itself in a different slop in the range of linear behavior (300-220 K). As obtained previously, the Si related values of activation barrier and pre-exponential factor ($\Delta H = 0.07 \pm 0.01$ eV and $ln(k_E/k_S) = 1 - 2$) are lower than those of the surface Ge activity ($\Delta H = 0.23 \pm 0.05$ eV and $ln(k_E/k_S) = 13 \pm 3$). If the difference in $k_E$ can be partially rationalized with the heavy atom effect, the different value of the activation barriers speaks for a different coupling with the local matrix. It is the case to note that we can not state that this difference is a general feature of the Si and Ge related surface activities because, at

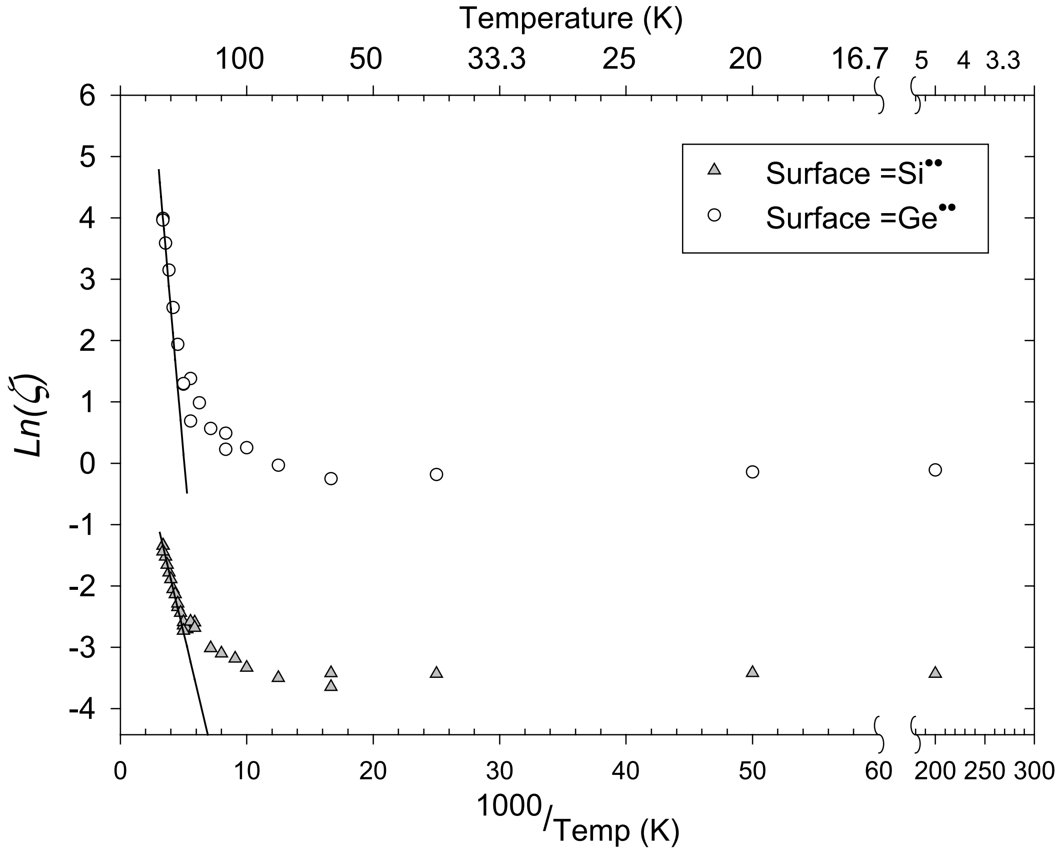

Figure 6.16. ISC relative efficiency $\zeta$ as a function of temperature for Si (triangles) and Ge (circles) related surface B-type activity, under excitation at 5.00 and 5.21 eV, respectively. The solid lines are the fitting of relative data in the range 300-220 K with an Arrheius law (equation (2.47)).

the variance of the bulk activity, we are not sure that these activities are independent on the particular manufacturing procedure since, at our knowledge, there are no similar data in literature to make a comparison. In this respect, the observed differences should be, for example, due to the different chemical treatments of the two samples (see paragraph 3.1.2). However, it is remarkable that both systems reach the plateau before 100 K, while for both the Sn and Ge related bulk activities, the constant behavior is attained below 40 K.

We have a final remark about the dependence on the excitation energy for the Si surface activity. The comparison of data in figure 6.4 and 6.11 reveals that the Si related $\zeta$ has nearly the same variation with excitation energy and with the temperature, at variance with the Ge activity, where the dependence on the excitation energy is a minor effect with respect to the temperature dependence.

## 6.3 Conclusions

The comparisons reported in the previous paragraph point out several new information on the B-type activity and on the role of local dynamics.

Firstly, the remarkable similarities in the optical features reveal that, despite the completely different manufacturing processes, both the surface and the bulk activity are related to defects that are structurally quite similar. So, B-type activity has a set of features (energy levels scheme, unitary emission quantum yield, excitation energy pathway, heavy atom effect, sensitivity to the local disorder) completely independent on the particular iso-electronic defect and on the local matrix

The fine investigation of the optical features reveals that the surface activity is characterized by a comparable spectral heterogeneity. The increasing of the surface related PL width and of the Stokes shift suggests a greater phonon coupling with respect to the bulk one, in agreement with the increasing of the total pre-exponential factor of ISC rates.

At the variance of the optical features, the surface ISC rates show a decreasing of the dependence on excitation energy and a smaller "elbow" region before the plateau.

Considering the structural model of the $=\mathrm{T}^{\bullet\bullet}$ centers and the electronic orbitals involved in the $\boldsymbol{S_0 \leftrightarrow S_1}$, $\boldsymbol{S_0 \leftrightarrow T_1}$ and $\boldsymbol{S_1 \rightarrow T_1}$ transitions, we can propose two possible rationalizations of these results. In figure 6.17(a), we report a schematic structure of the first three electronic states and a schematic diagram of the associated transitions in a $=\mathrm{T}^{\bullet\bullet}$ center [**Radzig, 1995a, Pacchioni and Ferrario, 1998**]. The $\boldsymbol{S_0 \rightarrow S_1}$ and $\boldsymbol{S_0 \rightarrow T_1}$ transitions are associated with a promotion of an electron of the lone pair to the unoccupied $3p_z$ orbital. In figure 6.17(b) a qualitative representation of the matrix arrangement in the case of bulk and surface activities is depicted. As discussed by **Radzig, 1995a**, and in agreement with **Pacchioni and Ferrario, 1998**, the orbitals and the energy levels are strongly dependent on the geometry of the defect and, in particular, on the O-T-O angle. An other relevant aspect is that the orbitals involved in the B-type activity extend themselves in the opposite direction of the basal O atoms. This configuration makes them particularly sensitive to the arrangement of the front matrix.

In the light of these considerations, the first rationalization assumes that the optical features are more sensitive to the geometry of the basal atoms, while a relevant role in the ISC efficiency is played also by the front matrix. In this frame, the surface ISC rates are less spread because of fewer perturbations, while the increase of the efficiency and of the pre-exponential factor suggests an important hindering effect of the front matrix on the ISC efficiency, corroborating a fundamental role of the defect dynamics in the ISC mechanism. In this picture, the matrix disorder affects the optical features by the basal O atoms, while it affects the ISC process also by the front matrix.

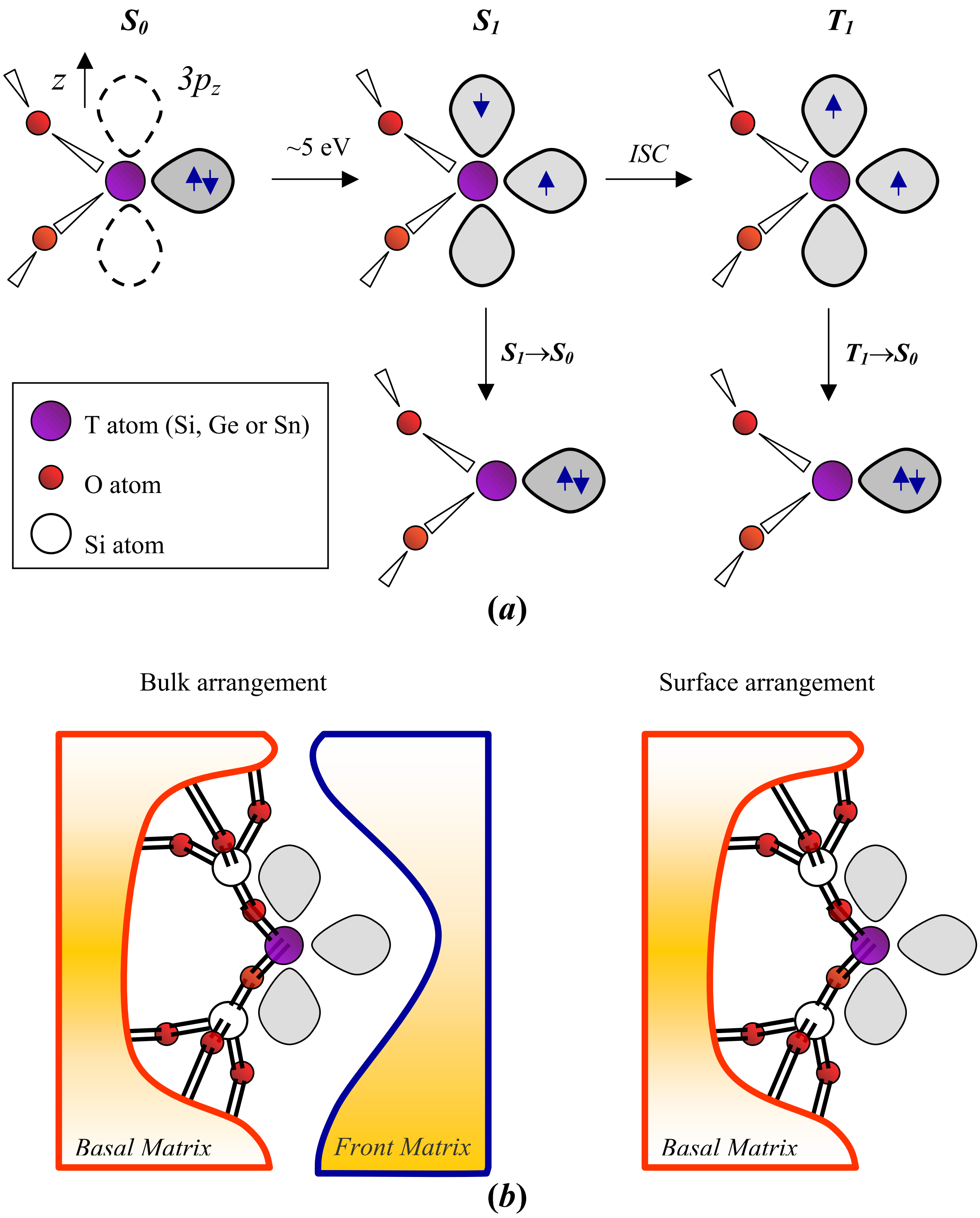

Figure 6.17. (a) Structure of the first three electronic states and schematic diagram of singlet-singlet and triplet-singlet transitions in a $=\mathrm{T}^{\bullet\bullet}$ center; note that the z axis is perpendicular to the plane of atoms. The arrows inside orbitals indicate the electrons involved in the transitions with the respective spins (from **Radzig, 1995a**). (b) Qualitative representation of the matrix arrangement in the case of bulk and surface activities.

This picture is also able to explain why the different matrix affects more the absorption band instead of the luminescence bands. Indeed, since a lone pare is characterized by a spatial distribution much wider than same orbital occupied by a single electron, the perturbation of the front matrix on the $\boldsymbol{S_0}$ state is expected to be greater than the effects on the $\boldsymbol{S_1}$ and $\boldsymbol{T_1}$ states.

An other further effect can be, in principle, present since the surface defect is characterized by more mobility (as proved by the pre-exponential factor). It implies that the observed increase of the ISC efficiency and of the coupling and a decrease of the ISC excitation dependence could be due to a easer motional averaging (in agreement with the usual minor dependence on excitation energy at higher T).

It is worth to note that the counter correlation of ISC efficiency and excitation energy for surface Si activity proves that the dependence on excitation is not due to some homogeneous mechanism which could affect defects with the same configuration (an usual explanation is to assume that, exciting at higher energy, we “help” the system to overcome the barrier, since we populate higher vibrational levels of the $\boldsymbol{S_1}$ state).

In conclusion, we observe that the not thermally activated ISC processes are present also in the surface Si activity which must have a negligible spin orbit term (see Si bulk activity), suggesting that they are not only due to “atomic” contributions (as singlet-triplet mixing).

# Chapter 7

# Relaxation processes from triplet excited electronic states under singlet - triplet excitation

In previous chapters we investigated the effect of dynamics and disorder of the local matrix exciting the direct transition $S_0 \rightarrow S_1$ of =Ge$^{\bullet\bullet}$ and =Sn$^{\bullet\bullet}$ centers and in particular the coupling of this transition with the low frequencies Frank-Condon active vibrational modes. Since the ISC processes in the Ge and Sn related activities are well effective, we were able to investigate finely not only the singlet but also the triplet emission in both cases under direct singlet-singlet excitation within the respective OA bands, varying both the temperature down to 4 K and the excitation energy. In such way, it was evidenced a great dependence of triplet band profile and of ISC efficiency on temperature and on excitation energy. In this respect, the fine study of spectroscopic features of the triplet emission is complicated by being indirectly induced, because the inhomogeneous spread of the ISC rates and their great dependence on the temperature reflect themselves on the behavior of the triplet band. In order to investigate a part from the ISC processes the phonon-coupling and the effects of local environment on the triplet-singlet transition, it would be necessary to perform a study exciting the $T_1$ state directly from the ground singlet state $S_0$. Even if the absorption band related to the $S_0 \rightarrow T_1$ transition was observed already 40 years ago [**Garino-Canina, 1958, Schultz, 1977, Levy, 1981, Yuen, 1982**], only in very few works it was reported a study of the $T_1 \rightarrow S_0$ transition for the Ge and the Sn related B-type activities with a direct excitation [**Skuja,**

**1992**]. At our knowledge, it has not been performed any investigation in order to look into the effects of the conformational disorder and of dynamics of host matrix on the spectroscopic features of the $T_1 \rightarrow S_0$ transition and on its phonon-coupling with the local low frequencies vibrational modes.

In this chapter we report an experimental study of triplet emission under direct excitation of the triplet state, as a function of temperature and of excitation energy for the two fold coordinated germanium and tin atoms. This comparative approach will allow to discuss the reported results in terms of iso-electronic properties of the two point defects and of the effect of vitreous matrix on their optical properties.

## 7.1 Experimental results and discussion

The results reported in this chapter were carried out with two silica specimens doped with tin and germanium atoms. The former has a nominal Sn content of 2000 molar ppm, the latter is nominally doped with 10000 molar ppm of Ge atoms.

In figure 7.1(a), we report the OA band of the Sn-doped sample in the spectral range 2.5 ÷ 6.0 eV. The main structure at ~ 4.9 eV is the OA band related to the transition $S_0 \rightarrow S_1$ in the two-fold coordinated Sn (see chapter 5), that appears distorted, in our sample, due to the excessive absorption. We show, in a magnified scale, the range 2.8 ÷ 4.3 eV, where it is present an absorption band which is ~ 100 times smaller than the former.

According to the data in figure 7.1(a), we report in figure 7.1(b) the PL spectra obtained under excitation at 5.0 and 3.7 eV. The former has the usual aspect for the B-type activity, with the singlet band at 4.07 eV and the triplet one at 3.16 eV. The PL band obtained under excitation at 3.70 eV shows the same profile of the triplet band. In the inset, we report the PLE spectrum obtained at the emission wavelength of 3.16 eV. As it can be seen, in the range

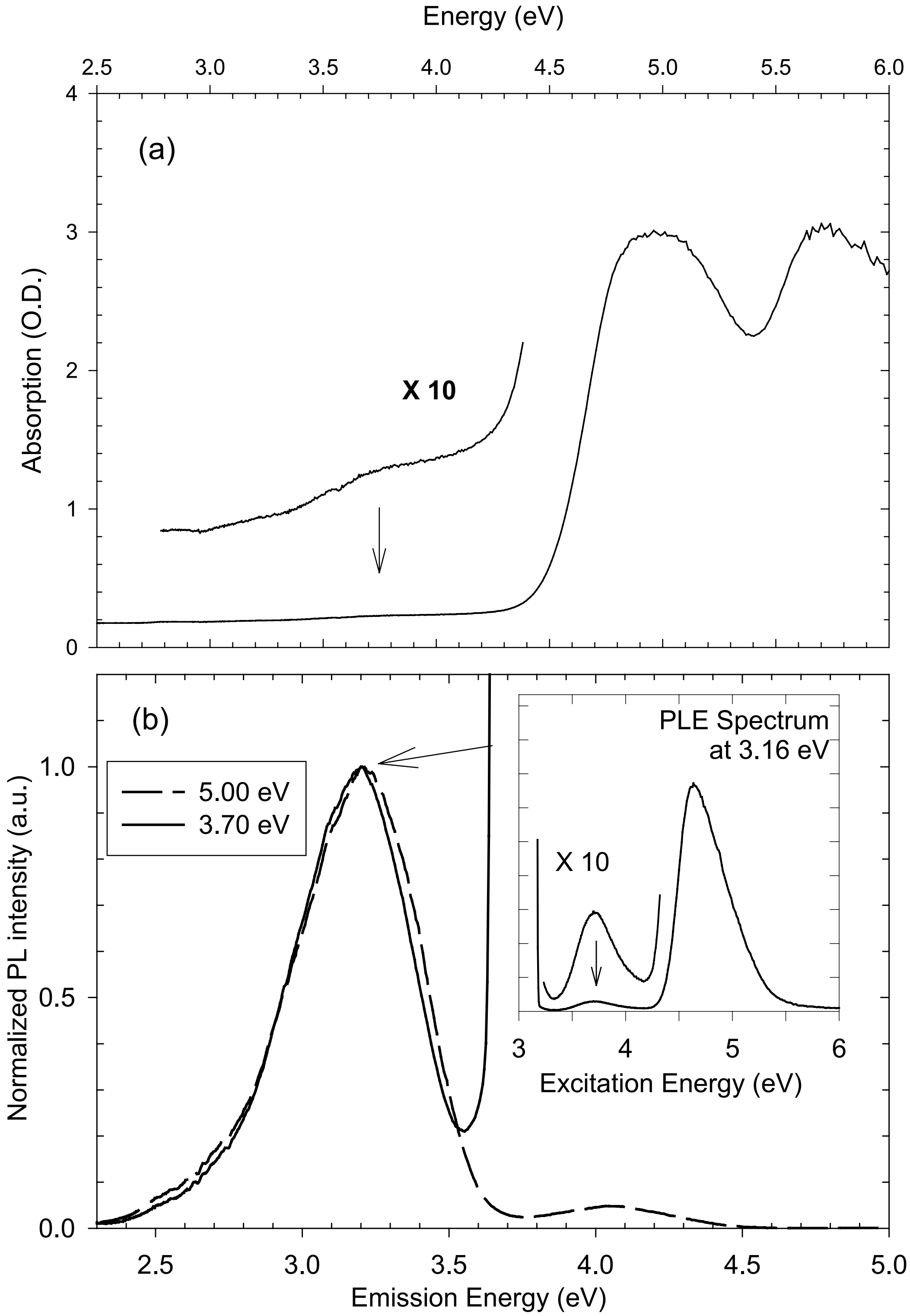

Figure 7.1. Optical activity in Sn-doped silica sample at room temperature. (a) Optical absorption band. (b) Normalized PL bands under excitation at 5.00 and 3.70 eV. In the inset, the PLE spectrum at the emission energy 3.16 eV is reported.

4.3 ÷ 5.8 eV it is present the excitation band ascribed to the $S_0 \rightarrow S_1$ transition, even if distorted by the excessive absorption, whereas, at about 3.7 eV, it is present the excitation band due to the direct $S_0 \rightarrow T_1$ transition. It is worth to note the clear correspondence between the PLE profile and the OA band in figure 7.1(a). In this respect, we can estimate the oscillator strength to be two orders of magnitude smaller the one related to the transition $S_0 \rightarrow S_1$ (see **Neustruev, 1994**).

We performed similar measurements on the Ge-doped silica sample. In figure 7.2(a), we report the OA spectrum in the range 2.5 ÷ 6 eV and we find a saturated OA band, related to the transition $S_0 \rightarrow S_1$, and a small OA band in the range 3.0 ÷ 4.2 eV. From the amplitude of the low energy tail of the otherwise distorted $B_{2Ge}$ band, compared with previous data in chapter 4 (see figure 4.3), we can estimate for this band an approximate amplitude of 10 O.D.. The OA band at about 3.7 eV is then about 1000 times smaller (see **Neustruev, 1994**). The PL spectra measured exciting at 3.7 and at 5.0 eV are compared in figure 7.2(b). The inset shows the PLE spectrum for the emission energy 3.16 eV and confirms that the PLE and the OA bands in the range 3.0 ÷ 4.5 eV, and the relative PL activity, are related to the transition $S_0 \leftrightarrow T_1$ localized on the same defect.

It is worth to note that, both in Ge and Sn related activities, the triplet PL band at about 3.16 eV and the 3.7 eV PLE spectrum show a sizeable Stoke's shift (≈0.5 eV), indicating the presence of a large conformational rearrangement also for the $S_0 \leftrightarrow T_1$ transition.

We studied, in both systems, the directly excited triplet band on varying the temperature from 300 down to 7 K. In figure 7.3(a), we report the PL spectra for the tin doped sample under excitation at 3.7 eV and at various temperatures; the same measurements for the Ge-doped sample are shown in figure 7.3(b). In both cases, we observe a red-shift and a narrowing on lowering the temperature.

To investigate the presence of a thermal quenching and to better evaluate the effect of the temperature on the band profile, we performed the analysis in terms of the zeroth ($M_{0T}$), first ($M_{1T}$) and second ($M_{2T}$) spectral moments of the emission bands, being $M_{0T}$ and $M_{1T}$

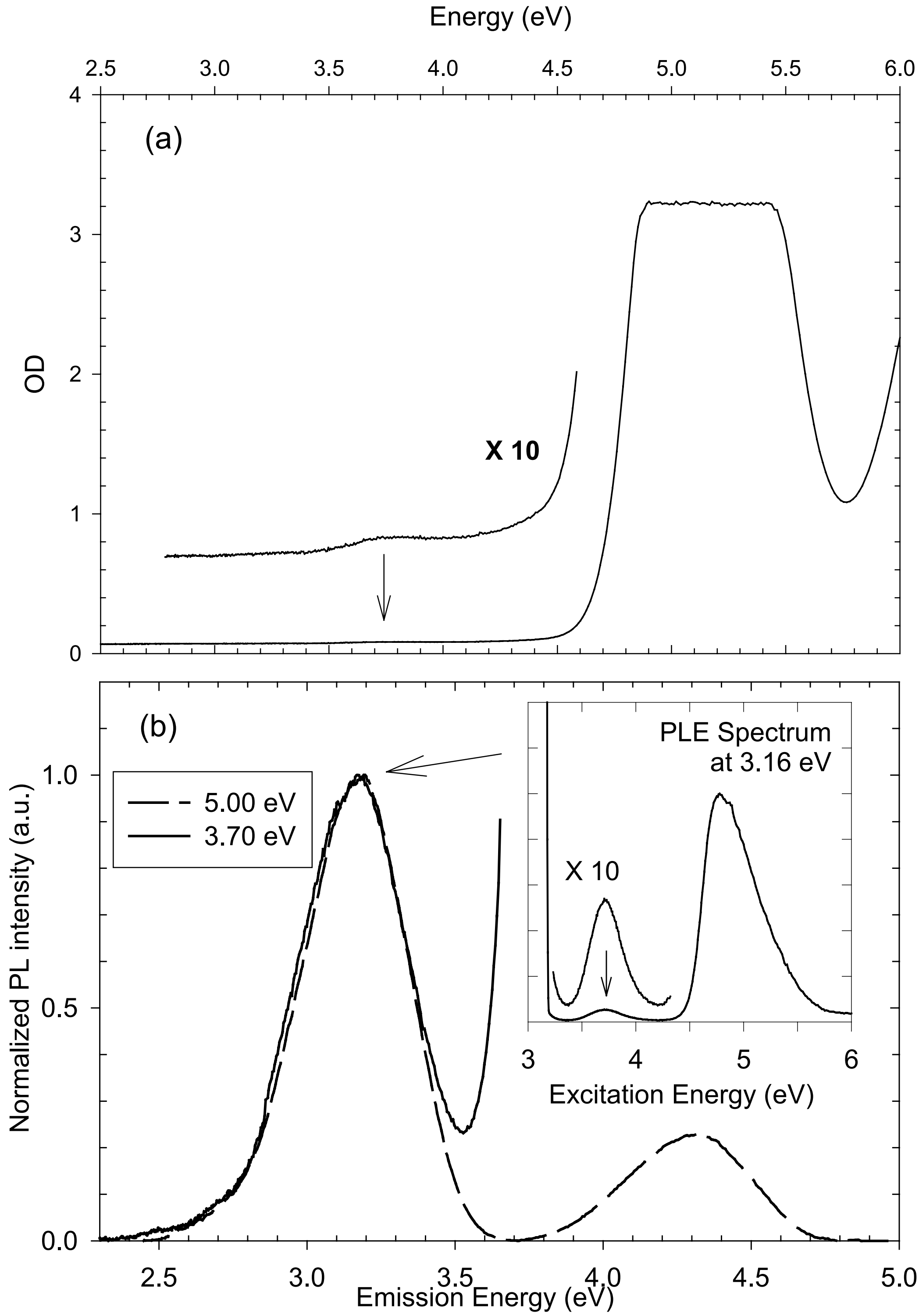

Figure 7.2. Optical activity in Ge-doped silica sample at room temperature. (a) Optical absorption band. (b) Normalized PL bands exciting at 5.00 and 3.70 eV. In the inset, the PLE spectrum at emission energy 3.16 eV is reported.

calculated accordingly to equations (2.44) and (2.46), respectively. Concerning $M_{2T}$ it is given by the expression:

$$M_{2T} = \frac{1}{M_{0T}} \cdot \left( \int_0^\infty E_{em}^2 \cdot T(E_{em}, E_{ex}) dE_{em} - M_{1T}^2 \right). \tag{7.1}$$

In the following we will omit the subscript $T$, being no confusion with the singlet emission.

In figure 7.4(a), we report $M_0$ as a function of the temperature for both bands, after a suitable normalization to the respective mean value. $M_1$ and $M_2$ moments are shown in figures 7.4(b) and (c), respectively. No temperature dependence for $M_0$ is found, in both systems. This result proves the absence of any radiationless relaxation process from the triplet to the ground state, in agreement with previous indirect measurements [**Leone *et al.*, 2001**]. The behavior of $M_1$ and $M_2$ confirms the red-shift and the narrowing observed in figure 7.3. This dependence reveals a remarkable coupling of the **$S_0 \leftrightarrow T_1$** transition with local low frequency vibrational modes. As reported in chapter 2, quantitative information on the coupling between the electronic transition responsible for the emission band and the Franck-Condon active vibrational modes of the surroundings can be obtained analyzing the $M_1$ and $M_2$ thermal behavior according to the equations (2.34) and (2.35). Continuous lines are the best fit to data, the relative parameters being reported in table 7.1. These results suggest that the **$T_1 \leftrightarrow S_0$** transition in the two samples is coupled with almost the same "bath" of local low frequency modes, in agreement with the similar values of Stokes shift. On the other hand, the fact that the band in the tin doped sample is broader and is characterized by a lower value of $M_1$ with respect to the Ge related activity suggests a greater coupling with the

Table 7.1. Values of the parameters obtained by the analysis of the thermal behavior of the spectral moments in figure 7.4(b) and (c) in terms of equations (2.34) and (2.35).

| B-type activity | $N_l \cdot S_l$ | $N_l \cdot (1-R_l)$ | $\langle E_l \rangle$ (meV) | $M_2^0$ (eV$^2$) | $M_1^0$ (eV) |
|---|---|---|---|---|---|
| Sn related | 13 ± 1 | -6.4 ± 0.3 | 28 ± 2 | 0.028 ± 0.001 | 3.042 ± 0.005 |
| Ge related | 14 ± 1 | -5.0 ± 0.3 | 22 ± 3 | 0.018 ± 0.001 | 3.091 ± 0.005 |

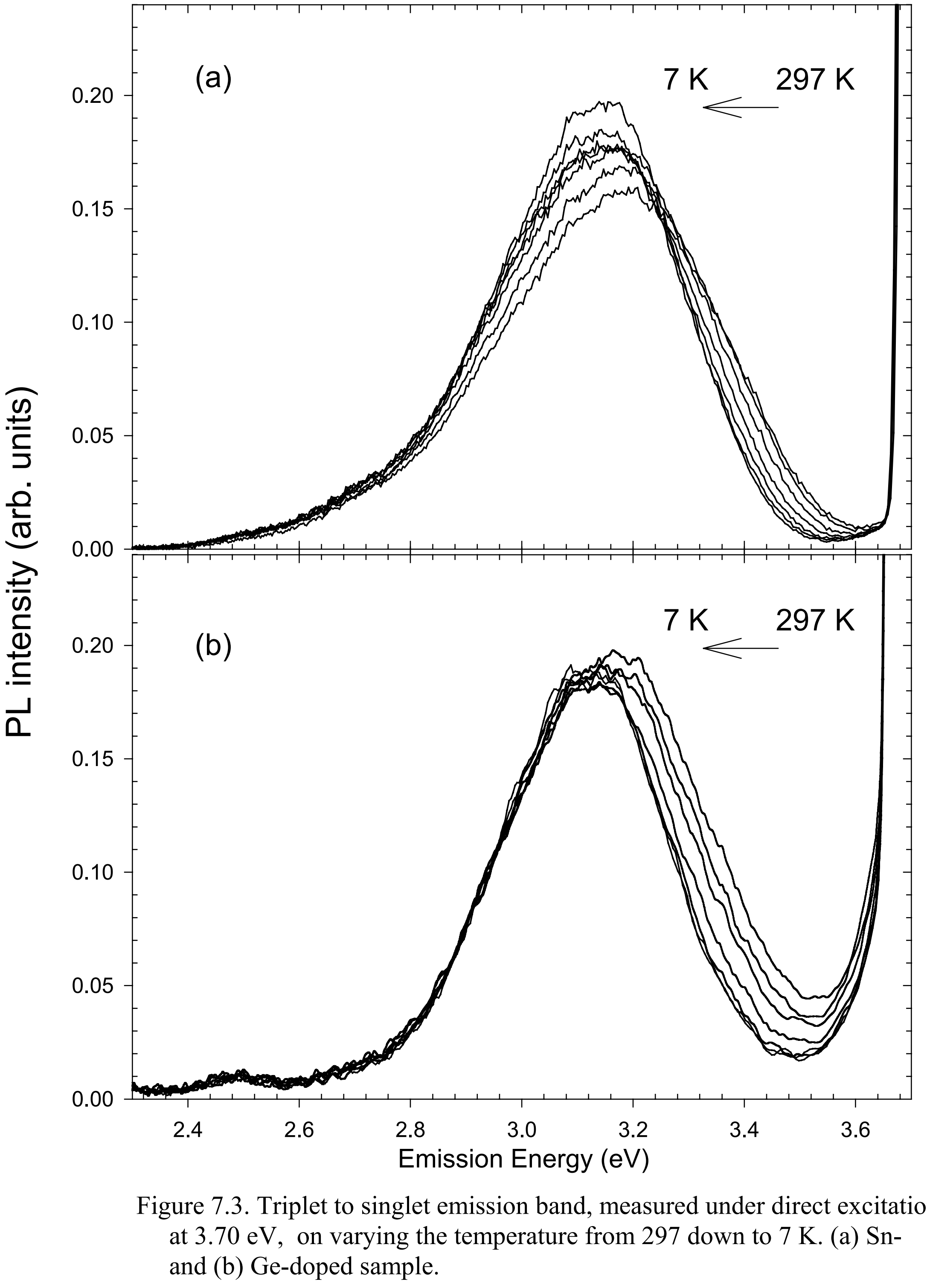

Figure 7.3. Triplet to singlet emission band, measured under direct excitation at 3.70 eV, on varying the temperature from 297 down to 7 K. (a) Sn- and (b) Ge-doped sample.

high frequency local modes for the Sn related activity.

In order to point out the presence of spectral inhomogeneity, we studied in both systems the dependence on the excitation energy at different temperatures, from 300 to 20 K. In figures 7.5(a) and (b), we report the PL spectra for Sn and Ge doped samples, respectively, at

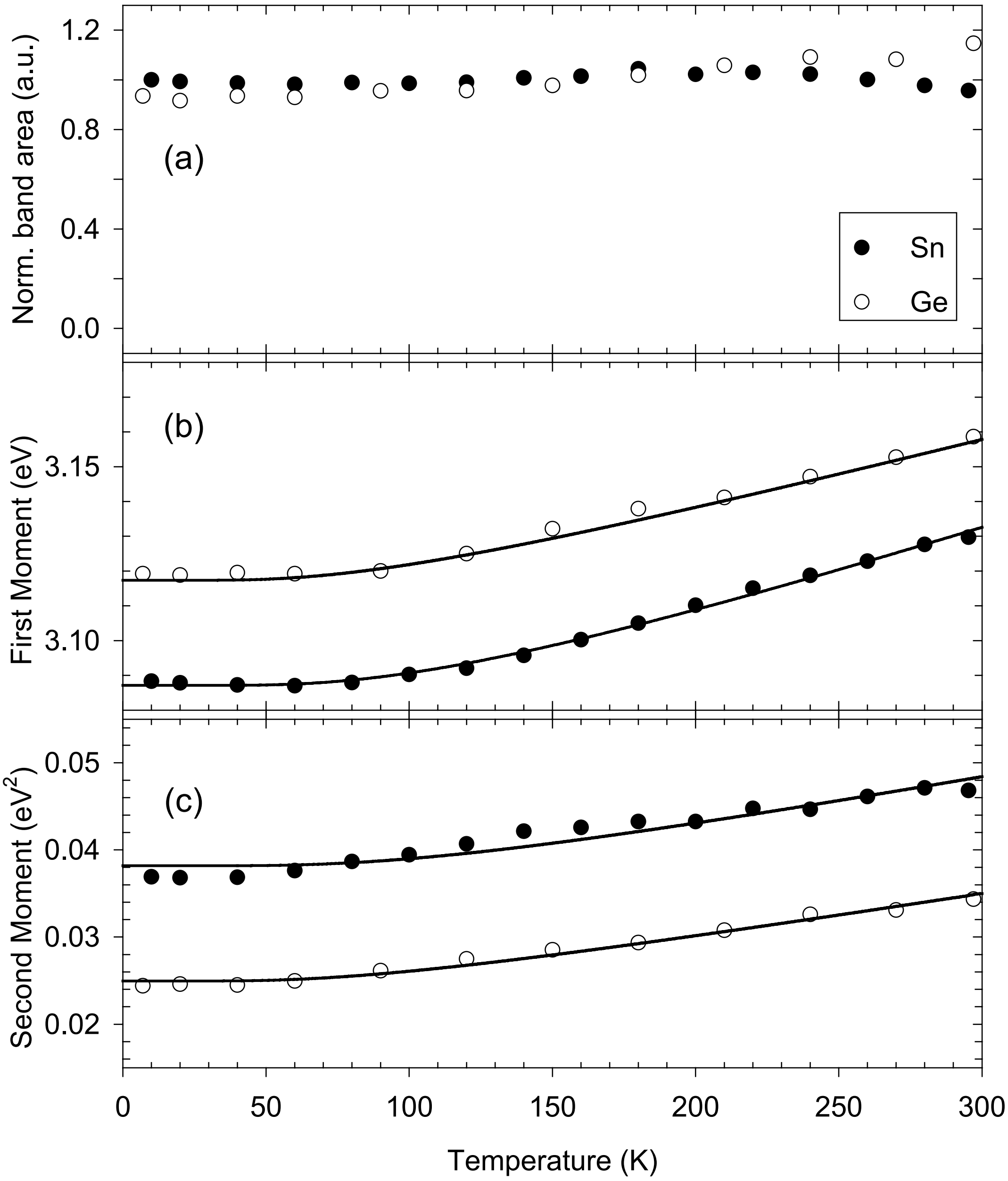

Figure 7.4. Zeroth (a), first (b) and second moment (c) of the triplet band for Sn- (open marks) and Ge-related activity (full marks), as a function of temperature. Continuous lines represent the fitting in terms of equations (2.34) and (2.35) of $M_1$ and $M_2$ values, respectively.

room temperature; we obtain similar spectra at lower temperatures. An evident dependence on the excitation energy is found, revealing an inhomogeneous broadening of this activity. In particular, it is evident a remarkable dependence of the band width.

Regarding the analysis in term of spectral moments, we obtain that the behavior of $M_0$ (data not reported here) is temperature independent at all excitation energies. This result

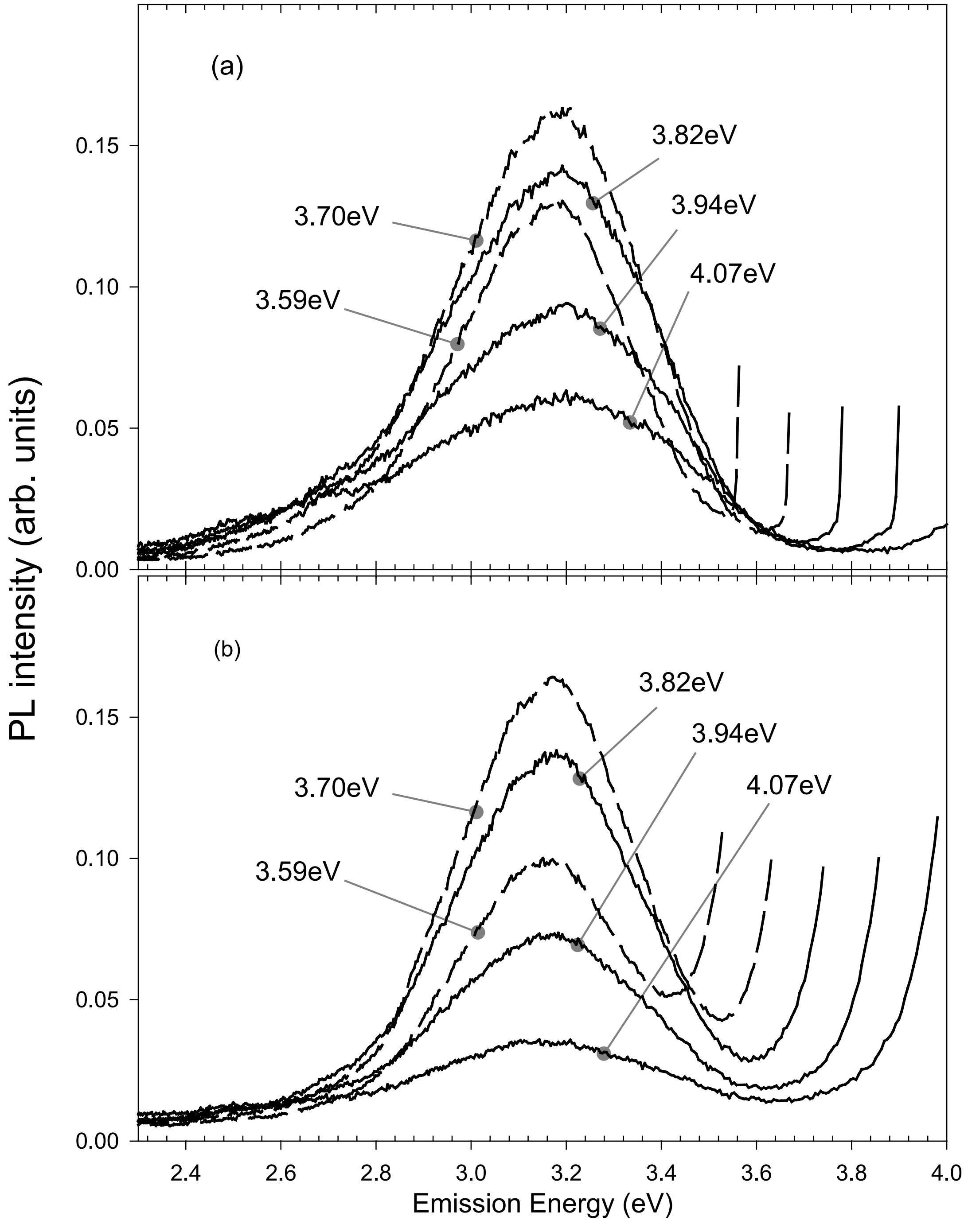

Figure 7.5. Triplet band, on varying the excitation energy at room temperature, for Sn- (a) and Ge-doped sample (b).

confirms the absence of any non radiative relaxation process and indicates that this result is not affected by the inhomogeneous distribution of point defects.

Concerning the first and the second moments, we report in figures 7.6(a) and (b) the relative data for both systems, at room temperature and at 20 K. $M_1$ shows the same non

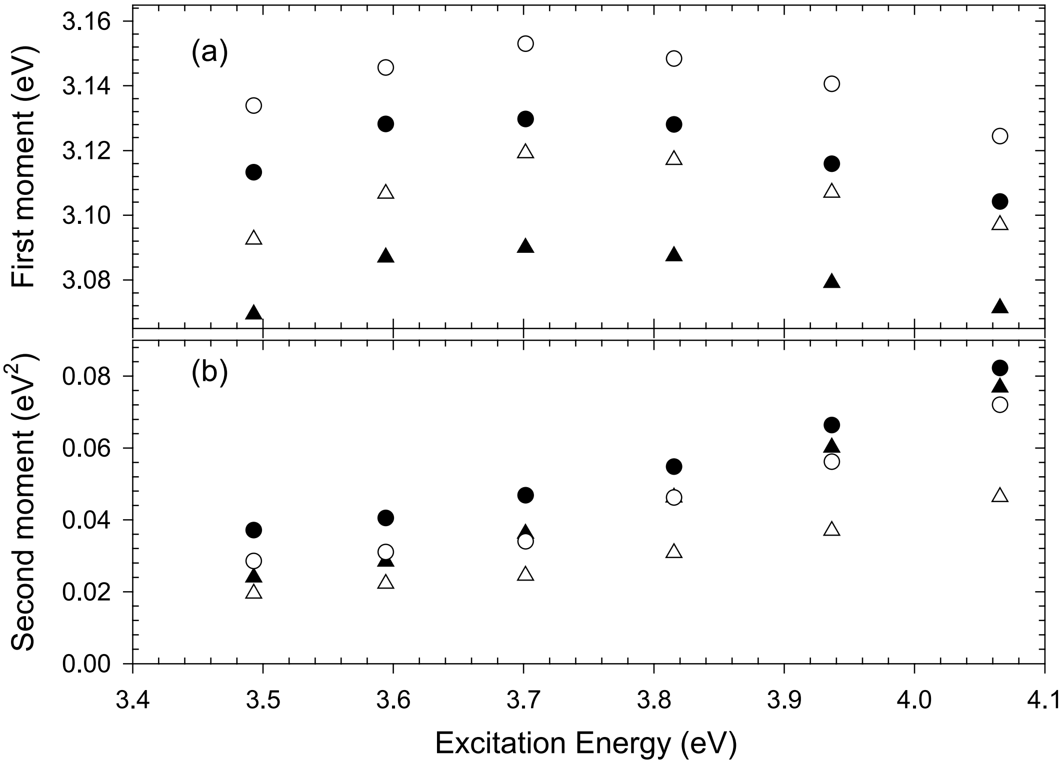

Figure 7.6. First moment (a) and second moment (b) of the triplet band for the Sn (full mark) and Ge (open mark) activity at room temperature (circles) and 20 K (triangles).

monotonic dependence on the excitation energy in both systems and independently from temperature. The only effect is a constant shift by lowering the temperature, regardless the excitation energy value.

The behavior of the second moment in figure 7.6(b) confirms the expected monotonic broadening by increasing the excitation energy, regardless the system and the temperature. Also for $M_2$, on lowering the temperature, an almost constant shift is induced, regardless the excitation energy. Finally, we note that similar results for $M_1$ and $M_2$ are also obtained at the intermediate temperature of 200 and 120 K (data not reported).

## 7.2 Cross-correlation effects: direct $S_0 \rightarrow T_1$ and indirect $S_1 \rightarrow T_1$ excitation

Introducing this chapter, we stressed that the inhomogeneous nature of the ISC process can be reflected on the $\beta_T$ band optical features, in particular in the excitation dependence. As observed both for the Ge and the Sn related optical activity, the ISC efficiency shows a remarkable dependence on excitation energy or, in others words, different defects are characterized by different $k_{ISC}$ rates. So, populating the triplet state via the $\boldsymbol{S_1\rightarrow T_1}$ transition, the contribution to the $\beta_T$ band are due more to defects with higher efficiency. In this respect, a fine tuning of excitation energy around the $B_{2T}$ band will reflect more the inhomogeneous dispersion of $\beta_T$ band properties related to these centers selected by ISC process. This effect is an example of *cross-correlations effect* [**Skuja, 1998**]. As discussed in the first chapter, this effect is peculiar of amorphous systems, where the disorder is able to perturb the defects from their minimum energy positions reveling the microscopic mutual dependence of different properties of the defect.

In this section we point out the cross-correlations between the ISC rate and the Ge and Sn related $\beta_T$ band properties by a comparative study of the $\beta_T$ band first moment $M_1$ under direct and indirect excitation, at room temperature and 20 K. With indirect excitation we will indicate the populating of triplet state, via the ISC process, from the $\boldsymbol{S_1}$ state populated by the $\boldsymbol{S_0\rightarrow S_1}$ transition. This excitation channel will be indicated as "$\boldsymbol{S_1\rightarrow T_1}$" transition.

In figure 7.7 we compare $M_1$ for the Ge related activity at 300 and 22 K, by tuning finely the excitation energy around 3.7 and 5.1 eV, the maxima of the $\boldsymbol{S_0\rightarrow T_1}$ and the $\boldsymbol{S_0\rightarrow S_1}$ absorption bands, respectively. We note that the two absorption bands are characterized by different widths, the FWHM of the PLE spectra (1) around 3.7 eV and 5.1 being 0.43 eV and 0.33 eV, respectively. To take in account this aspect, the scales in figure are centered at the relative maximum and the shown energy range is proportional to the width of the relative PLE band.

---

(1) We should compare the OA bands, but the one related to the direct transition is not clearly detectable (see figure 7.2). Since the PLE spectra are quite similar to the relative OA bands, we prefer compare them.

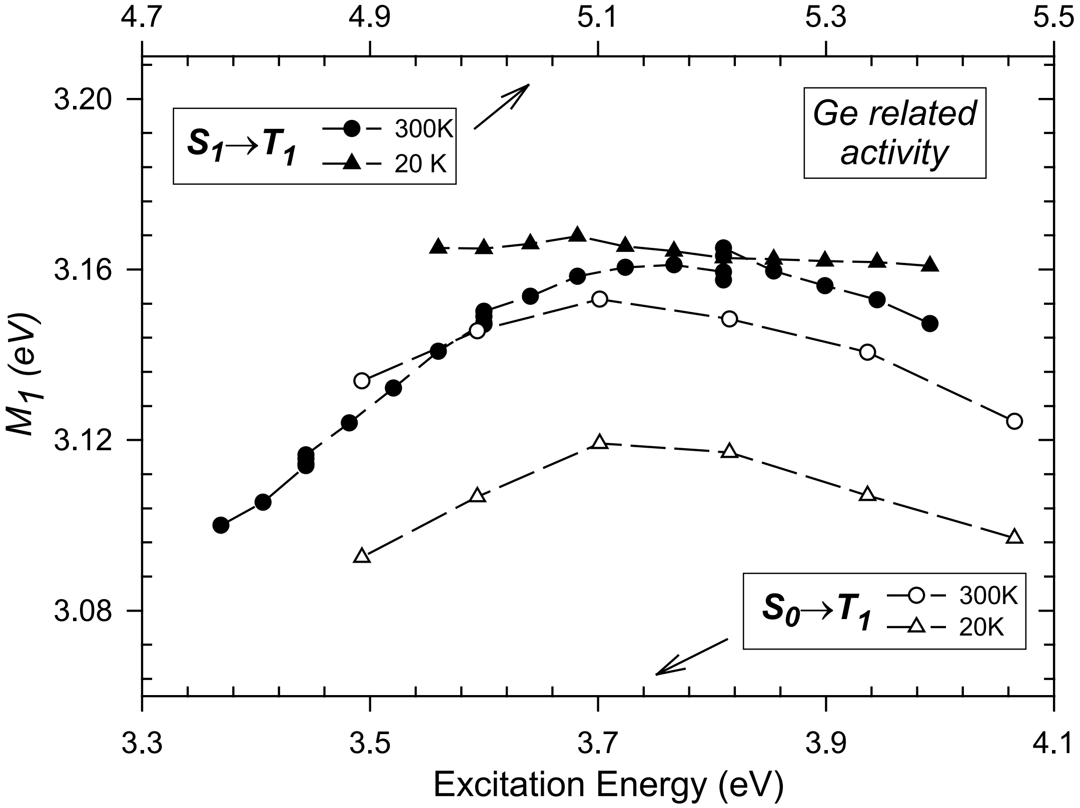

Figure 7.7. First moment of the triplet band for the Ge activity excited by direct $S_0 \rightarrow T_1$ transition (open marks, bottom scale) and by indirect $S_1 \rightarrow T_1$ transition (full marks, upper scale). Circles: 300 K; triangles: 20 K.

As a first impression, we note that the data at room temperature show a quite similar behavior, at variance of the data at 20 K. We also observe that the data excited via the $S_1 \rightarrow T_1$ transition at low temperature assume a constant value regardless the excitation energy.

Similar results are obtained for the Sn related activity, as reported in figure 7.8. We obtain indeed a similar behavior for both excitation channels at room temperature, whereas at 20 K the indirectly excited band assumes an almost constant value regardless the excitation.

These results prove that the spectral inhomogeneity observed for the $\beta_T$ band is greatly effected by the inhomogeneity of the ISC rate. In particular, data in figure 7.7 and 7.8 suggest that at room temperature, where the ISC process is very effective, it is not really selective and we obtain almost the same defect distribution exciting via both transitions. On the other hand, at low temperature the completely different behavior suggests that ISC processes are more selective than at room temperature, because only those particular centers with effective

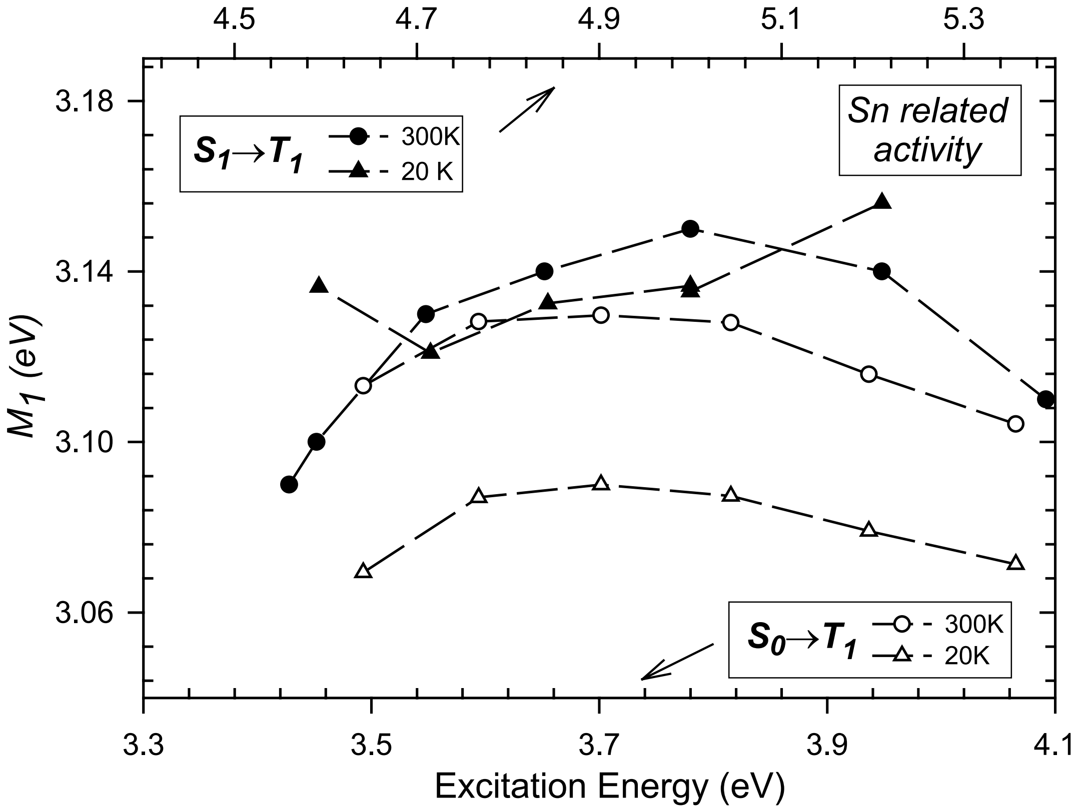

Figure 7.8. First moment of the triplet band for the Sn activity excited by direct $S_0 \to T_1$ transition (open marks, bottom scale) and by indirect $S_1 \to T_1$ transition (full marks, upper scale). Circles: 300 K; triangles: 20 K.

thermally independent ISC processes can convert. In this respect this rationalization is corroborated also by the second moment analysis (data not reported) for the indirectly excited $\beta_T$ band, which show the same behavior of the $M_1$: a remarkable dependence on excitation energy at room temperature which disappears at 20 K. In this respect, even if the temperature independent $k_{ISC}$ processes appear to be not an homogeneous feature, it look to be associated with an almost homogenous subset of defects.

## 7.3 Conclusions

The overall dependence of the spectral moments of the $T_1 \to S_0$ transition, as a function of the temperature and of the excitation energy, allows us to point out that the investigated systems are characterized by i) an inhomogeneous conformational distribution of the centers, that reflects itself in a spectral distribution, and ii) an essentially homogenous phonon coupling of the electronic transition, poorly affected by the local disorder and by the Ge - Sn substitution. This last statement is also proved by the comparison between the relative shifts of $M_1$ and $M_2$ for the Sn and the Ge activity (see figures 7.6(a) and 6(b)). We also note that the values of parameters which more properly account for the phonon coupling ($N_l \cdot S_l$, $N_l \cdot (1-R_l)$ and $\langle E_l \rangle$ in table 7.1) are very close to the values reported in table 5.1 for the direct $\boldsymbol{S_0 \rightarrow S_1}$ transition. In view of above reported results, we can affirm that, in these systems, different electronic transitions localized on the same defect are coupled with the same vibrational modes, regardless the different electronic levels involved and from their multiplicity. This is also confirmed by the large value of 0.5 eV for the Stokes shift found for the $\boldsymbol{S_0 \leftrightarrow T_1}$ transition, that evidences the weight of this coupling and that the excitation pathway is accompanied by a large conformational rearrangement, as observed for the $\boldsymbol{S_0 \leftrightarrow S_1}$ transition (chapter 4 and 5).

Finally, it worth to note that, since the phonon coupling has revealed an homogenous nature, the observed dependence on excitation energy speaks definitely for a significant role of the conformational heterogeneity mainly on the energy levels spacing and on the coupling with the high frequencies vibrational modes, i.e. on those features strictly depending on the defect structure and on the arrangement of the closest surroundings. In this respect, the comparison with experimental results on the allowed $\boldsymbol{S_0 \rightarrow S_1}$ transition, reveals that the local disorder affects the overall electronic structure of the centers and not only the phonon-assisted ISC process.

The comparison of triplet activity excited by the direct $\boldsymbol{S_0 \rightarrow T_1}$ or indirect $\boldsymbol{S_1 \rightarrow T_1}$ transitions has revealed the role of the ISC process in affecting the features of the triplet bands and it has allowed to separate the effects of the local disorder on the triplet energy level structure from the ones on the ISC rates.

# Chapter 8

## Ultrafast relaxation processes in non thermalized regime in excited states

In the previous chapters we reported several experimental evidences of the important role of matrix dynamics on defect optical features. In particular, the inter-system crossing efficiency has been revealed quite sensitive to the local dynamics and to the disorder of the host matrix. In this respect, all the investigated optical activities, regardless the particular defect (chapters 5 and 6), the local matrix (chapter 6) and the excitation channel (chapter 7) are characterized by large absorption-emission Stokes shifts (0.8 eV and 0.5 for the $S_0\leftrightarrow S_1$ and $S_0\leftrightarrow T_1$ transitions, respectively), which indicates the presence of a significant defect-matrix coupling.

All these measurements were obtained with steady state spectroscopy or time resolved emission spectroscopy in the nsec time domain. So, they involve transitions between states which had the time to relax toward the equilibrium position by thermalization with the matrix. In this respect, the role of the local dynamics were investigated by changing the phonon population. An attractive investigation should be to study the dynamics of defect-matrix complex immediately after the $S_0\rightarrow S_1$ excitation and during the thermalization (internal conversion), which occurs in a time scale comparable with the nuclear motions. This investigation is even more attractive considering the recent employment of femtosecond laser pulses in photosensitivity experiments [**Hirao and Miura, 1998, Streltsov and Borrelli, 2002**] and recent computational works on this subject [**Sen and Dickinson, 2003**].

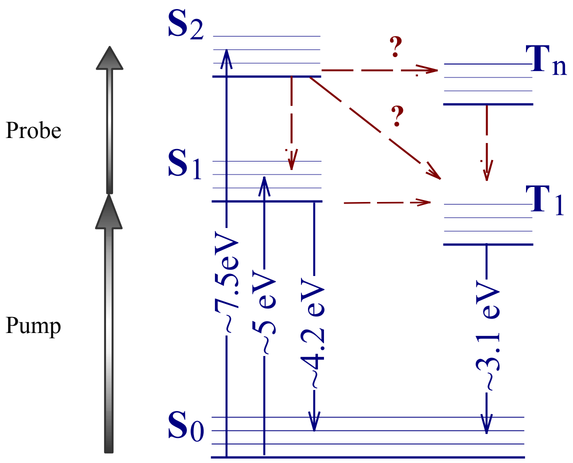

Figure 8.1. Energy levels scheme related to the B-type optical activity. The straight and the dashed lines refer to radiative and non radiative transitions, respectively. The thick grey arrows show the transitions induced by pump and probe pulses (see text for details).

In the last decade, the development of ultrafast spectroscopic techniques has allowed the investigation of processes in the nuclear motion time scale, i.e. the sub-picosecond domain, and, at our knowledge, no studies on point defects in silica matrices have been performed so far. In this chapter we report transient absorption (TA) measurements from $S_1$ to $S_2$ for Ge- and Sn-related B-type activity to investigate the ISC processes and the structural dynamics leading to the luminescence and to the internal conversion in femto and picosecond domain. Both defects are indeed characterized by an $S_2$ state which is located at 7.4 eV, as depicted in figure 8.1 [**Cannas *et al.*, 1997, Chiodini *et al.*, 2000**]. This state is affected by two non radiative processes: an internal conversion toward $S_1$, and a ISC process to $T_1$ [**Agnello *et al.*, 2003** and **2004**], directly or involving an higher excited triplet state, $T_n$. In figure 8.1 the pump and probe pulses are also shown (see subsection 3.2.3). We carried out the same measurements on two iso-electronic and iso-structural defects to discriminate if the observed kinetics are more affected by the local dynamics of the matrix or by peculiarities of the particular atomic structure of the defect, such as the homogenous spin-orbit coupling mechanism or heavy atom effects.

## 8.1 Experimental results and discussion

The results reported here were obtained on two silica specimens synthesized by Sol-Gel method and doped with Ge and Sn atoms, as described in chapter 3. The Ge enriched sample was prepared with a nominal Ge atoms concentration of $10^4$ molar ppm, while the Sn doped sample is characterized by a nominal Sn content of 2000 molar ppm. Both the $=\mathrm{Ge}^{\bullet\bullet}$ and $=\mathrm{Sn}^{\bullet\bullet}$ concentrations were estimated as $\sim 10^{18}$ /cm$^3$ by absorption measurements of the $B_{2T}$ band amplitude and assuming the same cross section [**Agnello *et al.*, 2000**]. For comparison, we used also an undoped sample of commercial origin (Suprasil-F300 by Shin-Etsu Quartz Products Co. Ltd), prepared by vapor deposition method, virtually free from Ge and Sn atoms, with optically polished surfaces and a thickness of 1 mm. As discussed in the paragraph 2.5, we will report measurements of probe absorption defined as the ratio of the probe depletion to the initial probe intensity (see equation (2.50) and related discussion)

In figure 8.2 we report the TA of the probe pulse as a function of pump-probe time delay at room temperature in the Sn and the Ge doped samples. The whole investigated range, from -100 to 500 psec, is shown in figure 8.2(a), whereas in figure 8.2(b) the first 12 psec range is displayed. Here, the results for both doped samples are compared with the response of the un-doped one. The absence of any signal in the un-doped sample and the linear dependence of the probe depletion on the pump and probe intensity prove that the observed behavior on the Sn and Ge doped samples is due only to respective B-type activities.

Both systems show a quite similar behavior with two distinct relaxation dynamics: a slower one, in the nsec domain, and a faster one, in the psec domain. In order to analyze these data, we characterize the observed relaxation process in terms of a sum of exponential decays. To take into account the time profile of the pump and probe pulses, each exponential decay

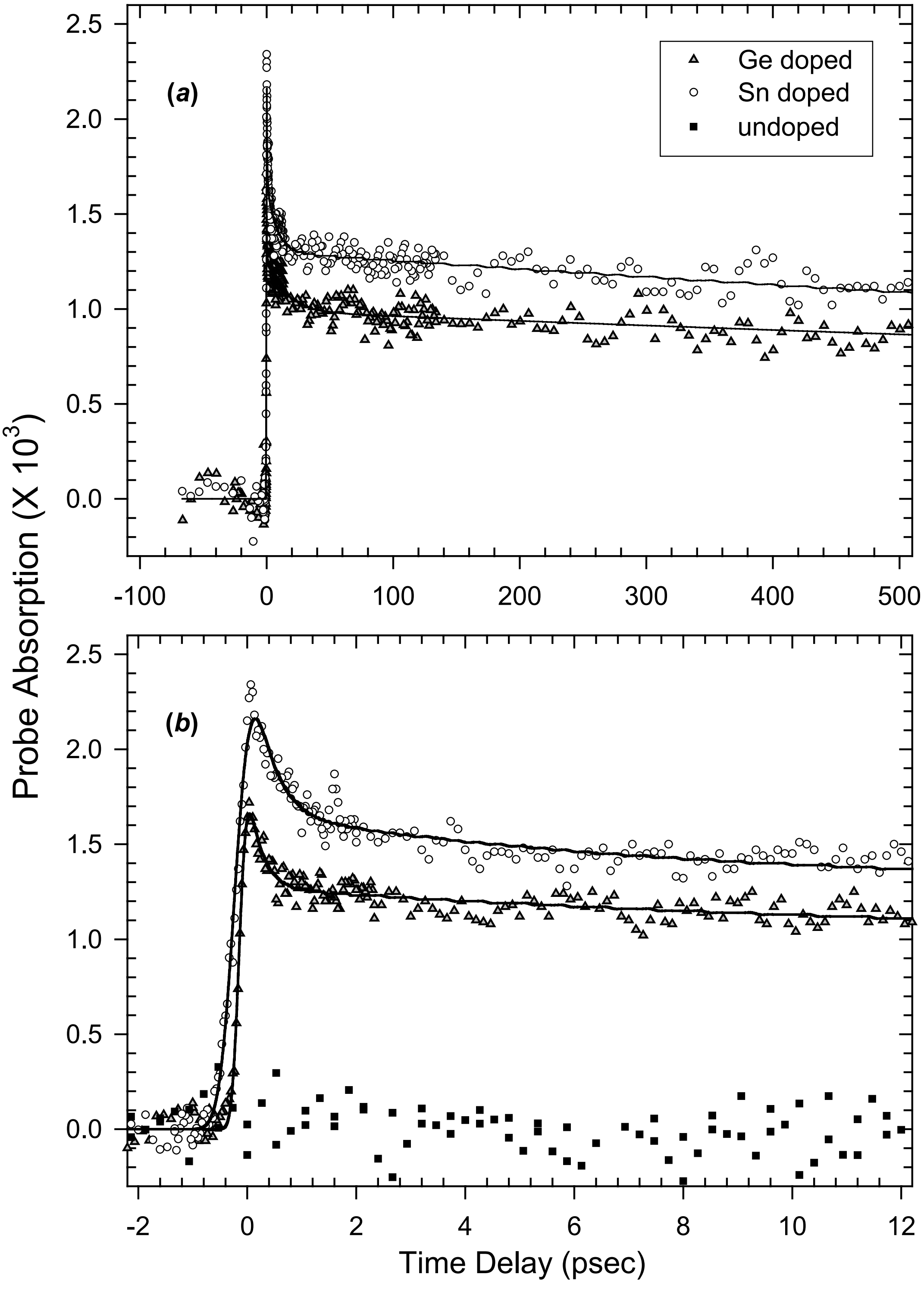

Figure 8.2. Probe absorption as a function of pump-probe time delay for the Ge (grey triangles) and Sn (white circles) doped samples in the -100 ÷ 500 psec (a) and -2 ÷ 12 psec (b) range. For comparison purpose, in figure (b) the results on the un-doped sample are reported. The solid lines are the outcomes of fitting procedure (see text for details)

function is convoluted with the same gaussian function which describes the cross-correlation of the two pulses:

$$I(t)=\left(u_{t>0}\cdot e^{-\frac{t}{\tau}}\right)\otimes\left(A\cdot e^{-\frac{1}{2}\left(\frac{t}{\sigma}\right)^2}\right)=A\cdot e^{\frac{1}{2}\left(\frac{\sigma}{\tau}\right)^2}\cdot e^{-\frac{t}{\tau}}\cdot\int_{-\infty}^{t}e^{-\frac{1}{2}\left(\frac{t'}{\sigma}-\frac{\sigma}{\tau}\right)^2}dt' \tag{8.1}$$

where $u_{t>0}$ is a step function, $\tau$ is the lifetime of the relaxation process, $A$ and $\sigma$ are the amplitude and the standard deviation of the cross-correlation gaussian function, respectively. In the fitting procedure, we considered the least amount of these decay functions, in order to describe reasonably the data. Regarding the gaussian function, the value of $\sigma$ was shared among all the functions employed in each fitting. For both systems, we found adequate to use two decay functions for the fast relaxation and a single exponential decay for the slow process.

The synthesized time behavior of this fitting procedure is represented by the solid lines in figure 8.2(*a*) and (*b*). In figure 8.3(*a*) and (*b*) it is reported, in the –2 ÷ 12 psec range, the detailed decomposition for the Ge and Sn related activity, respectively, the relative parameters being reported in table 8.1. In agreement with previous remarks, the fitting results reveal that both systems are characterized by a quite similar behavior.

Before further discussion on these results, we have to comment shortly the physical information supplied by them. In agreement with equation (2.51), the relaxation process shown in figures 8.2 and 8.3 speaks for a time dependence of the $\boldsymbol{S_1 \rightarrow S_2}$ absorption

Table 8.1: Values of the parameters obtained by the fitting procedure to the =Ge•• and =Sn•• related data in figure 8.2 in terms of sum of three decay functions (see equation (8.1) and text for details). The error reported are twice the standard deviation.

| =Ge•• | | =Sn•• | |
|---|---|---|---|
| Gaussian Amplitude | Lifetime (psec) | Gaussian Amplitude | Lifetime (psec) |
| $(5 \pm 2)\cdot 10^{-4}$ | $0.25 \pm 0.08$ | $(10 \pm 4)\cdot 10^{-4}$ | $0.36 \pm 0.12$ |
| $(142 \pm 14)\cdot 10^{-6}$ | $15 \pm 4$ | $(188 \pm 26)\cdot 10^{-6}$ | $7.6 \pm 1.8$ |
| $(494 \pm 8)\cdot 10^{-6}$ | $(3.8 \pm 0.8)\cdot 10^{3}$ | $(650 \pm 10)\cdot 10^{-6}$ | $(2.8 \pm 0.6)\cdot 10^{3}$ |

coefficient α, which can be thought as a product of the $\boldsymbol{S_1}$ population $n_S$ and the specific absorption coefficient $\varepsilon$ (see equation (2.23)): $\alpha = n_S \cdot \varepsilon$. In general, we have to suppose a time dependence in both factors. In particular, ε is expected to change due to the conformational rearrangement process toward the $\boldsymbol{S_1}$ minimum and $n_S$ is guessed to be affect by the presence of relaxation channels from $\boldsymbol{S_1}$ to other states ($\boldsymbol{S_0}$ and $\boldsymbol{T_1}$ in our case). It is worth to note that both effects reflect the coupling of the $\boldsymbol{S_1}$ transition with the local dynamics of the matrix and, in this respect, the observed decay rates are expected to be the counterpart of the frequencies of the coupled vibrational modes.

We consider firstly the slow dynamics. In this case, we can assume that all the internal relaxation processes of $\boldsymbol{S_1}$ occurred, and the observed decay can be related to an exponential empting of $\boldsymbol{S_1}$ with the value of lifetime reported in table 8.1. In agreement with this rationalization, these values have to be compared with the value of $\boldsymbol{S_1}$ lifetime previously determined for the Ge and Sn activity, which are 2.6 ± 0.1 nsec (see figure 4.15 (a) at excitation energy 4.7 eV and at room temperature) and 1.2 ± 0.6 (see figure 5.6(a) at room temperature), respectively. The agreement is acceptable considering that the $\boldsymbol{S_1}$ lifetime values obtained in the previous chapters have more the meaning of typical time of a process characterized by a spread.

Regarding the faster processes, we note that both systems show a quite similar behavior in the femto and picosecond time domain. So, regardless the particular rationalization of the two involved mechanisms, they are revealed to be not greatly affected by the Sn-Ge substitution. This result strongly suggests that, in this non thermalized regime, the dominant role is mainly played by the matrix dynamics. This result agrees with the hypothesis that the Sn-Ge substitution does not affect the defect-matrix coupling, consistently with steady state measurements.

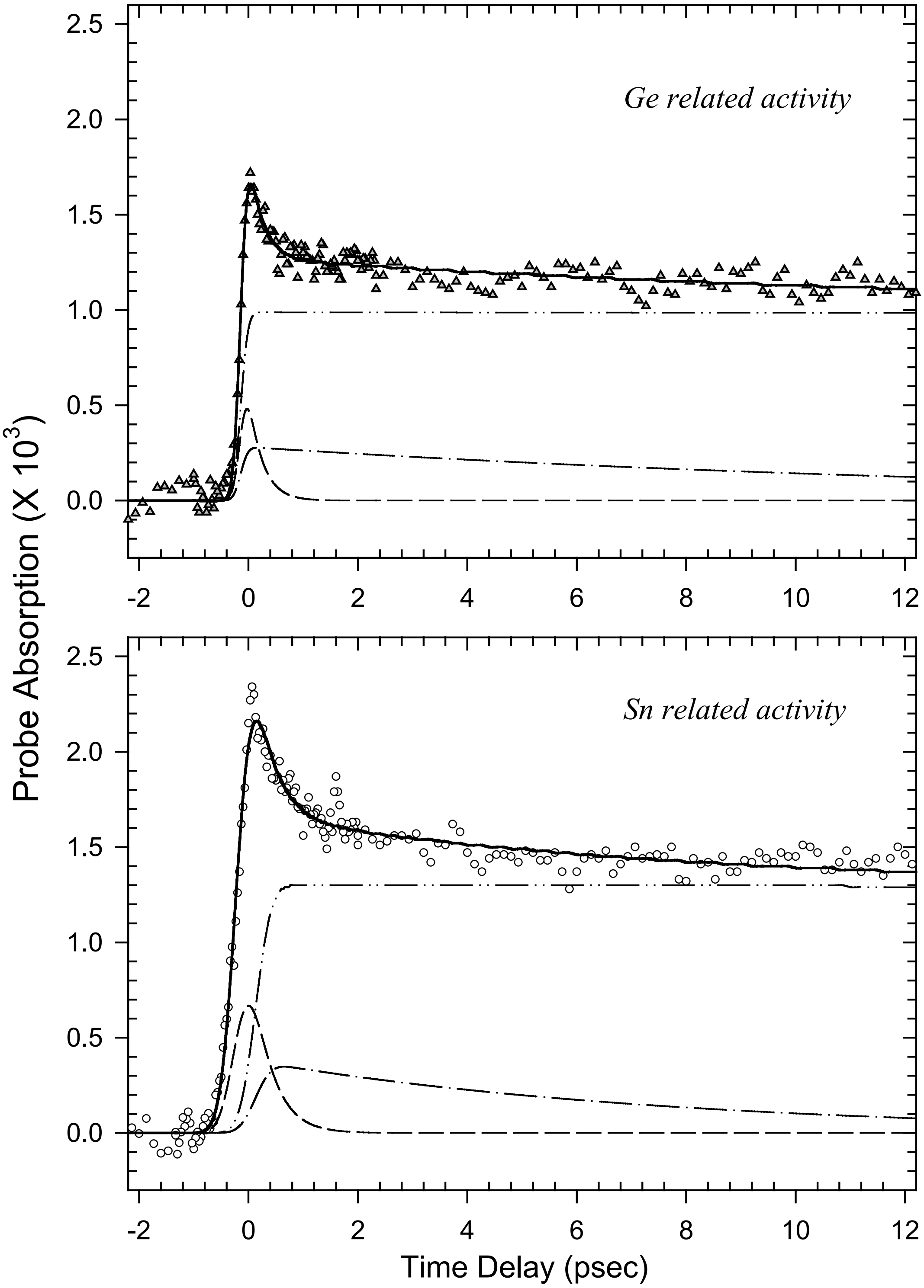

Figure 8.3. Probe absorption as a function of pump-probe time delay for the Ge (grey triangles) and Sn (white circles) doped samples in the -2 ÷ 12 psec range. For both sets of data, the three components (non solid lines) and the total outcome (solid lines) of the fitting procedure are reported (see text for details).

Regarding the fastest process, it occurs in a time scale which is typical of internal conversion (~$10^{-12}$ sec). It suggests that the corresponding component in figure 8.3 is due to the effects of the relaxation to the $\boldsymbol{S_1}$ equilibrium position on the $\boldsymbol{S_1 \rightarrow S_2}$ specific absorption coefficient. In this respect, it is worth to note that, even if in the case of Ge related activity the pump frequency is very close to the value of the ZPL, the population of the vibrational states immediately after the excitation can be different from the thermalized one, inducing the $\boldsymbol{S_1}$ internal conversion.

Concerning the relaxation with lifetime ~10 psec, it speaks for a subsequent slower thermalization after the system reached the equilibrium configuration. So, it can be thought as a cooling process where the system releases the excess of vibrational energy. In other words, it can be rationalized assuming the coupling with very low frequencies modes or a weak coupling with higher frequencies modes.

In agreement with these picture, the observed lifetimes are in agreement with the vibrational states density of silica, which is characterized by a maximum at the frequency of $10^{13}$ $sec^{-1}$ (= 400 $cm^{-1}$) and a relevant amplitude for values greater than $10^{12}$ $sec^{-1}$ (< 30 $cm^{-1}$) (see chapter 1). In addition, recent computational results [**Sen and Dickinson, 2003**] indicated a typical time of 250 fsec for the thermalization of silica network after a high intensity femtosecond laser pulse.

It is worth to note that, in this frame, it is possible to rationalize also the slight differences between the results on Sn and Ge related activities. In agreement with this picture, the fastest process is due to the coupling with the higher frequencies modes, which are expected to be more localized and involving a minor number of atoms around the defect. In this case, the substitution of only one atom can induce an appreciable reduced mass effect which causes a decreasing of the vibrational frequencies [**Galeener and Geissberger, 1983, Galeener *et al.*,1983**]. Regarding the psec decay process, the observed shortening can be explained as a partial effect of the Sn-Ge substitution different from the reduced mass effect. This is indeed not expected in this case, since the lower frequencies involve usually a greater amount of atoms. Since the Sn related ISC times at room temperature are typically hundreds of psec, whereas the Ge related ones are more the nsec (see figure 5.8), we could tentatively ascribe this differences to a small effect of the ISC process on the $S_1$ population $n_S$ of the =Sn•• centers not present in the =Ge•• centers.

## 8.2 Conclusions

We present a pioneer work on the relaxation dynamics, in non thermalized regime, of excited states localized on a defect embedded in silica matrix. In particular, we have investigate the structural dynamics leading to the luminescence and the internal conversion in femto- and picosecond domain performing transient absorption measurements from $S_1$ to $S_2$ of Ge and Sn related B-type activities with a pump-probe setup at room temperature. We have revealed two distinct time domains for the relaxation dynamics: a faster one in the psec domain and a slower one in the nsec domain. The former shows a multiexponential behavior that can be ascribed to an internal conversion toward the $S_1$ equilibrium configuration in hundreds of fsec, followed by a cooling with the phonon population of the matrix in about 10 psec. The slower decay can be attributed to the usual emptying after that the system in the $S_1$ state reaches the thermal equilibrium, leading to $\alpha_T$ emission.

The main result of this experimental investigation is that the psec and sub-psec dynamics are completely dominated by the matrix ones. In particular we have observed that the Sn-Ge substitution have no effect on the $S_1$ internal conversion processes which show to be completely driven by the matrix dynamics. The obtained results agree with the absence of ISC processes able to compete with the internal relaxations.

.

# Chapter 9

# Conclusions and perspectives

In this Ph.D. thesis we have investigated the optical properties and the relaxation processes of an iso-electronic and iso-structural series which consists of three optically active point defects involving a silicon, a germanium and a tin atom, and which exist both in the bulk and surface variants (chapter 1). These centers are characterized by optical activities with close similarities (the Si, Ge and Sn related B-type activity) and by the same defect structure (the two-fold coordinated T atom, where T stands for Si, Ge or Sn, and it is usually indicated with the symbol $=T^{\bullet\bullet}$). The experimental approach has consisted in the study of these optical activities both with steady state and with time resolved spectroscopic techniques, as a function of temperature and excitation energy (chapters 4-8).

As more widely discussed in the first chapter, recent studies preceding this thesis have indicated that, for a deeper understanding of the properties of point defects, the role of the matrix, of its flexibility and of its dynamics should be considered. In spite of these suggestions, only a few works have faced quantitatively this issue, and mainly concerning particular aspects of the Ge related activity. The research work during the Ph.D. course has tried to fill this lack by investigating the iso-structural and iso-electronic $=T^{\bullet\bullet}$ series, both in the bulk and in the surface variant, whose occurrence supplies a powerful tool in order to study the effective role of the conformational disorder and of the local low frequencies dynamics of the matrix on the properties of embedded point defects. The body of the experimental results reported in this thesis has shed new light on this issue, the main new ones being summarized in the following.

- The local dynamics of the matrix and its disorder play a crucial role in all the relaxation processes and optical features of point defects. In particular, the investigated relaxation processes, the radiationless ISC and the radiative $\boldsymbol{S_1}$ decay, have been revealed to be associated with a relevant dispersion of the respective rates, these results being common to the various defects (see chapters 4 and 5) both in the bulk and in the surface environments (chapter 6). We have finely investigated the absorption band profiles as a function of temperature, pointing out, for the first time, that the investigated activities are coupled with local vibrational modes characterized by very low frequencies, this result being in agreement with a remarkable thermally dependent homogeneous contribution to the band width (chapters 4 and 5).

- The study carried out on the heavy atom effect in bulk silica has definitively evidenced that relaxations and thermodynamics features of defects are mainly due to the local matrix dynamics, whose vibrational density of states and the coupling with defects are almost unaffected by the heavy atom substitution (chapter 5). The main effect of this substitution is to increase the spin-orbit coupling between the electronic states of different multiplicity localized on defects, this enhancement been essentially homogenous and related to the defect structure.
- We have found, by comparing the bulk and surface activities, that the same defect in different matrices shows remarkable differences regarding the thermally dependent ISC processes (chapter 6), whereas the heavy atom substitution in surface silica exhibits effects in agreement with the bulk case. Both results corroborate the previous comments on the role of the substitution on the dynamical properties of the defects and on the coupling with the matrix. Concerning the non thermally activated ISC processes, they have also been found to be dramatically affected by the local environment. It is particularly noteworthy that they have also been observed in the surface Si activity, which have a negligible spin orbit term, as

proved by their absence in the case of the respective bulk center. It points out that the efficiency of temperature independent relaxation processes is also significantly linked to the local matrix and its dynamics and not only to the particular defect structure.

- In chapter 7, we have also faced the role of the matrix in modulating the optical activities involving the forbidden $\boldsymbol{T_1 \rightarrow S_0}$ transition. A detailed study of this luminescence under direct $\boldsymbol{S_0 \rightarrow T_1}$ excitation and the comparison with the one induced by the $\boldsymbol{S_0 \rightarrow S_1}$ transition have revealed that the local disorder affects the overall electronic structure of the centers and not only the non radiative phonon-assisted ISC process. We have found that the phonon coupling is essentially homogenous and poorly affected both by the local disorder and by the heavy atom substitution. We also obtained, as a noteworthy result, that different electronic transitions localized on the same defects are coupled with the same vibrational modes, regardless the different involved electronic levels and their multiplicity. An interesting example of cross-correlation effect between the ISC rate and the triplet energy level structure has been evidenced and discussed by comparing the triplet activity excited with the direct $\boldsymbol{S_0 \rightarrow T_1}$ and indirect $\boldsymbol{S_1 \rightarrow T_1}$ transitions.
- We have reported in chapter 8 a pioneer experimental study of the sub-picoseconds relaxation dynamics in non thermalized regime in excited states, which has revealed that these dynamics are completely dominated by the matrix ones. In particular, in this regime, no consequences are associated with the heavy atom effect. The obtained results indicate the absence of ISC processes able to compete with the internal relaxations.
- The remarkable similarities in the optical properties have revealed that B-type activity has a set of features (energy levels scheme, unitary emission quantum yield,

excitation energy pathway, heavy atom effect, sensitivity to the local disorder) completely independent on the particular iso-electronic defect and on the local matrix (chapters 5 and 6). This consideration strongly supports the assignment of B-type activity to only one structural model and suggests that the two-fold coordinated center, even if sensitive to the local geometry, is characterized by a typical structure which can be hardly modified by the local matrix, or, in other words, the matrix is mainly perturbative. Thus, it corroborates the presence of only one defect structure perturbed to give an ensemble of almost degenerate configurational substates, instead of a set of distinct taxonomic configurations.

These new results have provided a clearer and more extensive picture of the physics of defect-matrix coupling and its effects on the electronic structure and related transitions localized on the defect. Furthermore, to rationalize these results, we also developed a theoretical model able to describe an ensemble of optically active point defects embedded in a disordered matrix. The model supposes a functional dependence (mapping) on a conformational coordinate of the optical properties of the centers and of their phonon coupling with the matrix. In this picture, the inhomogeneous broadening of the optical properties and of the coupling parameters are an effect of the conformational disorder of the amorphous matrix that, due to the mapping, reflects itself in a spread of the electronic and vibrational properties of the defect-matrix complex. The experimental cross-correlations are also explained as a consequence of the mapping, which induces a mutual dependence of the properties themselves. The good agreement between theory and experiment on Ge related activity leads to the determination of relevant information such as the homogeneous width of absorption band, its inhomogeneous broadening, the entropy and enthalpy distribution (see chapter 4).

The comparison of surface and bulk variants have revealed several new information on the microscopic mechanisms that put the defect properties in connection with the local dynamics matrix and its arrangement. We discussed these results in the light of the structural model of the =T$^{\bullet\bullet}$ centers and the related electronic orbitals, suggesting some possible microscopic mechanisms (see chapter 6).

Regarding the perspective and the new questions rinsing from this thesis, many aspects of the investigated features deserve further attention and more experimental evidences. In particular, new information could be obtained adopting more specific experimental techniques or varying the host system. Concerning the former point, new and stimulating results could be obtained by continuing the investigation in the femto and picosecond time domain with spectral analysis of the probe signal, also as a function of temperature and excitation energy of the pump. Further information on the conformational heterogeneity and on the relaxation dynamics could be obtained using stationary and time resolved hole burning techniques and single molecule fluorescence spectroscopy. The resonant Raman technique could provide a reliable estimation of the values of high frequency modes and related Huang-Rhys constants.

Concerning the modification of the host system, recent works (see for example **Agarwal and Tomazawa, 1997**) have shown that conformational distribution of silica (especially with respect to the Si-O-Si angle distribution) can be permanently changed by a very high external pressure (of the order of GPa). These results suggest an investigation of the =T$^{\bullet\bullet}$ centers in bulk silica as a function of external pressures in order to vary in a controlled way the local surroundings. A complementary method is a complete change of the host matrix. In this respect, several promising systems exist and in particular the amorphous form of the germanium dioxide (germania), which shows relevant similarity with silica and is characterized by the presence of the two-fold coordinated germanium (see **Skuja, 1992,** and reference therein). With the same methodological approach adopted in this thesis, it should be possible to study some important aspects, as the effect of a different vibrational density of states [**Galeener *et al.*, 1983a** and **c**] or the presence of a remarkable external heavy atom effect. An other possibility is to investigate the role of the dimensionality of the host system on the embedded point defects. This research could be performed using nano and microfilms and nano-particles of silica.

Works on these aspects are in progress.

# Appendices

## A. Fitting procedure details of the theoretical model

In this appendix, we will report the details of the fitting procedure in terms of the theoretical model discussed in paragraph 4.2 (see equations (4.6) - (4.8)) to the experimental data reported in chapter 4 (see figures 4.16 - 4.19).

Regarding the distribution $P(E_A)$ and in agreement with the discussion of section 4.2.1, we will consider the next expression to describe the experimental data:

$$P(E_A) = N\left\{\exp\left[-\frac{1}{2}\left(\frac{E_A - E_A^0}{\sigma_A}\right)^2\right] + R_\beta \cdot \delta\left(E_A - E_A^{\beta_0}\right)\right\} \tag{A.1}$$

where $N$ is a normalization factor. In agreement with equation (4.10), $E_A^\beta$ verifies:

$$E_A^{\beta_0} = -\frac{H_0}{a_H} + E_A^0 \tag{A.2}$$

and the values of $\Delta S$, $E_S$ and $E_T$ for the $\beta_0$ centers are obtained from equations (4.9), (4.11) and (4.12), calculated at $E_A = E_A^{\beta_0}$. Since it has no physical meaning to assume centers characterized by negative values of $\Delta H$, the $E_A$ integration range is constrained to have $\Delta H(E_A) \geq 0$. For this reason, the gaussian term will be all on one side respect to the $\delta$-function and will be abruptly trucked at $E_A^{\beta_0}$.

Concerning $E_A^0$, it has to be compared with the experimental values of first moment of the $B_{2Ge}$ band, $M_1$, which are reported in section 4.1.2 (figure 4.8(a)). Since we are neglecting the thermal behavior of the OA band, we can consider, as a good estimation of $E_A^0$, the average value of $M_1$ in the whole temperature range, which is $E_A^0 = 5.186 \pm 0.016$ eV.

Regarding $\sigma_A$, it is not directly measurable from experimental data but is constrained by the expression $\sigma^2 = \sigma_A^2 + \sigma_{Ex}^2$, where $\sigma^2$ has to be compared with the experimental values of

$M_2$, the second moment of the $B_{2Ge}$ band (see once more section 4.1.2 and figure 4.8(a)). Analogously with the first moment, we will consider the average value of $M_2$ on the whole temperature range as the proper estimation of $\sigma^2 = 0.045 \pm 0.003$ eV, corresponding to $\sigma = 0.212 \pm 0.007$ eV.

About $f(E_{Ex})$, it is a normalized gaussian function centered in zero and with standard deviation, $\sigma_{Ex}$ which obeys the condition $\sigma^2 = o_A^2 + \sigma_{Ex}^2$ too.

In spite of formulating the mapping for the $k_{ISC}$ parameters, it is important to note that all the equations (4.6)-(4.8) can be expressed in a more suitable form in terms of the ratio $k_{ISC}^{E_A}(T)/k_S$ . Considering the eqs. (2.16), this ratio, indeed, can be described by the following expression:

$$\frac{k_{ISC}}{k_S} = \exp\left(\Sigma + \frac{\Delta S}{k_B}\right) \cdot \exp\left(-\frac{\Delta H}{k_B T}\right), \tag{A.3}$$

where $\Sigma$ is a dimensionless constant which satisfies the condition $e^{\Sigma} = k_0/k_S$. In this respect, we note that we can not separate the value of $\Sigma$ from the one of $\widetilde{S}_0/k_B$ , the constant coefficient of equation (4.9) in the $\Delta S$ mapping expression. In other words, we are not able, with our measurements, to separate the entropy contribution to $\boldsymbol{S_1 \rightarrow T_1}$ transition from the homogeneous pre-exponential factor $k_0$, which we consider to be due to a single electronic process, and related more to the structure than to the thermodynamics of defect-matrix complex (see discussion in paragraph 2.2). So, we will set $S_0/k_B = \Sigma + \widetilde{S}_0/k_B$ and, considering equations (4.9) and (4.10), we will use for the fitting procedure the equation

$$\frac{k_{ISC}}{k_S} = \exp\left\{\frac{1}{k_B}\left[S_0 + a_E \cdot (E_A - E_A^0)\right]\right\} \cdot \exp\left\{-\frac{1}{k_B T}\left[H_0 + a_H \cdot (E_A - E_A^0)\right]\right\}. \tag{A.4}$$

Regarding $E_S$ and $E_T$ mapping coefficients, we will fit only $M_{1S}$ at 22 K and $M_{1T}$ at room temperature because, as explained before, they are more representative of $E_S$ and $E_T$

dependence on $E_A$. After the fitting, we will calculate the expected behavior for $M_{1S}$ at room temperature and $M_{1T}$ at 22 K and we will compare them with the relative experimental data.

To find the best fit parameters we fitted at once all experimental data reported in figures 4.16-4.19, except for $M_{1S}$ at room temperature and $M_{1T}$ at 22 K. For the fitting procedure we used the Marquardt‘s algorithm for least-squares estimation of non linear parameters [**Marquardt, 1963**] with a exit condition on the variation of the reduced squares less than $10^{-6}$ after the last iteration.

## B. List of related papers

The results reported in this thesis are subjects of the following works:

- S. Grandi, P. Mustarelli, S. Agnello, M. Cannas, A. Cannizzo: "*Sol-gel GeO2 -doped SiO2 glasses for optical applications*", Journal of Sol-Gel Science and Technology **26** (2003) 915.
- A. Cannizzo, S. Agnello, R. Boscaino, M. Cannas, F.M. Gelardi, S. Grandi, M. Leone: "*Role of vitreous matrix on the optical activity of Ge-doped silica*", Journal of Physics and Chemistry of Solids **64** (2003) 2437.
- S. Agnello, R. Boscaino, M. Cannas, A. Cannizzo, F.M. Gelardi, S. Grandi, and M. Leone: "*Temperature and excitation energy dependence of decay processes of luminescence in Ge-doped silica*", Physical Review B **68** (2003) 165201. *Selected for the November 2003 issue of Virtual Journal of Ultrafast Science published by the American Physical Society and the American Institute of Physics.*
- A. Cannizzo and M. Leone: "*Conformational disorder and optical properties of point defects in vitreous silica*", Philosophical Magazine **84** (2004) 1651.
- S. Agnello, R. Boscaino, M. Cannas, A. Cannizzo, F.M. Gelardi, S. Grandi, M. Leone: *"Spectral heterogeneity of oxygen-deficient centers in Ge-doped silica"*, Radiation Measurements **38** (2004) 645.
- A. Cannizzo, M. Leone, R. Boscaino, A. Paleari, N. Chiodini, S. Grandi, P. Mustarelli: "*Optical activity and conformational disorder in Sn- and Ge-doped vitreous silica. 1. Relaxation processes from excited electronic states under singlet-singlet excitation*", submitted to Physical Review B (2004).

- A. Cannizzo, M. Leone, R. Boscaino, A. Paleari, N. Chiodini, S. Grandi, P. Mustarelli: "*Optical activity and conformational disorder in Sn- and Ge-doped vitreous silica. 2. Relaxation processes from triplet excited electronic states under singlet-triplet excitation*", submitted to Physical Review B (2004).
- A. Cannizzo, S. Agnello, S. Grandi, M. Leone, A. Magistris, V.A. Radzig: "*Luminescence activity of surface and bulk Ge-oxygen deficient centers in silica*", submitted to Journal of Non-Crystalline Solids (2004).
- A. Cannizzo, S. Agnello, M. Cannas, N. Chiodini, M. Leone, A. Paleari: "*Temperature dependence of luminescence decay in Sn-doped silica*", submitted to Journal of Non-Crystalline Solids (2004).

# References

A. Agarwal and M. Tomazawa; J. Non-Cryst. Solids **209** (1997) 166.

S. Agnello, R. Boscaino, M. Cannas, F.M. Gelardi and M. Leone, *Phys. Rev. B* **61** (2000) 1946.

S. Agnello, R. Boscaino, G. Buscarino, M. Cannas and F.M. Gelardi, *Phys. Rev. B* **66** (2002) 113201.

S. Agnello, R. Boscaino, M. Cannas, A. Cannizzo, F.M. Gelardi, S. Grandi, and M. Leone, *Phys. Rev. B* **68** (2003) 165201.

S. Agnello, R. Boscaino, M. Cannas, A. Cannizzo, F.M. Gelardi, S. Grandi, M. Leone, *Rad. Meas.* **38** (2004) 645.

A.V. Amossov, A.O. Rybaltovsky, *J. Non-Cryst. Solids* **179** (1994) 75.

A. Anedda, R. Boscaino, M. Cannas, R. Corpino, F. M. Gelardi, M. Leone, *Nucl. Instrum. Methods B* **116** (1996) 360.

A. Anedda, C. M. Carbonaro, F. Clemente, R. Corpino, *J. Appl. Phys.* **92** (2002) 3038.

A. Anedda, C.M. Carbonaro, F. Clemente, R. Corpino, A. Serpi, *J. Non-Cryst. Solids* **315** (2003) 161.

C.A. Angell, *Chem. Rev.* **102** (2002) 2627.

G.W. Arnold, *IEEE Trans. Nucl. Sci.* **NS20** (1973) 220.

V.N. Bagratashvili, S.I. Tsypina, V.A. Radtsig, A.O. Rybaltovskii, P.V. Chernov, S.S. Alimpiev, Y.O. Simanovskii, *J. Non-Cryst. Solids* **180** (1995) 221.

V.N. Bagratashvili, S.I. Tsypina, P.V. Chernov, A.O. Rybaltovskii, Y.O. Zavorotny, in *Defects in $SiO_2$ and Related Dielectrics: Science and Technology*, edited by G. Pacchioni, L. Skuja, D.L. Griscom (Kluwer Academic Publishers, Netherlands, 2000), pp. 499-514.

R.A. Barrio, F.L. Galeener, E. Martinez, *Phys. Rev. B* **31** (1985) 7779.

M. Benoit and W. Kob, *Europhys. Lett.* **60** (2002) 269.

R. Boscaino, M. Cannas, F.M. Gelardi, M. Leone, *Phys. Rev. B* **54** (1996) 6194

B.H. Bransden, C.J. Joachain, *Physics of atoms and molecules* (JohnWiley & Sons, New York, 1983).

C.J. Brinker, W.L.Warren, and S.Wallace, in *Structure and imperfections in amorphous and crystalline silicon dioxide*, edited by R.A.B. Devine, J.-P. Duraud and E. Dooryhée (John Wiley & Sons, Chichester, 2000), chap. 17, pp.475-493.

R. Brückner, *J. Non-Cryst. Solids* **5** (1970) 123.

M. Cannas, *PhD thesis* (1998). University of Palermo, Department of Physical and Astronomical Sciences.

M. Cannas, R. Boscaino, F. M. Gelardi, and M. Leone, *J. Non-Cryst. Solids* **216** (1997) 99.

A. Cannizzo, S. Agnello, R. Boscaino, M. Cannas, F.M. Gelardi, S. Grandi, M. Leone, *J. Phys. Chem. Solids* **64** (2003) 2437.

N. Chiodini, F. Morazzoni, A. Paleari, R. Scotti, and G. Spinolo, *J. Mater. Chem.* **9** (1999) 2653.

N. Chiodini, F. Meinardi, F. Morazzotti, A. Paleari, R. Scotti, D. Di Martino, *J. Non Cryst. Solids* **261** (2000) 1.

N. Chiodini, F. Meinardi, F. Morazzoni, J. Padovani, A. Paleari, R. Scotti, G. Spinolo, *J. Mater. Chem.* **11** (2001) 926.

A.J. Cohen, Phys. Rev. **105** (1957) 1151.

A. Cupane, M. Leone, E. Vitrano, L. Cordone, *Eur. Biophys. J.* **23** (1995) 385.

K.M. Davis, M. Tomozawa, *J. Non-cryst. Solids* **185** (1995) 203.

J.-C. Diels and W. Rudolph, *Ultrashort Laser Pulse Phenomena* (Academic Press., London, 1996).

R.A.B. Devine, J.-P. Duraud and E. Dooryhée (Eds.), *Structure and imperfections in amorphous and crystalline silicon dioxide* (John Wiley & Sons, Chichester, 2000).

E. Dooryhée, J.-P. Duraud and R.A.B. Devine, in *Structure and imperfections in amorphous and crystalline silicon dioxide*, edited by R.A.B. Devine, J.-P. Duraud and E. Dooryhée (John Wiley & Sons, Chichester, 2000), chap. 14, pp. 349-421.

M.D. Ediger, *Annu. Rev. Phys. Chem.* **51** (2000) 99.

S.R. Elliot, *Physics of Amorphous Materials* (Longman Inc., New York, 1984).

M. Essid, J. Albert, J.L. Brebner, K. Awazu, *J. Non-Cryst. Solids* **246** (1999) 39.

M.L. Frankenheim, *Die Lehre von der Kohäsion*, Breslau (1835) p. 389.

H. Frauenfelder, F. Parak, R.D. Young, *Annu. Rev. Biophys. Chem.* **17** (1988) 451.

F.L. Galeener, A.J. Leadbetter, M.W. Stringfellow, *Phys. Rev. B* **27** (1983a) 1052.

F.L Galeener and A.E. Geissberger, *Phys. Rev. B* **27** (1983b) 6199.

F.L Galeener, A.E. Geissberger, G.W. Ogar Jr., R.E. Loehman, *Phys. Rev. B* **28** (1983c) 4768.

V. Garino-Canina: *Comptes Rendus Acad. Sci.* **238** (1954) 875, 1577.

V. Garino-Canina: *Comptes Rendus Acad. Sci.* **242** (1956) 1982.

V. Garino-Canina; *Verres et réfractaires* **6** (1958) 313.

M. Goldstein, *J. Chem. Phys.* **51** (1969) 3728.

S. Grandi, *PhD thesis* (1998). University of Pavia, Department of Physical Chemistry (in Italian).

S. Grandi, P. Mustarelli, A. Magistris, M. Gallorini, E. Rizzio, *J. Non-cryst. Solids* **303** (2002) 208.

S. Grandi, P. Mustarelli, S. Agnello, M. Cannas, A. Cannizzo, *J. Sol-Gel Sci. Techn.* **26** (2003) 915.

D.L. Griscom, *J. Ceramic Society of Japan* **99** (1991) 899.

D.L. Griscom, *Phys. Rev. B* **64** (2001) 174201.

H.F. Hameka, in *The Triplet State* edited by A.B. Zahlan et al. (Cambridge University Press, London, 1967), pp. 1-27.

D.C. Harris and M.D. Bertolucci, *Symmetry and Spectroscopy* (Oxford University Press, New York, 1978).

G. Herzberg, *Molecular Spectra and Molecular Structure*, vol. 3 (Van Nostrand Reinhold Company, New York, 1966).

H. Hosono and Y. Abe, *Phys Rev B* **46** (1992) 11445.

B.K. Huang and A. Rhys, *Proc. R. Soc. Ser.* A**204** (1950) 406.

H. Imai, K. Arai, H. Imagawa, H. Hosono, Y. Abe, *Phys.Rev. B* **38** (1988) 12772.

H.H. Jaffé and M. Orchin, *Theory and applications of UV spectroscopy* (J. Wiley and Sons, New York, 1970).

M. Kohketsu, K. Awazu, H. Kawazoe, M. Yamane, *Jpn. J. Appl. Phys.* **28** (1989) 615.

R. Kohlrausch, *Ann. Phys.* (Leipzig) **12**, 393 (1847).

J.R. Lakowicz, *Principles of Fluorescence Spectroscopy* (Plenum Press, New York, 1983).

A.A. Lebedev, *Trudy Gos. Opt. Instit.* **2** (1921) 1.

M. Leone, R. Boscaino, M. Cannas, F.M. Gelardi, *J. Non-Cryst. Solids* **216** (1997) 105.

M. Leone, S. Agnello, R. Boscaino, M. Cannas and F.M. Gelardi, *Phys. Rev. B* **60** (1999a) 11475.

M. Leone, R. Boscaino, M. Cannas, F.M. Gelardi, *J. Non-Cryst. Solids* **245** (1999b) 196.

M. Leone, S. Agnello, R. Boscaino, M. Cannas and F.M. Gelardi, in *Silicon-based materials and devices*, edited by H.S. Nalwa (Academic Press, San Diego, 2001), Vol. 2, Chap. 1, pp. 1-50.

N. Levy; *Appl. Opt.* **20** (1981) 460.

J.J. Markham, *Rev. Mod. Phys.* **31** (1959) 956.

D.W. Marquardt, *J. Soc. Ind. Appl. Math.* **11** (1963) 431.

M. Martini, F. Meinardi, A. Paleari, G. Spinolo, A. Vedda, *Phys. Rev. B* **57** (1998) 3718.

B. H. McMahon, J. D. Müller, C. A. Wraight, and G. U. Nienhaus, *Biophys. J.* **74** (1998) 2567.

P. Mezza, J. Phalippou, and R. Sempere, *J. Non Cryst. Solids* **243** (1999) 75.

T.F. Middleton and D.J. Wales, *Phys. Rev. B* **64** (2001) 024205.

E.W.J. Mitchell and E.G.S. Paige, *Phil. Mag.* **2** (1957) 941.

C. Morterra and M.J.D. Low, *Ann. N. -Y Acad. Sci.* **220** (1973) 133.

R.L. Mozzi and B.E. Warren, *J. Appl. Crystallogr.* **2** (1969) 164.

K. Nagasawa, H. Mizuno, Y. Yamasaka, R. Tohmon, Y. Ohki and Y. Hama, in *The Physics and Technology of Amorphous $SiO_2$*, edited by J. Arndt, R. Divine and A. Revesz (Plenum, New York, 1988) p. 193.

H.S. Nalwa (Ed.), *Silicon-based materials and devices* (Academic Press, San Diego, 2001).

V.B. Neustruev, *J. Phys. Condens. Matter* **6** (1994) 6901.

H. Nishikawa, E. Watanabe, D. Ito, and Y. Ohki, *Phys. Rev. Lett.* **72** (1994) 2101.

H. Nishikawa, Y. Miyake, E. Watanabe, D. Ito, K.S. Seol, Y. Ohki, K. Ishii, Y. Sakurai, K. Nagasawa, *J. Non Cryst. Solids* **222** (1997) 221.

G. Pacchioni and R. Ferrario, *Phys. Rev. B* **58** (1998) 6090.

G. Pacchioni, L. Skuja, D.L. Griscom (Eds.), *Defects in $SiO_2$ and Related Dielectrics: Science and Technology* (Kluwer Academic Publishers, Netherlands, 2000).

P. Paillet, J.L. Leray, and H.J. von Bardeleben, in *Structure and imperfections in amorphous and crystalline silicon dioxide*, edited by R.A.B. Devine, J.-P. Duraud and E. Dooryhée (John Wiley & Sons, Chichester, 2000), chap. 12, pp. 293-328.

A. Pasquarello and R. Car, *Phys. Rev. Lett.* **80** (1998) 5145.

M.H.L. Pryce, in *Phonons in perfect lattices and in lattices with point imperfections*, edited by R.W.H. Stevenson (Oliver & Boyd Edinburgh London, 1966).

V.A. Radzig, *Chem. Phys. Reports* **14** (8) (1995a) 1206.

V.A. Radzig, *J. Non-Cryst. Solids* **180** (1995b) 221.

V.A. Radzig, *J. Non-Cryst. Solids* **239** (1998) 49.

V.A. Radzig, in *Defects in $SiO_2$ and Related Dielectrics: Science and Technology*, edited by G. Pacchioni, L. Skuja, D.L. Griscom (Kluwer Academic Publishers, Netherlands, 2000), pp. 339-370.

K.K. Rebane, *Impurity Spectra of Solids* (Plenum Press, New York, 1970).

E.P. O'Reilly and J. Robertson, *Phys. Rev. B* **27** (1983) 3780.

C. Rullière (Ed.), *Femtosecond Laser Pulses* (Springer-Verlag, Berlin Heidelberg, 1998).

A.O. Rybaltovskii, I.A. Kamenskikh, V.V. Mikhailin, N.L. Semenova, D.A. Spasskii, G. Zimmerer, P.V. Chernov, and K.M. Golant, *Glass Phys. Chem.* **28** (2002) 379.

A. Sakoh, M. Takahashi, T. Yoko, J. Nishii, H. Nishiyama, I. Miyamoto, *Opt. Express* **11** (2003) 2679.

Y. Sakurai, *J. Non-Cryst. Solids* **271** (2000) 218.

Y. Sakurai and K. Nagasawa, *J. Non-Cryst. Solids* **291** (2001) 86.

V. Sanfratello, A. Boffi, A. Cupane and M. Leone, *Biopolymers (Biospectroscopy)* **57** (2000) 291.

P.C. Schultz; *Proc. 11th Int. Congr. On Glass* (Prague); vol. **III** (1977) 155.

K.S. Seol, Y. Ohki, H. Nishikawa, M.Takiyama, Y. Hama, *J. Appl. Phys.* **80** (1996) 6444.

J. Shen, J. Wang, B. Zhou, Z. Deng, Z. Weng, L. Zhu, L. Zhao, and Y. Li, *J. Non-Cryst. Solids* **225** (1998) 315.

W. Siebrand, in *The Triplet State* edited by A.B. Zahlan et al. (Cambridge University Press, London, 1967), pp. 31-45.

W. Siebrand, *J. Chem. Phys.* **44** (1966) 4055.

L.N. Skuja, A.R. Silin, J. Mares, *Phys. Status Solidi (b)* **50** (1978) K149.

L.N. Skuja, A.N. Streletsky, A.B. Pakovich, *Solid State Comm.* **50** (1984) 1069.

L.N. Skuja, *J. Non-Cryst. Solids* **149** (1992) 77.

L.N. Skuja, *J. Non-Cryst. Solids* **167** (1994a) 229.

L.N. Skuja, *J. Non-Cryst. Solids* **179** (1994b) 51.

L.N. Skuja, T. Suzuki, K. Tanimura, *Phys. Rev. B* **52** (1995) 15208.

L.N. Skuja, *J. Non Cryst. Solids* **239**, 16 (1998).

L.N. Skuja, in *Defects in $SiO_2$ and Related Dielectrics: Science and Technology*, edited by G. Pacchioni, L. Skuja, D.L. Griscom (Kluwer Academic Publishers, Netherlands, 2000), pp. 73-116.

B.B. Stefanov and K. Raghavachari, *Appl. Phys. Lett.* **71** (1997) 770.

A. Streltsov and N. F. Borrelli, *J. Opt. Soc. Am. B* **19** (2002) 2496.

R. Tohmon, H. Mizuno, Y. Ohki, K. Sasagane, K. Nagasawa, Y. Hama, *Phys. Rev. B* **39** (1989) 1337.

M. Tomozawa, K.M. Davis, *Mat. Sci. Eng. A* **272** (1999) 114.

M. Tomozawa, in *Silicon-based materials and devices*, edited by H.S. Nalwa (Academic Press, San Diego, 2001), Vol. 1, Chap. 3, pp. 127-154.

T.E. Tsai, E.J. Friebele, M. Rajaram, S. Mukhapadhayay, *Appl. Phys. Lett.* **64** (1994) 1481.

T. Uchino and T. Yoko, *J. Chem. Phys.* **108** (1997) 8130.

T. Uchino, M. Takahashi, T. Yoko, *Phys. Rev. B* **62** (2000) 2983.

P. Umari, X. Gonze, A. Pasquarello, *Phys. Rev. Lett.* **90** (2003) 027401.

H. Wakabayashi and M. Tomozawa, *J. Am. Ceram. Soc.* **72** (1989) 1850.

R.A. Weeks, *J. Appl. Phys.* **27** (1956) 1376.

M. Weissbluth, *Atoms and Molecules* (Academic Pres, New York, 1978).

A.C. Wright and R.N. Sinclair, in *Structure and imperfections in amorphous and crystalline silicon dioxide*, edited by R.A.B. Devine, J.-P. Duraud and E. Dooryhée (John Wiley & Sons, Chichester, 2000), chap. 5, pp. 121-150.

M.J. Yuen; *Appl. Opt.* **21** (1982) 136.

Yuhai Tu, J. Tersoff, G. Grinstein, D. Vanderbilt, *Phys. Rev. Lett.* **81** (1998) 4899.

B.L. Zang, K. Raghavachari, *Phys. Rev. B* 55 (1997) R15993.

G. Zimmerer, *Nucl. Instrum. Methods A* **308** (1991) 178.

N. Zotov, I. Ebsjö, D. Timpel and H. Keppler, *Phys. Rev. B* **60** (1999) 6383.

# Acknowledgements

In the previous 190 pages I discussed my research activity during the Ph.D. course. Thus, I wish to devote at least one page to my human and professional experience.

I believe that the highest aim of a Ph.D. course is not only to produce scientific results, but to achieve capabilities of autonomous research and of synthesis. These capabilities can be developed only with everyday discussions and collecting thoughts and suggestions from people around.

In particular, I wish to express my most sincere gratitude to Prof. Maurizio Leone who has closely followed me in all phases of my training. I thank also Profs. Roberto Boscaino and Franco M. Gelardi, who have been contributed all the time to my personal and professional improvement.

Drs. Marco Cannas and Simonpietro Agnello deserve a particular appreciation for their constant and skilful presence in any occasion. Only their patience has been equal to their encouragement.

I wish to acknowledge Mrs. Gaetano Lapis and Gianluca Napoli for their Technical help on cryogenic measurements.

It has been fundamental for my training the comparison with people and working environments external to the Department. I express gratitude for the precious and stimulating discussions to Profs. Giorgio M. Spinolo, Alberto Paleari and Gianfranco Pacchioni of the Department of Material Science (University of Milano-Bicocca, Italy), Prof. Piercarlo Mustarelli of the Department of Physical Chemistry (University of Pavia, Italy), Prof. Victor A. Radzig of the N.N. Semenov Institute of Chemical Physics (Russian Academy of Sciences of Moscow, Russian Federation), Profs. Anatoly Trukhin and Linards Skuja of the Institute of Solid State Physics (University of Latvia), Prof. Alberto Anedda and Dr. Carlo Maria Carbonaro from the Department of Physics (University of Cagliari, Italy), Prof. Alberto Diaspro from the Department of Physics (University of Genova, Italy), Prof. Giberto Chirico from the Department of Physics (University of Milano-Bicocca, Italy), and Dr. Davide Donadio from the Department of Chemistry and Applied Biosciences (Swiss Federal Institute of Technology of Zurich, Switzerland)

I wish to thank Prof. Majed Chergui and his group, particularly Dr. Frank Van Mourik, Wojciech Gawelda, Erwin Portuondo Campa and Luigi Bonacina, to have placed his laboratory at disposal and to have spent time in stimulating discussions with me.

Dr. Marco Kirm of the Prof. Georg Zimmerer's group and Prof. Alberto Paleari are acknowledged for measurements time at DESY HASYLAB (Hamburg).

A particular and sincere thankfulness to those people of the Department who have shared with me this period of my life and with whom I am happy to have established a real friendship.

I confirm to my family my deep gratefulness, and not only for these last three years.

I wish that the last thought of this work is to my wife, Michela.